Pontifícia Universidade Católica
do Rio de Janeiro

José Eduardo Sanson Portella de Carvalho

Seasonal modelling of integrated renewable energy storage systems: 4E analysis of CAES, hydrogen, and lithium-ion battery for residential buildings in Lyon and Rio de Janeiro

Tese de Doutorado

Thesis presented to the Programa de Pós-Graduação em Engenheria Mecânica of PUC-Rio in partial fulfillment of the requirements for the degree of Doutor em Engenheria Mecânica.

Advisor: Prof. Florian Alain Yannick Pradelle
Co-advisor: Prof. Rémi Revellin
Co-advisor: Prof. Romuald Rullière

Rio de Janeiro
May 2025

Pontifícia Universidade Católica
do Rio de Janeiro

José Eduardo Sanson Portella de Carvalho

Seasonal modelling of integrated renewable energy storage systems: 4E analysis of CAES, hydrogen, and lithium-ion battery for residential buildings in Lyon and Rio de Janeiro

Thesis presented to the Programa de Pós-Graduação em Engenharia Mecânica of PUC-Rio in partial fullfilment of the requirements for the degree of Doutor em Engenharia Mecânica. Approved by the Examination Committee.

Prof. Florian Alain Yannick Pradelle
Advisor
Pontifícia Universidade Católica do Rio de Janeiro

Prof. Rémi Revellin
Co-advisor
INSA Lyon

Prof. Romuald Rullière
Co-advisor
INSA Lyon

Prof. Lavinia Grosu
Université Paris Nanterre

Prof. Marc Clausse
INSA Lyon

Prof. Nolwenn Le Pierrès
Université Savoie Mont Blanc

Prof. Sergio Leal Braga
Pontifícia Universidade Católica do Rio de Janeiro

Prof. Silvio Oliveira Junior
Universidade de São Paulo

Prof. Waldyr Luiz Ribeiro Gallo
Universidade Estadual de Campinas

Rio de Janeiro,
May 2025

José Eduardo Sanson Portella de Carvalho

Graduated in mechanical engineering at Pontifícia Universidade Católica do Rio de Janeiro in 2017. Master's degree in mechanical engineering at Pontifícia Universidade Católica do Rio de Janeiro in 2020.

Bibliographic data

Carvalho, José Eduardo Sanson Portella de

Seasonal modelling of integrated renewable energy storage systems: 4E analysis of CAES, hydrogen, and lithium-ion battery for residential buildings in Lyon and Rio de Janeiro / José Eduardo Sanson Portella de Carvalho; advisor: Florian Alain Yannick Pradelle, co-advisor: Rémi Revellin; co-advisor: Romuald Rullière. – 2025.

230 f.: il. color.; 30 cm

Tese (doutorado)–Pontifícia Universidade Católica do Rio de Janeiro, Departamento de Engenharia Mecânica, 2025.

Inclui bibliografia

1. Engenharia Mecânica – Teses. 2. Energia. 3. Exergia. 4. Exergoeconomia. 5. Ambiental. 6. Energia solar. I. Pradelle, Florian Alain Yannick. II. Revellin, Rèmi. III. Rullière, Romuald. IV. Pontifícia Universidade Católica do Rio de Janeiro. Departamento de Engenharia Mecânica. V. Título.

CCD: 621

Acknowledgements

Finally, the moment has come!

A PhD thesis is a demanding and lengthy journey that requires the unconditional support of many loving and supportive people. These years have been a unique and intense experience, allowing me to spend a year living in Lyon, cherish new and lasting friendships, and grow both professionally and personally. I want to express my immense gratitude to each person who crossed my path and contributed to the completion of this project.

I would like to thank my advisors, who trusted me and gave me the autonomy to develop this work, always providing insightful advice. Florian Pradelle, who continuously encouraged me to pursue research and pushed me to give my best at all times. Thank you for also motivating me to spend a year in France and for assisting me throughout the entire process. I am grateful for all our exchanges, regardless of time-zone or country. Rémi Revellin and Romuald Rullière, who accepted me as a PhD student and welcomed me to INSA-Lyon and efforts in making me feel comfortable in a new country. I deeply appreciate all the opportunities given and our discussions, whether in person or over Zoom.

My family – Joanna, Matê, Aloysio and Scotch - who may not fully understand my studies but always show interest and support. Thank you for being there for me during the difficult moments of this journey.

My girlfriend, Tali, who has shown unconditional support throughout these years, both during our time apart and together. Thank you for your patience on the days I had to stay home studying and for all the love and care that made each day easier.

My friends in Brazil - Serpa, Sergio (Γεια μας!), Gabi, Argento, Bizzo, Resende, Julia, Guilherme, Fernanda, André, Mayara, Edson, Lucas, Pedro, João and Maria —who made my days in Rio de Janeiro lighter, bringing laughter and smiles even through tough times.

My friends in France - Marcelo, Baroni, Barboza, Carol, Daniel, Igor, Enrique, Milena, Leo, Vic, Antoine, Cong, Kiki, and Taha—who made me feel at home, supported me during tough times, taught me French, and shared so many wonderful moments in the city of Lyon.

To my psychologist, Andrea, who has stood by me for a long time and always encouraged me to pursue my dreams. To Parise, my first advisor, who introduced

me to research. To Laura, my French teacher which was pivotal for me to survive France. And to Ghady Dib, which previous works served as a base for mine.

To the members of the jury –Lavinia Grosu, Nolwenn Le Pierrès, Marc Clausse, Silvio Oliveira Junior, Waldyr Luiz Ribeiro Gallo, and Sergio Leal Braga - who kindly agreed to be part of such an important moment for me.

To all the professors and staff at PUC-Rio who have accompanied me on this journey since I entered the university in 2012.

This study was financed in part by the Coordenação de Aperfeiçoamento de Pessoal de Nível Superior - Brasil (CAPES) - Finance Code 001.

This study was financed in part by Campus France through the French government's Eiffel Excellence Scholarship Program (grant number: n° P850049E).

Abstract

Carvalho, José Eduardo Sanson Portella de; Pradelle, Florian Alain Yannick (Advisor); Revellin, Rémi (Co-advisor); Rullière, Romuald (Co-Advisor). **Seasonal modelling of integrated renewable energy storage systems: 4E analysis of CAES, hydrogen, and lithium-ion battery for residential buildings in Lyon and Rio de Janeiro.** Rio de Janeiro, 2025. 230p. Tese de Doutorado - Departamento de Engenharia Mecânica, Pontifícia Universidade Católica do Rio de Janeiro.

Integrating intermittent renewable sources with energy storage systems is an effective strategy to enhance energy network reliability and ensure power availability. This study examines three different energy storage technologies: Compressed Air Energy Storage (CAES), hydrogen, and lithium-ion batteries. These systems are coupled with photovoltaic panels and applied to a residential building in Lyon (France) and Rio de Janeiro (Brazil). The analysis spans a full year of operation and is evaluated using a 4E approach, assessing energy, exergy, exergoeconomics, and environmental impact. In terms of efficiency, CAES and hydrogen systems exhibit similar performance, except in the trigeneration configuration, where hydrogen demonstrates superior results. From an economic standpoint in both Rio de Janeiro and Lyon, when compared to business as usual, the hydrogen system incurs the highest costs (+260.9% and +244.1%), followed by CAES (+206.4% and +197.8%) and the lithium-ion batteries (+71.0% and +67.6%). Regarding environmental impact, CAES and lithium-ion batteries effectively reduce CO_2 equivalent emissions in both cities, with greater benefits observed in Rio de Janeiro. In contrast, the hydrogen system only becomes viable when biogas replaces natural gas, as the system's performance improves significantly, substantially reducing the cost of avoided CO_2 emissions. With this configuration, all systems are able to avoid emission, notably in Rio de Janeiro, with 24.3 tons, 50.0 tons, and 26.1 tons for CAES, hydrogen and lithium-ion batteries. In Lyon, the values are lower with 2.45 tons, 15.3 tons and 1.49 tons. Overall, all three systems show promising potential, but their feasibility depends on cost reductions and efficiency improvements of its components.

Keywords

Energy; exergy; exergoeconomy; environmental; solar energy.

Resumo

Carvalho, José Eduardo Sanson Portella de; Pradelle, Florian Alain Yannick (Advisor); Revellin, Rémi (Co-advisor); Rullière, Romuald (Co-advisor). **Modelagem sazonal de sistemas renováveis de armazenamento de energia integrado: análise 4E de CAES, hidrogênio, e bateria ion-litio para prédios residenciais em Lyon e Rio de Janeiro.** Rio de Janeiro, 2025. 230p. Tese de Doutorado - Departamento de Engenharia Mecânica, Pontifícia Universidade Católica do Rio de Janeiro.

Integraração de fontes renováveis intermitentes com sistemas de armazenamento de energia é uma estratégia eficaz para aumentar a confiabilidade da rede elétrica e garantir a disponibilidade de energia. Este estudo analisa três diferentes tecnologias de armazenamento de energia: Armazenamento de Energia por Ar Comprimido (CAES), hidrogênio e baterias de íons de lítio. Esses sistemas são acoplados a painéis fotovoltaicos e aplicados a um edifício residencial em Lyon (França) e no Rio de Janeiro (Brasil). A análise abrange um ano completo de operação e é avaliada por meio da abordagem 4E, considerando energia, exergia, exergoeconomia e impacto ambiental. Em termos de eficiência, os sistemas de CAES e hidrogênio apresentam desempenhos similares, exceto na configuração de trigeração, onde o hidrogênio demonstra resultados superiores. Do ponto de vista econômico, tanto no Rio de Janeiro quanto em Lyon, comparado ao cenário de referência, o sistema de hidrogênio apresenta os maiores custos (+260,9% e +244,1%), seguido pelo CAES (+206,4% e +197,8%) e pelas baterias de íons de lítio (+71,0% e +67,6%). Em relação ao impacto ambiental, CAES e baterias de íons de lítio reduzem efetivamente as emissões equivalentes de CO_2 em ambas as cidades, com maiores benefícios observados no Rio de Janeiro. Em contraste, o sistema de hidrogênio só se torna viável quando o biogás substitui o gás natural, pois o desempenho do sistema melhora significativamente, reduzindo substancialmente o custo das emissões evitadas de CO_2. Com essa configuração, todos os sistemas conseguem evitar emissões, destacando-se o Rio de Janeiro, com 24,3 toneladas, 50,0 toneladas e 26,1 toneladas para CAES, hidrogênio e baterias de íons de lítio, respectivamente. Em Lyon, os valores são menores, com 2,45 toneladas, 15,3 toneladas e 1,49 toneladas. De modo geral, os três sistemas apresentam um potencial promissor, mas sua viabilidade depende da redução de custos e da melhoria da eficiência de seus componentes.

Palavras-chave

Energia; exergia; exergoeconomia; ambiental; energia solar.

Summary

List of Figures

List of Tables

Nomenclature

a	Equation of state constant [-], extent of steam reforming reaction [mol/s], ideal factor [-]
A	Area [m²]
b	Equation of state constant [-], extent of water-shift reaction [mol/s]
B	Empiric constant [-]
C	Heat capacity [kJ/K], Cost [$]
c	Extent of electrochemical reaction [mol/s], unit cost [$/kWh]
$\dot{C}$	Cost rate [$/h]
Cap	Rated Capacity [kJ]
c_p	Specific heat at constant pressure [kJ/(kg.K)]
C_r	Heat capacity ratio [-]
CRF	Capital recovery factor [-]
c_v	Specific heat at constant volume [kJ/(kg.K)]
D	Effective gaseous diffusivity [m²/s]
e	Air excess [%], specific emission per unit of energy [kg/kWh], specific exergy [kJ/kg]
E	Activation energy level [J/mol] ,energy [kJ]
E_t	Total energy [kJ]
$\boldsymbol{e}$	Specific exergy [kJ/kg]
$\dot{E}$	Energy rate [kW]
E_n	Nernst potential [V]
Ex	Exergy [kJ]
$\dot{E}x$	Exergy rate [kW]
F	Faraday coefficient [C/mol]
f	Exergoeconomic factor [-]
G	Molar Gibbs free energy [kJ/mol], solar radiation [kW/m²]
g	Gravity [m/s²]
h	Specific enthalpy [kJ/kg]
I	Electric current [A]
I_0	Reverse saturation current [A]
I_L	Light current [A]
i_r	Interest rate [%]
j	Current density [A/m²]
j_0	Exchange current density [A/m²]
k_b	Boltzmann constant [m².kg/(s².K)]
k_t	Temperature coefficient of short-circuit current [A/K]
K	Equilibrium constant [-]
L	Length [m]
m	Amount of oxygen per mol of feedstock [-], mass [kg]
M	Molecular weight [g/mol]
$\dot{m}$	Mass flow rate [kg/s]
n	Number of moles [-]
$\dot{n}$	Molar flow rate [mol/s]
n_c	Number of compressors [-]
n_{cell}	Number of cells [-]
n_e	Number of transferred electrons [-]
n_{stack}	Number of stacks [-]

n_t	Number of turbines [-]
n_y	Lifetime operation [y]
P	Pressure [kPa]
q	Electron charge [C], equation of state constant [-]
Q	Heat [kJ]
Q_{id}	Ideal electric charge [C]
Q_{re}	Actual electric charge [C]
$\dot{Q}$	Rate of energy transfer by heat [kW]
R	Electrical resistance [Ω]
$\bar{R}$	Universal gas constant [kJ/(kmol.K)]
r	Recirculation ratio [-], relative cost [-]
R_g	Gas constant [kJ/(kg.K)]
s	Specific entropy [kJ/(kg.K)]
T	Temperature [K]
t	Time [s]
u	Specific internal energy [kJ/kg]
U	Overall heat transfer coefficient [kW/(m².K)]
U_f	Fuel utilization ratio [-]
U_o	Air utilization ratio [-]
V	Molar volume [m³/mol], voltage [V]
v	Specific volume [m³/kg], stoichiometry coefficient [-], velocity [m/s]
V_b	Bus Voltage [V]
w	Amount of moisture per mol of feedstock [-], specific work [kJ/kg]
W	Work [kJ]
$\dot{W}$	Rate of energy transfer by work [kW]
x	Molar fraction [-], number of atoms of hydrogen per number of atoms of carbon in feedstock [-]
y	Molar concentration [-], number of atoms of oxygen per number of atoms of carbon in feedstock [-]
z	Height [m], number of atoms of nitrogen per number of atoms of carbon in feedstock [-]
Z	Purchased equipment cost [$]
$\dot{Z}$	Investment cost rate of a component [$/h]

Greek Letter

ω	Acentric fator [-]
η_a	Activation overpotential [V]
α	Air-to-Fuel ratio [-]
τ	Annual operation hours [h]
μ	Chemical potential [kJ/mol]
ρ	Density [kg/m³], Electrical resistivity [Ω.m]
ε	Diode diffusion factor [-], equation of state constant [-]
ϵ	Effectiveness [-]
η	Efficiency [-]
ϑ	Emission per unit of energy [kg/kJ]
λ	Empiric constant [-], stoichiometric ratio [-], water content [-]
Ω	Equation of state constant [-]
ψ	Equation of state constant [-]
β	Equation of state constant [-], pressure Ratio [-],
σ	Equation of state constant [-], proton conductivity [S/m], self-discharge rate [%/h]
ξ	Extent of reaction [-]
γ	Maintenance factor [-], shape factor [-], specific heat ratio [-]
δ	Thickness [m]
$\forall$	Volume [m³]

Subscript

0	Ambient
a	Anode
ab	Afterburner, absorption chiller
act	Activation
air	Air
bat	Battery
bu	Burner
c	Compressor, cold, cathode, critical point
cell	Cell
ch	Chemical
cha	Charging
conc	Concentration
conv	Convertion
cool	Cooling
$CO_{2,eq}$	CO_2 equivalent
d	Destroyed, Desorber
des	Design
dis	Discharging
e	Electrolyte
elec	Electric
en	Energy
ev	Expansion valve
exe	Exergy
f	Faraday, final, fuel

grid	Grid
h	Hot
he	Heat Exchanger
heat	Heating
i	Inlet
id	Ideal
ig	Ideal gas
int	Interconnect
ise	Isentropic
ki	Kinectic
lim	Limit
max	Maximum
min	Minimum
mix	Mixer
mp	Maximum power point
o	Outlet
oc	Open circuit
ohm	Ohmic
op	Operation
p	Product, pump
PEMEC	Proton exchanger membrane electrolyzer
ph	Physical
pt	Potential
PV	Photovoltaic Panel
r	Reduced condition
re	Real
ref	Reference, reformer
s	System
sc	Short-circuit
SOFC	Solid Oxide Fuel Cell
sr	Steam reforming
st	Stored
stack	Stack
stg	Storage
sto	Stoichiometric
sun	Sun
t	Turbine, time
TES	Thermal energy storage
water	Water
wind	Wind
ws	Water gas shifting

Superscript

0	Standard
CI	Capital investment
ch,0	Standard chemical
OM	Operation and Maintenance
ref	Reference

Abbreviation

A-CAES	Adiabatic compressed air energy storage
BAU	Business as usual
BECCS	Bioenergy with carbon capture and storage
CAES	Compressed air energy storage
CCD	Central composite design
CCS	Carbon capture and storage
CCUS	Carbon capture utilization and storage
CEPCI	Chemical engineering plant cost index
COP	Coefficient of performance
CPS	Cell per stack
CRF	Capital recovery factor
DAC	Direct air capture
DoE	Design of Experiments
EER	Energy efficiency ratio
EoS	Equation of State
ESS	Energy storage sources
GHG	Greenhouse gas
GT	Gas turbine
GTCC	Gas turbine combined cycle
HP	Heat pump
LHV	Low heating value
NCS	Number of cells connected in series
NG	Natural gas
NP	Number of modules connected in parallel
NS	Number of modules connected in series
NTU	Number of transfer units
NZE	Net zero emissions
PEMEC	Proton exchange membrane electrolyzer
PV	Photovoltaic
RES	Renewable energy storage
RTE	Round-trip efficiency
SOC	State of charge
SOEC	Solid oxide electrolyzer
SOFC	Solid oxide fuel cell
TES	Thermal energy storage
VCC	Vapour compression cycle

“All we have to decide is what to do with the time that is given us” ***Gandalf***

1
Introduction

This chapter explores the global energy transition toward a net-zero emissions scenario, highlighting the growing role of photovoltaic and wind power in the energy mix, examines their integration with energy storage systems and the future prospects of hydrogen in both the near and long term.

1.1.
Context

Human activities have been the primary driver of observed warming since the mid-20th century. The resulting temperature rise has already led to significant changes in both human and natural systems, including droughts, floods, other extreme weather events, sea level rise, and biodiversity loss. In 2015, the Paris Agreement, a legally binding international treaty on climate change, was adopted by 196 Parties during the United Nations Climate Change Conference (COP21) in Paris. Its main objective is to limit the global average temperature increase to below 2°C above pre-industrial levels, while striving to keep the rise within 1.5°C (1,2).

Net Zero Emissions (NZE) scenario portrays a pathway for the global energy sector to achieve net zero CO_2 emissions by 2050 while limiting long-term global warming to 1.5 °C. This scenario meets the key energy-related UN Sustainable Development Goals, in particular by achieving universal access to modern energy services by 2030. Stated Policies Scenario (STEPS) projects energy demand and supply, and their implications for emissions taking account of established and planned policies and regulations. It incorporates recent available data and projections on technology cost, manufacturing capacity and industrial strategies (3).

The global average temperature rise above pre-industrial levels is currently around 1.2°C. However, many regions already experience higher regional warming, with 20-40% of the global population enduring over 1.5°C of warming during at least one season. When comparing the NZE and STEPS scenarios, the projected temperature trends show distinct patterns. The International Energy Agency's STEPS scenario anticipates a moderate decline in energy sector CO_2

emissions by 2050, leading to continued global warming. Under this scenario, temperatures are projected to exceed 1.9°C by 2050 and reach approximately 2.4°C by 2100. In contrast, the NZE scenario sees a peak temperature rise just below 1.6°C by 2040, followed by a gradual decline to 1.4°C (2,3). These scenarios are illustrated in Figure 1.

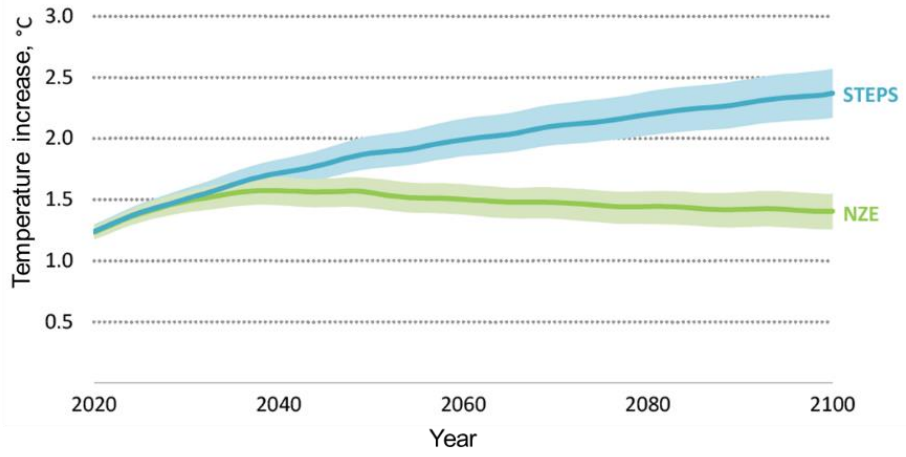

Figure 1: Median warming in the STEPS and NZE Scenario, 2020-2100 (3).

In the NZE scenario, CO_2 emissions from the energy sector decline sharply from 37 Gt in 2022 to 24 Gt by 2030 and 13.5 Gt by 2035. By 2050, a transformation of the energy matrix, along with advancements in direct air capture and storage (DACS) and bioenergy with carbon capture and storage (BECCS), enables the energy sector to achieve net zero CO_2 emissions (3), as illustrated in Figure 2.

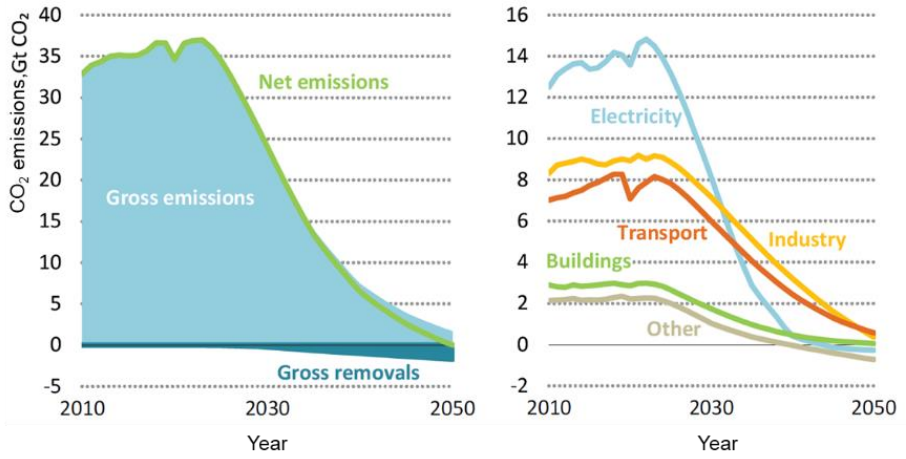

Figure 2: Energy sector gross emissions and removals, total net CO_2 emissions, and net emissions by sector in NZE scenario, 2010-2050 (3).

Achieving net zero emissions in the energy sector by 2050 requires utilizing all available measures to reduce emissions. The majority of these reductions are

achieved through technologies and solutions that are already available, scalable, and cost-effective today (3), as shown by Figure 3.

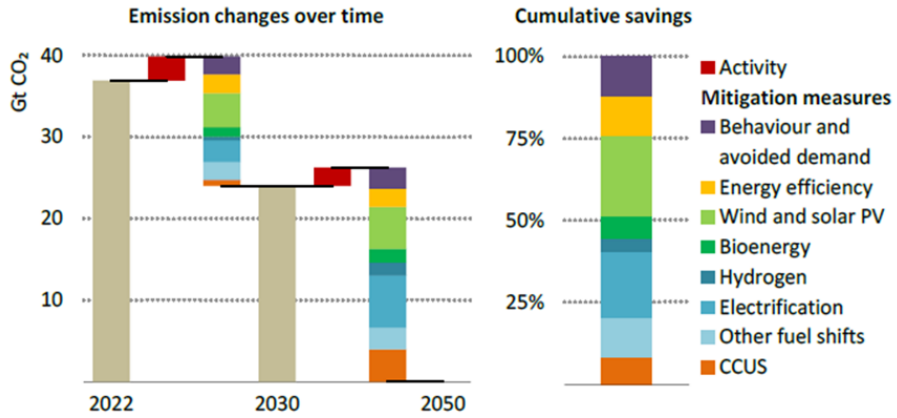

Figure 3: CO_2 emissions reductions by mitigation measures in the NZE scenario, 2022-2050 (3).

Figure 3 displays the global CO_2 emissions (in beige), the increase due to human activity (in red), and the different measure to mitigate this amount of emission. The rapid expansion of solar photovoltaic panels (PV) and wind energy contributes to the majority of emissions reductions. By 2030 it accounts for 4 Gt of CO_2 emissions (equivalent to the combined emissions of European Union, Japan and Koren today). Electrification also plays a key role, as the decarbonization of the electricity sector drives emissions reductions through the wider adoption of technologies such as electric vehicles and heat pumps, resulting in a reduction in emission of 3 Gt by 2030. This not only significantly reduces emissions but also leads to substantial energy savings. Additional near-term reductions come from more efficient use of emission-intensive materials, lower material intensity in production, and behavioural changes by consumers, cutting emissions by 2 Gt in 2030. Fuel switching is another critical factor in the NZE scenario, involving a transition from conventional fossil fuels to renewable energy sources like bioenergy, hydropower, solar thermal, and geothermal. Increased reliance on nuclear energy and a shift from coal to natural gas further enhance emissions reductions. All of these measures together provide more than 3 Gt of emission reduction by 2030 Improvements in energy efficiency across equipment, appliances, vehicles, and buildings are also essential measures, reducing emissions by 2 Gt by 2030. Lastly, while hydrogen technologies and carbon capture, utilization, and storage take time to scale up in the NZE scenario, they hold significant potential for reducing emissions in the long term, delivering a further 1Gt of reductions by 2030 (3).

By 2050, the outlook shifts significantly, as achieving net-zero emissions demands proactive measures in high-emission sectors. CCUS along with hydrogen and hydrogen-based fuels, contribute to one-fifth of the total emissions reduction. Electrification, particularly in buildings and industry, accounts for nearly one-fourth. Solar PV and wind energy are expected to deliver 25% of the cumulative emissions reduction. Additionally, demand reduction through improved energy efficiency, optimized material use, and behavioural changes collectively contribute another 25%. Lastly, increased reliance on bioenergy and fuel switching accounts for approximately 20% of the reductions (3).

The year 2023 saw a record increase in renewable power capacity, with 473 GW added worldwide, accounting for 83% of the total power capacity added during the year. This growth was driven by supportive industrial policies, incentives, regulatory and market frameworks, advancements in technology, improved cost-effectiveness, and concerns over energy security and environmental sustainability. Renewables now represent 43% of the global total power generation capacity (4). Figure 4 highlights the cumulative growth in power capacity from 2015 to 2023.

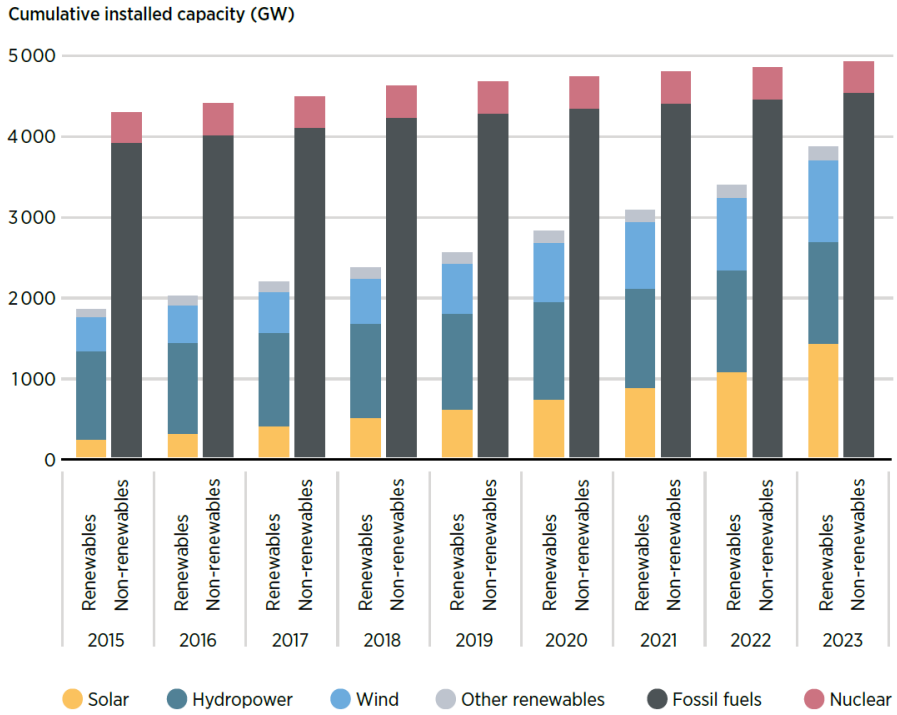

Figure 4: Global power capacity by technology, 2015-2023 (4).

In Brazil, in 2024, renewable energy sources make up 49.1% of the country's energy matrix, with the largest contributions coming from sugarcane biomass (16.9%) and hydropower (12.1%). Wind and solar energy together account for 4.3%, firewood and charcoal for 8.6%, and biodiesel/black liquor/biogas for 7.2%.

Among non-renewable sources, 35.1% of the energy comes from petroleum and its derivatives, while natural gas accounts for 9.6%, coal for 4.4%, uranium for 1.2%, and other non-renewables for 0.6%. Energy consumption in Brazil is primarily distributed across transportation (33%) and industry (31.8%), with the residential sector accounting for 10.7%. To a lesser extent, energy sector takes up 8.8% in energy consumption, agriculture 5.0%, the tertiary sector 5.1%, and 5.7% is utilized for non-energy purpose (5).

France's energy matrix, as reported in 2024, is significantly different from Brazil's, with nuclear energy accounting for the largest share at 38.6%, followed by petroleum at 29.6%, natural gas at 13.5%, coal at 2.1%, non-renewable waste at 0.8% and renewable energy at 15.4%. Within the renewable energy share, biomass contributes 4.8%, hydropower 2.2%, wind power 2.1%, and solar 0.9%. In terms of energy consumption by sector, 34% is used for transportation, 28% for residential purposes, 19% for industry, 16% for the tertiary sector and 3% for the agriculture (6).

Although Renewable Energy Sources (RES) offer environmentally friendly benefits, their intermittent nature poses challenges, leading to operational difficulties, grid instability, and load imbalances that result in a mismatch between supply and demand. Implementing Energy Storage Systems (ESS) can effectively address these issues by improving reliability, while also providing technical, and environmental benefits to the energy system network (7).

Energy storage is primarily implemented through electrical ESS, which are designed to handle unexpected fluctuations during peak and off-peak periods. When integrated with other energy generation sources, these systems can significantly lower electricity production costs and reduce carbon emissions.

EESs come in various types, primarily categorized as follows (8,9):

- **Mechanical**: Mechanical energy can be stored as either kinetic or potential energy. Common types of mechanical ESSs include pumped hydro, flywheels, and compressed air.
- **Thermal**: Energy storage in this category involves altering the temperature of a substance (sensible heat), changing its phase (latent heat), or a combination of both. It can involve storing heat or cold in different conditions—temperature, location, and power—and includes applications such as sensible and latent heat, absorption, and adsorption heat.
- **Electrochemical**: Energy is stored in systems composed of chemical compounds that either release or absorb energy during reactions that form other compounds.

- **Magnetic**: In this type of storage, energy is stored in a magnetic field, with capacitors and supercapacitors being the primary examples.
- **Chemical**: This storage involves energy stored in chemical compounds that can release or absorb energy through endothermic and exothermic reactions in a cyclical process. Common compounds used include hydrogen, ammonia, synthetic natural gas, liquid natural gas, and hydrocarbons.
- **Biological**: Energy is stored in chemical form via biological processes, such as the production of biofuels.

Figure 5 presents the aforementioned division for storage typing.

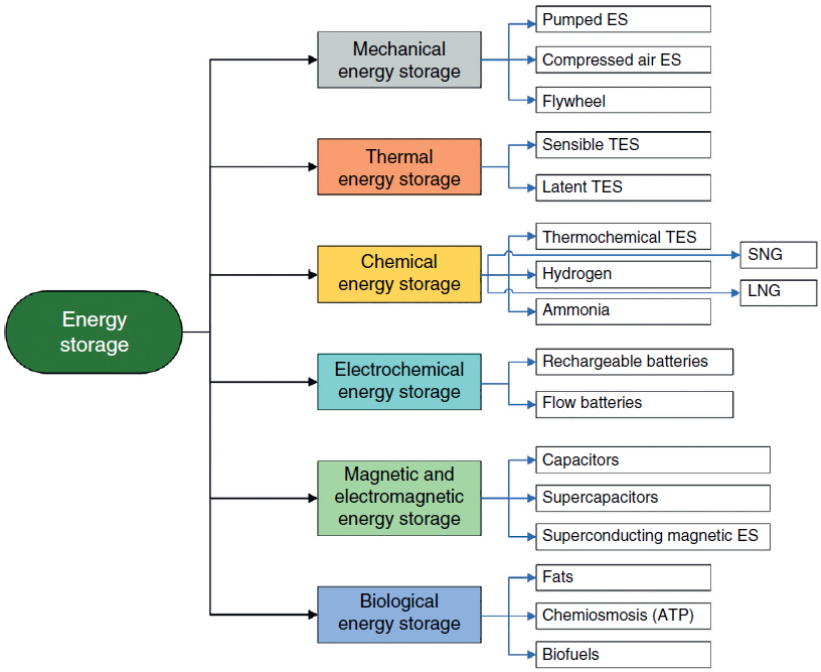

Figure 5: A classification of energy storage methods (9).

Figure 6 display the different technologies and compare them in respect to their discharge time at rated power and power rating.

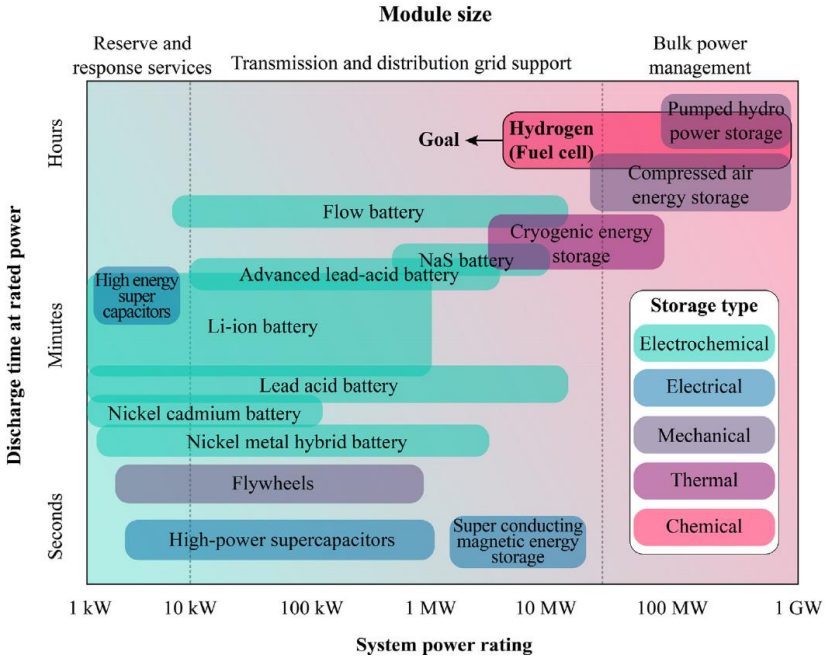

Figure 6: Capacity and discharge time of common types of EES (10).

Both compressed air energy storage (CAES) and hydrogen technologies are well-suited for large-capacity systems, given their high-power ratings compared to other storage technologies. However, there is potential value in scaling them down, which could make their applicability more versatile, albeit at the expense of slower discharge response times, similar to lithium-ion batteries. To further compare these three technologies, Table 1 presents their key categories.

Table 1: Specifications of some common EES (10).

Systems	Power rating (MW)	Energy density (Wh/kg)	Power density (W/kg)	Storage duration	Discharge time	Lifetime [year]
CAES	5 - 300	30 - 60	-	hr - months	hr - days	20 - 40
Hydrogen	0 - 50	80 – 10,000	500 +	hr - months	s – days	5 – 15
Lithium-ion	0 - 0.01	75 - 200	150 - 315	min - days	s - hr	5 - 15

Each EES exhibits distinct characteristics. Various studies in the literature (8,11,12) provide detailed descriptions of each energy storage technology and compare their characteristics. CAES has the highest power rating compared to the other two systems, primarily due to its large-scale application, often involving the use of salt caverns as storage media. Among the three, the hydrogen system has the highest energy density, offering the advantage of using hydrogen as an energy source for power generation. However, hydrogen presents challenges, as it has a low volumetric density and needs to be compressed to extremely high pressures

(13,14). While the battery system shows the lowest values in terms of power and energy density, it benefits from its scalability, lower capital costs, ease of application, and mature development.

Hydrogen is crucial for the energy transition, acting as an energy carrier and enabling decarbonization in hard-to-abate sectors. However, in 2023, its production is largely dependent on unabated fossil fuels. Of this share, two-thirds come from natural gas, 20% from coal gasification, and more than 15% of produced hydrogen is a by-product from refineries and petrochemical industry. Low-emissions hydrogen production constitutes less than 1% of global production, as shown in Figure 7. Most low-emissions hydrogen is produced through fossil fuels combined with CCUS, with electrolytic production making up only a small portion of the total (15).

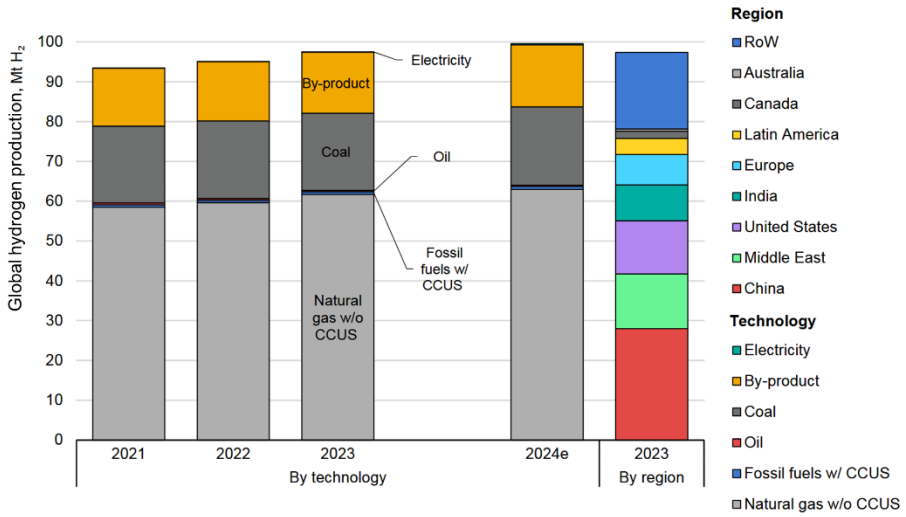

Figure 7: Hydrogen production by technology and region, 2021-2024 (15).

The announcement of additional low-emission hydrogen production projects points to a more promising future for the sector. Production is projected to reach 49 Mtpa by 2030 (including projects still in the early stages), up from just 1 Mtpa in 2023. Europe, Latin America, and the United States are expected to collectively account for more than half of the potential low-emissions hydrogen production by 2030, with shares of 25%, 15%, and 15%, respectively, as show in Figure 8 (15).

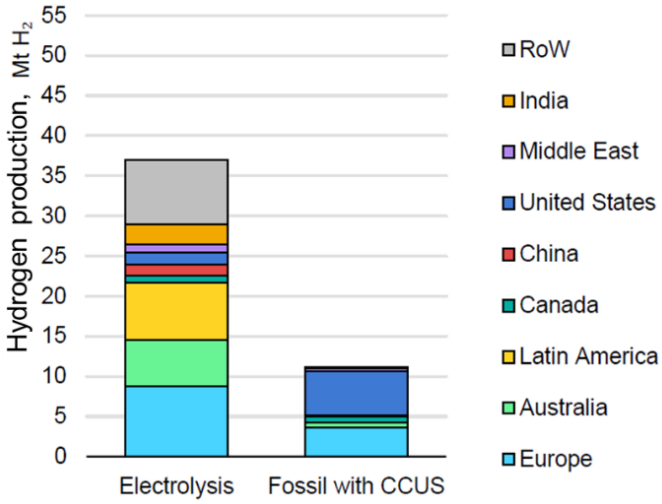

Figure 8: Low-emissions hydrogen production by technology and region based in the Announced Pledges and Net Zero Emissions Scenario, 2030 (15).

Although the number of announced low-emissions hydrogen production projects is increasing, there are several challenges hindering their adoption. The most common barriers include regulatory uncertainty, demand volatility, financial obstacles, delays in incentives, licensing and permitting issues, and operational difficulties (15).

The cost of hydrogen production still needs to decrease, particularly for hydrogen produced from renewable sources. The price of hydrogen from natural gas increased in 2022, especially in Europe due to the Russia-Ukraine crisis. However, it declined in the following year, though it remains vulnerable to fluctuations in natural gas prices. Hydrogen produced from renewable sources, such as wind or solar PV, remains costly, ranging from 4 USD/kgH_2 to nearly 12 USD/kgH_2, as shown in Figure 9. With large-scale deployment and improvements in electrolyzer efficiency and material cost reductions, the cost of renewable hydrogen could potentially be lowered to 2 USD/kgH_2 (15,16,17).

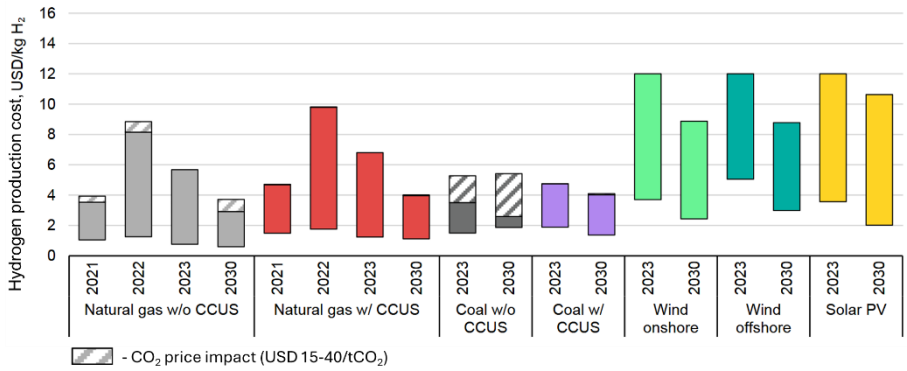

Figure 9: Hydrogen production cost by pathway, 2023 and in the NZE scenario, 2030 (15).

Both Brazil and France have developed strategies and plans to incorporate hydrogen production and use into their energy mix. Brazil has outlined its energy transition plans toward the NZE scenario by 2050 and, in 2022, established the "National Program of Hydrogen – PNH2" to strengthen the hydrogen market and industry as an energy vector. These plans involve deploying pilot plants for low-carbon hydrogen across the country by 2025, positioning Brazil as a competitive producer of green hydrogen, and developing green hydrogen hubs. As part of these efforts, on August 2, 2024, Brazil introduced a legal framework for low-carbon hydrogen, establishing national policies, incentivizing the industry, and creating the "Developing Program of Low Carbon Emission Hydrogen – PHBC" (18,19,20,21).

Through its National Hydrogen Strategy, France has outlined plans for incorporating renewable hydrogen into its energy mix. Key objectives include installing enough electrolyzer capacity to significantly contribute to the decarbonization of the economy, targeting 6.5 GW by 2030, which would produce 600 kt/year of decarbonized hydrogen. The strategy also focuses on decarbonizing the mobility sector by promoting fuel cells electric vehicles, particularly for heavy vehicles. A third priority is to strongly support research and innovation in this field. Under the SNH framework, two calls for projects were launched in October 2020 with an investment target of 625 million euros (22,23).

Several projects are exploring the potential of hydrogen for residential applications. In Europe, efforts have primarily focused on stationary fuel cells for the residential sector, with most large-scale projects concentrated in Germany. Key findings highlight the CO_2 and cost savings of residential fuel cells compared to natural gas burners. Japan serves as a notable example of a well-developed initiative, with the ENE-FARM project successfully integrating fuel cells into residential buildings. (24,25).

1.2. Thesis objectives

The goal of this study is to evaluate the viability and performance of renewable ESSs in two distinct scenarios: Brazil and France. These countries have differing geographical and climatic conditions, as well as varying electricity demands and thermal loads, with a focus on both heating and cooling. These factors provide an opportunity to conduct a detailed analysis of the feasibility of operating these systems in both contexts.

The main objective is to assess the feasibility of three ESSs from energetic, exergetic, economic, and environmental perspectives (4E) through numerical simulations. The evaluation focuses on supplying electricity, heating, and cooling demands for a residential combined cooling, heating and power (CCHP) system in the selected cities of Rio de Janeiro and Lyon. The first system utilizes green hydrogen, consisting primarily of a proton exchange membrane electrolyzer (PEMEC), a high-pressure tank, and a solid oxide fuel cell (SOFC). The second system is a CAES system, which includes compressors, turbines, and a high-pressure tank. The third system is based solely on lithium-ion battery stacks. All three storage systems are integrated with a renewable energy module, consisting of PV panels, and an auxiliary system that operates when the proposed system cannot meet the demand.

The numerical model involves hourly assessments over the course of a year, enabling the observation of how seasonality affects system performance.

Additional objectives include:

- Validation of the main components (SOFC, PEMEC, storage tank, PV panels).
- Sizing the systems based on the system autonomy.
- Setting operational limits by applying exergoeconomy concepts.
- Developing an operational control strategy for the storage medias.
- Performing a multi parameters evaluation using Design of Experiments (DoE) method.

This evaluation allows a comparison of each system's performance under different energy demand and climate conditions (southern and northern hemispheres), enabling a comprehensive assessment of their advantages and disadvantages, and a comparison among them.

1.3. Thesis structure

The thesis is organized into six different chapters, described as follow:

2. **Literature review:** This chapter reviews existing studies related to the thesis topics, focusing on systems that use solid oxide fuel cells, proton exchange membrane electrolyzers, compressed air energy storage, and lithium-ion batteries.
3. **Modelling:** Here, the equations involved in the numerical model for all three systems are outlined. Thermodynamic and

exergoeconomic principles are described, and the parameters for the 4E analysis are introduced.

4. **Methodology:** This chapter details the approach for constructing the numerical model, including assumptions, case descriptions, control logic, system sizing, establishment of operational limits, and the used Design of Experiments approach.
5. **Results:** The results of the study are presented, including validation of the main components, a comparison of the systems across different locations, and a multi parametric evaluation.
6. **Conclusion/Future works:** This section summarizes the study's key findings, discusses the outcomes, and provides recommendations for future research and developments in these systems.

1.4.Chapter conclusion

This chapter provides an overview of the energy transition and the role of renewable energy sources, particularly solar photovoltaic, in achieving a NZE Scenario. It also covers various energy storage technologies that support the integration of renewable energy sources. A comparison of the key characteristics of CAES, hydrogen, and lithium-ion batteries, which are evaluated in this study, is included. Special emphasis is placed on hydrogen, highlighting its potential as a key enabler of decarbonization in the energy sector. The chapter also outlines the main objectives of the current study, detailing the methodology used. Finally, the thesis structure is presented, with a description of the purpose of each chapter.

2
Literature review

This chapter explores the fundamentals of some ESSs, namely hydrogen, compressed air, and lithium-ion batteries. It also presents works from the literature to highlight the significance of investigating these systems, the tools employed in their analysis, and their applications and operational conditions in multigeneration systems.

2.1.
Hydrogen system

2.1.1.
Fundamentals

Hydrogen can be produced through various processes and from different primary energy sources, leading to the adoption of a color-coded nomenclature. However, there is no universal consensus on this naming system. Table 2 presents the most widely recognized colour classifications.

Table 2: Hydrogen colours (18,26,27).

Colour	Process	Source
White	Naturally occurring molecules	Natural
Grey	Steam methane reforming without CCS	Methane or coal
Blue	Steam methane reforming with CCUS	Methane or coal
Turquoise	Pyrolysis	Methane or coal
Green	Water electrolysis	Renewable electricity source
Pink	Water electrolysis	Nuclear
Yellow	Water electrolysis	Electric grid
Black Brown	Coal gasification	Coal (anthracite/ Bituminous)
Moss green	Catalytic reforming, gasification or anaerobic biodigestion	Biomass or biofuels

Grey hydrogen is produced from fossil fuels, such as methane via steam methane reforming or coal through gasification. This process results in significant CO_2 emissions, making it unsuitable for achieving net-zero emissions. Blue hydrogen, on the other hand, is essentially grey hydrogen paired with carbon capture and storage (CCS) technology. While blue hydrogen can help expand the

hydrogen market by reducing greenhouse gas (GHG) emissions and easing the demand on renewable energy capacity needed for green hydrogen production, it is considered a short-term transitional solution. It cannot fully meet the requirements of a net-zero future and serves primarily to facilitate the eventual adoption of green hydrogen. Green hydrogen, produced using renewable energy, is the most suitable option for a sustainable energy transition. The leading technology for its production is water electrolysis powered by renewable electricity. Other methods include pyrolysis, which produces turquoise hydrogen, and the use of nuclear energy to create pink hydrogen. The hydrogen nomenclature also includes a broader range of colours, such as black, brown, white, and moss green, reflecting various production methods (26,27,18).

Green hydrogen bridges the gap between expanding renewable electricity generation and hard-to-electrify sectors. It serves as an effective energy carrier for remote applications, electricity grids, or scenarios requiring high energy density. Additionally, it can act as a feedstock for chemical processes to produce various synthetic fuels and materials. Green hydrogen enhances system flexibility and provides storage solutions, supporting the integration of variable renewable energy sources. It also contributes to energy security, reduces air pollution, and offers socio-economic benefits such as economic growth, job creation, and improved industrial competitiveness (27). Despite its many benefits, green hydrogen has some drawbacks, including its low volumetric energy density. On a mass basis, hydrogen has close to three times the energy content of gasoline – 120 MJ/kg for hydrogen and 44 MJ/kg for gasoline. When comparing on volume basis, however, the situation is reversed. Considering liquid hydrogen, it has a density of 8 MJ/L whereas gasoline has a density of 32 MJ/L. Considering gaseous hydrogen, its values is even lower at 700 bar (4.7 MJ/L) and 350 bar (2.8 MJ/L), presenting itself as a challenge for storage and transportation (13,14).

Electrolyzers are electrochemical devices used to split water into hydrogen and oxygen through the process of electrolysis. The three main types of electrolyzers are alkaline, proton exchange membrane, and solid oxide (SOEC). While the first two technologies are commercially available, the solid oxide electrolyzer is still in the research and development phase (28,29). Table 3 displays the main characteristics of the electrolyzers.

Table 3: Different electrolyzers types of characteristics (30).

Characteristics	SOEC	PEMEC	Alkaline
Electrolyte	Ceramic	Polymer	KOH
Operating temperature [°C]	500 - 1000	50 - 90	60 - 90
Cell voltage [V]	0.7 - 1.5	1.8 - 2.2	1.8 - 2.4
Voltage efficiency [%]	81 - 86	67 - 82	62 - 82
H2 capacity [Nm³/h]	< 40	< 40	< 760
Hydrogen purity [%]	99.9	99.999	>99.8
Energy consumption [kWh/Nm³]	> 3.7	4.5 - 7.5	4.5 - 7
Charger carrier	O^{2-}	H^+	OH^-

The PEMEC schematic is shown in Figure 10.

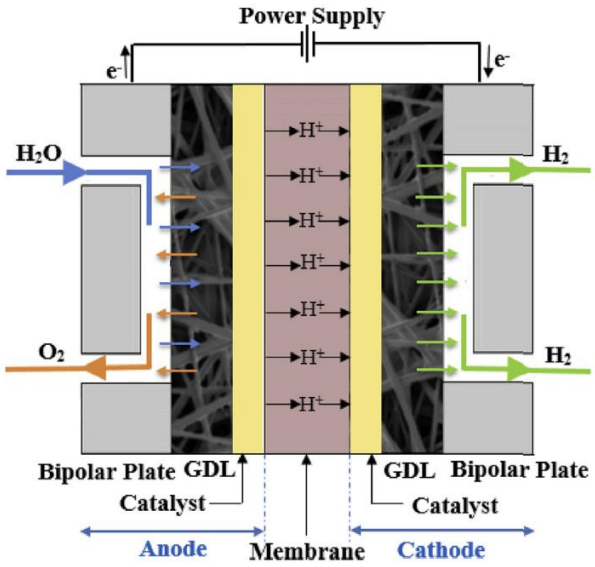

Figure 10: Schematic view of PEMEC (31).

Water splitting, or electrolysis, is powered by electricity and involves two electrochemical half-reactions: the oxygen evolution reaction at the anode and the hydrogen evolution reaction at the cathode. At the anode, water molecules decompose, producing oxygen, protons, and electrons. The protons then travel through the membrane and are ultimately reduced to hydrogen at the cathode. (32). The process is represented by Eqs.(1-3):

$$\text{Anode: } H_2O \rightarrow \frac{1}{2}\,O_2 + 2H^+ + 2e^- \quad (1)$$

$$\text{Cathode: } 2H^+ + 2e^- \rightarrow H_2 \quad (2)$$

$$\text{Overall: } H_2O \rightarrow H_2 + \frac{1}{2}\,O_2 \quad (3)$$

Proton exchange membrane electrolyzers are ideal for integration with renewable energy sources due to their ability to operate at high current densities and their quick response times (28). These systems convert electrical energy into chemical energy by producing hydrogen, which can later be converted back into electricity using fuel cells. The key components of PEMECs include the membrane, anode, and cathode. The membrane is typically made of Nafion, which offers high proton conductivity and chemical stability, enabling the electrolyzer to achieve higher current densities and more efficient hydrogen production. Platinum and iridium oxide are commonly used for the cathode and anode, respectively, because of their high reactivity and stability under the acidic operating conditions (32,33).

Fuel cells are devices that convert energy by generating electricity through an electrochemical reaction between a fuel (such as hydrogen) and an oxidizing agent. This direct conversion of chemical energy into electricity eliminates the need for a combustion process (34). While fuel cells offer higher overall efficiency (45% to 65%) compared to combustion engines (25% to 35%), they still produce waste products, such as heat and exhaust gases, resulting from the redox reactions. These by-products can be harnessed through cogeneration to produce additional electricity. There are various types of fuel cells, including alkaline (AFC), solid oxide (SOFC), molten carbonate (MCFC), phosphoric acid (PAFC), proton exchange membrane (PEMFC), and direct methanol (DMFC). A comparison of the different types and their key characteristics is provided in Table 4.

Table 4: Different fuel cell types of characteristics (8).

Characteristic	**PEMFC**	**AFC**	**PAFC**	**MCFC**	**SOFC**	**DMFC**
Electrolyte	Nafion	Alkaline	Phosphoric acid	Molten Carbonate	Yttria Stabilized Zirconia	Nafion
Operating temperature [°C]	~80	23 – 70	180	~ 650	800 - 100	60
Fuel	Hydrogen	Hydrogen	Hydrogen	Hydrogen, CO_2	Hydrogen, CO_2	Methanol, hydrogen
Efficiency [%]	50 – 70	60 – 70	55	55	60 - 65	60 – 65
Cell voltage [V]	1.1	1	1.1	0.7 – 1	0.8 - 1	0.2 - 0.4
Power Range	1W to 500 kW	10W to 200 kW	50kW to 1MW	<1kW to 1MW	5kW to 3MW	5kW to 3MW

Among the various types, SOFCs operate at high temperatures ranging from 800 to 1000°C, which facilitates the reforming reaction and water-gas shift inside the cell. These fuel cells have garnered significant attention due to their clean and highly efficient operation, as they convert hydrocarbon fuels into hydrogen without

producing nitrogen or sulphur oxides (35). The ability to operate under such conditions makes SOFCs well-suited for integration with other subsystems, enabling efficient cogeneration, trigeneration, and multigeneration systems (36,37,38). Compared to other fuel cells, they are versatile, capable of using a wide range of fuels, including hydrogen, hydrocarbons, carbon monoxide, natural gas, and syngas (34,39).

The SOFC consists of a solid electrolyte positioned between two porous electrodes: the anode and the cathode. The electrochemical process taking place in the SOFC is shown in Figure 11.

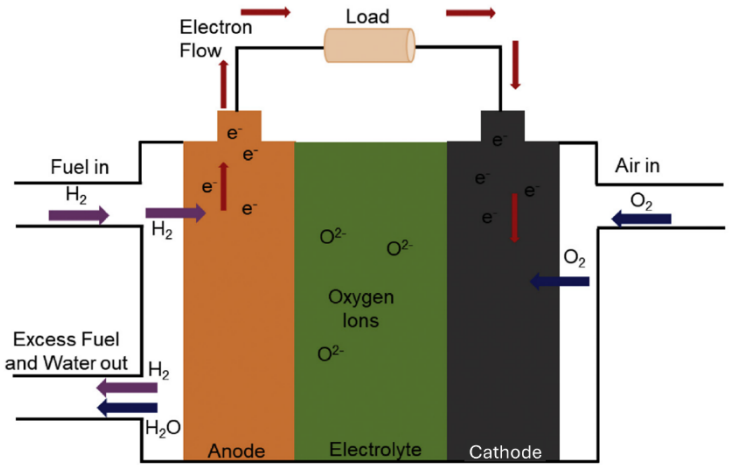

Figure 11: SOFC structure and electrochemical process (34).

Fuel and air are introduced separately into the cell, with fuel supplied to the anode and oxygen to the cathode. Due to the chemical attraction between hydrogen and oxygen, they are drawn toward the electrodes and diffuse through the porous structure to the electrolyte interface, where they are adsorbed. At the cathode, oxygen atoms combine with incoming electrons to form oxygen ions, which travel through the electrolyte to the anode. There, they react with the oxidized fuel, forming water vapor as a by-product and releasing electrons to the external circuit. The electron potential at the anode is higher than that of oxygen, generating net electrical power. This movement of electrons produces electrical energy, which is transmitted via an external circuit, while the water is removed (40,41,34,42). The reactions occurring at each electrode are represented by the following Eqs. (4-6):

$$\text{Anode: } H_2 + O^{2-} \rightarrow H_2O + 2e^- \quad (4)$$

$$\text{Cathode: } \frac{1}{2}\, O_2 + 2e^- \rightarrow 2O^{2-} \quad (5)$$

$$\text{Overall: } H_2 + \frac{1}{2}\, O_2 \rightarrow H_2O \quad (6)$$

The key components of the SOFC—the anode, cathode, and electrolyte—must exhibit excellent physical and chemical stability, high mechanical strength, adequate thermal expansion, and cost-effectiveness. The anode, typically made from nickel-yttria-stabilized zirconia (Ni-YSZ) due to its high conductivity and catalytic properties (43), serves as the negative terminal, helps distribute the fuel, and provides electrocatalytic activity for fuel oxidation and hydrocarbon reforming (42,44). The cathode, usually constructed from perovskite-based materials such as strontium-doped lanthanum manganite, must have high catalytic activity for oxygen reduction, sufficient porosity to allow oxygen flow, and chemical compatibility with the other components to ensure effective long-term operation at high temperatures (45).

2.1.2. Applications involving proton exchange membrane electrolyzer

Literature studies have highlighted the potential of hydrogen production in multigeneration systems, where the electricity generated by the system contributes to improving efficiency and advancing toward carbon neutrality. Zheng et al. proposed a poly-generation system that integrates PEMEC, SOFC, mechanical compression energy storage, and thermal energy storage. Under design conditions, the energy efficiencies for summer, transitional seasons, and winter were 86.61%, 79.36%, and 87.30%, respectively, while the exergy efficiencies were 43.85%, 44.47%, and 45.58%. A sensitivity analysis showed that increasing both the pressure and temperature of the PEMEC and SOFC resulted in improved performance (46). Mehdikhani et al. proposed a system integrating an Organic Rankine Cycle (ORC), Liquefied Natural Gas, PEMEC, and two geothermal wells, evaluating the system from energetic, exergetic, and exergoeconomic perspectives. The optimization yielded a hydrogen production rate of 3.575 kg/hr, net output power of 13,490 kW, total exergy destruction of 21,654 kW, thermal efficiency of 17.14%, exergy efficiency of 44.16%, and a power-specific cost of $19.86/GJ (47). Razmi et al. proposes a novel configuration of green hydrogen

production for power generation during peak demand periods. It consists of the hybridization of parabolic trough collectors (PTC) with a PEMEC and PEMFC. The system is able to produce 9, 14,9 and 20.1 MW of power during a cycle at off-, mid- and on-peak times, accomplished by the ratio of excess hydrogen to the produced of 2.3. The system achieves an exergy efficiency of 17.6%, and most of exergy destruction is verified in the PTC unit. Exergoeconomic analysis shows that the PTC subsystem accounts for almost 82% of the total cost of the base load part, and electrolyzer and fuel cell are responsible for around 39% of total cost. Finally, it is verified an optimal cost rate of the systems products equals to 492.4 $/hr (10). Zhao et al. investigated a novel hydrogen ESS consisting of an asymmetric PEMEC for producing high-pressure hydrogen, a SOFC, and an ORC-supercritical CO_2 waste heat recovery system for carbon-free power generation. The system achieved round-trip thermal and exergy efficiencies of 54.29% and 50.34%, respectively. The authors found that hydrogen production rate and SOFC operating temperature were the key factors influencing system efficiency, with the PEMEC exhibiting the highest exergy destruction (48).

2.1.3. Applications involving solid oxide fuel cell

Due to their high operating temperature, SOFCs have been explored for applications that take advantage of this feature. Cogeneration and even trigeneration are examples where the exhaust gases can be used for heating and cooling. Wang et al. studied a trigeneration system based on both atmospheric and pressurized SOFCs. The system included an SOFC top cycle and a bottom cycle that combined a transcritical CO_2 cycle, transcritical organic Rankine cycle, and LNG cold energy utilization system. Under design conditions, the atmospheric system showed better electrical, overall, and exergy efficiencies of 68.1%, 68.7%, and 65.7%, respectively, compared to the pressurized one. The optimal conditions indicated an exergy efficiency of 66.83% and a total cost rate of 12.02 $/h (49). Liu et al. proposed a CCHP system that combines an SOFC with a gas turbine and a transcritical CO_2 power/refrigeration cycle for trigeneration purposes. The system achieved a trigeneration cost of 37.12 $/GJ per unit of exergy, with electrical and exergetic efficiencies of 62.65% and 62.27%, respectively. Multi-objective optimization revealed a 0.2% increase in exergy efficiency, accompanied by a cost increase of 0.21 $/GJ (50). Wang et al. assessed a new integrated energy system that includes solar-methanol hydrogen production, an energy storage device, an

SOFC, and a dual-effect absorption chiller/heat pump. Power efficiency varied by season, reaching 48.03% in summer, 65.38% in transition seasons, and 53.26% in winter. Exergy analysis identified the solar collector as the main source of exergy destruction, with a total exergy efficiency of 37.59% (51). Gao and Zhou proposed an integrated, self-sufficient SOFC system for CCHP applications. Electrolyzers, powered by PV panels, produce hydrogen, while an adsorption chiller provides cooling, a district hot water heat exchanger supplies heating, and a battery ensures electricity supply. The authors optimized the design of the battery, electrolyzer, and fuel cell, resulting in total energy efficiencies ranging from 70.86% to 72.18%, with annual total costs between 67,230$ and 73,250$ (52).

To address the challenges associated with SOFC operation in complex systems, exergoeconomic analysis has become a crucial tool for optimizing performance and evaluating economic feasibility. Wu et al. proposed a novel hybrid system consisting of a biomass gasification unit, SOFC, charge compression engine, and waste heat recovery unit. The system achieved overall energy and exergy efficiencies of 68% and 51%, respectively. The exergoeconomic analysis showed a high exergoeconomic factor and a product cost of 9.7 $/GJ. Regarding exergy destruction, the gasifier accounted for the largest share, up to 21%. The system also exhibited low carbon dioxide emissions, ranging from 0.119 to 0.139 t/GJ (35). Wang et al. investigated a system that combines biomass gasification (BioG) with SOFC for combined heat and power (CHP) applications and a solar-assisted solid oxide electrolyzer cell (SOEC) methanation process. The BioG-SOFC subsystem reached energy and exergy efficiencies of 59% and 44.7%, respectively, while the SOEC-methanation subsystem achieved 78.5% and 73.8%. Exergoeconomic analysis revealed a unit cost of power generation and methane production of $0.052/kWh and $29.5/GJ, respectively. The system also exhibited a low environmental impact, with CO_2 emissions ranging from 0.13 to 0.166 t/GJ (53). You et al. studied a trigeneration system integrating an SOFC, gas turbine, ORC, steam ejector refrigerator, and heat exchanger. The system achieved electrical, exergy, and energy efficiencies of 64.2%, 65.7%, and 70.6%, respectively. The generator, afterburner, and SOFC exhibited the highest exergy destruction costs, with an average product cost of 9.77 $/GJ (54). Lu et al. examined an SOFC integrated solar combined cycle system. Their findings showed that the system, using solar collectors, achieved the highest exergy efficiency of 52.91%, the lowest unit cost of 0.102 $/kWh, and the lowest specific CO_2 emission rate of 475.27 g/kWh (55).

Due to their scalability and modularity, SOFCs can be integrated into more complex systems, including polygeneration or cycles, to enhance efficiency and minimize emissions. Ghorbani et al. investigated the optimal design and performance analysis of an integrated system combining SOFC, gas turbine, and ORC using R407C and R404A as working fluids. The results showed that the system performed better with R407C, achieving energy and exergy efficiencies of 49.42% and 46.83%, respectively (56). Chitgar and Moghimi proposed a novel integrated system combining a SOFC and Gas turbine (GT) for producing electricity, fresh water, and hydrogen. The authors optimized several parameters, including exergy efficiency, freshwater production rate, and hydrogen production rate. At optimal conditions, the exergy efficiency reached 54.2%, with a total unit cost of products of $34.5/GJ. When focusing on freshwater production, the optimal rate was 90.1 m^3/h, with a total unit cost of $32.9/GJ. For hydrogen production, the optimum rate was 11.6 kg/h, resulting in a product unit cost of $32.8/GJ (57). Griffiths et al. assessed the technical and economic feasibility of using SOFCs for both electricity generation and high-grade heat for direct air carbon capture. Their analysis showed that a 50 MW SOFC system could remove over 270 kt/year of CO_2. The levelized cost of capture for the system varied significantly with the price of renewable hydrogen production, estimated to range from £314 to £1,505 per tonne of CO_2 captured (58). Yang et al. proposed a novel SOFC-based cogeneration system that includes biomass co-gasification, SOFC power generation, and ORC waste heat recovery. The system reached a peak energy efficiency of 44.7%, with electricity and heat production of 162 kW and 52.4 kW, respectively. The biomass gasifier and SOFC were responsible for the highest exergy destructions, totalling 44.4%. The optimal solution indicated an exergy efficiency of 41.95% and an overall unit cost of 42.35 $/GJ (59).

2.2. Fundamentals of compressed air energy storage

The concept of CAES is simple. Energy is stored by using electrically powered compressors, which convert electrical energy into potential energy, or more precisely the exergy, of compressed air. This stored air can then be released on demand, expanding through an air turbine to generate electricity once again (60).

CAES technology can be classified into three concepts: diabatic (D-CAES), adiabatic (A-CAES), and isothermal (I-CAES). In D-CAES, the heat generated

during air compression is wasted to the environment, requiring an external heat source to prevent condensation and icing in the expansion machinery by preheating the compressed air before it enters the expander. In A-CAES, the heat from compression is captured using additional thermal energy storage (TES) devices and is reused before expansion, eliminating the need for external heat sources during discharge. In I-CAES, both compression and expansion occur at nearly constant temperatures, facilitated by advanced heat exchanger systems. Focusing on A-CAES, the use of TES allows the compressed air to be cooled before storage, enabling the system to handle much higher final pressures and achieve higher energy densities. A simple configuration of A-CAES is shown in Figure 12 (60,61).

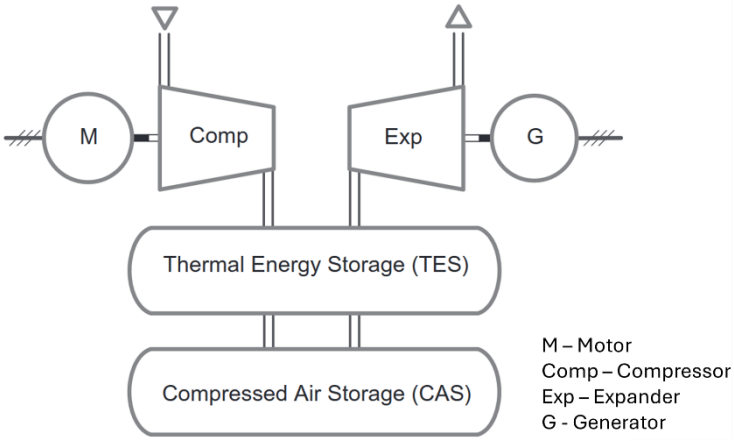

Figure 12: Basic configuration of an A-CAES (60).

Compressed air can be stored either at constant volume (isochoric) or at constant pressure (isobaric). In an isochoric system, the pressure fluctuates continuously, reflecting the charge and discharge states. This presents a drawback, as it causes the compression and expansion machinery to operate outside their optimal design pressure ratios, resulting in reduced efficiencies. Common storage media include steel pressure vessels for smaller scales and salt caverns for larger-scale storage.

2.2.1. Applications involving compressed air energy storage

The CAES system has been evaluated at many CCHP applications, due to its capability of heat recovery during both charging and discharging process. Yao et al. combined a CAES with a gas engine and an ammonia-water absorption refrigeration system for trigeneration purposes. The optimal conditions identified

by the authors resulted in an overall exergy efficiency of 53.0 % and a total product unit cost of 205.4 $/MWh. Their exergoeconomic analysis suggests that the best trade-off solution involves reducing the investment costs for compressors and heat exchangers used in heat recovery while improving the thermodynamic performance of the turbine (62). He et al. proposed a CCHP system that couples a CAES with a gas turbine combined cycle (GTCC) with steam turbine, capable of achieving a steady power capacity of 164.0 MW and a maximum power capacity of 257.5 MW. The authors found that the electric efficiency of the CAES alone is 48.7%, while the coupled CAES-GTCC system achieved electric, energy, and exergy efficiencies of 74.5%, 90.8%, and 52.9%, respectively (63). Xu et al. proposed a CCHP system with a 10 MW gas turbine (simple or regenerative cycle) and a constant-pressure CAES. The scheme using a regenerative cycle for both the gas turbine and expander demonstrated better economic performance, with lower fuel costs and higher profits. The integration of the CAES also expanded the heat-to-electricity ratio adjustment range (64). Rahimimotlagh and Ahmadi introduced a CCHP system integrating parabolic solar dish collectors, an absorption chiller, a steam Rankine cycle, and CAES. At baseline conditions, the system achieved a roundtrip efficiency of 62.7% and a levelized production cost of 24.23 USD/GJ. It is capable of generating 7.59 MW of electricity while reducing CO_2 emissions by 3,810 tons (65).

The 3E analysis is also vastly applied to CAES systems, providing a robust and comprehensive approach for understanding and improving CAES applications. Some works also dedicates to the 4E analysis which also comprehends the environmental analysis. Rahbari et al. proposes a trigeneration system combining CAES and an ORC for heat recovery, integrated with a wind farm and offering a capacity of 5 MW. The system's exergetic efficiency ranges from 58% to 64% depending on the load profile. The levelized cost of storage varies between 141 €/MWh and 153.7 €/MWh, with potential annual emission reductions between 4,163 and 3,640 tonnes of CO_2 equivalent (66). Shi and Asgari proposed a CAES cycle integrated with a dual-pressure ORC combined with an ejector refrigeration cycle. A multi-objective optimization was performed to find the best trade-off between thermodynamic performance and economic parameters through energetic, exergetic, and exergoeconomic analyses. Under the base conditions, the system displayed energy and exergy efficiencies of 13.24% and 25.92%, respectively. The results suggested that under optimal conditions, the system's round-trip efficiency reaches 54.3%, and the unit cost of the product is 48.77 $/MWh (67). Xue et al. (2024) studied the integration of a biomass power

generation system with a CAES, assessing the energy, exergy, economic, and environmental perspectives. The round-trip, overall, and exergy efficiencies were found to be 84.9%, 39.98%, and 80.46%, respectively. The payback period was estimated to be 4.2 years, with CO_2 emissions per unit of power equal to 258 g/MWh (68).

Energy storage systems offer a compelling solution to the intermittent nature of renewable energy source. Dib et al. investigated the annual operation of a micro-A-CAES system coupled with photovoltaic panels for a residential building. The authors found that the system can cover 64.4% of the total electrical load with an efficiency of 33.7%. They also observed that increasing the storage pressure from 40 to 200 bar leads to a reduction of the levelized cost of energy from 2.03 $/kWh to 0.63 $/kWh (69). Dib et al. also simulated the micro-A-CAES system in two modes of operation—autonomous and grid-connected—for trigeneration purposes in a building of 6,813 m². The grid-connected mode showed more advantages compared to the autonomous mode in all three French cities considered. Cold coverage exhibited poor performance in both modes, while the best electric and trigeneration efficiencies achieved were 42.0% and 52.4%, respectively (70). Alirahmi et al. investigated a green ESS capable of providing both power and potable water, based on the combination of a CAES system with a solar heliostat and a multi-effect thermal vapor compression desalination unit. The round-trip efficiency of the system was found to be 48.7%, and the total cost rate was $3,056 per hour under optimal design conditions. For the studied case, the system was projected to generate 27.5 GWh annually and produce 226.78 m³ of potable water (71). Bazdar et al. proposed an enhanced energy management strategy to optimize the performance of an adiabatic CAES system designed to meet an annual electricity demand of 4,500 MWh. Their findings suggest that a minimum storage volume of 200 m³ is required to achieve the highest coverage ratio. Sensitivity analysis reveals that pressure has a more significant impact on the analysed parameters than the storage tank volume or thermal energy storage (72). Migliari et al. examined the integration of a photovoltaic-hydrogen-fuelled CAES system. Their study evaluates both annual and seasonal performance, concluding that the system can reach efficiencies of up to 62% and support the grid by supplying power during 20% of nighttime hours (73).

2.3. Fundamentals of lithium-ion batteries

This type of ESS is one of the most common across various technologies. It consists of multiple batteries connected in series or parallel to achieve the desired voltage and capacity. Each battery contains two conductive electrodes and an electrolyte, all housed in a sealed container and connected to an external source or load. The chemical reaction involves the transfer of electrons between the two electrodes, with the electrons flowing through an external electrical circuit or load.

Lithium-ion batteries have become a prominent energy storage technology due to their high specific energy and power values, as well as low self-discharge rates compared to other types of batteries, and their easy integration with renewable energy sources (74). Table 5 outlines the characteristics of different battery types.

Table 5: Batteries characteristics (75).

Technology	Efficiency (%)	Specific energy (Wh/kg)	Specific power (W/kg)	Life cycle
Lead-acid	70 - 90	25 - 40	75-300	500-2000
Lithium-ion	80 - 98	100 - 250	100-300	1000-5000

The primary mechanism of lithium-ion batteries involves the intercalation and deintercalation of Li-ions into and out of the electrode materials. During charging, Li-ions are extracted from the cathode and inserted into the anode. Conversely, during discharge, the Li-ions move back from the anode to the cathode. The electrolyte serves as a medium that facilitates the movement of the ions while maintaining electrical insulation (75,76). The key electrochemical reaction during charging is as follows, Eqs. (8-7):

$$\text{Anode: } C + Li^+ + e^- \rightarrow LiC_6 \quad (7)$$

$$\text{Cathode: } LiCoO_2 \rightarrow Li^+ + CoO_2 + e^- \quad (8)$$

The majority of studies in the literature regarding the use of lithium-ion batteries for energy storage focus on optimizing the sizing and operation of the battery stacks. Rosati et al. assessed the environmental and economic impacts of integrating a lithium-ion battery into an existing residential building. The system analysed includes a reversible heat pump, a PV system, and the battery. The results indicate that sizing the battery based on variations in self-consumed renewable energy leads to a sustainable investment across all climate conditions

(77). From a techno-economic standpoint, lithium-ion batteries are more suitable for daily energy storage rather than seasonal storage. However, the system alone cannot fully address the mismatch between energy production and consumption, suggesting that additional technologies are necessary to utilize all the energy generated by the PV system. Among energy storage technologies, lithium-ion batteries are among the most developed, especially when compared to hydrogen and CAES (77).

2.4. Chapter conclusion

The chapter presented the fundamentals behind each considered ESS, while presented works from the literature which have similar applications. To better summarize the presented references, Table 6 categorizes the works for hydrogen system, and Table 7 for CAES system.

Table 6: References categorization of hydrogen system.

Ref.	Seasonal	CHP	CCHP	1E	2E	3E	4E	Size	Other byproducts
10	x	x	x	x	x	✓	x	20 MW	Hydrogen
35	x	✓	x	x	x	x	✓	1.06 MW	-
46	x	x	x	x	x	✓	x	21.6 MW	Hydrogen Natural gas
47	x	x	✓	x	✓	x	x	334 kW	Hydrogen
48	x	x	x	x	✓	x	x	350 kW	Hydrogen
49	x	✓	x	x	✓	x	x	400 kW	-
50	x	x	✓	x	x	✓	x	250 kW	-
51	✓	x	✓	x	✓	x	x	834 kW	-
52	✓	x	✓	✓	x	x	x	9 kW	-
53	✓	x	✓	x	x	x	✓	834 kW	-
54	x	x	✓	x	x	x	✓	300 kW	-
55	x	x	✓	x	x	x	✓	500 MW	-
56	x	x	x	x	x	x	✓	420 kW	-
57	x	x	x	x	x	✓	x	4.9 MW	Hydrogen Fresh water
58	x	x	x	x	x	x	✓	50 MW	CO_2
59	x	✓	x	x	x	x	✓	175 kW	-

1E – Energy

2E – Energy and exergy

3E – Energy, exergy and exergoeconomy

4E – Energy, exergy, exergoeconomy and environmental

Table 7: References categorization of CAES system.

Ref.	Seasonal	CHP	CCHP	1E	2E	3E	4E	Size	Other byproducts
62	x	x	✓	x	x	✓	x	18 MW	-
63	x	x	✓	x	x	✓	x	250 MW	-
64	x	x	✓	x	✓	x	x	10 MW	-
65	x	x	✓	x	x	x	✓	7.59 MW	-
66	x	x	✓	x	x	x	✓	5 MW	-
67	x	x	x	x	x	✓	x	10.5 MW	-
68	x	x	x	x	x	x	✓	4 MW	-
69	✓	x	x	x	✓	x	x	23.5 kW	-
70	✓	x	x	x	✓	x	x	100 kW	-
71	✓	x	x	x	x	x	✓	27.5 MW	Fresh water
72	✓	x	x	✓	x	x	x	570 kW	-
73	✓	x	x	✓	x	x	x	42 MW	Hydrogen

1E – Energy
2E – Energy and exergy
3E – Energy, exergy and exergoeconomy
4E – Energy, exergy, exergoeconomy and environmental

Although both tables do not encompass all the studies available in the literature, certain trends are evident. Most research on energy storage focuses on large-scale systems, revealing a lack of studies addressing small-scale energy storage solutions, particularly for residential applications. While trigeneration has been extensively explored in the literature, the majority of these studies do not target the specific demands of residential buildings, which can be attributed to the scale of the systems analysed. Most analyses are based on fixed design conditions, restricting evaluations to specific parameters and making it difficult to assess different, especially dynamic, conditions. While some studies perform parametric analyses, they often focus on a single parameter, limiting their ability to evaluate complex systems. Additionally, many seasonal assessments consider only a representative week rather than an entire year, failing to capture daily variations. Additionally, most of the selected studies focus on exergy analysis (25 out of 26), with a smaller subset incorporating exergoeconomic aspects (17 out of 23) and even fewer addressing environmental factors (11 out of 23). However, the data suggests a growing interest in integrating economic and environmental considerations alongside exergy analysis. Considering these gaps, the present study aims to fill the void in the literature by providing a comprehensive understanding of ESSs for lower-capacity applications and their behaviour under

varying conditions, including weather, location, and seasons. Notably, no studies were identified that compare different storage systems under identical conditions.

3
System modelling

This chapter outlines the equations employed in the numerical model used in this study. It aims to detail the analysis of all the components from energetic, exergetic, exergoeconomic, and environmental perspectives. Additionally, the parameters used for system evaluation are presented.

3.1.
Model's assumptions and considerations

Some assumptions and considerations are contemplated to simplify the modelling and future analysis:

- The systems operate at quasi-steady state and under thermodynamic equilibrium, except the storage tanks which are considered in transient regime.
- Kinetic and potential energy are disregarded.
- Components in the system are assumed to be well insulated, avoiding heat loss to the environment – except the storage tanks.
- Air is considered as dry air with molar composition of air 21% O_2 and 79% N_2.
- Natural gas fed to the system is considered to be pure methane (CH_4).
- All gases species behave as ideal gas.
- Compressors, turbines, and pumps operate with constant isentropic efficiency equal to 85% (78).
- Pressure drops across components are neglected.
- Heat exchangers operate with constant efficiency of 90% (79).
- The system operates at the same frequency as the grid.
- Startup time is not factored in, all components are assumed to respond instantaneously.
- The steam-to-carbon ratio on the steam reforming process is equal to 3.2 (80).

3.2. Energetic modelling

Considering each component as a control volume, the mass and energy balance equations are written as follows, Eqs. (9-10):

$$\frac{dm}{dt} = \sum_{i} \dot{m}_i - \sum_{o} \dot{m}_o \tag{9}$$

$$\frac{dE_t}{dt} = \pm\dot{Q} \pm \dot{W} + \sum_{i} \dot{m}_i \cdot \left(h_i + \frac{v_i^2}{2} + g \cdot z_i\right) - \sum_{o} \dot{m}_o \cdot \left(h_o + \frac{v_o^2}{2} + g \cdot z_o\right) \tag{10}$$

Where m is the mass in kg, $\dot{m}$ is the mass flow rate in kg/s, E_t is the total energy in kJ, $\dot{Q}$ is the module of the heat transfer rate in kW (positive signal when provided, and negative signal when realized), $\dot{W}$ is the module of the power in kW (positive signal when provided, and negative signal when realized), h is the specific enthalpy in kJ/kg, v is the velocity in m/s, g is the acceleration of gravity in m/s², z is the height in m, and the subscript i corresponds to the inlet, and o to the outlet.

3.2.1. Photovoltaic system

A photovoltaic system consists of a combination of cells in series and parallels producing desired current and voltage output. The performance of this system displays a non-linear current-voltage (I-V) curves, Eq.(11) (81,82):

$$I = I_L - I_0 \cdot \left[\exp\left(\frac{q \cdot (V + I \cdot R)}{\gamma \cdot k_b \cdot T_{cell}}\right) - 1\right] \tag{11}$$

Where I is the electric current in A, I_L is the light current in A, I_0 is the reverse saturation current in A, q is the electron charge in C, V is the voltage in V, R is the electrical resistance in Ω, γ is the shape factor (dimensionless), k_b is the Boltzmann constant in m²kg/(s².K), and T is temperature in K.

The light current I_L depends on solar irradiance and temperature, Eq. (12):

$$I_L = \left(\frac{G}{G_{ref}}\right) \cdot [I_{L,ref} + k_t \cdot (T_{cell} - T_{ref})] \tag{12}$$

Where G is the solar irradiance in kW/m², G_{ref} the solar irradiance at design condition (ambient pressure and 25 °C) in kW/m², $I_{L,ref}$ is the light current calculated based on the manufacturer data in A, k_t is the manufacturer-supplied temperature coefficient in A/°C.

The reverse saturation current is described by Eq. (13):

$$I_0 = I_{L,ref} \cdot \exp\left(-\frac{q \cdot V_{oc}}{k_b \cdot \gamma \cdot T_{ref}}\right)\left(\frac{T_{cell}}{T_{ref}}\right)^3 \cdot \exp\left(\frac{q \cdot \varepsilon}{k_b \cdot a} \cdot \left(\frac{1}{T_{ref}} - \frac{1}{T_{cell}}\right)\right) \quad (13)$$

Where V_{oc} is the open-circuit voltage in V, ε is the diode diffusion factor (dimensionless), and a is the ideal factor (dimensionless).

Figure 13 displays the typical I-V curve together with the P-V curve for a PV module.

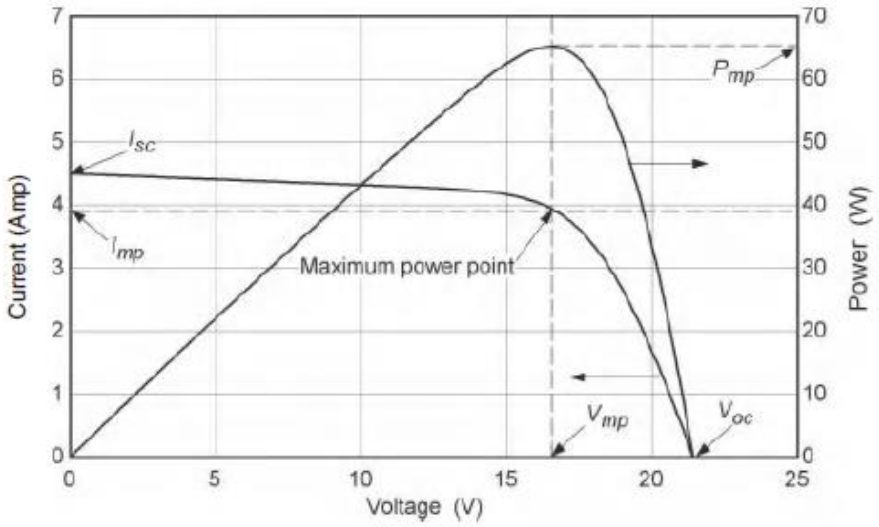

Figure 13: Typical I-V and P-V curves for a PV module (81).

The short-circuit (*sc*) current occurs when the voltage is zero (*oc*), while the open-circuit voltage occurs when the current is zero. Ideally, the cell should always operate at the maximum power point (*mp*). However, in practice, it operates at a point determined by the I-V characteristics of the load (81).

Both ambient temperature and wind speed are responsible for affecting the PV system performance through the PV cell temperature, Eq. (14):

$$T_{cell} = 0.943 \cdot T_0 + 0.028 \cdot G - 1.528 \cdot v_{wind} + 4.3 \quad (14)$$

Where v_{wind} is the wind velocity in m/s.

Shape factor, γ, is a measurement of the cell imperfection, and is related to the completion factor and the number of cells, Eq. (15).

$$\gamma = a \cdot NS \cdot NCS \tag{15}$$

Where NS is the number of modules connected in series, and NCS is the number of cells connected in series in each module.

The total area of the photovoltaic system is calculated accordingly, Eq. (16):

$$A_t = NS \cdot NP \cdot A_{cell} \tag{16}$$

Where NP is the number of modules connected in parallel, and A_{cell} is the area of the photovoltaic cell in m².

Finally, it is interesting to express the energy and exergy rates associated with the photovoltaic panels, Eqs. (17-18) (83):

$$\dot{E}_{PV} = G \cdot A_{cell} \tag{17}$$

$$\dot{E}x_{PV} = G \cdot A_{cell} \cdot \left(1 - \frac{4}{3} \cdot \frac{T_0}{T_{sun}} + \frac{1}{3} \cdot \left(\frac{T_0}{T_{sun}}\right)^4\right) \tag{18}$$

Where $\dot{E}_{PV}$ is the energy rate from the PV panels in kW, and $\dot{E}x_{PV}$ is the exergy rate in kW.

3.2.2. Compressed air energy storage system

3.2.2.1. System description

The CAES system is described in Figure 14.

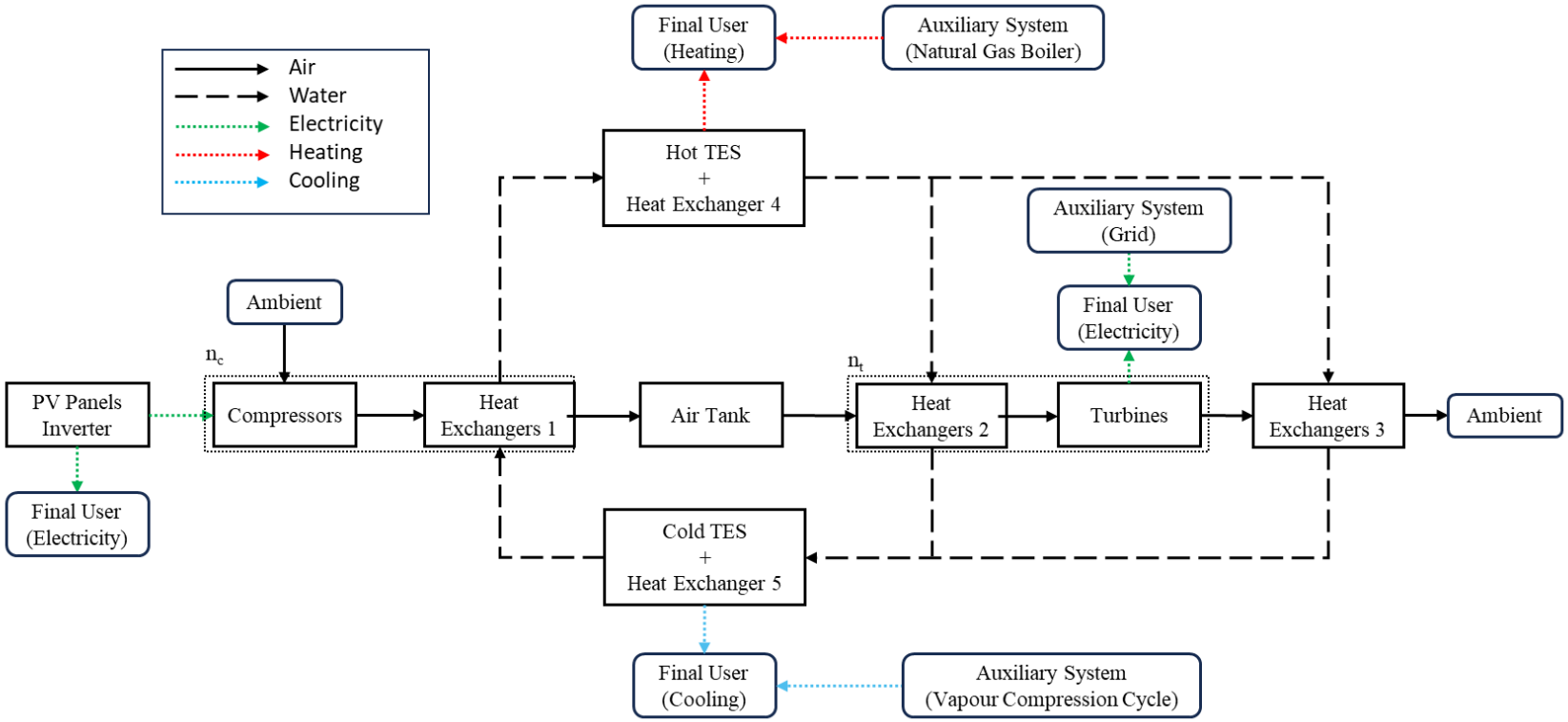

Figure 14: Compressed Air Energy Storage system.

Photovoltaic panels capture solar energy, which is directed to a control unit. This unit either supplies electricity directly to meet the demand or powers compressors to store excess energy by compressing air into tanks. Heat exchangers (1), acting as intercoolers, are placed between the compressors to cool the air entering them, improving efficiency by using water from the cold TES. When the PV panels cannot fully meet electrical demand, the compressed air is released from the tanks and expanded through turbines to generate power. Heat exchangers (2) between the turbines heat the air, improving turbine efficiency, by utilizing water from the hot TES. A heat exchanger (3) is placed after the last turbine uses the cold expanded air to cool water, which is then partially used to meet the building's cooling demand by the combination of cold TES and heat exchanger (5). Meanwhile, the heat demand is satisfied with hot water from the hot TES through another heat exchanger (4). If the system cannot meet energy demands, auxiliary systems are activated: the grid supplies additional electricity, a natural gas burner or heat pump meets heat requirements, and a vapor compression refrigeration system handles cooling needs.

3.2.2.2. Compressors

Multi-stage compressors are employed to raise the air pressure from atmospheric levels to the storage pressure. This process is assumed to occur at steady state, with a constant air mass flow rate through all compressors. To minimize the total compression power, the pressure ratios are assumed to be evenly distributed among the compressors, Eq. (19):

$$\beta_c = (P_{st}(t)/P_0)^{\frac{1}{n_c}} \tag{19}$$

Where β_c is the pressure ratio of the compressors (dimensionless), P is the pressure in MPa, and n_c is the number of compressors considered. The subscript st corresponds to the storage, and *0* to ambient condition.

Compressors undergo an adiabatic process, having their outlet temperature calculated as Eq. (20) (84,85,86):

$$T_{c,o} = T_{c,i} \cdot \left(1 + \frac{\beta_c^{(\gamma-1)/\gamma} - 1}{\eta_{ise}}\right) \tag{20}$$

Where η_{ise} is the isentropic efficiency (dimensionless), and γ is the specific heat ratio (dimensionless).

The compressor's specific work consumption is calculated as a function of the operation conditions, Eq. (21):

$$w_c = c_p \cdot T_{c,i} \cdot \left(\beta_c^{(\gamma-1)/\gamma} - 1\right)/\eta_{ise} \quad (21)$$

Where c_p is the specific heat at constant pressure in kJ/(kg.K).

The total power consumption rate of all compressors in the system is calculated as, Eq. (22):

$$\dot{W}_{c,s} = \dot{m}_{air} \cdot \sum_{n=1}^{n_c} w_{c,n} \quad (22)$$

3.2.2.3. Turbine

Multi-stage turbines expand the air from the tanks to generate electrical power. The operating conditions are assumed to be similar to those of the compressors. The expansion ratio is defined accordingly, Eq. (23):

$$\beta_t = (P_0/P_{st}(t))^{1/n_t} \quad (23)$$

Where β_t is the turbines pressure ratio (dimensionless), and n_t is the number of turbines.

As compressors, the turbines undergo an adiabatic process, and their outlet temperature and specific work are calculated by Eqs. (24-25) (84,85,86):

$$T_{t,o} = T_{t,i} \cdot \left(1 - \left(1 - \beta_t^{(\gamma-1)/\gamma}\right) \cdot \eta_{ise}\right) \quad (24)$$

$$w_t = c_p \cdot T_{t,i} \cdot \left(1 - \left(1 - \beta_t^{(\gamma-1)/\gamma}\right) \cdot \eta_{ise}\right) \quad (25)$$

Finally, the total power generation rate of all turbines is expressed by Eq. (26):

$$\dot{W}_{t,s} = \dot{m}_{air} \cdot \sum_{n=1}^{n_t} w_{t,n} \quad (26)$$

3.2.2.4. Air storage tank

The air storage tank is designed to store compressed air during the charging process and release it during the discharge process. The flow of air into or out of the chamber is governed by the mass conservation equation Eq. (9). A simple representation of the storage tank is shown in Figure 15.

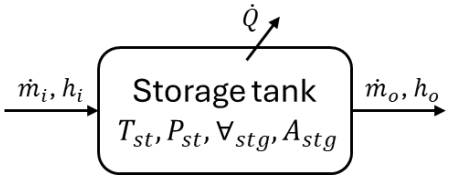

Figure 15: Storage tank control volume.

The first law of thermodynamics, Eq. (10), is described by Eq. (27):

$$\frac{d\,(m \cdot u)}{dt} = \dot{m}_i \cdot h_i - \dot{m}_o \cdot h_o - U_{stg} \cdot A_{stg} \cdot (T_{st} - T_0) \tag{27}$$

Where u is the specific internal energy in kJ/kg, U is the overall heat transfer coefficient in kW/(m².K), A is the area in m², the subscript *stg* to the storage, and *st* to stored.

Simplifying the equation of state of an ideal gas result in Eq. (28):

$$dP/P + d\forall/\forall - dT/T - dm/m = 0 \tag{28}$$

Where ∀ is the volume in m³.

Both Eqs. (27-28) are used to describe the variations of temperature and pressure inside the air storage chamber, Eqs. (29-30) (84,85,86):

$$\frac{dT_{st}}{dt} = \frac{\dot{m}_i \cdot \gamma \cdot T_i + \left((1-\gamma) \cdot \dot{m}_o - \dot{m}_i\right) \cdot T_{st}}{m_{st}} - \frac{U_{stg} \cdot A_{stg} \cdot (T_{st} - T_0)}{m_{st} \cdot c_v} \tag{29}$$

$$\frac{dP_{st}}{st} = \frac{\left(R_g \cdot c_p \cdot (\dot{m}_i \cdot T_i - \dot{m}_o \cdot T_o)\right)}{\forall_{stg} \cdot c_v} - \frac{U_{stg} \cdot A_{stg} \cdot R_g \cdot (T_{st} - T_0)}{\forall_{stg} \cdot c_v} \tag{30}$$

Where is R_g is the gas constant in kJ/(kg.K), and c_v is the specific heat at constant volume in kJ/(kg.K).

3.2.2.5. Heat exchanger

Before each compression and expansion, a heat exchange process is carried out between air and water (secondary fluid). The effectiveness of the heat exchanger is used in the calculations as follow, Eq. (31) (87):

$$\epsilon = \frac{\dot{Q}}{\dot{Q}_{max}} = \frac{C_h \cdot \left(T_{h,i} - T_{h,o}\right)}{C_{min} \cdot \left(T_{h,i} - T_{c,i}\right)} = \frac{C_c \cdot \left(T_{c,o} - T_{c,i}\right)}{C_{min} \cdot \left(T_{h,i} - T_{c,i}\right)} \quad (31)$$

Where C is the heat capacity in kJ/K, the subscript h corresponds to the hot side, c to the cold side, and *min* to minimum.

Effectiveness can be written as a function of the number of transfer units (NTU) and the ratio of heat capacities, Eq. (32) (87):

$$\epsilon = f\left(NTU, C_r = \frac{C_{min}}{C_{max}}\right) \quad (32)$$

The number of transfer unit is a dimensionless parameter utilized for analysing heat exchangers, Eq. (33):

$$NTU = \frac{UA}{C_{min}} \quad (33)$$

In a counter-flow arrangement, effectiveness can be written as Eq. (34):

$$\epsilon = \frac{1 - \exp\left(-NTU \cdot (1 - C_r)\right)}{1 - C_r \cdot exp(-NTU \cdot (1 - C_r))} \quad (34)$$

Considering the compression, the outlet temperatures of air and water are calculated as follows, Eqs. (35-36):

$$T_{air,o} = (1 - \epsilon) \cdot \ T_{air,i} + \epsilon \cdot \ T_{water,i} \quad (35)$$

$$T_{water,o} = \epsilon \cdot T_{air,i} + (1 - \epsilon) \cdot T_{water,i} \quad (36)$$

Considering the expansion, the outlet temperatures of air and water are calculated as follows, Eqs. (37-38):

$$T_{air,o} = T_{air,i} + \epsilon \cdot \left(T_{water,i} - T_{air,i}\right) \quad (37)$$

$$T_{water,o} = T_{water,i} - \epsilon \cdot \left(T_{water,i} - T_{air,i}\right) \quad (38)$$

3.2.2.6. Thermal energy storage

During compression, thermal energy is absorbed by the heat carrier as it exits the cold storage medium and is transferred to heat the hot storage medium. Conversely, during expansion, the thermal energy stored in the hot medium is utilized to heat the air, which is then transferred back to the cold medium. The thermal energy storage process is governed by the energy conservation equation, as expressed in Eq. (39) (88):

$$\rho_{TES} \cdot \forall_{TES} \cdot c_{p_{TES}} \cdot \frac{dT_{TES}}{dt} = \dot{m}_i \cdot h_i - \dot{m}_o \cdot h_o - A_{TES} \cdot U_{TES} \cdot (T_{TES} - T_0) \quad (39)$$

Where ρ is the density in kg/m³.

3.2.3. Hydrogen system

3.2.3.1. System description

The hydrogen system is described in Figure 16.

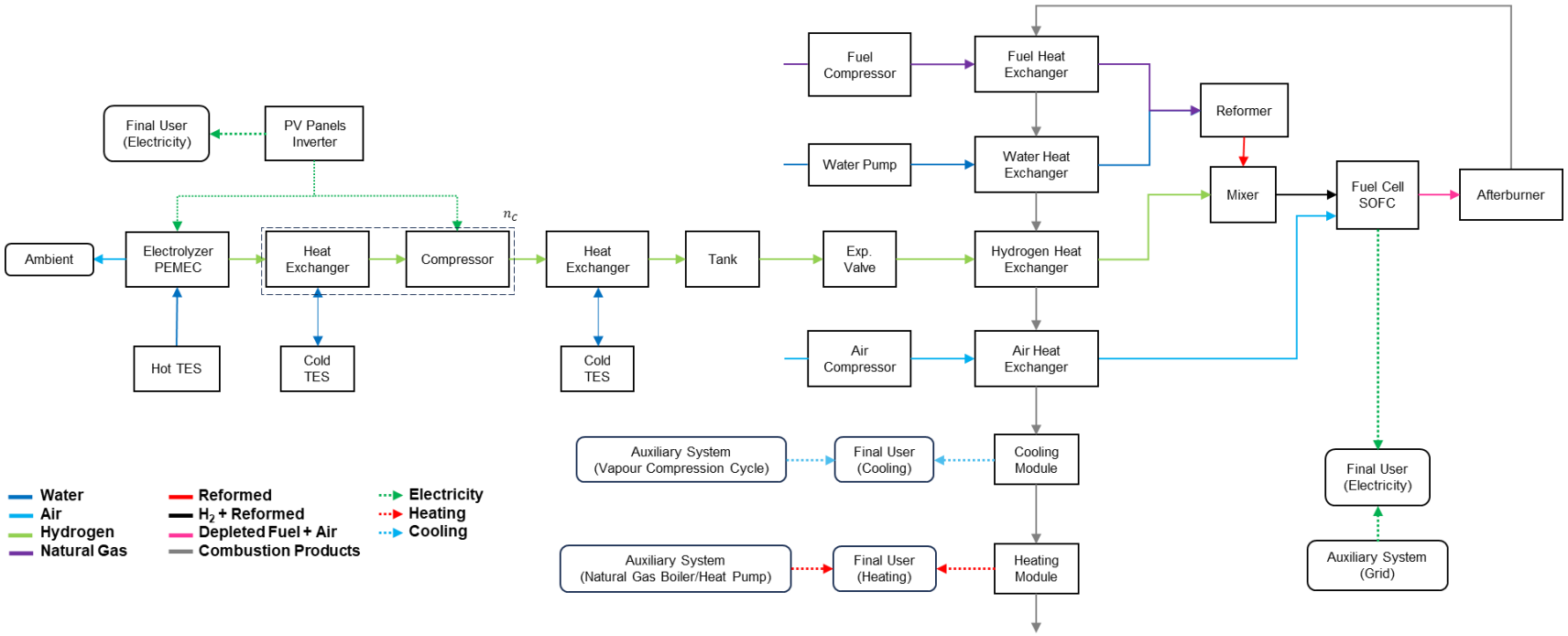

Figure 16: Hydrogen system.

Similar to the CAES system, a set of PV panels captures solar energy to meet the building's electricity demand. Any surplus energy is used to generate and store electricity in a storage tank. The surplus energy, along with heated water from the hot TES, powers PEMECs to produce green hydrogen, with oxygen as a by-product. Before entering the compressor, the hydrogen is cooled in a heat exchanger using chilled water from the cold TES. The hydrogen storage process involves multi-stage compression, with alternating heat exchangers and compressors. When the PV panels cannot meet the full electricity demand, the system switches to the discharging phase, utilizing SOFCs. In this phase, natural gas and water are fed into a reformer, where steam reforming generates hydrogen. The reforming process also produces carbon monoxide and carbon dioxide, steam, and residual methane. The generated hydrogen is mixed with the stored hydrogen and used as fuel in the SOFC. For the electrochemical reaction to occur, air is also supplied to the fuel cell. After operation, the depleted fuel and air are sent to an afterburner, where complete combustion takes place. The hot exhaust gases are used to preheat all incoming streams (natural gas, water, hydrogen, and air) and to support the system's cooling and heating modules, meeting the building's thermal demands. As with the CAES system, auxiliary systems are employed to cover any unmet energy or thermal demands.

3.2.3.2. Reformer

Fuel reforming reactions allow the conversion of fuel into another through catalytic reaction, from a less active fuel into a more active one (89). A global chemical formula of feedstock, $\mathrm{CH_xO_yN_z}$, is defined in Eq. (40):

$$CH_xO_yN_z + wH_2O + m(O_2 + 3.76N_2) = n_{H2}H_2 + n_{CO}CO + n_{CO_2}CO_2 + n_{H_2O}H_2O + n_{CH_4}CH_4 + \left(\frac{z}{2} + 3.76m\right)N_2 \quad (40)$$

Where x is the number of atoms of hydrogen per number of atoms of carbon in the feedstock, y is the number for oxygen per number of atoms of carbon in the feedstock, z is the number of nitrogen per number of atoms of carbon in the feedstock, m is the number of oxygen per mol of feedstock, and n is the number of mols.

Steam reforming reaction of methane and water gas shift, can be derived from the Eq. (40), and are described in Eqs. (41-42) (90):

$$CH_4\,(g) + H_2O\,(g) \leftrightarrow 3H_2(g) + CO(g) \tag{41}$$

$$CO(g) + H_2O(g) \leftrightarrow CO_2(g) + H_2(g) \tag{42}$$

In the steam reforming and water-gas shift reactions, there are five unknown species, requiring five equations to solve the system. These equations are derived from the chemical reaction balances for carbon, hydrogen, and oxygen, as presented in Eqs. (43-45) (80,91):

$$n_{CO} + n_{CO_2} + n_{CH_4} - 1 = 0 \tag{43}$$

$$2n_{H_2} + 2n_{H_2O} + 4n_{CH_4} - x - 2w = 0 \tag{44}$$

$$n_{CO} + 2n_{CO_2} + n_{H_2O} - w - 2m - y = 0 \tag{45}$$

Chemical equilibrium is typically described using either equilibrium constants or the minimization of Gibbs free energy. In this work, equilibrium constants are used to define the two remaining equations. The general expression for the equilibrium constant is provided in Eq. (46):

$$K = \prod_i x_i^{v_i} \cdot \left(\frac{P}{P_0}\right)^{\sum_i v_i} \tag{46}$$

Where K is the equilibrium constant (dimensionless), x is the molar fraction, v is the stoichiometric coefficient, and the subscript *i* corresponds to the species.

The equilibrium constants for the reactions in the steam reforming *(sr)* and water gas shift *(ws)* are described by Eqs. (47-48):

$$K_{sr} = \frac{(n_{CO}) \cdot (n_{H_2})^3}{(n_{CH_4}) \cdot (n_{H_2O})} \cdot \left(\frac{P}{P_0}\right)^2 \tag{47}$$

$$K_{ws} = \frac{(n_{CO_2}) \cdot (n_{H_2})}{(n_{CO}) \cdot (n_{H_2O})} \tag{48}$$

The equilibrium constant for an ideal gas can be described by Eq. (49):

$$ln\,K = \frac{-\Delta G^0}{\bar{R} \cdot T} \tag{49}$$

Where ΔG^0 is the standard Gibbs free energy change of reaction in kJ/mol.

Consequently, the two remaining equations based on the constants are, Eqs. (50-51):

$$K_{sr} \cdot (n_{CH_4}) \cdot (n_{H_2O}) - (n_{CO}) \cdot (n_{H_2})^3 \cdot \left(\frac{P}{P_0}\right)^2 = 0 \tag{50}$$

$$K_{ws} \cdot (n_{CO}) \cdot (n_{H_2O}) - (n_{CO_2}) \cdot (n_{H_2}) = 0 \tag{51}$$

Figure 17 displays the outlet results for the reforming considering an inlet stream of one mol of methane in function of the steam-to-carbon ratio at ambient pressure and temperature of 800 °C.

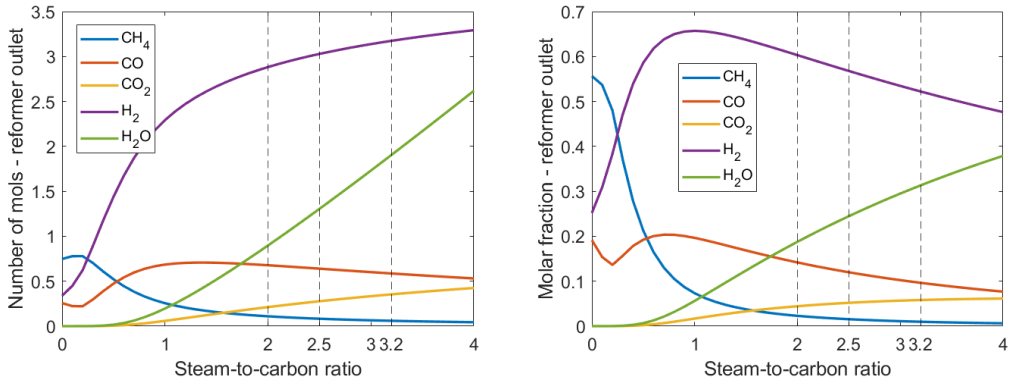

(a) Number of mols (b) Molar fraction

Figure 17: Reformer outlet at ambient pressure and temperature of 800 °C.

As seen in Figure 17, increasing the steam-to-carbon ratio enhances hydrogen production, as desired, due to the greater conversion of methane. Consequently, there is a slight increase in CO_2 formation, as anticipated by Eq. (42).

3.2.3.3.
Proton exchange membrane electrolyzer / Solid oxide fuel cell

3.2.3.3.1.
Nernst voltage

In a fuel cell, the electrical work (electromotive force) is calculated as the product of the charge flowing through it and the potential difference driving that flow, Eq. (52) (92,38):

$$E_n = -\frac{\Delta G}{n_e F} \tag{52}$$

Where n_e is the number of transferred electrons, F is the Faraday constant in C/mol, and E_n is the Nernst potential in V.

For the equation to hold true, the Nernst potential must represent the reversible cell potential, which serves as a reliable approximation of the open-circuit voltage. It is expressed as the difference between the chemical potentials of the reactants and products in the ideal gas stream, Eq. (53):

$$E_n = \frac{1}{n_e \cdot F}\left\{\sum_{reactants,i} n_i \cdot \left[\mu_i^0 + \bar{R}\cdot T \cdot ln\left(\frac{P_i}{P_0}\right)\right] - \sum_{products,j} n_j \cdot \left[\mu_j^0 + \bar{R}\cdot T \cdot ln\left(\frac{P_j}{P_0}\right)\right]\right\} \tag{53}$$

Where μ° is the chemical standard potential in kJ/mol, and $\bar{R}$ is the universal gas constant in kJ/(kmol.K).

Introducing the standard Gibbs free energy, ΔG^o, together with the stoichiometric coefficient of the reaction, the following manipulation of the aforenoted equation can be made, Eq. (54):

$$E_n = -\frac{\Delta G^0}{n_e \cdot F} - \frac{\bar{R}\cdot T}{n_e \cdot F} \cdot ln \prod_i \left(\frac{P_i}{P_0}\right)^{v_i} \tag{54}$$

The SOFC reaction is based on the oxidation of hydrogen by oxygen anions, Eq. (55) (45,93,57,36):

$$E_n = -\frac{\Delta G^0}{n_e \cdot F} - \frac{\bar{R}\cdot T}{n_e \cdot F} \cdot ln\left(\frac{P_{H_2O}}{P_{H_2}\left(P_{O_2}\right)^{\frac{1}{2}}}\right) \tag{55}$$

The above equation is the measurement of the driving force generating current in a cell, and its sensitivity to the cell temperature, hydrogen, and water concentration on the anode side, and oxygen concentration on the cathode side. The logarithmic term in the partial pressure is to gauge the changes in potential caused by the reactant or product concentration, called the Nernstian loss.

Regarding the SOFC, the first term on the right of Eq. (55) can be estimated by a semi-empiric equation, Eq. (56) (94), and for the PEMEC the whole equation can be estimated as Eq. (57) (95,96,97,98,57):

$$E_0 = -\frac{\Delta G^0}{n_e \cdot F} = 1.253 - 2.4516 \cdot 10^{-4} \cdot T \tag{56}$$

$$E_n = 1.229 - 8.5 \cdot 10^{-4} \cdot (T - T_0) \tag{57}$$

When current is drawn the cells does not operate at the Nernst potential due to irreversible losses (polarization), associated with charge transfer (activation), mass transfer (concentration), and ohmic resistance. They are described as follow, Eqs. (58-59):

$$V_{SOFC} = E_n - V_{act} - V_{conc} - V_{ohm} \tag{58}$$

$$V_{PEMEC} = E_n + V_{act} + V_{ohm} \tag{59}$$

Where V corresponds to the voltage in V, and the subscripts act to activation, conc to concentration, and ohm to ohmic. Concentration losses are considered negligible in the PEMEC.

Voltage behaviour of a fuel cell is displayed in Figure 18. Activation losses are more prominent on small current densities, especially at low-temperature operations, and as its current grows ohmic losses outstand growing linearly with electrical current. At higher currents, concentration losses are stronger as it approaches the limiting current operation.

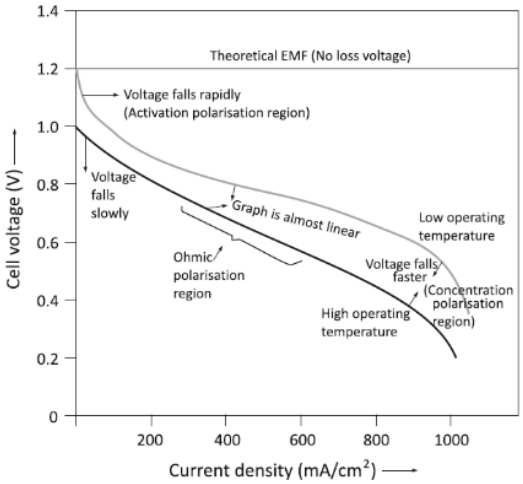

Figure 18: Fuel cell polarization losses (92).

3.2.3.3.2. Activation losses

At low currents, the losses are primarily governed by the activation effect at the electrode, which results from the reaction of a dissolved gas molecule at the catalyst surface, including processes like adsorption and dissociation(92,38).

The Butler-Volmer equation is used to describe the losses associated with activation, Eq. (60):

$$j = j_0 \cdot \left(exp\left(\frac{E_a \cdot n_e \cdot F \cdot \eta_{act}}{\bar{R} \cdot T}\right) - exp\left(-\frac{E_c \cdot n_e \cdot F \cdot \eta_{act}}{\bar{R} \cdot T}\right)\right) \qquad (60)$$

Where j is the electrode current density in A/m², j_o is the exchange current density in A/m², E is the activation energy levels in kJ/mol, and η_{act} is the activation overpotential in V. The subscript *a* corresponds to the anode, and *c* to the cathode.

The exponential terms characterize the forward and backward reactions named cathodic (reduction) and anodic (oxidation). The influence of the concentration is combined into an effective value for a change current density, which strongly depends on the specific experimental condition.

The equation can be arranged to use the inverse hyperbolic sine, Eqs. (61-62):

$$V_{act} = V_{act,a} + V_{act,c} \qquad (61)$$

$$V_{act,i} = \frac{\bar{R} \cdot T}{F} \cdot \left(sinh^{-1}\left(\frac{j}{2 \cdot j_{o,i}}\right)\right) \qquad (62)$$

Eq. (63) can be rewritten as:

$$V_{act,i} = \frac{\bar{R} \cdot T}{F} \cdot \ln\left(\frac{j}{2 \cdot j_{0,i}} + \sqrt{\left(\frac{j}{2 \cdot j_{0,i}}\right)^2 + 1}\right) \quad (63)$$

The effective exchange current density represents the readiness of an electrode to proceed with an electrochemical reaction. It heavily depends on the electrode microstructure properties, and operating conditions (gas composition and operating temperature and pressure) (94,99,100). Based on experimental observations, the dependence of exchange current density is expressed as, Eqs. (64-65):

$$j_{0,a} = \lambda_a \cdot \left(\frac{P_{H_2}}{P_0}\right) \cdot \left(\frac{P_{H_2O}}{P_0}\right) \cdot e^{-\frac{E_a}{\bar{R} \cdot T}} \quad (64)$$

$$j_{0,c} = \lambda_c \cdot \left(\frac{P_{O_2}}{P_0}\right)^{0.25} \cdot e^{-\frac{E_c}{\bar{R} \cdot T}} \quad (65)$$

Where λ is an empiric constant (dimensionless).

It is also possible to see in the literature, which does not consider the effects of gas composition and partial pressure. So, the effective exchange current density can be written as Eq. (66):

$$j_{0,i} = j_i^{ref} \cdot e^{\left(-\frac{E_i}{\bar{R} \cdot T}\right)} \quad (66)$$

3.2.3.3.3. Ohmic losses

The overall ohmic resistance of a fuel cell is primarily influenced by three processes: ionic, electronic, and contact resistances. This overpotential can be described by Ohm's law, which relates the cell's characteristics to the cell current, Eq. (67) (92,38):

$$V_{ohm} = R \cdot I = \frac{\delta}{\sigma} \cdot I = \left(\frac{\delta_a}{\sigma_a} + \frac{\delta_c}{\sigma_c} + \frac{\delta_e}{\sigma_e}\right) \cdot I \quad (67)$$

Where R is the electric resistance in Ω, δ is the component thickness in m, and σ is the proton conductivity in S/m. The subscripts e corresponds to the electrolyte.

For the SOFC, ohmic polarization is described by Eqs. (68-72) (57,36,101,102,35):

$$V_{ohm,SOFC} = (R_c + \rho_c \cdot \delta_c + \rho_a \cdot \delta_a + \rho_e \cdot \delta_e + \rho_{int} \cdot \delta_{int}) \cdot j \quad (68)$$

$$\rho_e = \left(3.34 \cdot 10^4 \cdot \exp\left(-\frac{10{,}300}{T}\right)\right)^{-1} \quad (69)$$

$$\rho_a = \left(\frac{95 \cdot 10^6}{T} \cdot \exp\left(-\frac{1{,}150}{T}\right)\right)^{-1} \quad (70)$$

$$\rho_c = \left(\frac{42 \cdot 10^6}{T} \cdot \exp\left(-\frac{1{,}200}{T}\right)\right)^{-1} \quad (71)$$

$$\rho_{int} = \left(\frac{9.3 \cdot 10^6}{T} \cdot \exp\left(-\frac{1{,}100}{T}\right)\right)^{-1} \quad (72)$$

Where ρ corresponds to electrical resistivity in Ω.m, and the subscript int is the interconnects.

Considering the PEMEC, ohmic losses are calculated as follow, Eqs. (73-76) (103,95,104,57,96,97):

$$V_{ohm,PEMEC} = j \cdot R \quad (73)$$

$$R_{pemec} = \int_0^L \frac{dx}{\sigma[\lambda(x)]} \quad (74)$$

$$\sigma[\lambda(x)] = (0.5139 \cdot \lambda(x) - 0.326) \cdot \exp\left(1268 \cdot \left(\frac{1}{303} - \frac{1}{T}\right)\right) \quad (75)$$

$$\lambda(x) = \frac{\lambda_a - \lambda_c}{\delta} + \lambda_c \quad (76)$$

Where λ is the water content (dimensionless) on the anode *(a)* and cathode *(c)*.

3.2.3.3.4. Concentration losses

Hydrogen and oxygen must reach the electrode surface, and the water produced needs to be removed from the catalyst into the porous layers and channels. While electrochemical reactions can occur quickly, the movement of gases and liquids happens at specific speeds, meaning mass transport can limit the overall current. This effect becomes noticeable at moderate to high current densities. A straightforward approach to modelling this process involves assuming diffusion governed by Fick's law (92,38). The voltage loss of transport limitation, η_{conc}, can be described by the limiting current density, Eq. (77):

$$\eta_{conc} = \frac{\bar{R} \cdot T}{n_e \cdot F} \cdot \ln\left(\frac{j_{lim}}{j_{\lim} - j}\right) \tag{77}$$

Where j_{lim} is the limiting current density in A/m².

For the SOFC, the concentration losses are calculated as follows, Eqs. (78-82) (57,93,36):

$$V_{conc} = V_{conc,a} + V_{conc,c} \tag{78}$$

$$V_{conc,a} = \frac{\bar{R} \cdot T}{2 \cdot F} \cdot \left(ln\left(1 + \frac{P_{H_2} \cdot j}{P_{H_2O} \cdot j_a}\right) - ln\left(1 - \frac{j}{j_a}\right)\right) \tag{79}$$

$$V_{conc,c} = -\left(\frac{\bar{R} \cdot T}{4 \cdot F} \cdot ln\left(1 - \frac{j}{j_c}\right)\right) \tag{80}$$

$$j_{as} = \frac{4 \cdot F \cdot P_{H_2} \cdot D_a}{\bar{R} \cdot T \cdot L_A} \tag{81}$$

$$j_{cs} = \frac{4 \cdot F \cdot P_{O_2} \cdot D_c}{\left(\left(\frac{P - P_{O_2}}{P}\right) \cdot \bar{R} \cdot T \cdot L_c\right)} \tag{82}$$

Where j_{as} and j_{cs} are the limiting current density from the anode and cathode, respectively, in A/m², and D_a and D_c are the effective gaseous diffusivity through anode and cathode, respectively, in m²/s.

In the case of PEMEC, it is not common considering concentration losses as it usually does not operate at high current densities.

3.2.3.3.5. Hydrogen flux

In a SOFC, it is important to evaluate the flow of fuel and air in both the anode and cathode, as displayed in Figure 19.

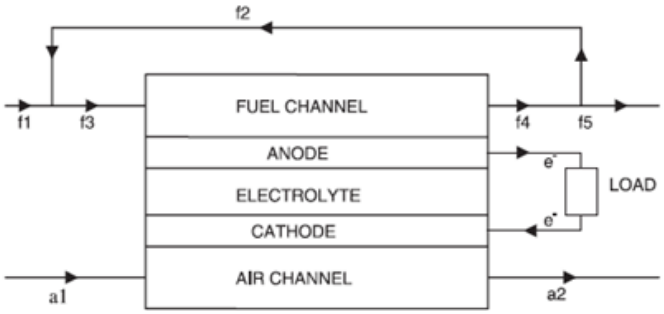

Figure 19: Solid oxide fuel cell fluxes representation (93).

The relation for calculating the composition at each point indicated in Figure 19 is shown in Eqs. (83-91) (93):

$$\dot{n}_{f_1}^{i} = x_{f_1}^{i} \cdot \frac{\dot{m}_{f_1}}{\sum x_{f_1}^{i} \cdot M_w^{i}} \tag{83}$$

$$\dot{n}_{f_2}^{i} = \dot{n}_{f_4} \cdot r \tag{84}$$

$$\dot{n}_{f_3}^{i} = \dot{n}_{f_1}^{i} + \dot{n}_{f_2}^{i} = \dot{n}_{f_1}^{i} + x^{i}(r \cdot \dot{n}_{f_4}) \tag{85}$$

$$\dot{n}_{f_4}^{i} = \left(1 - U_f\right)\dot{n}_{f_3}^{i} \tag{86}$$

$$\dot{n}_{f_5}^{i} = \dot{n}_{f_4}^{i} \cdot (1 - r) \tag{87}$$

$$\dot{n}_1^{O_2} = \frac{c}{2 \cdot U_o} \tag{88}$$

$$\dot{n}_1^{N_2} = \frac{79}{42} \cdot \frac{c}{U_o} \tag{89}$$

$$\dot{n}_2^{O_2} = \frac{c}{2 \cdot (U_o - 1)} \tag{90}$$

$$\dot{n}_1^{N_2} = \frac{79}{42} \cdot \frac{c}{U_o} \tag{91}$$

Where $\dot{n}$ is the molar flow in mol/s, c is the extent of an electrochemical reaction in mol/s, a is the extent of steam reforming reaction for methane in mol/s, b is the extent of the water-shift reaction in mol/s, U_f is the fuel utilization ratio (dimensionless), r is the recirculation ratio (dimensionless) and U_o is the air utilization ratio (dimensionless).

Calculating the amount of hydrogen consumed during operation requires using the relationship between electrical current and the molar flow rate of hydrogen, Eqs. (92-93) (93):

$$I = j \cdot A = 2 \cdot F \cdot c = 2 \cdot F \cdot \frac{(\dot{n}_{H_2,i} + 3a + b) \cdot U_f}{1 - r + r \cdot U_f} \tag{92}$$

$$\dot{n}_{H_2,i} = \frac{j \cdot A \cdot \left(1 - r + r \cdot U_f\right) \cdot n_{cell}}{2 \cdot F \cdot U_f} - 3a - b \tag{93}$$

Where n_{cell} is the number of cells.

In a PEMEC, the production of hydrogen and oxygen is governed by Faraday's law, or Faraday efficiency. This is expressed as the ratio of the ideal electric charge to the actual electric charge needed to produce a specific amount of hydrogen, Eq. (94) (28,105,106):

$$\eta_f = \frac{Q_{id}}{Q_{re}} \tag{94}$$

Where Q_{id} is the ideal electric charge in C, and Q_{re} is the actual electric charge in C.

Empirical models have been developed in the literature regarding Faraday's efficiency (28,107), with results shown in Figure 20.

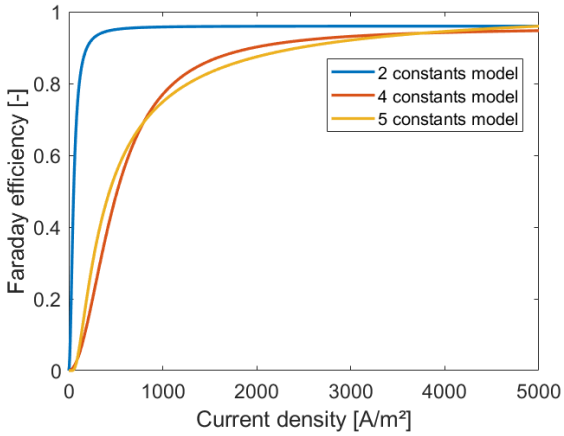

Figure 20: Faraday efficiency.

All models show an increase with current density; however, the model with 2 constants exhibits a steeper growth rate compared to the other two models. In this study, the model with 5 constants, given by Eq. (95), is used, and its parameters are provided in Table 8:

$$\eta_f = B_1 + B_2 \cdot \exp\left(\frac{B_3 + B_4 \cdot T + B_5 \cdot T^2}{j}\right) \tag{95}$$

Table 8: Faraday efficiency parameters (28,107).

Parameter	Value
B_1	4,50424 x 10^{-5} [-]
B_2	1,02116 [-]
B_3	-247,26 [A/m²]
B_4	2,06972 [A/ (m² °C)]
B_5	-0,03571 [A/ (m² °C²]

Figure 21 displays the flow associated with a PEMEC operation.

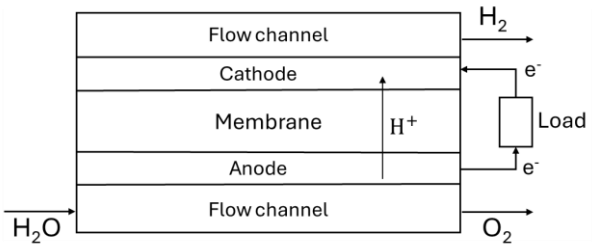

Figure 21: Proton exchange membrane electrolyzer flows representation.

Produced hydrogen is directly proportional to Faraday's efficiency and electric current. The rate of hydrogen is dictated by Eq. (96):

$$\dot{n}_{H_2} = \eta_f \cdot \frac{n_{cell} \cdot I}{n_e \cdot F} \tag{96}$$

The rate of water consumption, and oxygen production is defined by Eq. (97):

$$\dot{n}_{H_2} = \dot{n}_{H_2O} = \frac{\dot{n}_{O_2}}{2} \tag{97}$$

3.2.3.4. Afterburner

During a chemical reaction, the bonds within the molecules of the reactants are broken, causing their atoms and electrons to rearrange and form products. In a combustion reaction, the rapid oxidation of combustible elements releases energy and produces various products. In this work, the combustion process is considered complete. In other words, all the carbon in the fuel is converted to carbon dioxide, all the hydrogen to water, all the sulphur to sulphur dioxide, and all other elements are fully oxidized. (88,108).

Fossil fuels is a complex mixture of hydrocarbons (C_mH_n), which oxidation is written by the stoichiometry equation, Eq. (98):

$$C_mH_n + \left(m + \frac{n}{4}\right) O_2 \rightarrow mCO_2 + \frac{n}{2} H_2O \tag{98}$$

So, for a complete combustion process, it is necessary ($m + \frac{n}{4}$) moles of oxygen for one mole of C_mH_n. For methane, carbon monoxide, and hydrogen, the equation above is given by Eqs. (99-101):

$$CH_4 + 2O_2 \rightarrow CO_2 + 2H_2O \tag{99}$$

$$2CO + O_2 \rightarrow 2CO_2 \tag{100}$$

$$2H_2 + O_2 \rightarrow H_2O \tag{101}$$

The air-fuel ratio is defined as the ratio of the mass of air to the mass of fuel used in the process, Eq. (102) (108):

$$\alpha = \frac{\dot{m}_{air}}{\dot{m}_{fuel}} \tag{102}$$

In combustion processes, oxidizers could be oxygen (O_2), air (21% O_2 and 79% N_2), air enriched with oxygen (O_2 > 21%), and other compounds containing oxygen. There are different types of combustible mixtures, being rich (excess of fuel), stoichiometric, and lean (excess of oxidizer).

The amount of air required for complete fuel combustion is determined by the oxygen-fuel stoichiometric reaction equation, which represents the minimum air needed. The stoichiometric ratio is defined as Eq. (103):

$$\lambda = \frac{\alpha_{actual}}{\alpha_{ideal}} \tag{103}$$

For a rich mixture, the stoichiometric ratio has a value over unity, while, for lean cases, its value is under unity. When a stoichiometric mixture is considered, the value is unity.

Usually, it is necessary to use a higher amount of air than stoichiometric combustion (108). So, the percentage of excess air is defined as Eq. (104):

$$e = \frac{\dot{m}_{air} - \dot{m}_{air,sto}}{\dot{m}_{air,sto}} \tag{104}$$

The actual air-to-fuel ratio can be written as a function of the stoichiometric ratio and excess air, Eq. (105):

$$\alpha = (1 + e) \cdot \alpha_{sto} \tag{105}$$

The composition of the exhaust product depends on the composition of the fuel entering the burner, the stoichiometric coefficient of the specie considered, and the extended reaction, Eq. (106):

$$\dot{n}_{out} = \dot{n}_{in} + \nu_i \xi \tag{106}$$

Where ν_i is the stoichiometric coefficient of the specie, and ξ the extent of combustion reaction in mol/s.

3.2.3.5. Auxiliary component

The compressors, storage tank, heat exchangers and thermal energy storage utilizes the same equations found in Sections 3.2.2.2, 3.2.2.4, 3.2.2.5, and 3.2.2.6, respectively.

The expansion valve is used to lower the pressure of the flowing fluid and often regulates its flow rate, without generating power, it is assumed to operate adiabatically and typically neglects the kinetic and potential energy changes associated with its operation. With these simplifications, the expansion valve is considered to have an isenthalpic operation, Eq. (107):

$$h_i = h_o \tag{107}$$

Pumps are designed to displace fluid and create a pressure difference. It is assumed that the pump operates adiabatically and that the effects of kinetic and potential energy are negligible. In this study, the work done by the pump is characterized by its isentropic efficiency, Eq. (108):

$$\eta_{p,ise} = \frac{\dot{W}_{ise}}{\dot{W}_{real}} \tag{108}$$

3.2.4. Heating and cooling module

3.2.4.1. CAES system

In the CAES system, heating and cooling are provided using heat exchangers to leverage the charging and discharging processes, as shown in Figure 14. Heating is supplied by the hot thermal energy storage in combination with a heat exchanger during both operations. Cooling, however, can only be provided during discharge by utilizing the cold air exiting the turbines, coupled with a heat exchanger to meet the demand. When the system is unable to meet these demands, it relies on the auxiliary system. Both natural gas burner and heat pump are used to supply heating, while a vapor compression refrigeration cycle is employed for cooling.

3.2.4.2. Hydrogen system

The SOFC operates at high temperatures, allowing the use of hot exhaust gases from the afterburner to provide both heating and cooling, as show in Figure 16.

An absorption chiller, shown in Figure 22, is used to supply the cooling during the discharge operation.

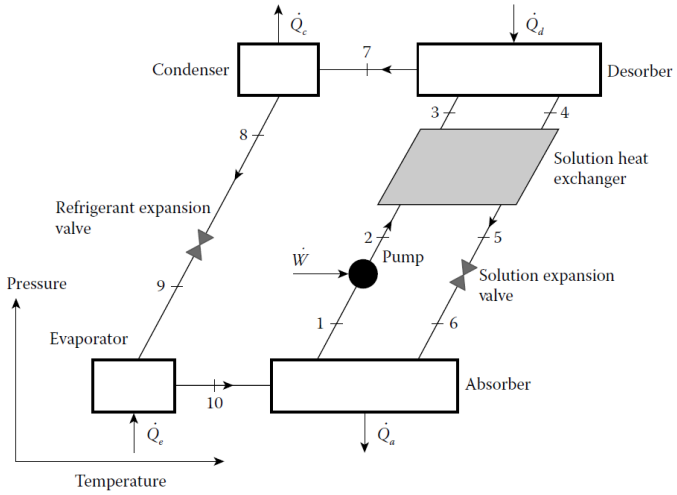

Figure 22: Cycle schematic of a single-effect water/lithium bromide absorption chiller (109).

In this study, for a sake of simplicity, exergy streams are not assessed, and a simpler approach considers the cooling demand and the temperatures at which heat is supplied to the desorber, and cooling is provided in the evaporator. To achieve this, a zero-order model is used to calculate the Energy Efficiency Ratio (EER) (109), Eq. (109):

$$EER = \frac{T_c}{T_h} = \frac{\dot{Q}_{cool}}{\dot{Q}_d} \tag{109}$$

Where $\dot{Q}_{cool}$ is the cooling capacity in kW, and $\dot{Q}_d$ is the rate of energy transfer by heat in the desorber in kW.

This approach does not represent the optimal design, but it provides a reasonable approximation (109). An additional benefit of this approach is that it is independent of the heat rejection temperature in the condenser.

Heating module consists of a combination of a heat exchanger and hot thermal energy storage, Figure 23.

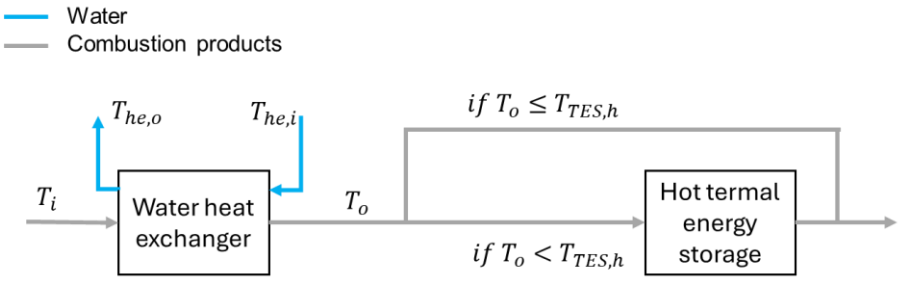

Figure 23: Heating module.

Where T_i represents the exiting temperature of the hot exhaust gases from the desorber, T_o the temperature exiting the water heat exchanger, $T_{TES,h}$ the temperature of the hot TES, and $T_{he,i}$ and $T_{he,o}$ the inlet and outlet temperature of the water stream of the heat exchanger.

After flowing through the desorber, the hot exhaust gases pass through a water heat exchanger to meet the heating demand. If possible, the exhaust gases can be used to heat the hot TES; otherwise, they bypass the storage tank and are released into the ambient. The hot TES can then be used to supply any unmet heating demand during both the charging and discharging phases.

3.2.4.3. Auxiliary systems

When any system is unable to supply the heating demand of the building, the auxiliary system is turned on to supply the missing demand. Both systems have different approaches on this matter: Rio de Janeiro utilizes a natural gas burner, and Lyon a heat pump.

The natural gas burner considers a constant efficiency system to calculate the amount of fuel to supply the missing heat, Eq. (110):

$$\dot{m}_{plus,CH_4} = \frac{\dot{Q}_{miss,heat}}{\eta_{bu} \cdot LHV_{CH_4}} \tag{110}$$

Where $\dot{m}_{plus,CH_4}$ is the amount of natural gas burnt to supply missing heat demand in kg/s, $\dot{Q}_{miss,heat}$ is the missing heat demand in kW, η_{bu} is the natural gas burner efficiency, and *LHV* is the low heating value in kJ/kg..

The heat pump utilizes the Coefficient of Performance (COP) in order to estimates the amount of electricity necessary to supply the missing heat demand, Eq. (111):

$$\dot{E}_{elec,heat} = \frac{\dot{Q}_{miss,heat}}{COP_h} \quad (111)$$

Where $\dot{E}_{elec,heat}$ is the electric power in kW to supply the missing heat demand ($\dot{Q}_{miss,heat}$), and COP_h is the heating COP.

In a similar approach, the missing cooling demand is based on the COP approach much like the one previously mentioned, Eq.(112):

$$\dot{E}_{elec,cool} = \frac{\dot{Q}_{miss,cool}}{COP_c} \quad (112)$$

Where $\dot{E}_{elec,cool}$ is the electric power in kW to supply the missing cooling demand ($\dot{Q}_{miss,cool}$), and COP_c is the cooling COP.

For the sake of simplicity, both COPs are based on the Carnot COP, which is described as follows, Eqs. (113-114):

$$COP_h = \frac{T_h}{T_h - T_c} \quad (113)$$

$$COP_c = \frac{T_c}{T_h - T_c} \quad (114)$$

3.2.5. Lithium-ion battery

The lithium-ion battery system is shown in Figure 24.

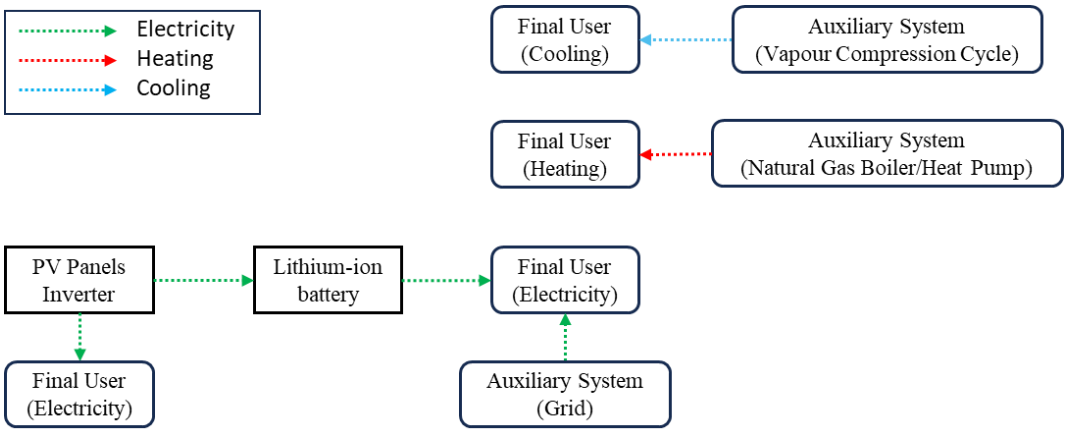

Figure 24: Lithium-ion battery system.

The PV panels, like the other two systems, are used to meet the building's electricity demand. When there is energy surplus, it is stored in the battery stack. Otherwise, if the panels cannot fully cover the electricity demand, the battery discharges to supply the missing energy. If neither the PV panels nor the battery can meet the demand, the auxiliary system draws energy from the electric grid. In the case of the lithium-ion battery system, both heating and cooling are provided by auxiliary systems.

The battery storage system has a simpler approach compared to the other two, considering a state-of-charge (SOC) approach. The SOC represents the ratio between the total amount of energy currently contained in the battery bank and its maximum capacity, defined as follows, Eq. (115-116) (110,111):

$$SOC(t) = SOC(t-1) \cdot (1-\sigma) + \frac{E_{cha} \cdot \eta_{b,cha} \cdot \eta_{b,conv}}{Cap_{bat}} \quad (115)$$

$$SOC(t) = SOC(t-1) \cdot (1-\sigma) - \frac{E_{dis}}{\eta_{b,dis} \cdot \eta_{b,conv} \cdot Cap_{bat}} \quad (116)$$

Where σ is the self-discharge rate in %/h, Cap is the battery rated capacity in kj, and the subscript bat refers to the battery, cha to charging, dis to discharging, and $conv$ to convertion.

3.3. Exergy modelling

Useful work can be performed whenever two systems with different conditions are brought into interaction, as work can be generated when they move toward equilibrium. One of these systems is an idealized reference, typically called the environment, while the other is the system of interest. Exergy represents the maximum theoretical (reversible) work that can be achieved as the two systems interact until equilibrium is reached. In essence, exergy quantifies the deviation of a system's state from that of the environment. Like other extensive properties such as mass, energy, and entropy, exergy can be transferred between systems. However, unlike energy, exergy is not conserved. The general expression for exergy balance is given by Eq. (117) (112):

$$\frac{dEx}{dt} = \sum_j \pm\left(1 - \frac{T_0}{T_j}\right) \cdot \dot{Q}_j + \left(\pm\dot{W} - P_0 \cdot \frac{d\forall}{dt}\right) + \sum_i \dot{m}_i \cdot e_i - \sum_o \dot{m}_o \cdot e_o - \dot{E}x_d \qquad (117)$$

Where Ex is the exergy in kJ, e is the specific exergy in kJ/kg, and $\dot{E}x_d$ is the rate of exergy destruction in kW. It is worth remembering that $\dot{Q}$ is the module of heat transfer rate in kW (positive signal when provided, and negative signal when realized), $\dot{W}$ is the module of power in kW (positive signal when provided, and negative signal when realized).

In the absence of nuclear, magnetic, electrical, and surface tension effects, total exergy of a system can be divided into four main components: kinetic, potential, physical and chemical, Eq. (118):

$$Ex = Ex_{ki} + Ex_{pt} + Ex_{ph} + Ex_{ch} \qquad (118)$$

Evaluating relative to the environment, kinetic and potential energies of the system are, in principle, fully convertible to work, so their corresponding kinetic and potential exergies are written as Eqs. (119-120):

$$Ex_{ki} = \frac{m \cdot v^2}{2} \qquad (119)$$

$$Ex_{pt} = m \cdot g \cdot z \qquad (120)$$

For a system at rest relative to its environment, where kinetic and potential energy components are disregarded, physical exergy represents the maximum theoretical useful work from the system when its temperature and pressure changes to match those of the reference, and chemical exergy refers to the maximum useful work when the substance is brought into equilibrium with the reference environment. Both components are mathematically described in the following Eqs. (121-122):

$$\dot{E}x_{ph} = \sum_i \dot{m}_i \cdot \left((h_i - h_0) - T_0 \cdot (s_i - s_0)\right) \qquad (121)$$

$$\dot{E}x_{ch} = \dot{n} \cdot \left(\sum_i y_i \cdot e_i^{ch,0} + \bar{R} \cdot T_0 \cdot \sum_i y_i \cdot \ln(y_i)\right) \qquad (122)$$

Where s is the specific entropy in kJ/(kg.K), $\dot{n}$ is the molar flow rate in mol/s, y is the molar concentration of each species, and $e^{ch,0}$ is the standard chemical exergy of the species in kJ/mol.

Table 9 displays the exergy balance considered for each component on this study.

Table 9: Exergy balance equations.

Component	Exergy Balance	Eq.
Renewable module	$\dot{E}x_{sun} = \dot{W}_{PV} + \dot{E}x_{d,PV}$	(123)
Compressor	$\dot{E}x_i + \dot{W}_c = \dot{E}x_o + \dot{E}x_{d,c}$	(124)
Turbine	$\dot{E}x_i = \dot{E}x_o + \dot{W}_t + \dot{E}x_{d,t}$	(125)
Heat Exchanger	$\dot{E}x_{c,i} + \dot{E}x_{h,i} = \dot{E}x_{c,o} + \dot{E}x_{h,o} + \dot{E}x_{d,he}$	(126)
Storage Tank	$\frac{dEx_{st}}{dt} = \dot{E}x_i - \dot{E}x_o - \dot{E}x_{d,stg}$	(127)
Thermal Energy Storage	$\frac{dEx_{TES}}{dt} = \dot{E}x_i - \dot{E}x_o - \dot{E}x_{\ d,TES}$	(128)
Electrolyzer	$\dot{W}_{PEMEC} + \dot{E}x_{H_2O} = \dot{E}x_{O_2} + \dot{E}x_{H_2} + \dot{E}x_{d,PEMEC}$	(129)
Fuel cell	$\dot{E}x_{a,i} + \dot{E}x_{c,i} = \dot{W}_{SOFC} + \dot{E}x_{a,o} + \dot{E}x_{c,o} + \dot{E}x_{d,SOFC}$	(130)
Reformer	$\dot{E}x_i = \dot{E}x_o + \dot{E}x_{d,ref}$	(131)
Mixer	$\dot{E}x_{1,i} + \dot{E}x_{2,i} = \dot{E}x_o + \dot{E}x_{d,mix}$	(132)
Afterburner	$\dot{E}x_{fuel,in} + \dot{E}x_{air,in} = \dot{E}x_{out} + \dot{E}x_{d,ab}$	(133)
Pump	$\dot{E}x_i + \dot{W}_p = \dot{E}x_o + \dot{E}x_{d,p}$	(134)
Expansion Valve	$\dot{E}x_i = \dot{E}x_o + \dot{E}x_{d,ev}$	(135)
Battery	$\dot{E}x_i = \dot{E}x_o + \dot{E}x_{d,bat}$	(136)

3.4. Exergoeconomy modelling

This approach combines exergy analysis with economic principles to offer insights that are not captured by traditional energy and economic evaluations but are crucial for designing and operating cost-effective systems. In conventional economic analysis, a cost balance is typically applied to the overall system or individual equipment operating in a steady state, expressed by the accompanying equation (137) (113,114):

$$\sum \dot{C}_i + \dot{Z} = \sum \dot{C}_o \tag{137}$$

Where $\dot{C}$ is the cost rate in \$/h, and $\dot{Z}$ is the investment cost rate of a component in \$/h.

A system operating at steady state may involve multiple incoming and outgoing material streams, along with heat and work interactions with its surroundings. These transfers involve not only matter and energy but also exergy, which flows into and out of the system and is partially destroyed due to irreversibilities within the system. Exergoeconomic is based on the principle that exergy provides a logical foundation for assigning costs to interactions within a thermal system and identifying inefficiencies—an approach known as exergy costing (113,114). This method assigns a cost to each exergy stream, as described by the accompanying Eq. (138).

$$\dot{C} = c \cdot \dot{E}x \tag{138}$$

Where c is the unit cost in $/kWh.

The investment cost rate of a component is defined by two components: one related to the capital investment ($\dot{Z}^{CI}$), and the other to the operation and maintenance ($\dot{Z}^{OM}$), as shown in Eqs. (139-141):

$$\dot{Z} = \dot{Z}^{CI} + \dot{Z}^{OM} \tag{139}$$

$$\dot{Z}^{CI} = \frac{CRF}{\tau} \cdot Z \tag{140}$$

$$\dot{Z}^{OM} = \frac{\gamma}{\tau} \cdot Z \tag{141}$$

Where *CRF* is the capital recovery factor (dimensionless), τ is the annual operating hours in hr, and Z is the purchased equipment cost in $.

The CRF corresponds to the capital recovery factor, Eq. (142).

$$CRF = \frac{i_r(1+i_r)^{n_y}}{(1+i_r)^{n_y} - 1} \tag{142}$$

Where i_r is the interest rate (dimensionless), and n_y is the lifetime operation in years.

The cost of each component should be based on the same reference year. The Chemical Engineering Plant Cost Index (CEPCI) is used to bring all cost data of components to the present year. The conversion is shown in Eq. (143):

$$Z = Z^{ref} \cdot \frac{CEPCI\ (present\ year)}{CEPCI^{ref}\ (reference\ year)} \tag{143}$$

When evaluating the performance of a component, all exergy loss stream should be costed as if they were to be further used by the system, calculating later the monetary loss associated with it, Eq. (144):

$$\dot{C}_d = c_f \cdot \dot{E}x_d \tag{144}$$

Where $\dot{C}_d$ is the cost rate associated to the exergy destruction in \$/h, and c_f is the fuel unit cost in \$/kWh. The equation assumes that exergy losses are compensated by supplying additional fuel to the components, with the average cost remaining constant despite changes in exergy loss. The exergy cost can be interpreted as the additional cost rate of fuel required to account for exergy destruction (113,114).

The unit cost of the stored mean of energy (air, hydrogen or electricity) updates depending on the system's operational mode. The calculations for charging, resting, and discharging modes are presented accordingly, Eqs. (145-147):

$$c_{st,t+1} = \frac{c_i \cdot \dot{E}x_i \cdot \Delta t + Ex_{st,t}}{Ex_{st,t+1}} \tag{145}$$

$$c_{st,t+1} = \frac{c_{st,i} \cdot Ex_{st,i}}{Ex_{st,t+1}} \tag{146}$$

$$c_{st,t+1} = \frac{Ex_{st,t} - c_o \cdot \dot{E}x_o \cdot \Delta t}{Ex_{st,t+1}} \tag{147}$$

For the exergoeconomic analysis, the balance cost balance and auxiliary equations for each component in the system are described in Table 10, and the capital cost equations in Table 11. The capital cost of each component is updated to the present year of this work, 2025, by utilizing Eq. (143).

Table 10: Components cost balance and auxiliary equations.

Component	Cost Balance	Eq.	Auxiliary
Renewable module	$\dot{C}_{in} + \dot{Z}_{PV} = \dot{C}_{out}$	(148)	$c_{sun} = 0$
Compressor	$\dot{C}_{in} + \dot{C}_{\dot{W}} + \dot{Z}_c = \dot{C}_{out}$	(149)	-
Turbine	$\dot{C}_{in} + \dot{Z}_t = \dot{C}_{out} + \dot{C}_{\dot{W}}$	(150)	-
Heat Exchanger	$\dot{C}_{h,in} + \dot{C}_{c,in} + \dot{Z}_{he} = \dot{C}_{h,out} + \dot{C}_{c,out}$	(151)	$c_{h,i} = c_{h,o}$
Storage Tank	$\dot{C}_{in} + \dot{Z}_{stg} = \dot{C}_{out}$	(152)	-
Thermal Energy Storage	$\dot{C}_{in} + \dot{Z}_{TES} = \dot{C}_{out}$	(153)	-
Electrolyzer	$\dot{C}_w + \dot{C}_{H_2O} + \dot{Z}_{PEMEC} = \dot{C}_{O_2} + \dot{C}_{H_2}$	(154)	-
Fuel cell	$\dot{C}_{an,in} + \dot{C}_{cat,in} + \dot{Z}_{SOFC} = \dot{C}_w + \dot{C}_{an,out} + \dot{C}_{cat,out}$	(155)	$\frac{\dot{C}_W}{\dot{W}} = \frac{\dot{C}_{an,o}}{\dot{E}_{an,o}} = \frac{\dot{C}_{cat,o}}{\dot{E}_{cat,o}}$
Reformer	$\dot{C}_{in} + \dot{Z}_{ref} = \dot{C}_{out}$	(156)	-
Mixer	$\dot{C}_{1,in} + \dot{C}_{2,in} + \dot{Z}_{mix} = \dot{C}_{oout}$	(157)	-
Afterburner	$\dot{C}_{fuel,in} + \dot{C}_{ox,in} + \dot{Z}_{ab} = \dot{C}_{out}$	(158)	-
Pump	$\dot{C}_{in} + \dot{C}_w + \dot{Z}_p = \dot{C}_{out}$	(159)	-
Expansion Valve	$\dot{C}_{in} + \dot{Z}_{ev} = \dot{C}_{out}$	(160)	-
Battery	$\dot{C}_{in} + \dot{Z}_{bat} = \dot{C}_{out}$	(161)	-

Even though the storage tank and thermal energy storage are assumed to operate at transient regime, in Eqs. (152-153), in particular, the calculations assume a steady-state regime with the contribution of the inlet and outlet streams and the components itself for finding the unit cost.

Table 11: Component capital cost equations [36,37,51,55,57,58,63,117,118].

Component	Capital Cost Equation	Eq.
Renewable Module	$Z_{PV} = 2.45 \cdot \dot{W}_{PV}$	(162)
Compressor	$Z_c = 91{,}562 \cdot \left(\frac{\dot{W}_c}{455}\right)^{0.7}$	(163)
Turbine	$Z_t = 1{,}100 \cdot \left(\dot{W}_t\right)^{0.81}$	(164)
Heat Exchanger	$Z_{he,CAES} = 12{,}000 \cdot \left(\frac{A_{he}}{100}\right)^{0.6}$	(165)
Storage tank	$Z_{st} = 1.218\, f_m \exp\left(2.631 + 1.3673 \cdot \ln\left(\forall_{stg}\right) - 0.06309 \cdot ln\left(\forall_{stg}\right)^2\right)$ $f_m = 1$ (Carbon steel)	(166)
Thermal Energy Storage	$Z_{TES} = 5{,}941.7\, \forall_{TES}^{-0.389}$	(167)
Reformer + Fuel Cell	$Z_{ref} = 0;\ Z_{SOFC} = A_{SOFC} \cdot n \cdot (2.96 \cdot T_{SOFC} - 1907)$	(168)
Electrolyzer	$Z_{PEMEC} = 1{,}000 \cdot \dot{W}_{PEMEC}$	(169)
Heat Exchanger	$Z_{he,H_2} = 130 \cdot \left(\frac{A_{he}}{0.093}\right)^{0.78}$	(170)
Afterburner	$Z_{ab} = 46.64 \cdot \dot{m}_{air} \cdot \left(1 + exp \cdot (0.018 \cdot T_{ab} - 26.4)\right)\left(\frac{1}{0.995 - \frac{P_{out}}{P_{in}}}\right)$	(171)
Pump	$Z_p = 3 \cdot 422 \cdot \left(\dot{W}_p\right)^{0.71} \cdot 1.41 \cdot f_n$ $f_n = 1 + \left(0.2/(1 - \eta_p)\right)$	(172) (173)
Mixer	$Z_{mix} = 0$	-
Expansion valve	$Z_{EV} = 0$	-
Battery	$Z_{bat} = 140 \cdot \dot{W}_{bat}$	(174)

Note: 1) all powers are given in kW, except for the PV panel peak power in Eq. (162) given in W; 2) Temperature in K; 3) Absolute pressure in kPa; 4) Volume in m³; 5) Area in m²; 6) Air mass flow rate in kg/s.

As the reformer is integrated with the SOFC in the numerical model, its capital cost equation is integrated with it, and in Table 11 considered to be null. Finally, Eqs. (163-164) were chosen among other capital cost equations found in literature, as their final result have a better consistency with the values reported in existing plants (119).

3.5. 4E parameters

The 4E analysis consists of the evaluation of the system from an energetic, exegetic, exergoeconomic and environmental point of view. For this study, it is necessary to take into consideration the two different modes of operation, since both charging and discharging processes happens during different periods. The parameters are evaluated hourly throughout the day. To compute the average values, both the numerator and denominator are integrated over the desired time

period, and the final average is obtained by taking the ratio of these integrated quantities.

3.5.1. Energy

Energy efficiency is defined as the ratio of useful energy produced by the total energy input, Eq. (175):

$$\eta_{en} = \frac{\dot{W}_o}{\dot{W}_i} \tag{175}$$

Three are the efficiencies evaluated in this section: electric, cogeneration, and trigeneration. The first one corresponds to the performance of the system in supplying solely the electric demand, as well as the components involved in the process to store air, hydrogen or electricity. The cogeneration contemplates the same aspect while also considering the system capacity to supply the heat demand. Finally, the trigeneration efficiency evaluates the performance of the system to supply all three demands.

3.5.1.1. CAES system

The electric efficiency in charging and discharging modes are described respectively, Eqs. (176-177):

$$\eta_{elec,cha} = \frac{E_{elec} + E_{st,c}}{E_{sun}} \tag{176}$$

$$\eta_{elec,dis} = \frac{W_{PV} + W_t + E_{grid}}{E_{sun} + E_{st,t} + E_{grid}} \tag{177}$$

Where E_{elec} corresponds to the electric demand in kJ, $E_{st,c}$ to the energy stored during the charging process in kJ, E_{sun} is the energy harness from the sun in kJ, $E_{st,t}$ is the energy from the mass of air utilized during the discharging process in kJ, W_{PV} is the energy from the PV panels in kJ, W_t is the work provided by the turbines matching the electric demand in kJ, and E_{grid} is the energy from the electric grid in kJ. The subscript cha referes to the charging process, and dis to the discharge.

The cogeneration efficiency for both modes of operation is shown in Eqs. (178-179):

$$\eta_{cog,cha} = \frac{E_{elec} + E_{st,c} + Q_{heat}}{E_{sun} + Q_{h,TES} + Q_{bu}} \quad (178)$$

$$\eta_{cog,dis} = \frac{W_{PV} + W_t + E_{grid} + Q_{heat}}{E_{sun} + E_{st,t} + E_{grid} + Q_{h,TES} + Q_{bu}} \quad (179)$$

Where Q_{heat} corresponds to the heat demand in kJ, $Q_{h,TES}$ is the energy from the hot TES in kJ, and Q_{bu} is the energy from the natural gas burner in kJ.

Finally, trigeneration can only be evaluated during the discharge phase, when the system can produce cooling as the turbine expands, Eq. (180):

$$\eta_{tri,dis} = \frac{W_{PV} + W_t + Q_{heat} + Q_{cool} + E_{grid}}{E_{sun} + E_{st,t} + E_{grid} + Q_{H,TES} + Q_{bu} + Q_{cool,HE}} \quad (180)$$

Where Q_{cool} is the cooling demand in kJ, and $Q_{cool,HE}$ is the energy from the cooling heat exchanger in kJ.

3.5.1.2. Hydrogen system

The efficiencies for the hydrogen system are described similarly to the CAES system. Electric efficiency is defined as Eqs. (181-182):

$$\eta_{ele,cha} = \frac{E_{elec} + m_{H_2} LHV_{H_2} + W_c}{E_{sun}} \quad (181)$$

$$\eta_{elec,dis} = \frac{W_{PV} + W_{SOFC} + E_{grid}}{E_{sun} + m_{H_2} \cdot LHV_{H_2} + m_{CH_4} \cdot LHV_{CH_4} + E_{grid}} \quad (182)$$

Where m_{H_2} is the hydrogen mass in kg, LHV_{H_2} is the hydrogen lower heating value in kJ/kg, W_c is the energy to compress the hydrogen into the storage tank in kJ, W_{SOFC} is the energy from the SOFC in kJ, m_{CH_4} is the methane mass in kg, LHV_{CH_4} is the methane lower heating value in kJ/kg.

Cogeneration efficiencies are described as follows, Eqs. (183-184):

$$\eta_{cog,cha} = \frac{E_{elec} + m_{H_2} LHV_{H_2} + W_c + Q_{heat}}{E_{sun} + Q_{H,mod} + Q_{bu}} \quad (183)$$

$$\eta_{cog,dis} = \frac{W_{PV} + W_{SOFC} + Q_{heat} + E_{grid}}{E_{sun} + m_{H_2} LHV_{H_2} + m_{CH_4} LHV_{CH_4} + W_{grid} + Q_{H,mod} + Q_{bu}} \quad (184)$$

Where $Q_{H,mod}$ corresponds to the energy provided by the heating module in kJ.

Finally, trigeneration efficiency, Eq. (185):

$$\eta_{tri,dis} = \frac{W_{PV} + W_{SOFC} + Q_{heat} + Q_{cool} + E_{grid}}{E_{sun} + m_{H_2} LHV_{H_2} + m_{CH_4} LHV_{CH_4} + W_{grid} + Q_{H,mod} + Q_{bu} + Q_{C,ab}} \quad (185)$$

Where $Q_{C,ab}$ is the energy from the absorption chiller in kJ.

3.5.1.3. Lithium-ion battery system

In the case of , only the electric efficiency is of interest, Eqs.(186-187):

$$\eta_{elec,cha} = \frac{E_{elec} + E_{st,cha}}{E_{sun}} \quad (186)$$

$$\eta_{elec,dis} = \frac{W_{PV} + E_{bat} + E_{grid}}{E_{sun} + E_{st,dis} + E_{grid}} \quad (187)$$

Where $E_{st,cha}$ is the energy stored in the battery during charging in kJ, E_{bat} is the energy from the battery in kJ, and $E_{st,dis}$ is the energy from the stored electricity being released during discharge in kJ.

3.5.2. Exergy

Exergy efficiency provides a true measure of the performance of an energy system from the thermodynamic viewpoint. It expressed by the ratio of product and fuel, Eq. (188)

$$\eta_{exe} = \frac{Ex_p}{Ex_f} \quad (188)$$

Where Ex_f is the fuel exergy in kJ, and Ex_p is the product exergy in kJ.

3.5.2.1. CAES system

Charging and discharging exergy efficiencies for the CAES system are described, Eqs. (189-190):

$$\eta_{exe,cha} = \frac{W_{PV} + Ex_{st,c}}{Ex_{sun}} \tag{189}$$

$$\eta_{exe,dis} = \frac{W_{PV} + W_t}{Ex_{sun} + Ex_{st,t} + Ex_o} \tag{190}$$

Where $Ex_{st,c}$ is the exergy associated with the air being stored in kJ, Ex_{sun} the exergy harness from the sun in kJ, $Ex_{st,t}$ is the exergy associated with the mass of air stored to be expanded in the turbines in kJ, and Ex_o is the exergy associated with the stream of air exiting the system to ambient in kJ.

3.5.2.2. Hydrogen system

Charging and discharging exergy efficiencies for the hydrogen system are described, Eqs. (191-192):

$$\eta_{exe,cha} = \frac{W_{PV} + Ex_{H_2,st}}{Ex_{sun}} \tag{191}$$

$$\eta_{exe,dis} = \frac{W_{PV} + W_{SOFC}}{Ex_{sun} + Ex_{H_2,in} + Ex_{CH_4,in} - Ex_o} \tag{192}$$

Where $Ex_{H_2,st}$ is the exergy associated with the hydrogen being stored in kJ, $Ex_{H_2,in}$ is the exergy related to the hydrogen being withdrawn from the storage tanks in kJ, $Ex_{CH_4,in}$ is the exergy associated with the natural gas being withdrawn from the grid in kJ, and Ex_o is the exergy from the exhaust gas being release in the ambient in kJ.

3.5.2.3. Lithium-ion battery system

Charging and discharging exergy efficiencies for the lithium-ion system are described, Eqs. (193-194):

$$\eta_{exe,cha} = \frac{W_{PV} + Ex_{st,cha}}{Ex_{sun}} \tag{193}$$

$$\eta_{exe,dis} = \frac{E_{bat} + W_{PV}}{Ex_{sun} + Ex_{st,dis}} \tag{194}$$

Where $Ex_{st,cha}$ is the exergy associated with the charging procedure of the battery in kJ, and $Ex_{st,dis}$ is the exergy associated with the stored electricity being released during discharge in kJ.

3.5.3. Exergoeconomy

The relative cost difference is defined as, Eqs. (195-197):

$$r = \frac{c_p - c_f}{c_f} \tag{195}$$

$$c_f = \frac{\dot{C}_f}{\dot{E}x_f} \tag{196}$$

$$c_p = \frac{\dot{C}_p}{\dot{E}x_p} \tag{197}$$

Where *r* is the relative cost difference (dimensionless), c_f is the fuel average unit cost in $/kWh, and c_p is the product average unit cost in $/kWh.

Another important parameter is the exergoeconomic factor expressed in Eq. (198):

$$f = \frac{\dot{Z}}{\dot{Z} + \dot{C}_d} \tag{198}$$

Where *f* is the exergoeconomic factor (dimensionless).

This variable connects two distinct cost sources: non-exergy-related costs (including capital investment and operation and maintenance expenses) and exergy-related costs (stemming from exergy destruction and losses). It represents the ratio of non-exergy-related costs to the total cost increase. A low value indicates that cost savings could be achieved by enhancing the component's efficiency. Conversely, a high value suggests that reducing investment costs might be necessary, even if it comes at the expense of exergy efficiency (113).

3.5.4. Environmental

To measure emissions, three distinct scopes are used to classify the type of emission:

- Scope 1: Includes emissions from sources directly controlled/produced by companies, such as electricity or heat generation, chemical processing or manufacturing, material transport, or leaks.
- Scope 2: Covers indirect emissions resulting from a company's consumption of energy generated elsewhere.
- Scope 3: Encompasses all emissions linked to a company's activities but originating from sources not directly controlled by the company.

The environmental analysis involves calculating the equivalent CO_2 emissions per kWh of electricity generated and evaluating the potential reduction of gas burned by the system (Scope 2) when providing heating. During discharge, turbines, fuel cells and batteries are used to generate electricity, minimizing direct emissions. Meanwhile, during charging, photovoltaic panels supply electricity, reducing reliance on the electric grid and thereby lowering indirect emissions.

It is evaluated the amount of CO_2 equivalent avoided during the operation of the system (scope 1). To do so, it is considered the amount of energy produced/withdrawn from the grid, as well as the amount of natural gas consumed/avoided, Eq. (199)

$$\dot{m}_{CO_{2,eq}} = \dot{W} \cdot \Delta t \cdot e_{CO_2,grid} + \dot{m}_{NG} \cdot \Delta t \cdot e_{CO_2,NG} \quad (199)$$

Where *e* is the specific emissions in kg/kWh of CO_2 equivalent, and the subscript *NG* to natural gas.

The Brazilian and French energy matrix heavily relies on hydropower and nuclear, respectively, which both have a low average emission per MWh. For the analysis, a historical average value from 2013 to 2023 (120) was considered, resulting in a 147.3 kg and 67.6 kg of equivalent CO_2 per MWh generated for the Brazilian and French scenario respectively. These values in comparison, using the database, are way lower than the global average emission rate for the same period of 510.0 kg of equivalent CO_2 per MWh.

Calculated both the operational cost of the system and the total emission avoided during operation, it is possible to calculate the cost per emission avoided, Eq. (200):

$$C_{CO_2,avoid} = \frac{\Delta C_{op,BAU}}{m_{CO_2,avoid}} \tag{200}$$

Where C_{op} is the difference between operational cost and business as usual (BAU) in $, and $m_{CO_2,avoid}$ is the total avoided emission during the operation in comparison to business as usual scenario kg.

The final parameter being evaluated is the emissions per unit of energy, simply described by, Eq. (201):

$$\vartheta = \frac{m_{CO_2,emitted}}{W} \tag{201}$$

Where ϑ is the emission per unit of energy kg/kWh, and $m_{CO_2,emitted}$ is the total mass of CO_2 emitted in kg.

3.6. Chapter conclusion

The equations presented in this section detail the numerical modelling of the system from four perspectives: energetic, exergetic, exergoeconomic, and environmental. These 4E parameters are crucial for evaluating the system's behaviour and gaining a clear understanding of its feasibility in different scenarios.

4
Methodology

Both case studies (Rio de Janeiro in Brazil and Lyon in France) are presented in this chapter with a focus on their energy demands—electricity, heating, and cooling—and climate conditions, particularly solar radiation. These factors are essential for the proper modelling of the systems. Additionally, the control strategies of the CCHP and the criteria used for convergence are detailed, along with the tools used to determine system sizing and operational limits.

Simulation is performed with MATLAB 2024b software, and the properties of all fluids for the hydrogen system during discharge are based on the Peng-Robinson equation of state and mixing rules, using the Eqs. (A1-A26) in the Appendix A, and for CAES system utilizing the REFPROP 9.0 software.

4.1.
Cases description

The interaction between photovoltaic panels and electric demand is a key factor in system operation. The difference between these two determines whether the system operates in charging mode or discharging mode, as illustrated in Figure 25.

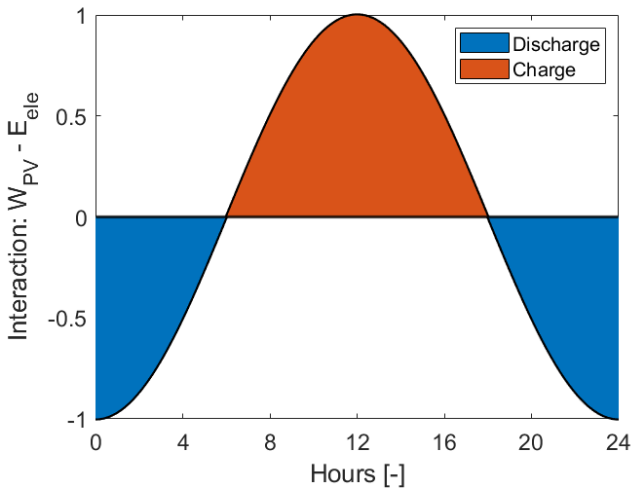

Figure 25: Interaction between PV panels power output and electric demand.

Whenever the difference is negative, it indicates an energy shortage and the system functions in discharging mode (blue area). During this mode, air or hydrogen is withdrawn from the storage tank to power turbines or fuel cells, or in the case of the lithium-ion battery, it uses the stored electricity. Conversely, when there is an energy surplus, the system transitions to charging mode (orange area),operating the electrolyzer and compressors, storing hydrogen or air, respectively, or charging the battery.

The simulations consider the electricity, heating, and cooling demands of a typical residential building in both locations in an hourly basis for a typical year (available in Appendix B). For a sake of simplicity and to reduce the volume of data, this section only focuses on annual average data, while seasonal averages are also presented in Appendix B (both datasets are not used in the simulations).

For Rio de Janeiro, typical electricity consumption profiles are utilized alongside average hourly consumption data, which current design follows the real data specified by EPE (Energy Research Company in English) (121,122). The raw data included only electricity demand, which was divided into different categories: household appliances, electric resistance heating for water in showers, and air conditioning. The heating demand was estimated based on an electric resistance of 95% efficiency used for hot showers. Cooling demand was determined from the electricity consumption of air conditioners, assuming an operating COP equal to 20% of the Carnot COP. Finally, the remaining electricity demand, after subtracting the portions allocated to heating and cooling, corresponded to household appliances.

Figure 26 illustrates the annual average demands for the considered building configuration (after the aforementioned treatment) and solar radiation, and Figure 27 the daily average electric demand and photovoltaic electric power output for the city of Rio de Janeiro.

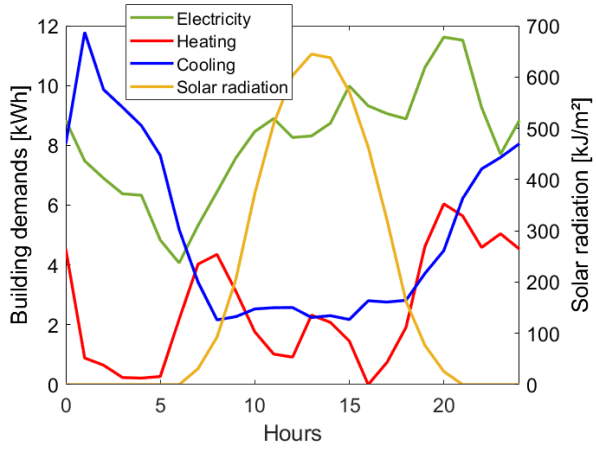

Figure 26: Annual hourly average building demands and solar radiation – Rio de Janeiro.

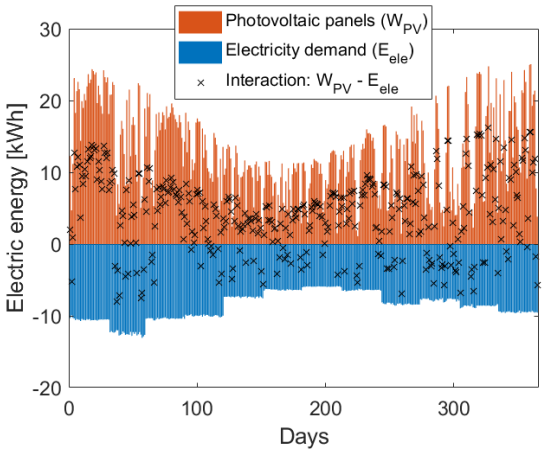

Figure 27: Daily average photovoltaic panels power, electricity demand and its interaction – Rio de Janeiro.

Figure 26 shows that the highest solar radiation occurs around midday, while the peaks for all three types of demand take place at night, with the lowest values in the morning and early afternoon. Figure 27 depicts the daily average interaction between photovoltaic power and electric demand. A positive difference (orange area) indicates charging of the storage tanks by the end of day, whereas a negative difference (blue area) represents tank discharging.

For Lyon, the data from Dib et al. (79) was used. The author's study analyses three cities—Nice, Strasbourg, and Nantes—for all three types of demand. Strasbourg was selected to represent Lyon's demands, as it shares more similarities with Lyon compared to the other cities (123). Solar radiation data, however, was sourced from the nearby area of Vaulx-en-Velin in Lyon. Following the same pattern as in the Brazilian case, Figure 28 presents the annual average values for the building in Lyon, along with the daily interaction in Figure 29.

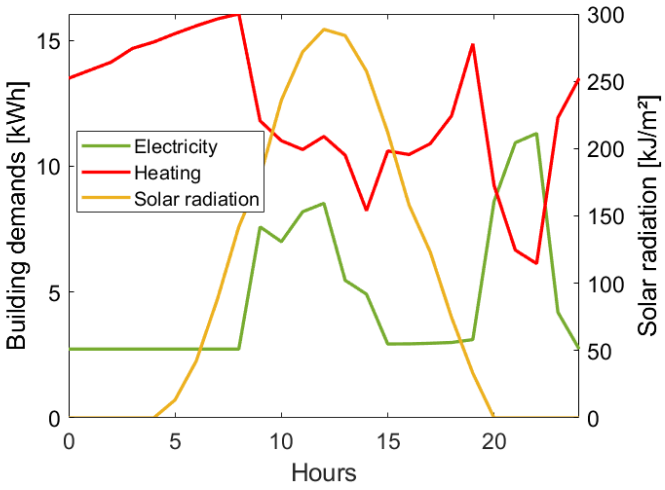

Figure 28: Annual hourly average building demands and solar radiation - Lyon.

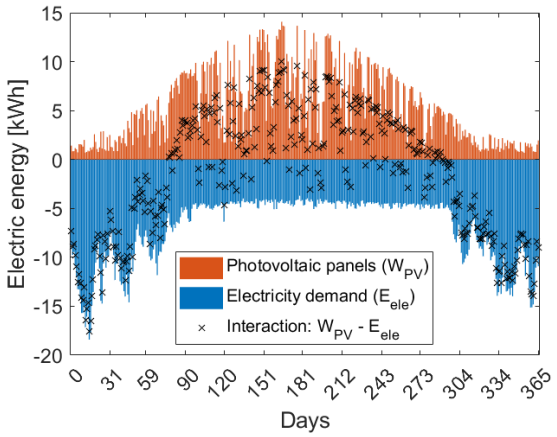

Figure 29: Daily average photovoltaic panels power, electricity demand and its interaction - Lyon.

The difference between both cities is clear. Notably, there is no cooling demand in Lyon, unlike in Rio de Janeiro. Heating demand in Lyon is significantly higher due to its colder winters and autumns. Additionally, Lyon's annual average solar radiation is nearly half that of Rio de Janeiro. These differences are further emphasized in Figures 27 and 29. In Lyon, the system is only able to store air in the tanks during summer and spring, while during autumn and winter, it relies entirely on the storage or grid.

The high heating demand during autumn and winter exceeds the capacity of the proposed hot TES system. To address this, heat pumps are utilized as an auxiliary system to supply heat, consuming additional electricity. For this conversion, the heat pump's COP is assumed to be 40% of the Carnot COP. Figure 30 illustrates the adjusted electricity demand across all seasons.

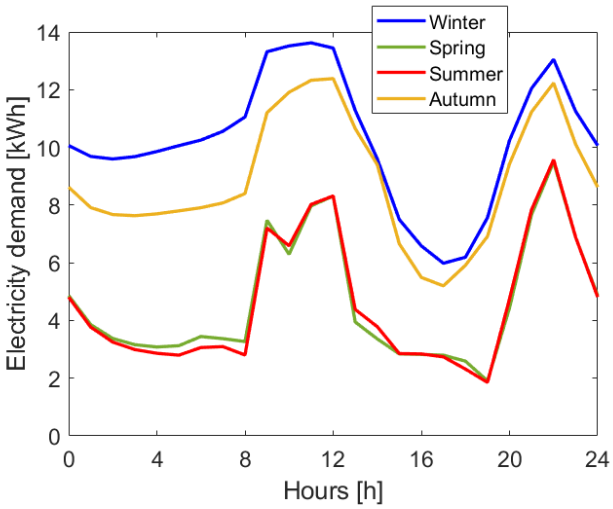

Figure 30: Seasonal hourly average building electricity demand - Lyon.

4.2. Control and operation

4.2.1. Storage tanks

4.2.1.1. Air and hydrogen

Two storage tanks are considered in this work to avoid the operation of one of a bigger size. While one is experiencing either the charging or discharging procedure, the other one is at rest.

The charging process is presented in Figure 31.

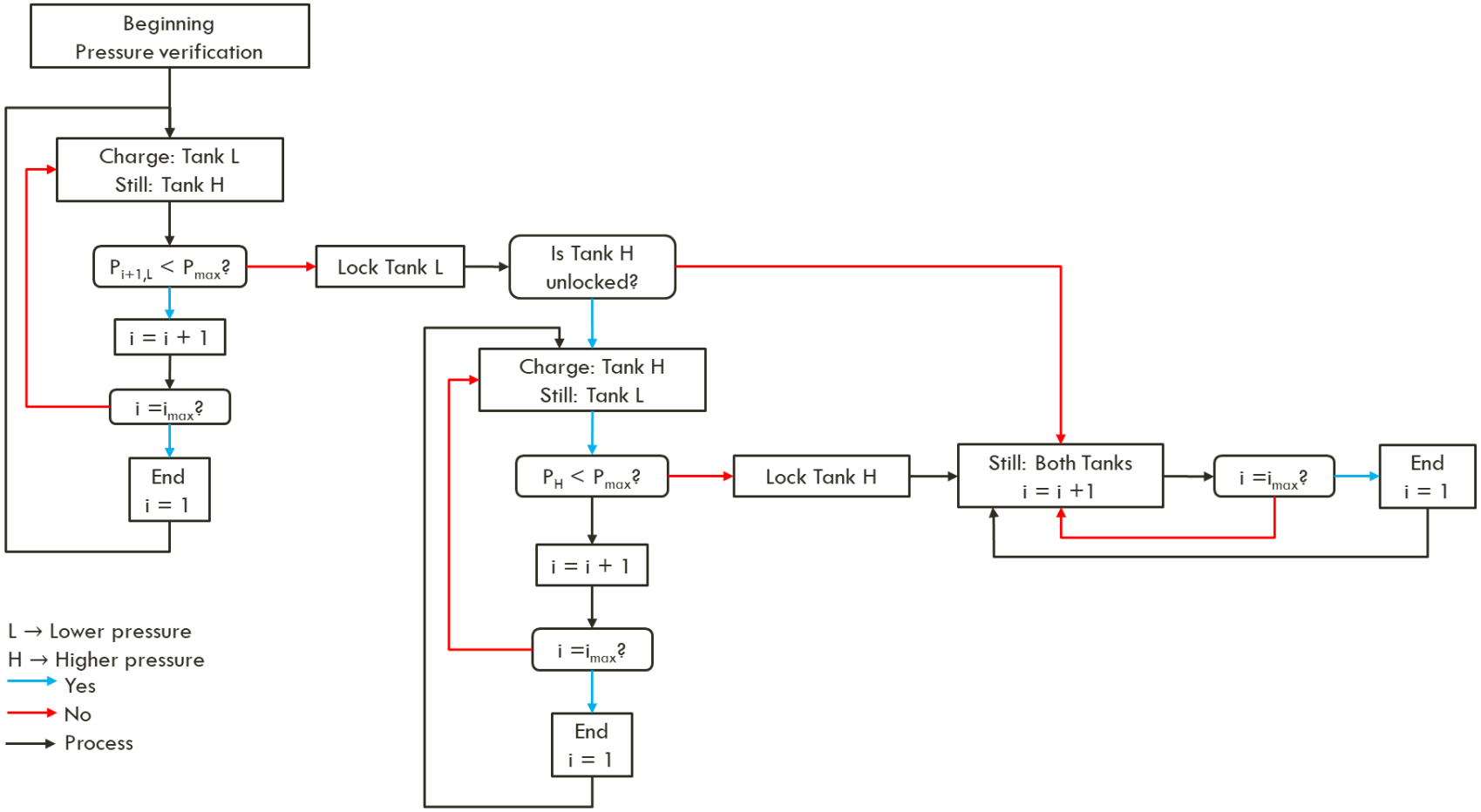

Figure 31: Storage tank charging control flowchart.

The procedure starts by checking the pressure in both storage tanks: one at lower pressure (L) and the other at higher pressure (H). The system prioritizes charging the tank with the lower pressure until it is completely full. Once this condition is met, the tank is locked, and the other tank is charged, provided it is not already locked. If both tanks are locked, no charging occurs, and the excess electric power from the photovoltaic panels is directed to the grid. A tank is unlocked whenever it undergoes a discharging process.

Figure 32 display the procedure during discharge.

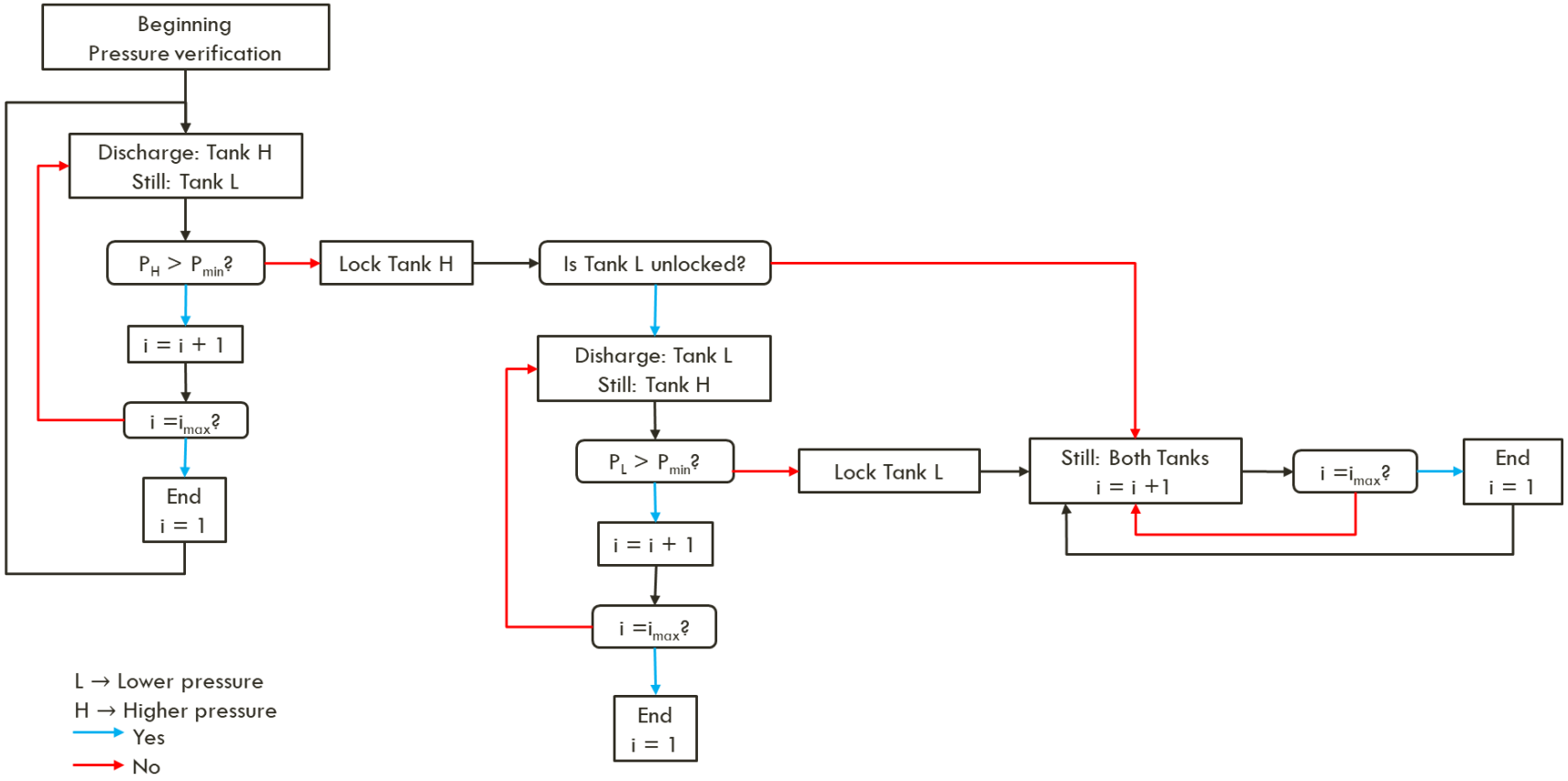

Figure 32: Storage tank discharging control flowchart.

The control process for discharging is similar to that of charging. Initially, the storage tanks are assessed to identify the one with higher pressure (H) and the one with lower pressure (L). The system prioritizes discharging the tank with higher pressure until it is fully depleted. Once depleted, the tank is locked, and if possible, the other tank is discharged. If both tanks are depleted, the electricity demand is met by the grid. A tank is unlocked for future operations once it undergoes any charging.

4.2.1.2. Thermal energy storage

During charging and discharging operations, water flows into or out of the thermal energy storage tanks. To prevent either tank from being completely depleted, the system is designed to ensure that water is always present in both tanks. Figure 33 illustrates the control configuration for managing the thermal energy storage.

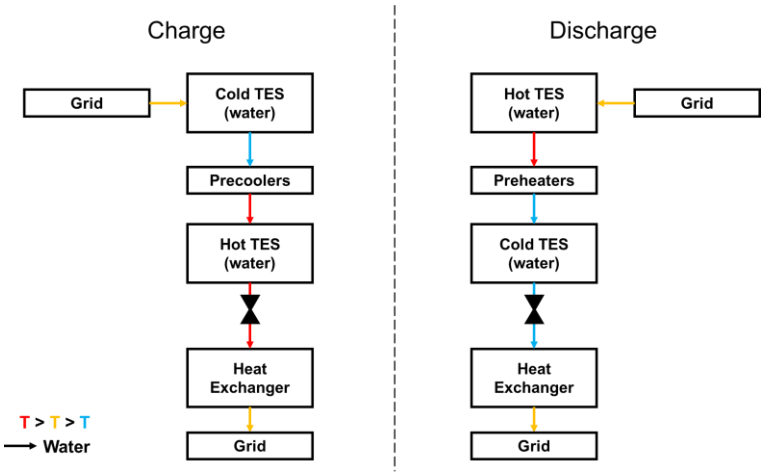

Figure 33: Thermal energy storage control.

For the hot TES, water is withdrawn to preheat the air entering the turbines and is replenished after precooling the air entering the compressors in the CAES system. In the hydrogen system, water is used to supply electrolyzers for green hydrogen production. For the cold TES, water is withdrawn to precool the air entering the compressors and is replenished with chilled water after preheating the air entering the turbines. In both cases, the storage tanks may reach their maximum or minimum volume limits. If the volume falls below the minimum, the tank is refilled with ambient-temperature water from the grid. Conversely, if the volume exceeds the maximum limit, the excess water is drained and returned to the grid.

4.2.2.
Fuel cell / electrolyzer

The operation of the fuel cells and electrolyzers depends on the interaction between the bus voltage (stack voltage) and the current density. The system is designed so that the incoming power from the PV panels during the charging phase, or the electric power output from the SOFC during the discharging phase, can be precisely matched within the operational range by adjusting the number of stacks in operation.

Operational parameters, including current density, maximum number of stacks, active area, bus voltage, and cells per stack, are set to allow the system to adapt to varying demand. The number of operating stacks is determined by design conditions, Eqs. (202-204), while current density and bus voltage are adjusted by matching the stack power ($\dot{W}_{PEMEC,SOFC}$) with the power surplus or demand ($\dot{W}_{match}$) using the correlations from section 3.2.3.3 for PEMEC or SOFC voltage ($V_{PEMEC,SOFC}$), Eqs. (205-206):

$$I_{des} = j_{des} A \tag{202}$$

$$\dot{W}_{stack,des} = V_{bus} I_{des} \tag{203}$$

$$n_{stack} = \frac{\dot{W}_{match}}{\dot{W}_{stack,des}} \tag{204}$$

$$I_f = \frac{\dot{W}_{match}}{V_{bus,f} \cdot n_{stack}} \tag{205}$$

$$\dot{W}_{PEMEC,SOFC} = V_{PEMEC,SOFC} \cdot I_f \cdot n_{cell} \tag{206}$$

Where I_{des} is the design electric current in A, j_{des} is the design current density in A/m², A is the area in m², $\dot{W}_{stack,des}$ is the power of the stack at design condition in kW, V_{bus} is the bus voltage in V, n_{stack} is the number of stacks, $\dot{W}_{match}$ is the electric power surplus or demand in kW, $\dot{W}_{PEMEC,SOFC}$ is the final power input/output from the PEMEC or SOFC in kW, n_{cell} is the number of cells, and the subscript f corresponds to final.

It is important to note that the bus voltage adjustment is kept within 10% of its nominal value, while there are no restrictions on current density. However, to activate the cell stacks, the current density must remain within 20% of the design

condition. If this condition is not met, the system may adjust the number of stacks until the maximum or minimum value is reached. In case the condition cannot be met, the system interacts with the grid to supply or export the electric power. This procedure is highlighted in Figure 34.

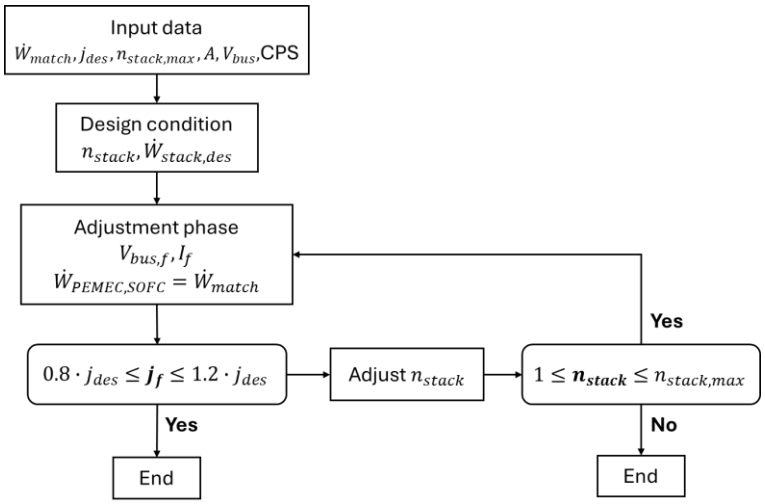

Figure 34: Scheme of the fuel cell and electrolyzer operation.

Where j_f is the final current density A/m², and CPS is the cells per stack.

4.2.2.1. Charge phase

During the charging phase, surplus energy is used to operate the system responsible for storing either air or hydrogen or directly charging the battery with electricity. In the case of the CAES system, the energy is almost equally distributed across the compressors, assuming a uniform pressure ratio among them. However, in the hydrogen system, the surplus power is divided between the PEMEC and the compressor (also uniform pressure ratio), with the distribution heavily influenced by the pressure inside the storage tank. Figure 35 shows the distribution between these components as a function of the storage tank pressure.

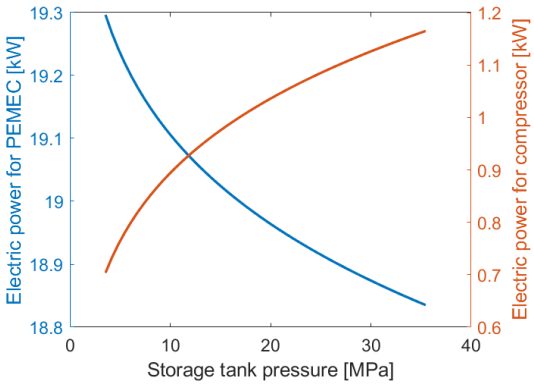

Figure 35: PEMEC and compressors electric power surplus share at 20 kW rate, and inlet pressure of the first compressor at constant ambient pressure.

As the storage pressure increases, the amount of power required to operate the compressors also increases, even though the rate of hydrogen production decreases. This trend is illustrated in Figure 35, assuming a surplus power rate of 20 kW. As pressure rises from ambient pressure to 35 MPa, the portion of power allocated to the PEMEC decreases from 96.5% to 94.2%. It was observed that the supplied power rate has little effect on the distribution between the components.

4.2.2.2. Discharge phase

During the discharge phase, either air or hydrogen is withdrawn from the storage tank to power the turbines or fuel cells, providing electricity to meet the demand. In the case of the CAES system, the turbines generate nearly the same amount of power using the air from storage The hydrogen system, however, includes not only the SOFCs but also two compressors and a pump, which require electricity to operate. It is assumed that the fuel cells can supply the necessary power, which is then added to the overall electric demand. From an operational perspective, it was found that of the power supplied by the SOFCs, 87.35% is directed to the building's electricity demand, 12.44% to the air compressor, 0.21% to the fuel compressor, and the power required for the water pump is negligible in comparison.

The amount of hydrogen withdrawn from the storage tank is determined by the energy from methane in the reforming process that needs to be replaced. Figure 36 illustrates the substitution behaviour, assuming an inlet methane molar flow of 1 mol/s.

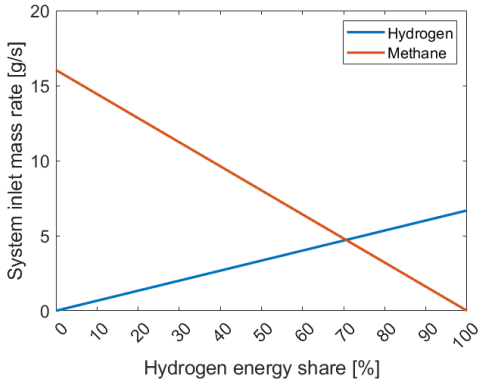

Figure 36: Methane substitution by hydrogen considering molar rate of 1 mol/s.

Increasing the amount of hydrogen withdrawn from the storage tank helps reduce the amount of methane introduced into the system, as shown in Figure 36, thereby lowering the CO_2 emissions during operation.

Determining the appropriate share of hydrogen for this substitution is challenging. A high share would result in the storage tank being depleted most of the time, while a low share would not fully utilize the hydrogen produced. To estimate an optimal value, the monthly average values of the PV panel power output and electric demand are calculated. The share that best aligns with the hydrogen production and consumption rate throughout the year is selected for the numerical simulation, presented in Figure 37. Figure 38 presents the average hydrogen mass rate during consumption and production at each month for both Rio de Janeiro and Lyon.

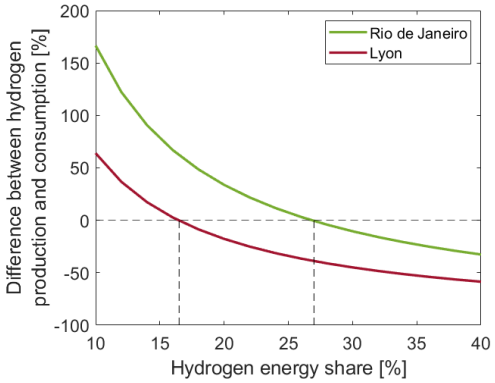

Figure 37: Production and consumption difference – Rio de Janeiro and Lyon.

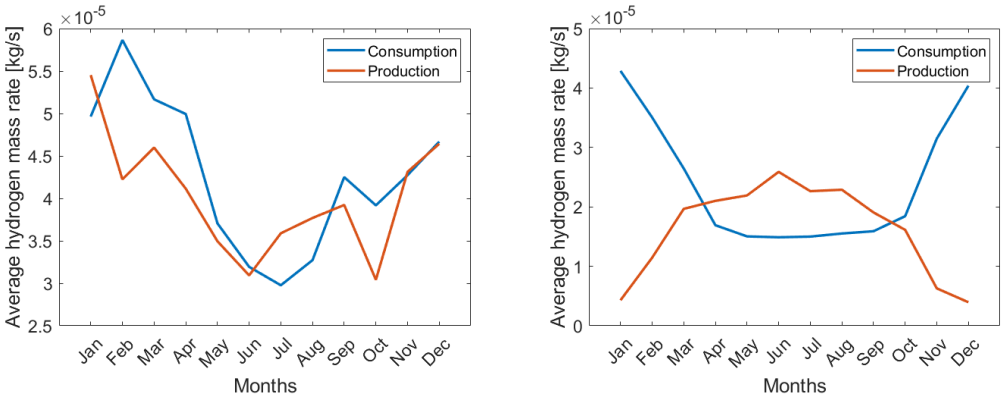

(a) Rio de Janeiro (b) Lyon

Figure 38: Monthly hydrogen average mass flow rate.

In Figure 37, the region above zero indicates that hydrogen production exceeds consumption over the year, while the area below zero shows the opposite. It is found that a share of 27% optimizes the balance between hydrogen production and consumption throughout the year in the Brazilian case, whereas for the French one, its value corresponds to 16.5%. Figure 38(a) displays the monthly values for consumption and production for Rio de Janeiro, and Figure 38(b) for Lyon. It shows that, assuming a constant share, there are months when production exceeds consumption and others when the opposite occurs, ultimately achieving a balance by the end of the year. For the Brazilian scenario, regardless of the month, it can be seen that consumption and generation present similar values. The French scenario clearly illustrates the seasonal differences in hydrogen production and consumption, with notable contrasts between colder and warmer seasons.

4.3. System sizing

The sizing of all three ESSs, in both cities, is based on the need to supply the electricity demand of a reference residential building during a specific week of the year. The photovoltaic panels were initially sized to fit the building's rooftop area. However, it was determined that this area would be too small to meet both the energy demand and the storage requirements for air or hydrogen, particularly during colder seasons. Therefore, an area 50% larger than the rooftop is considered, which could be installed near the building (for instance, on the rooftop of a parking lot). Table 12 presents the parameters used for sizing the building, Table 13 the costs associated with electricity and natural gas costs for both cities, and Table 14 the PV panels.

Table 12: Building sizing.

Variable	Value
Residents	48
Floors	4
Apartments per floor	4
Apartment area [m²]	72

Table 13: Electricity and natural gas cost (124,125,126,127).

Variable	Value
Electricity cost – Rio de Janeiro [$/kWh]	0.14
Natural gas cost – Rio de Janeiro [$/kg]	2.02
Electricity cost – Lyon [$/kWh]	0.15
Natural gas cost – Lyon [$/kg]	1.63

Table 14: PV panels sizing.

Variable	Value
Panel area [m²]	1.224
Number of photovoltaic panels [-]	345
Photovoltaic panel total surface area [m²]	429

The storage tanks are sized similarly across all systems. The goal is to determine a sufficient storage volume to meet the electric demand for an entire week of operation. The week selected for evaluation is the one that best represents an "average" week of the year. It is identified analysing the total power output from the photovoltaic panels and the electric demand for each week, as shown in Figure 39 for Rio de Janeiro and Lyon. The week closest to the total average is then selected.

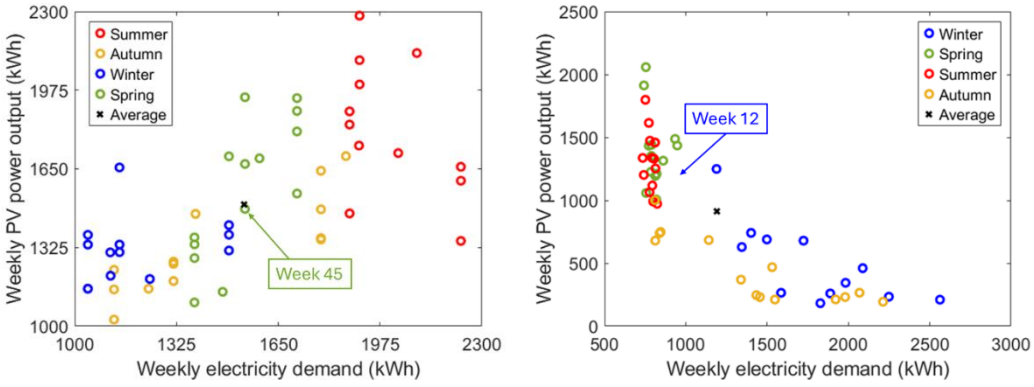

(a) Rio de Janeiro (b) Lyon

Figure 39: Total weekly PV power output and electric demand.

Figure 39(a) shows the results for Rio de Janeiro, indicating that the week closest to the average value occurs in the spring (week 45, early November). Figure 39(b) illustrates the results for Lyon, where three weeks stand out as potential averages: two in winter and one in autumn. Week 12 (late March) was chosen due to its higher weekly PV power output, allowing for a smaller system

size. This selection also aligns with operational patterns observed in summer and spring.

Identifying the maximum power output from the PV panels and the electricity demand is crucial for sizing the system's prime movers: compressors, turbines, SOFCs, and PEMECs. Figures 40 and 41 present the histogram of the power level during charge and discharge for both Rio de Janeiro and Lyon, respectively. The French case has two different histograms, as the electric demand is different for the CAES/lithium-ion battery systems and hydrogen system, as explained in Section 4.1.

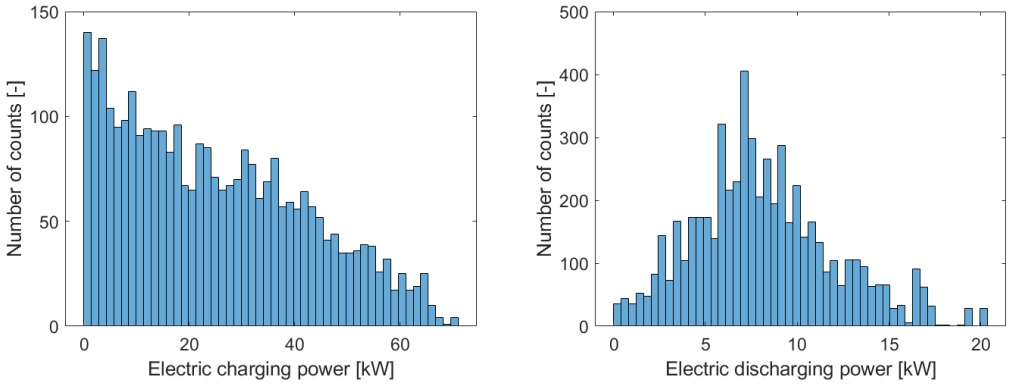

(a) During charge (b) During discharge

Figure 40: Brazilian electric power level.

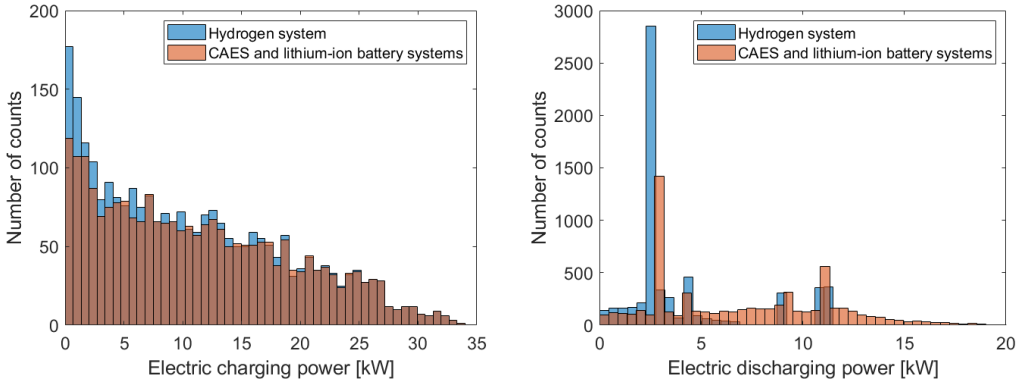

(a) During charge (b) During discharge

Figure 41: French electric power level.

By evaluating Figures 40 and 41, the maximum power outputs from the PV panels are found to be 70 kW for the Brazilian case and 34 kW for the French case. Similarly, the maximum electricity demands are 20 kW for Brazil and 23 kW (CAES/battery) and 12 kW (hydrogen) for France.

The system sizing is a key step on the system modelling as it defines the capital cost of each component following the equations displayed in Table 11, and consequently on the unit cost during operation.

4.3.1. CAES system

The compressors are sized to handle the highest electric power surplus from the photovoltaic panels, while the turbines are designed to meet the peak electric demand. The heat exchangers are sized based on these conditions.

As previously mentioned, the air storage tank is sized to ensure the system can operate for a full week during spring. Figure 42 shows the pressure inside the tank during this week of operation for both cases, resulting from air storage tanks with volumes of 39 m³ for Rio de Janeiro and 25 m³ for Lyon.

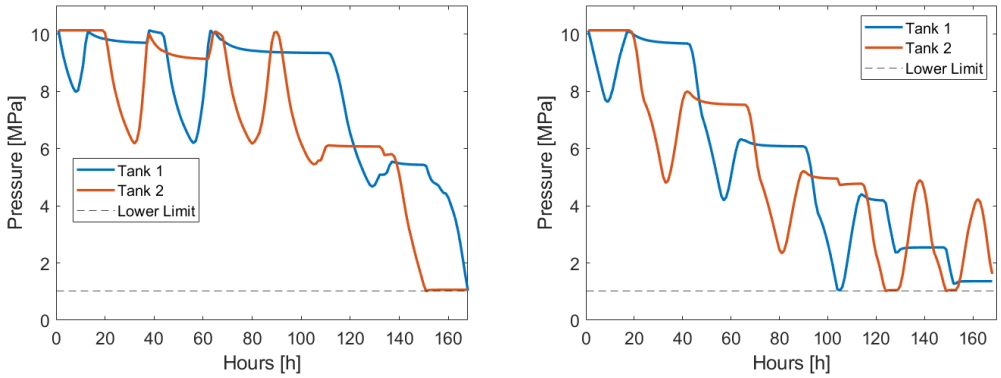

(a) Rio de Janeiro (b) Lyon

Figure 42: Pressure evolution during chosen week – CAES system.

In this study, multi-stage compression and expansion are used, consisting of three compressors and three turbines for charging and discharging modes, respectively. This setup includes three precoolers, three preheaters, and two heat exchangers to supply heating and cooling demands. The results for this approach are presented in Table 15.

Table 15: System sizing and operation parameters – CAES system.

Parameter	Rio de Janeiro	Lyon
Storage tank volume [m³]	39	25
Storage tank surface area [m²]	54.0	41.5
Number of storage tanks [-]	2	2
Maximum storage pressure [bar]	100	
Minimum storage pressure [bar]	10	
Number of compressors [-]	3	
Number of precoolers [-]	3	
Number of turbines [-]	3	
Number of preheaters [-]	3	
Number of heat recovery heat exchangers [-]	1	0
Turbines train maximum power [kW]	20	22
Turbines train minimum power [kW]	3.3	1.5
Compressors train maximum power [kW]	70	34
Compressors train minimum power [kW]	4.5	2.2
Hot thermal energy storage system volume [m³]	7.5	1
Hot thermal energy storage system surface area [m²]	20.8	7.1
Cold thermal energy storage system volume [m³]	7.5	1
Cold thermal energy storage system surface area [m²]	20.8	7.1

After defining the system sizing, to have a better understand of its operation, a simple procedure for filling and emptying the tank is conducted, Figure 43.

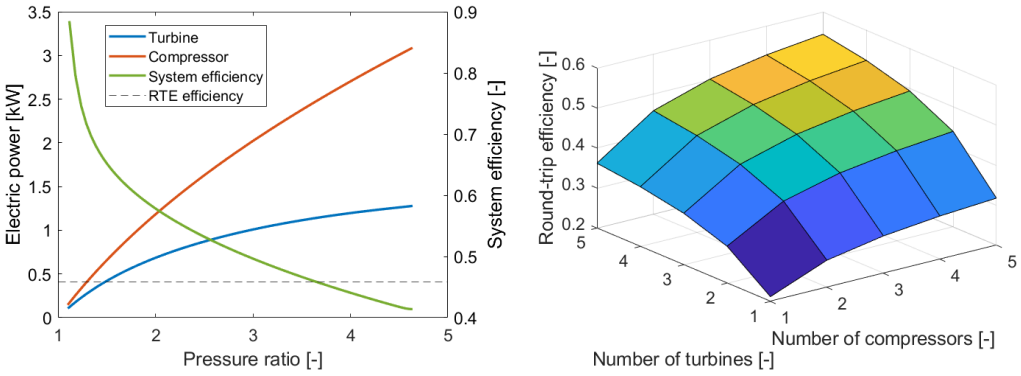

(a) In function of pressure ratio (b) In function of the number of components

Figure 43: CAES system round-trip efficiency.

The results in Figure 43(a) indicate that the electric power required by the compressors to fill the tanks, particularly at higher pressure ratios, exceeds the power provided by the turbines during air expansion. This suggests that operating at a lower pressure would be more advantageous for the system. This is reflected in the round-trip efficiency (RTE) in green, which represents the ratio of turbine output to compressor input without accounting for heat recovery and is calculated to be 46.0%. The impact of the number of components on round-trip efficiency was analysed in Figure 43(b). The results indicate that operating with more compressors or turbines improves the system's round-trip efficiency. This improvement is due to the lower pressure ratio, which is assumed to be the same

for all components. However, adding more compressors and turbines may also lead to higher associated costs due to the increased number of components.

4.3.2. Hydrogen system

The approach is similar to the one used in the CAES system, but in this case, the goal is to calculate the number of stacks allocated to the PEMECs and SOFCs. As explained in Section 4.2.2, current density is adjusted to meet power requirements, within the voltage bus limits. The electrolyzer stack is sized to handle all the surplus energy from the PV panels, while the SOFC is sized to meet the maximum electric demand.

First, the operating current density and the number of cells per stack must be defined. For both SOFC and PEMEC stacks, a current density range of 2000 to 4000 A/m² is considered. For the fuel cell, the number of cells per stack is set between 50 and 66, while for the electrolyzer, it is set between 22 and 28. The current density range is selected based on the validation results, which are later presented in Section 5.1. This range ensures that both the fuel cell and electrolyzer operate within safe limits, avoiding their maximum current density while maintaining satisfactory efficiency and power output. The number of cells per stack is chosen to optimize the design bus voltage of the stack (48 V), as discussed in Section 4.3.2.

The optimal configuration is determined by considering the highest power output for each. Tables 16 and 17 display the results for the SOFC supplying an electric demand of 20 kW.

Table 16: SOFC sizing - current density analysis.

Current density difference: design - calculated									
j \ CPS	50	52	54	56	58	60	62	64	66
2000	192.72	93.75	3.20	79.96	156.59	196.25	196.25	196.25	196.25
2500	223.31	194.20	73.91	36.22	137.42	230.76	271.84	271.84	271.84
3000	306.88	306.88	268.01	122.63	10.39	132.59	245.27	294.37	294.37
3500	358.02	358.02	358.02	299.35	130.45	23.85	165.45	295.92	343.43
4000	208.75	208.75	208.75	208.75	68.32	110.02	272.94	422.51	556.46

Table 17: SOFC sizing – bus voltage analysis.

Voltage bus									
j \ CPS	50	52	54	56	58	60	62	64	66
2000	43.4	45.5	47.5	49.6	51.7	52.8	52.8	52.8	52.8
2500	43.2	43.7	45.7	47.8	49.8	51.8	52.8	52.8	52.8
3000	43.2	43.2	43.7	45.7	47.8	49.8	51.9	52.8	52.8
3500	43.2	43.2	43.2	43.9	45.9	47.9	50.0	52.0	52.8
4000	43.2	43.2	43.2	43.2	44.7	46.7	48.8	50.8	52.8

The evaluation of the best fit involves analysing the results from both tables simultaneously. A colour scheme is used, where darker green represents values closest to the design target, while red indicates the least favourable results. Based on the data from Tables 16 and 17, the optimal configuration is a current density of 3000 A/m² with 58 cells per stack. It is worth noting that other combinations could have been selected; however, this might result in a greater number of stacks (for lower current densities) or increased hydrogen consumption (for higher cell counts per stack and higher current densities).

A similar analysis is conducted for the electrolyzers at an electric power level of 35 kW. The results are shown in Tables 18 and 19.

Table 18: PEMEC sizing - current density analysis.

Current density difference: design - calculated							
j \ CPS	22	23	24	25	26	27	28
2000	132.07	115.90	31.50	46.31	118.26	185.00	247.08
2500	200.62	152.49	46.76	50.71	140.86	224.47	290.40
3000	116.10	41.12	80.04	191.73	295.03	390.86	450.47
3500	182.66	66.98	75.01	205.91	327.00	439.32	486.91
4000	50.93	93.46	248.88	392.18	524.73	647.70	685.61

Table 19: PEMEC sizing – bus voltage analysis.

Bus voltage							
j \ CPS	22	23	24	25	26	27	28
2000	43.2	43.5	45.3	47.1	48.9	50.7	52.5
2500	43.2	44.0	45.8	47.6	49.5	51.3	52.8
3000	43.2	44.3	46.1	47.9	49.8	51.6	52.8
3500	43.2	44.6	46.4	48.3	50.1	52.0	52.8
4000	43.2	44.8	46.7	48.5	50.4	52.2	52.8

A similar evaluation is conducted for the PEMEC, selecting a current density of 3000 A/m² with 25 cells per stack. This number of cells is chosen as it best approximates the bus voltage presented in Table 19. The current density is set to match that of the SOFC, although a higher value could lead to an increased hydrogen production rate.

To assess the robustness of this choice, the current density is evaluated at different power levels. Based on the design current density and the number of cells per stack for both SOFC and PEMEC, the fuel cells demonstrate the ability to adjust the current density within the specified limits across different power levels. The results are presented in Figure 44.

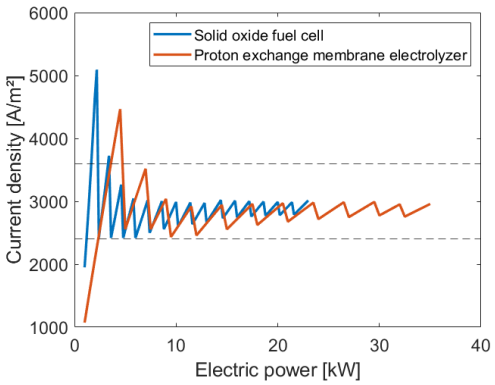

Figure 44: Current density evaluation.

The results shown in Figure 44 indicate that both the electrolyzer and fuel cell stacks can operate within the set current density range (denoted by the dashed lines) for most of the operation. At low electric power levels, both stacks fail to operate because they cannot adjust to the current density limits, however later it will be seen that by setting the operational limits, such conditions will be avoided during the component operation.

Once the operational parameters are defined, the number of stacks required for each system is determined. For the Brazilian configuration, 18 SOFC stacks and 13 PEMEC stacks are needed, while for the French configuration, 20 and 6 stacks are required, respectively.

Similar to the CAES system, the storage tank is sized to sustain operation during the reference week. For this evaluation, it is assumed that all hydrogen supplied to the SOFC comes from the storage tanks, which results in an oversized tank. The results show that the storage tank sizes are 1.0 m³ for Rio de Janeiro and 0.8 m³ for Lyon. Pressure evolution inside the tanks is displayed in Figure 45.

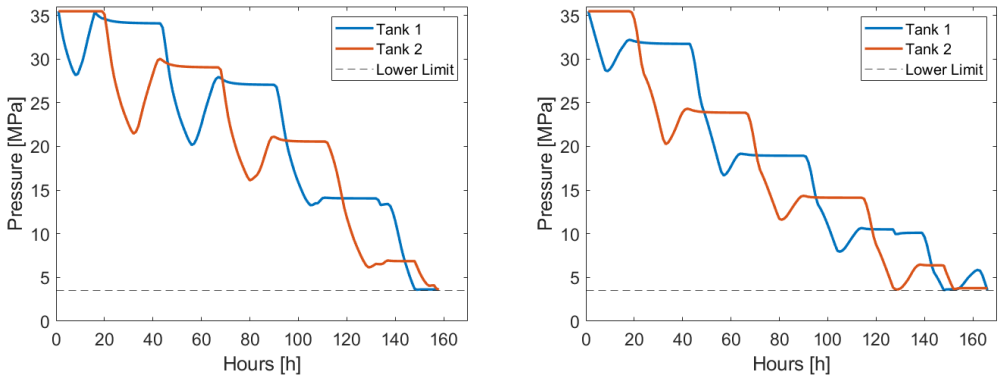

(a) Rio de Janeiro (b) Lyon

Figure 45: Pressure evolution during chosen week – hydrogen system.

Table 20 presents the value for all parameters considered for the hydrogen system.

Table 20: System sizing and operation parameters – hydrogen system.

Parameter	Rio de Janeiro	Lyon
Storage tank volume [m³]	1.0	0.8
Storage tank surface area [m²]	7.1	6.3
Number of storage tanks [-]	2	
Maximum storage pressure [bar]	350	
Minimum storage pressure [bar]	35	
SOFC inlet temperature [°C]	800	
SOFC outlet temperature [°C]	900	
SOFC operational pressure [bar]	1.5	
PEMEC inlet temperature [°C]	80	
PEMEC outlet temperature [°C]	180	
Energy share [%]	27	23
SOFC - Total number of stacks	18	20
PEMEC - Total number of stacks	13	6
SOFC - design density current [A/m²]	3000	
PEMEC - design current density [A/m²]	3000	
SOFC - Cell per stacks	58	
PEMEC - Cell per stacks	25	
Number of compressors - charging	3	
Number of heat exchangers - charging	4	
Hot thermal energy storage volume [m³]	1	
Hot thermal energy storage surface area [m²]	7.1	
Cold thermal energy storage volume [m³]	0.125	
Cold thermal energy storage surface area [m²]	2.62	

4.3.3. Lithium-ion battery system

The procedure to size the lithium-ion system is analogous to the previous ones. The Brazilian system has a rated capacity of 530 kWh, while the French system of 400 kWh. Table 21 display the parameters considered, and Figure 46 displays its SOC.

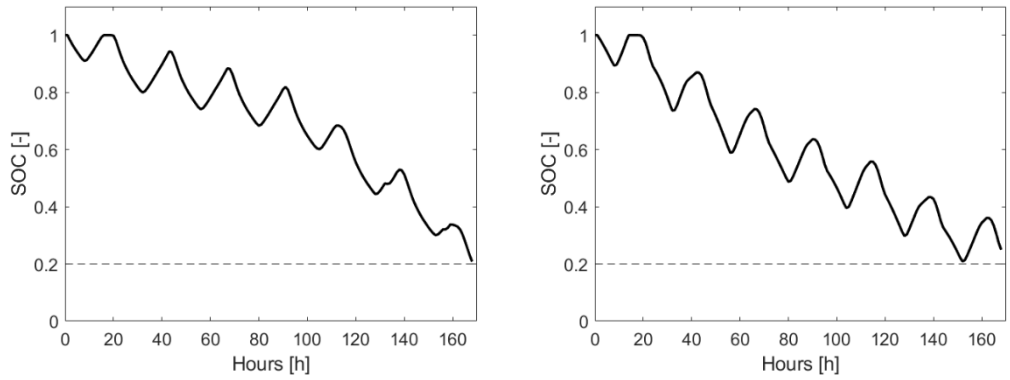

(a) Rio de Janeiro (b) Lyon

Figure 46: SOC evolution during chosen week – hydrogen system.

Table 21: System sizing and operation parameters – lithium-ion battery system.

Variable	Rio de Janeiro	Lyon
Rated capacity [kWh]	530	400
Minimum SOC [-]	0.2	
Maximum SOC [-]	1	
Battery self-discharging coefficient [%/month]	5	
Charging efficiency [-]	0.95	
Discharging efficiency [-]	0.95	
Battery converter efficiency [-]	0.95	

4.4. Operation limits

Lower operational limits were established for all systems based on a preliminary data analysis. The initial assessment revealed conditions – operating at low power rates - that were not favourable, leading to high unit costs. To address this, a procedure was developed to pre-assess the available data alongside the established system, identifying a minimum operational limit to avoid high unit costs for the prime movers. The steps of this procedure are illustrated in Figure 47.

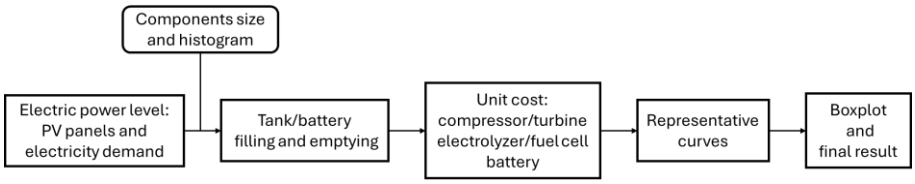

Figure 47: Operation limits defining procedure.

The procedure involves analysing the filling and emptying processes of the storage media. This is done by considering different power rates for both operations and evaluating the unit cost during charging and discharging. It was observed that higher power rates lead to a reduction in unit cost (in exergy basis) for both processes, as illustrated in Figure 48 for CAES system charging.

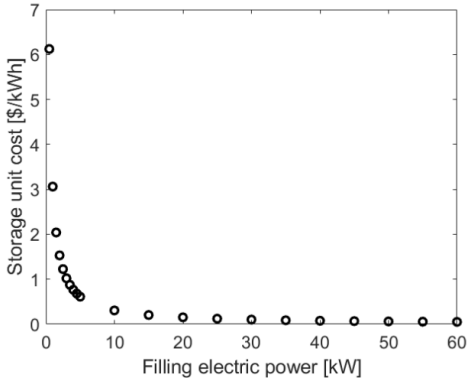

Figure 48: CAES system storing unit cost in function of electric power - Rio de Janeiro.

To evaluate the system at their respective cases, the bins from the histograms (Figures 40 and 41) are used as weight to create its representative curve (in blue), shown in Figure 49.

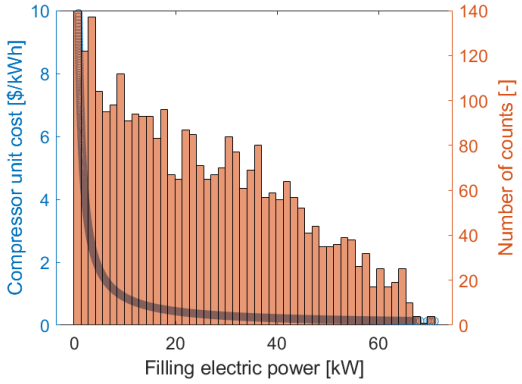

Figure 49: CAES system storing unit cost and histogram – Rio de Janeiro.

Finally, a boxplot allows the identification of the outliers that are considered as unfavourable conditions to operate (high unit cost). Then, this process defines the lower limit of operation, Figure 50.

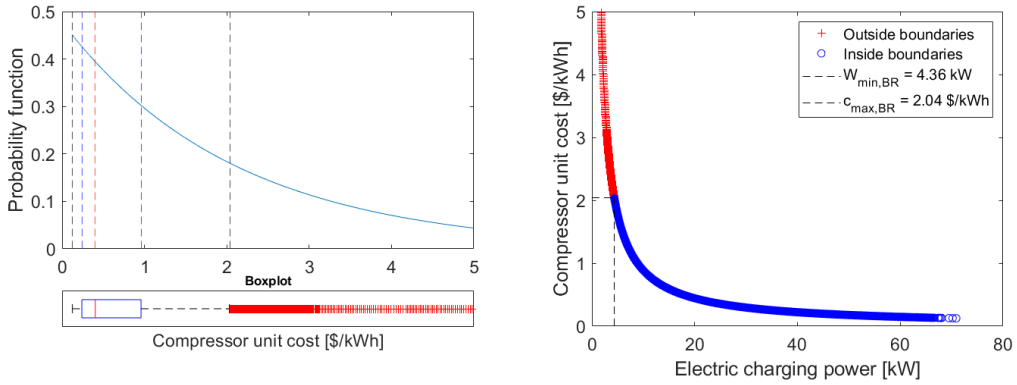

(a) Probability function and boxplot (b) Final result

Figure 50: CAES system storing unit cost.

This procedure is repeated for all three systems in both Brazil and France, and the final results is displayed on the next sections. The remaining boxplot can be found in the Appendix C.

4.4.1. CAES system

Figure 51 shows the results for the CAES system.

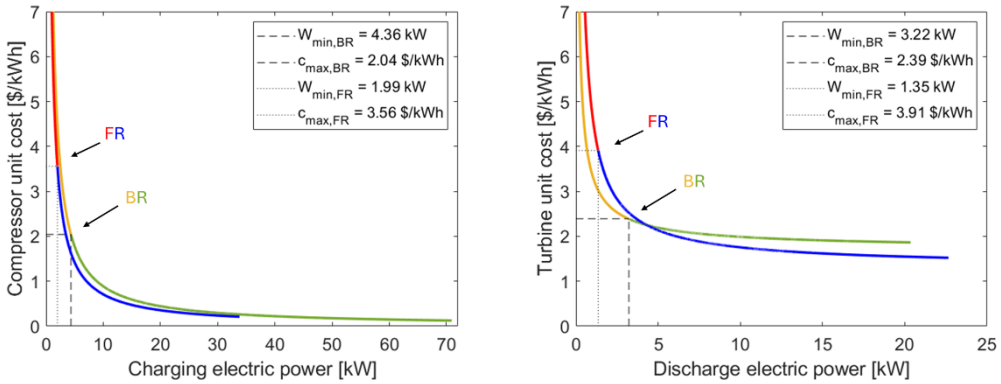

(a) Compressor (b) Turbine

Figure 51: Lower limit final result – CAES system.

This approach suggests an operational lower limit for the compressors of 4.36 kW and 1.98 kW for the Brazilian and French contexts, respectively. For the turbines, the lower limits are 3.22 kW and 1.35 kW.

4.4.2. Hydrogen system

For the hydrogen system, an additional step is necessary to size the electrolyzers due to their high capital cost. Using the equations outlined in Section 3.4, the unit cost of the electrolyzers at various power levels is calculated.

To prevent excessive capital investment, as described by Eq. (169), and subsequently reduce operating costs, a maximum operational limit is established. This limit is determined by calculating the weekly seasonal average PV panels power output, from the results show in Figure 52.

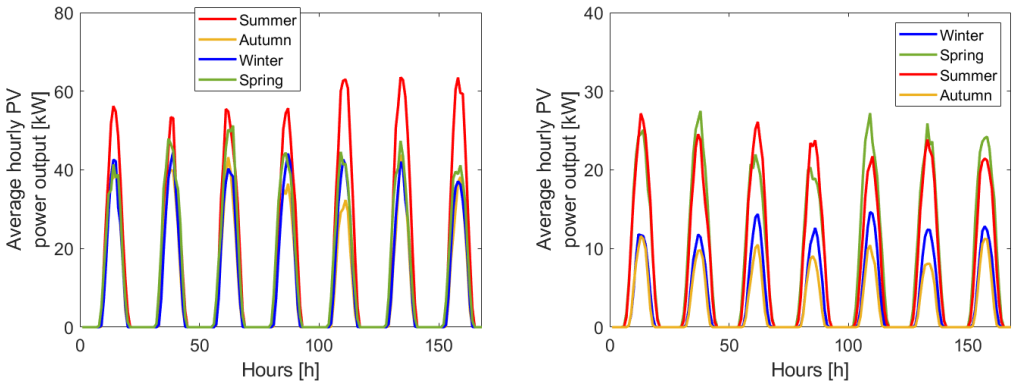

(a) Rio de Janeiro (b) Lyon

Figure 52: Seasonal hourly average photovoltaic power output.

For each season, considering the hours where the PV panels are capable of producing power, an average value is calculated to be set as the upper limit of operation. From the four possible outcomes, summer was selected to set the limit. For the Brazilian case, the maximum limit is set at 35 kW, while for the French case is set at 15 kW.

Once the upper limits are defined, the lower limits can be calculated in a similar manner to the procedure used for the CAES system. Figure 53 display the results.

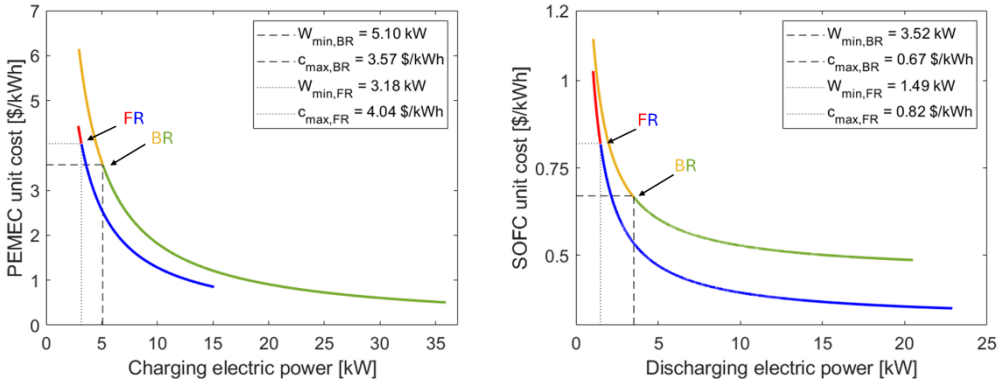

(a) PEMEC (b) SOFC

Figure 53: Lower limit final result – hydrogen system.

This approach suggests an operational lower limit for the PEMEC of 5.10 kW and 3.18 kW for the Brazilian and French contexts, respectively. For the SOFC, the lower limits are 3.52 kW and 1.49 kW.

4.4.3.
Lithium-ion battery system

Finally, the limitations are set to the lithium-ion battery similarly to the other systems. The results are shown in Figure 54 .

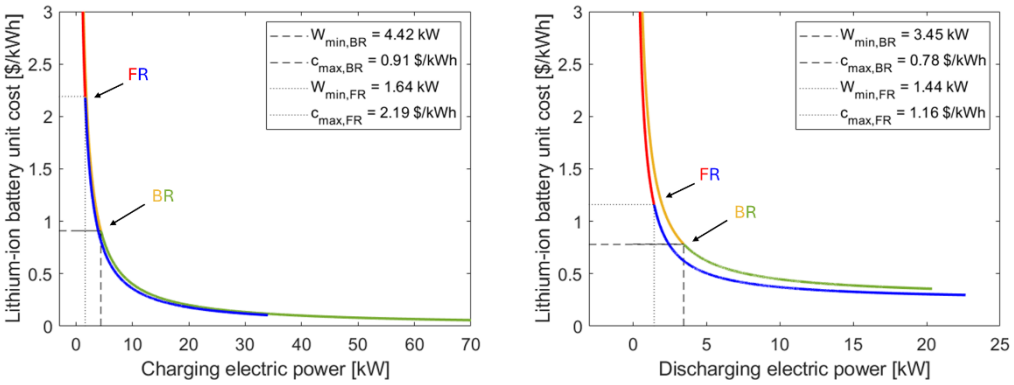

(a) Charging (b) Discharging

Figure 54: Lower limit final result – lithium-ion battery system.

This approach suggests an operational lower limit for the lithium-ion battery of 4.42 kW and 1.64 kW for the Brazilian and French contexts during charge, respectively. During discharge the lower limits are 3.45 kW and 1.44 kW.

4.5.
Electricity, heating and cooling

All three demands are met simultaneously, with each having the potential to influence the value of the others, as explained in greater detail later. All equations described in Section 3 are utilized for solving the numerical model, considering initially an hourly time step.

The logic behind supplying electricity is similar among all systems and shown in Figure 55.

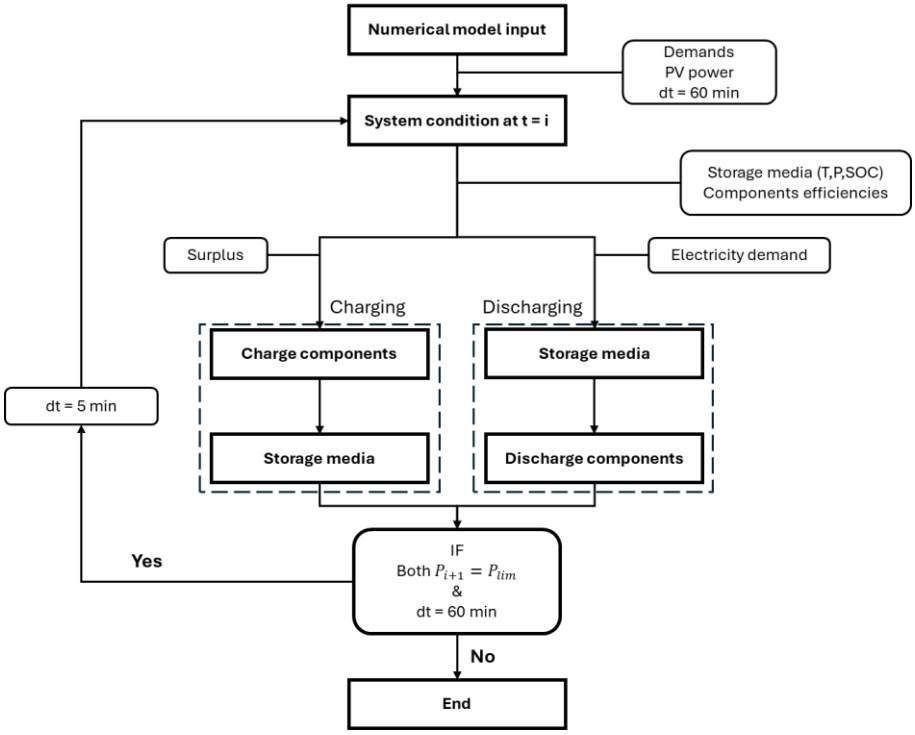

Figure 55: All system electricity supply.

Firstly, the electric demand is supplied with the power from the PV panels, and the surplus is utilized to run the charging components, considering the storage media condition and the components efficiency. After the filling process, it is verified the limit condition is achieved. If so, the procedure is ran again considering a smaller time step to have more accurate results. The procedure for discharging procedure verifies the electric demand to be supplied, verifies the condition of the storage media and the efficiencies of the dedicated components. If during procedure, the lower limit from the storage media is verified, the model runs once again at a smaller time step for more accurate results.

Both systems can meet both heating and cooling demands by using a combination of heat exchangers and thermal storage tanks, as described in Section 3.2.4.

In the Brazilian case, the CAES system provides cooling by utilizing the chilled, pressurized air from the air expander. During this process, water from the hot TES is used to preheat the air before expansion, resulting in chilled water exiting the heat exchanger. The chilled air stream is then passed through a heat exchanger to provide cooling. If the cooling demand exceeds this capacity, a vapor compression refrigeration cycle is activated, increasing electricity consumption and requiring additional air withdrawal from the tank, while the heat exchanger continues to contribute to cooling. For the hydrogen system, cooling is primarily

supplied by the absorption chiller, which utilizes the heated exhaust gas exiting the air heat exchanger. If further cooling is required, the process mirrors that of the CAES system, with an increased electricity demand to activate the vapor compression system. In both systems, increasing the electricity also increases the cooling capacity of both systems, resulting in an iterative method to match the cooling demand. In both systems, the auxiliary system considers a COP corresponding to 20% of the Carnot COP, as described in Section 4.1. Figure 56 illustrates this procedure.

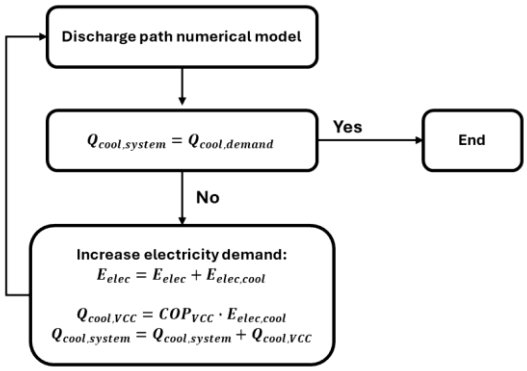

Figure 56: CAES/Hydrogen systems cooling supply in Brazilian scenario.

Where $E_{elet,cool}$ is the electric energy necessary to supply the missing cooling demand in kJ, and $Q_{heat,HP}$ is the cooling supplied by the vapour compression cycle auxiliary system in kJ.

During the charging phase, the cooling is supplied by the auxiliary system utilizing the power from the PV panels.

The approach to heating supply in Brazil is more straightforward. Heat is mainly supplied by a combination of the hot TES and a heat exchanger by both systems, and when it is not enough an auxiliary system using natural gas burner is utilized.

In the French case, the method of heat supply differs across systems. For the CAES and lithium-ion battery systems, heat is provided by heat pumps. The hydrogen system can supply heat during its operation; however, if it cannot meet the full heating demand, an auxiliary system with heat pumps is activated. In such cases, the system's power output is increased to meet both the electrical demand and the energy required to operate the heat pumps. Similarly to the cooling case, an iterative method is applied to match the exact heating demand. The heat pumps are assumed to have a COP corresponding to 40% of the Carnot COP, as described in Section 4.1. The procedure is illustrated in Figure 57.

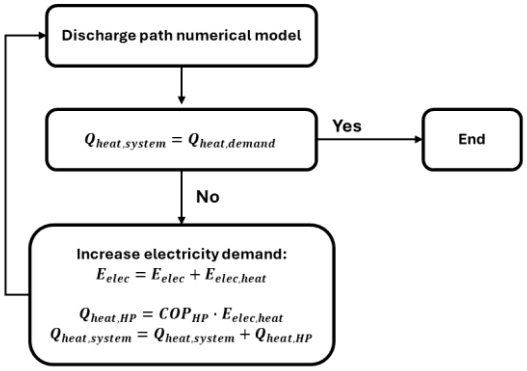

Figure 57: Hydrogen system heating supply in French scenario.

Where $E_{elet,heat}$ is the electric energy necessary to supply the missing heating demand in kJ, and $Q_{heat,HP}$ is the heat supplied by the heat pumps in kJ.

It is worth mentioning that for the French case, the order of the cooling and heating modules are inverted from the one shown in Figure 16, so it prioritizes supplying the heat demand rather than the cooling one, as in Rio de Janeiro.

During the charging phase, the heating is supplied by the auxiliary system utilizing the power from the PV panels.

4.6. Design of Experiments

Design of Experiments (DoE) is a widely used method for examining the effects of multiple variables on a response while accounting for potential interactions between factors within the mathematical model. This approach is more powerful than a simple univariate analysis, which evaluates one variable at a time in isolation. The DoE model depends on the number of variables selected for evaluation, as this determines the levels incorporated into the analysis. In DoE terminology, a run refers to a specific combination of factor levels whose impact on the output is being assessed (128).

In this study, among the various polynomial models available in the literature, the Central Composite Design (CCD) is selected to analyse the data. For both the CAES and hydrogen systems, three variables are chosen to assess system performance, resulting in a three-level model. Figure 58 illustrates the cube representing the distribution of points.

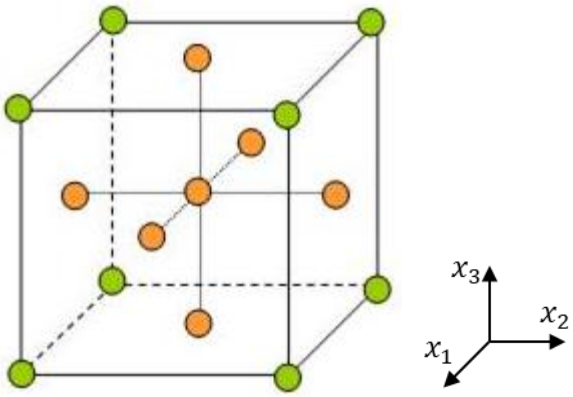

Figure 58: Central Composite Design representation.

The three-level CCD model requires a total of 17 evaluation points: 8 corresponding to the vertices of the cube, 6 located along the domain's axes at a fixed distance (α = 1) from the centre, and 3 at the centre. In this study, since it involves numerical simulations, 2 of the 3 centre points are assigned small deviations, randomly selected within 1% of the centre value.

The DoE response is represented by a second-order polynomial fitter model, Eq.(207) :

$$y = a_o + \sum a_i \cdot x_i + \sum a_{ii} \cdot x_i^2 + \sum a_{ij} \cdot x_i \cdot x_j \tag{207}$$

Where y is the predicted response, a_o is the intercept coefficient, a_i are the linear coefficients, a_{ii} are the quadratic coefficients, and a_{ij} are the interaction coefficients, and x_i and $x_j$are the dimensionless variables of interest.

When building the surface response from Eqs. (208-209), the factor x_i are written as reduced variables, by utilizing the following relations:

$$x = \frac{X_i - X_i^0}{\Delta X_i} \tag{208}$$

$$\Delta X_i = \frac{X_i^{max} - X_i^{min}}{2} \tag{209}$$

Where X_i is the real variable, the superscripts *0* to the central point of the experimental region, and *max* and *min* to the maximum and minimum values of the real variable X_i.

The model's performance is evaluated using a Pareto Chart and the response surface of Observed vs. Predicted Values. This process begins with a

Student's t-test to determine whether the differences between the responses of two groups are statistically significant. The Pareto Chart ranks and identifies the most significant factors in the dataset, enabling prioritization for further analysis. Additionally, it helps determine which factors are relevant or insignificant for each response. Finally, the response surfaces are created to represent the parameters of interest in function of the chosen variables. These analyses are performed with the software Statistica.

Table 22 display each case involved in the CCD, and Table 23 the levels considered.

Table 22: CCD cases.

Case	Variable 1	Variable 2	Variable 3
1	0	0	0
2	0	1	0
3	0	0	1
4	0	-1	0
5	0	0	-1
6	1	0	0
7	1	-1	1
8	1	-1	-1
9	1	1	-1
10	1	1	1
11	-1	0	0
12	-1	-1	1
13	-1	-1	-1
14	-1	1	-1
15	-1	1	1
16	0	0	0
17	0	0	0

Table 23: Both system's levels.

System	#	Variable	Levels		
			-1	0	1
CAES	1	Tank's volume [m³]	19.5	39	58.5
	2	PV area [m²]	343.2	429	514.8
	3	Householders [-]	38	48	58
Hydrogen	1	Hydrogen share [%]	21.6	27	32.4
	2	Current density [A/m²]	2400	3000	3600
	3	Maximum storage pressure [MPa]	28	35	42

In the CAES system, the selected variables include storage tank volume, PV area, and the number of households. These choices enabled an assessment of the interaction between PV power output and electricity demand (Figure 25) and the impact of storage tank sizing. For the hydrogen system, considering the hydrogen share and the current densities of both PEMEC and SOFC allowed for an evaluation of their influence on system performance. Additionally, the storage

tank pressure was analysed to assess the impact of this parameter on the overall system.

4.7. Chapter conclusion

This chapter introduces the two cities considered for the case studies – Rio de Janeiro and Lyon. The varying climate conditions and building demands (electricity, heating, and cooling) provide an opportunity to explore different parameters from the 4E (energy, exergy, exergoeconomy, and environmental) analysis for the three ESSs – CAES, hydrogen, and lithium-ion batteries, which will be discussed in Chapter 5.

This chapter outlines the tools and methodology for evaluating the systems, using the equations presented in Chapter 3. It introduces the concepts of controlling and operating storage tanks, electrolyzers, and fuel cells to ensure optimal performance. The procedure for determining the system sizing, based on climate and demand data, is provided for each system. The approach for defining operational limits to achieve more efficient performance, based on exergoeconomy optimization, is also discussed. Finally, with the help of the defined DoE, the impact of variables on system performance can be investigated, allowing for the identification of potential optimizations, rather than relying on traditional sensitivity analysis.

5
Results and discussion

This chapter covers the validation of the model for the photovoltaic panels, PEMEC, storage tank, and SOFC, since all other components will use a fixed efficiency for evaluation. The previously outlined methodology is applied to both Rio de Janeiro and Lyon, and the results of the 4E analysis for all systems are discussed and compared. Lastly, the DoE is conducted to assess the impact of various variables on the key parameters.

5.1.
Model validation

5.1.1.
Photovoltaic system

Figure 59 shows the IV curves of the photovoltaic panels, along with their power curve at maximum solar radiation. The values used for the parameters are listed in Table 24.

Table 24: Validation data for the photovoltaic panels (82,129).

Parameter	Value
Reference solar radiation [W/m²]	1000
Manufacturer light current [A]	5.75
Short circuit temperature coefficient	0.0035
Open circuit voltage	47.7
Resistance [Ω]	0.0277

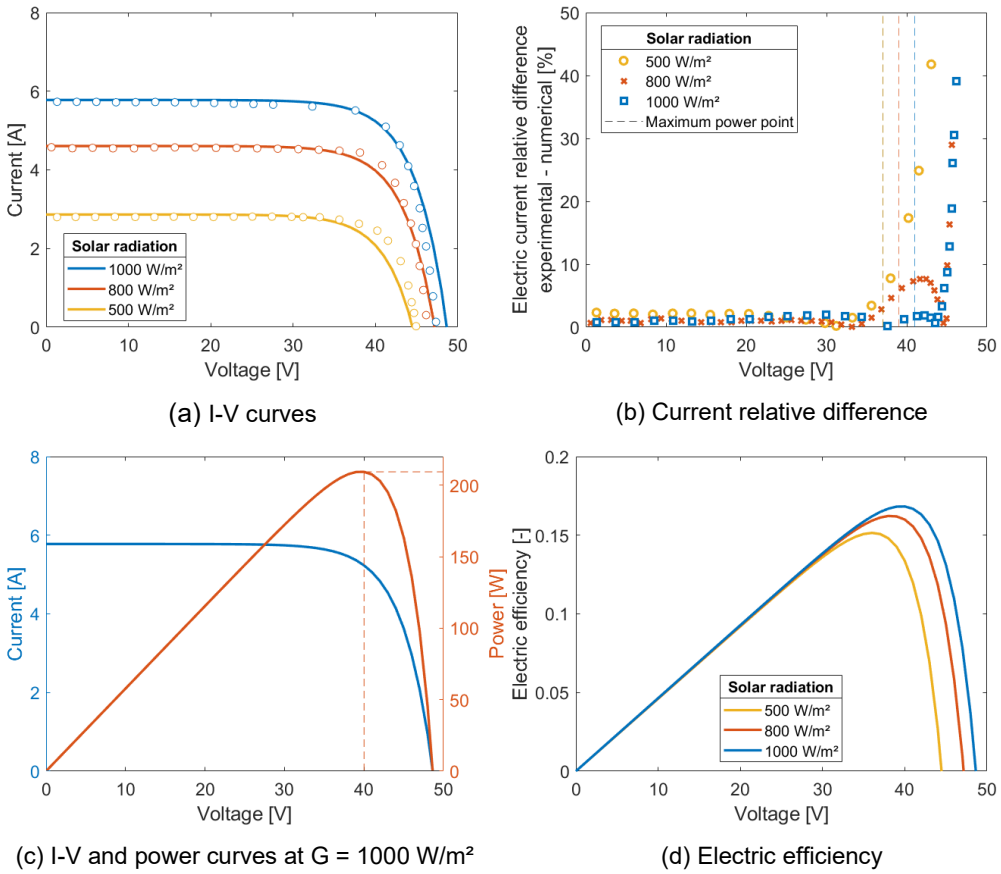

(a) I-V curves

(b) Current relative difference

(c) I-V and power curves at G = 1000 W/m²

(d) Electric efficiency

Figure 59: Photovoltaic panels validation as a function of voltage.

As shown in Figure 59(a), the model accurately replicates the manufacturer data (129), represented by the scatter plot, with improved performance at higher solar radiation levels. Even though at higher voltages the model has trouble to retrieve experimental data, especially at lower solar radiation, the model is set to work at the point of highest power. Figure 59(b) shows the relative difference in electric current between the numerical and experimental (manufacturer) data at different voltages, highlighting the model's difficulty at high voltage, as the difference increases significantly. Figure 59(b) also illustrates the point of maximum power output, matched at the operating voltage, at different solar radiation levels. It reveals that under desired operating conditions, the relative differences are 7.77%, 6.18%, and 1.73% for solar radiations of 500, 800, and 1000 W/m², respectively. Figure 59(c) illustrates the relationship between the I-V and power curves. As voltage increases, the power from the PV panel also rises. However, at a certain point, the current begins to decrease, and the power reaches its peak before dropping to zero. As it can be seen in Figure 59(d), the electric efficiency follows the same behaviour of the power curves, benefiting from higher solar radiations.

5.1.2.
Proton exchange membrane electrolyzer

The PEMEC validation is carried out using two different sets of experimental data from Ioroi et al. (130) and Ni et al. (99). The parameters used by both studies are shown in Table 25. The key difference between the two lies in the treatment of the pre-exponential factor, J_i^{ref}. Ioroi et al. calculates it using Eqs. (64-65), whereas Ni et al. considers constants values (10^{-5} A/m² for the anode, 10 A/m² for the cathode). Results are displayed in Figure 60.

Table 25: Validation data for the PEMEC **(130,99)**.

Parameter	Value
Area [m²]	0.02
Temperature [°C]	80
E_a [kJ/mol]	76
E_c [kJ/mol]	18
λ_a [-]	14
λ_c [-]	10
Electrolyte thickness [µm]	100
P_{O_2}, P_{H_2} [atm]	1

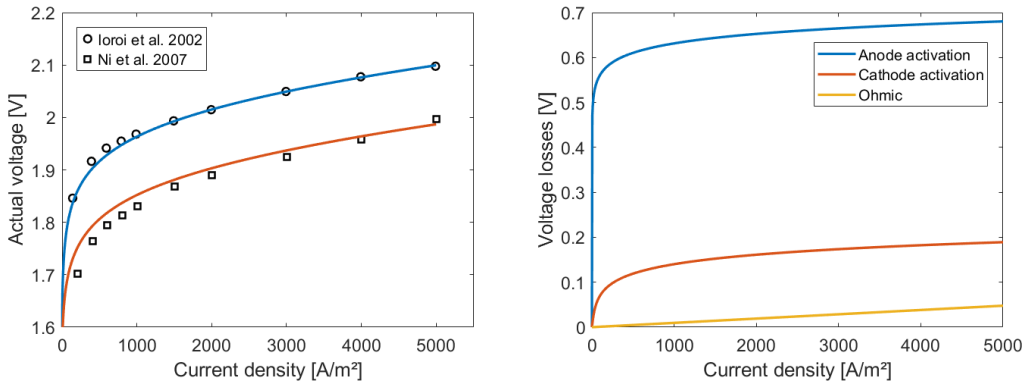

(a) Actual voltage

(b) Voltage losses

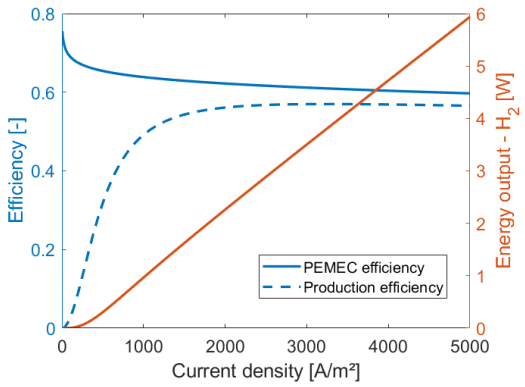

(c) Efficiencies and energy output

Figure 60: Proton exchange membrane electrolyzer validation as function of current density.

It can be observed in Figure 60(a) that both datasets show good agreement between the experimental data and the results obtained from the numerical model.

The maximum relative difference using the model by Ni et al. (99) is 9.3%, while the model by Ioroi et al. (130) shows a much lower difference of 0.81%. To help understands the nature of PEMEC functioning, the results highlight greater activation losses, particularly from the anode, while ohmic losses exhibit a linear trend with increasing current density, Figure 60(b). Figure 60(c) presents two types of efficiencies. The first, related to the PEMEC, shows that component performance decreases with increasing current density due to higher voltage losses. In contrast, production efficiency, which combines PEMEC and Faraday efficiencies (Figure 20), benefits from higher current densities. The increasing current density is responsible for a higher rate of hydrogen production, consequently increasing the Faraday efficiency. So, the hydrogen production efficiency also increases until reaching a plateau defined by the PEMEC operation condition.

5.1.3. Storage tank

The storage tank was validated using data from the Huntorf plant (131), despite the significant difference in storage sizes. The parameters used for the validation are provided in Table 26.

Table 26: Validation data for the air storage tank (132,133).

Parameter	Value
Cavern volume [m³]	141,000
Cavern surface area [m²]	25,000
Heat transfer coefficient [W/(m².K)]	30
Initial air and rock temperature [°C]	40
Initial air pressure in cavern [MPa]	5.9

Figure 61 illustrates the results for the temporal evolution of pressure and temperature, comparing them with those reported in the reference (134,132,133) as the scattered data.

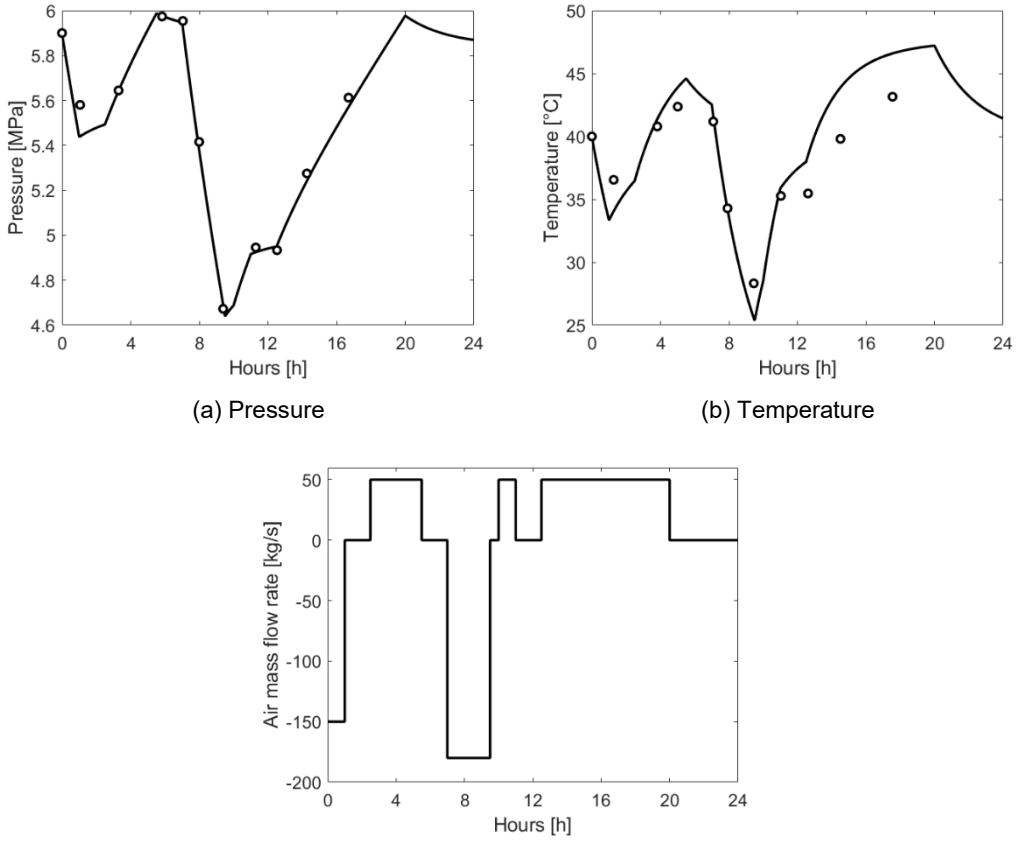

(a) Pressure

(b) Temperature

(c) Air mass flow rate

Figure 61: Air storage tank validation as function of time.

The numerical model demonstrates strong reliability in predicting the pressure and temperature of the air inside the storage tank at all times, as shown in Figures 61(a) and (b). For temperature, a larger deviation from the experimental results is observed at higher inlet flow rates, with a maximum relative difference of 10.4%. In contrast, the model predicts pressure with greater accuracy, with maximum deviation of 2.3%. Figure 61(c) corresponds to the air mass flow rate, found in the reference, used for the validation of both temperature and pressure.

5.1.4. Solid oxide fuel cell

The validation of the SOFC is performed using data provided by Tao and Virkar (135), serves as a benchmark for validation in numerous studies (36,57,93,136). The values of the parameters considered are presented in Table 27.

Table 27: Validation data for the SOFC (36,57,93,136).

Parameter	Value
Temperature [°C]	800
Active area [m²]	0.01
Anode thickness [µm]	500
Cathode thickness [µm]	50
Electrolyte thickness [µm]	10
Interconnect thickness [µm]	3000
D_a [m²/s]	0.2×10^{-4}
D_c [m²/s]	0.05×10^{-4}
$j_{0,a}$ [A/m²]	6500
$j_{0,c}$ [A/m²]	2500
E_a [J/mol]	1.1×10^5
E_c [J/mol]	1.55×10^5
λi [-]	7×10^9

Two approaches are considered for evaluating the activation losses in the SOFC. The first approach assumes that the properties of the effective current density remain constant, as described by Eq. (66), while the second approach accounts for their dependence on temperature and pressure, as shown in Eqs. (64-65). Both approaches utilize the same correlations for ohmic and concentration losses. Figure 62 presents the results, including comparisons with other authors, performance, and the contribution of each type of loss.

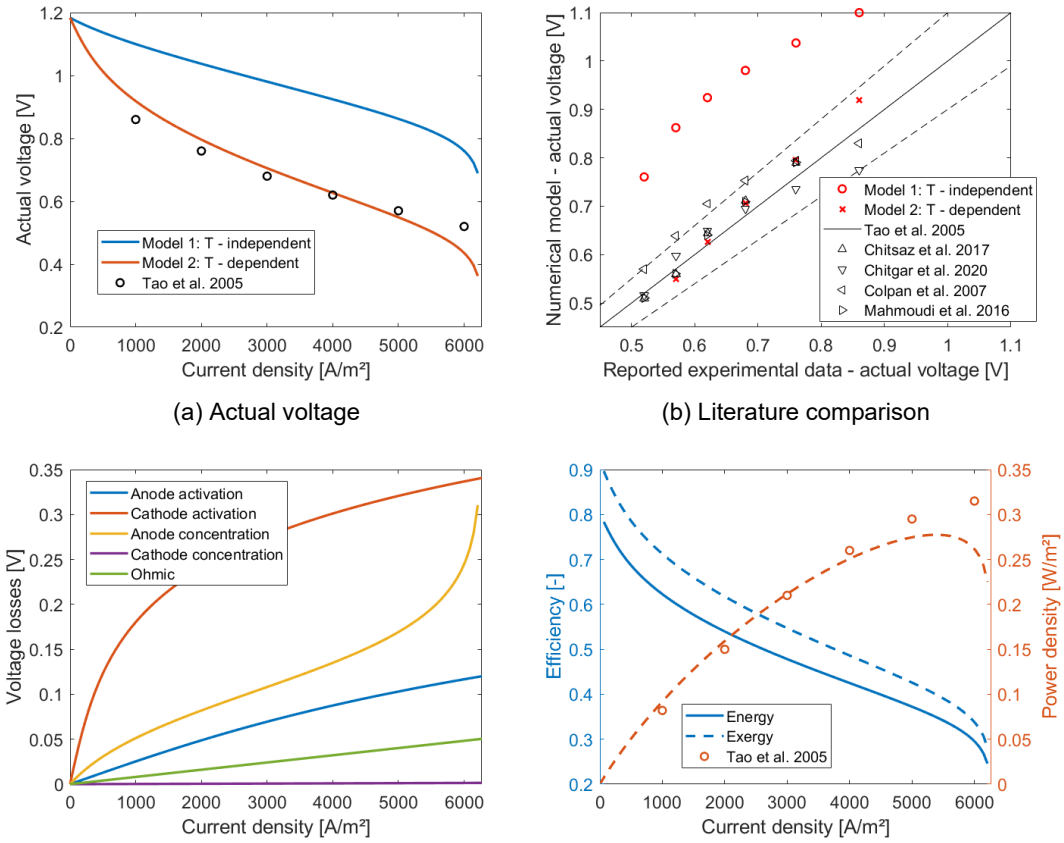

(a) Actual voltage

(b) Literature comparison

(c) Voltage losses

(d) Efficiencies and power density

Figure 62: Solid oxide fuel cell validation as function of current density.

Figure 62(a) presents the validation results for the SOFC using both approaches. The second model demonstrates better accuracy, showing a significant effect of activation losses at lower current densities, making it more suitable for the numerical model. Figure 62(b) compares the results with those available in the literature, showing good agreement of the T-dependent model with a relative difference below 10%, as indicated by the dashed lines. Figures 62(c) and (d) highlight the key characteristics of the SOFC. At low current densities, cathode activation losses dominate, while at higher current densities, anode concentration losses become more significant. Ohmic losses, meanwhile, increase linearly with current density. The power output increases with current density, reaching a maximum value as it approaches its operational limits. Conversely, the efficiencies decrease with the current density increase, resulting in voltage losses, as shown in Figure 62(d).

5.2.
Comparison of the hybrid system in Brazil and France

Considering the interactions displayed in Figures 26 and 28, all three systems are evaluated and compared. The parameters are seasonally evaluated by calculating their hourly average throughout the day. As so, it is possible to evaluate the seasonal variance as well as the impact of charging and discharging.

5.2.1.
Brazil

5.2.1.1.
General

Figure 63 display the evolution of the storage media for all three systems.

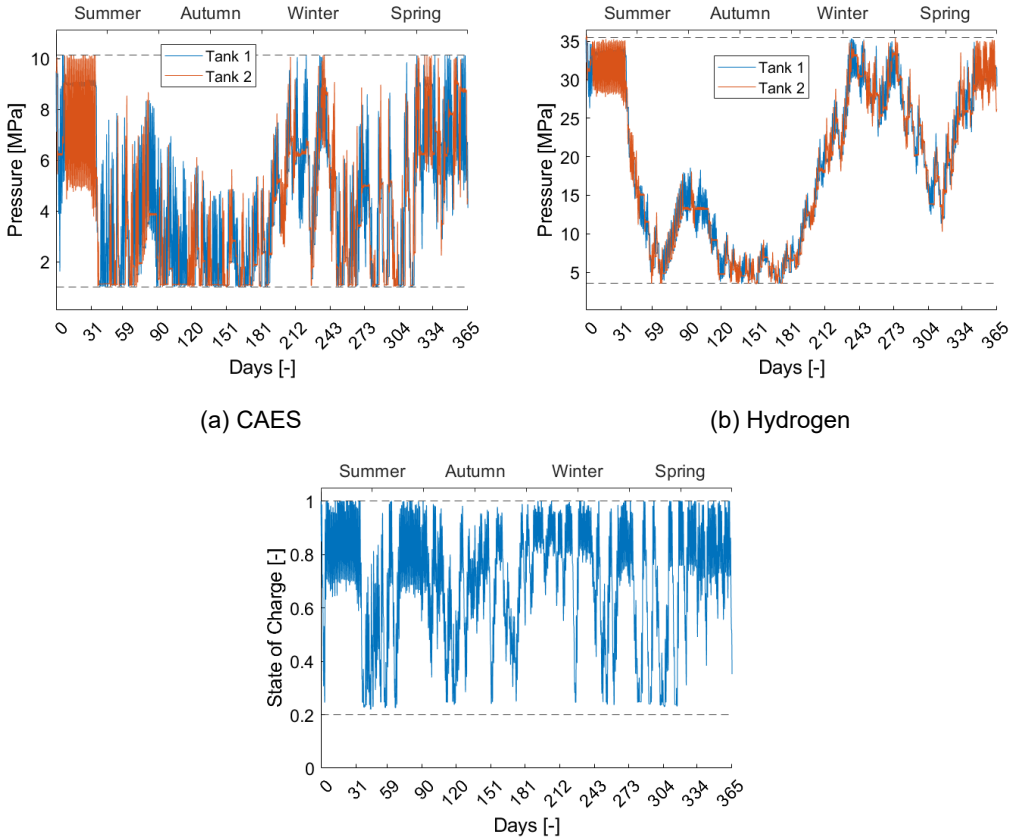

(a) CAES

(b) Hydrogen

(c) Lithium-ion battery

Figure 63: Storage media behaviour as a function of time – Rio de Janeiro.

All three systems exhibit similar behaviour in terms of their storage media, indicating that seasonality is influenced more by demand patterns and climate conditions than by the systems themselves. Focusing on the CAES and hydrogen

systems, as shown in Figures 63 (a) and (b), the storage media are mostly full during summer when favourable climate conditions facilitate charging while meeting high electricity demands. Towards the end of summer, air and hydrogen levels in the storage tanks decrease due to the increased electricity demands for cooling. In autumn, as electricity demand and solar radiation decline, and heat demand rises, the storage media experience a recharging phase followed by a discharge, stabilizing at lower levels until winter begins. Winter, characterized by the lowest electricity demand, provides favourable conditions for recharging the storage tanks, particularly for the hydrogen system. In spring, both systems manage to meet the higher electricity demands while maintaining higher pressure levels within the tanks. The lithium-ion battery system, Figure 63(c), demonstrates similar characteristics to the other two but, due to its higher efficiency, it charges quickly and remain most of the time with elevated SOC. It also has a higher discharge efficiency, allowing for better utilization of stored energy. When comparing the average pressure and SOC levels throughout the year, the systems show values of 40.2%, 52.1%, and 69.6% of their maximum levels for the CAES, hydrogen, and lithium-ion battery systems, respectively.

Figure 64 shows the TES system temperature.

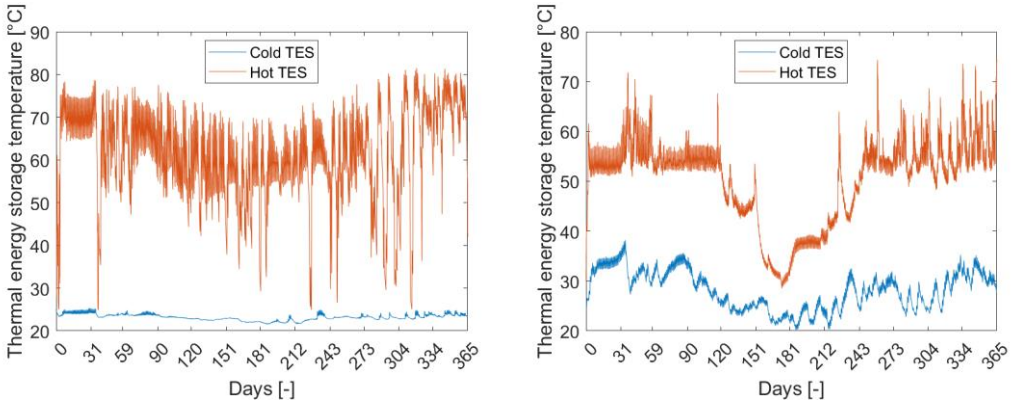

(a) CAES (b) Hydrogen

Figure 64: Thermal energy storage system temperature as a function of time – Rio de Janeiro.

Throughout the year, in both CAES and hydrogen systems, there is not a significant change in temperature for the cold TES as for the hot one. The hot TES maintains high temperatures year-round by utilizing the charging process in the CAES system and discharging in the hydrogen system. During winter, both systems experience lower temperatures due to increased heat demand and reduced solar radiation, leading to greater dependence on the auxiliary system. In the hydrogen system, the hot TES undergoes a temperature variation of 58°C, while the cold TES experiences a variation of 20°C. The CAES system has a

similar temperature range for the hot TES, with a variation of 56°C, while the cold TES fluctuates by about 4°C. Both hot TES systems experience significant variations due to the compression of air or exhaust gases from the SOFC. The cold TES systems behave differently due to varying operation strategies. In the CAES system, the water in the cold TES is frequently replenished with water from the grid (at 25°C) to prevent depletion. In contrast, the hydrogen system has smaller storage tanks that are less affected by charging or discharging cycles, so the temperature variations in this system are mainly a result of ambient temperature changes.

Figure 65 presents the water volume inside both TES in the case of CAES system.

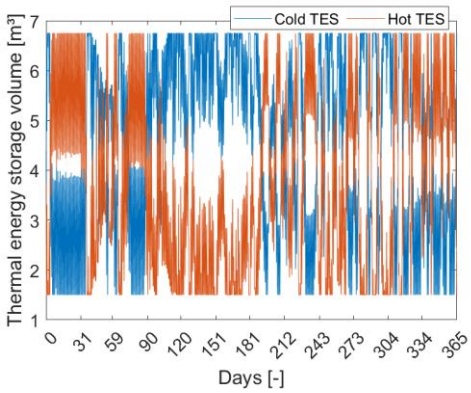

Figure 65: Thermal energy storage volume, for CAES, as a function of time – Rio de Janeiro.

By observing Figure 65, it is possible to observe that both TES operate within the limits set. The volume inside both TES units reflects the charging and discharging patterns shown in Figure 63. As the hot TES charges, hot water levels rise, while cold water enters the cold TES during discharge. The hot TES remains nearly full during summer and spring, whereas the cold TES holds more water during the colder seasons, autumn and winter.

Figure 66 presents the current density during the operation of both PEMEC and SOFC in hydrogen system.

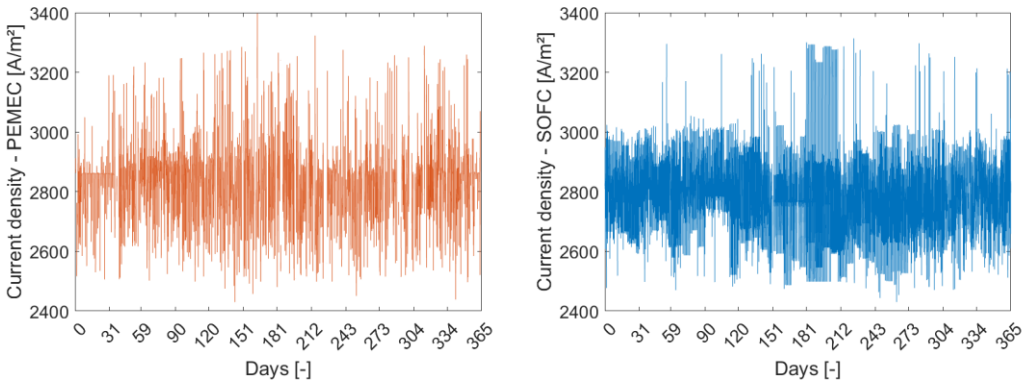

(a) PEMEC (b) SOFC

Figure 66: Operational current density as a function of time – Rio de Janeiro.

Figure 66 is a representation of the system ability to adequate the current density due to the operation. To this configuration, the PEMEC had its operation current mostly adjusted to the value of 2860 A/m², and the SOFC to 2830 A/m², a deviation lower than 10% from its design condition.

5.2.1.2. Energy

Energy is the first parameters from the 4E analysis to be assessed. Figure 67 displays the energy management from the systems.

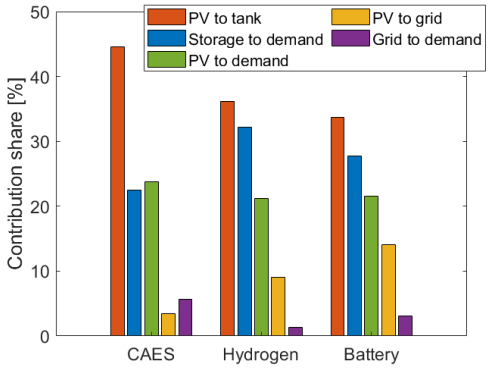

Figure 67: Energy management for all three systems – Rio de Janeiro.

Among the three systems, photovoltaic panels serve as the primary energy source, benefiting from the city's high solar radiation throughout the year. The majority of the generated energy is used to charge the storage systems, as indicated by the orange bar (33.7% to 44.6%), directly meet the electricity demand, shown in green (21.2% to 23.8%), and supply excess energy back to the grid, represented in yellow (3.4% to 14.1%). The ESS acts as the main electricity

provider for the building, as depicted by the blue bar (22.5% to 32.2%), while the grid plays a minimal role, contributing only 1.3% to 5.7% in purple. It is notable that the CAES system is the only one that imports (5.7%) more energy from the grid than it exports (3.4%). The hydrogen system has been downsized to reduce operational costs, while the lithium-ion battery is more efficient in converting power from the PV panels. These two factors contribute to the hydrogen and lithium-ion battery systems having a lower dependency on the electric grid, 1.3% and 3.1% respectively, compared to the CAES system, as well as able to export more energy – 9.1% and 14.1%.

Figures 68 to 71 illustrate the previous results hourly for each season.

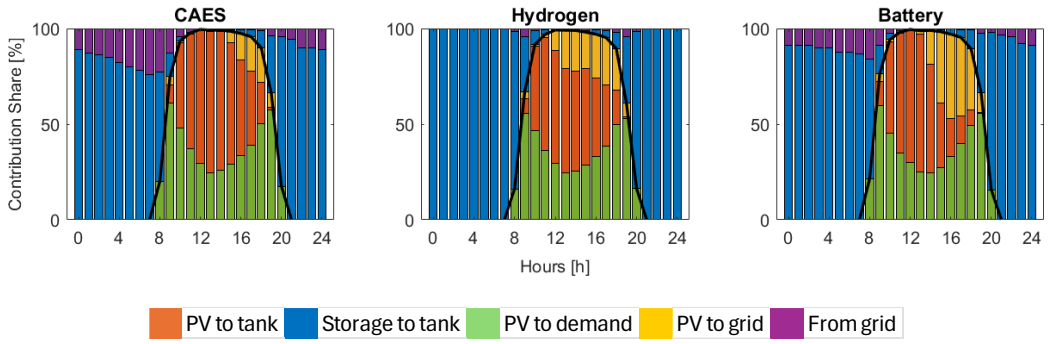

Figure 68: Summer hourly average energy assessment – Rio de Janeiro.

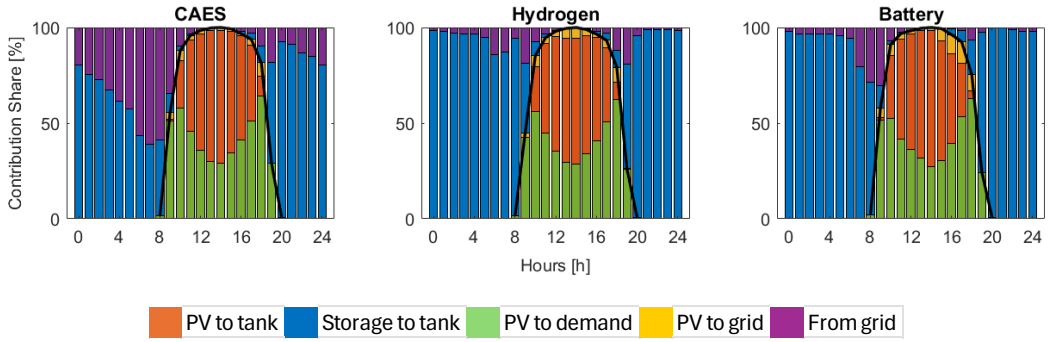

Figure 69: Autumn hourly average energy management – Rio de Janeiro.

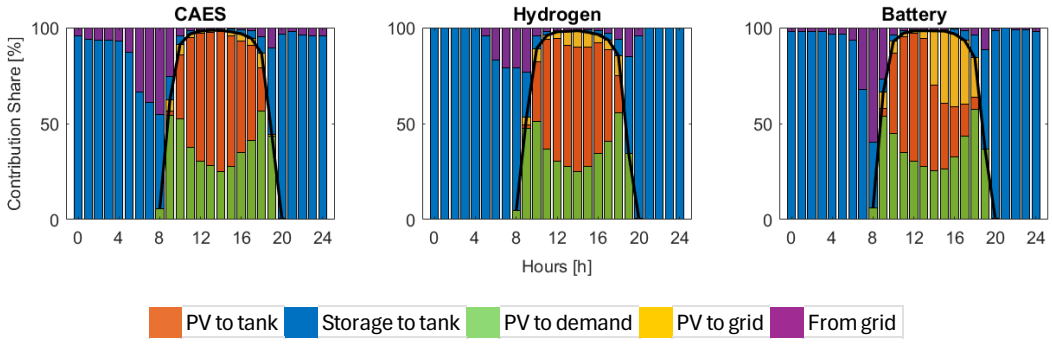

Figure 70: Winter hourly average energy management – Rio de Janeiro.

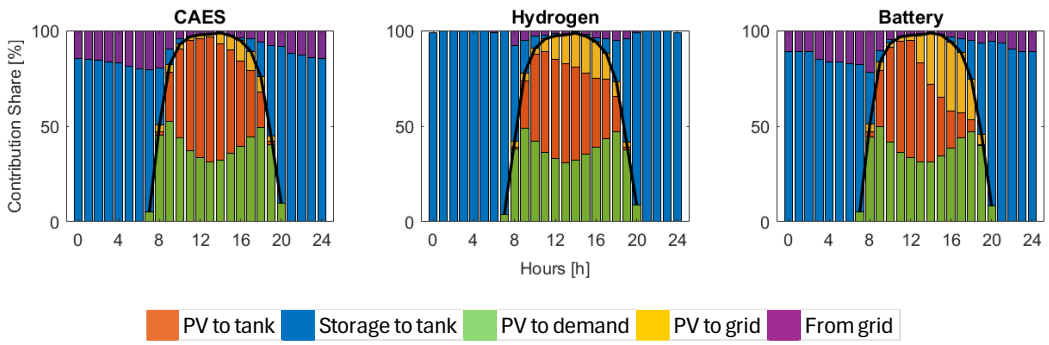

Figure 71: Spring hourly average energy management – Rio de Janeiro.

A trend is seen among all systems, as the night approaches the morning there is a higher participation of the grid in supplying the electricity demand (purple bar), with this effect being more prominent for the CAES system, as discharging process occurs. Conversely, as the day go by, by the end of it, the share of energy being sent to the grid increases (yellow bar), as the storage tanks are getting full due to the charging process. This effect is stronger for the lithium-ion battery system, as its charging is more efficient, and for the hydrogen system it is seen at more times of the day due to the maximum limit of operation set allowing more energy to be sent to the grid. The black line drawn in the figures displays the PV panels action in supplying energy. From its action, suppling the electric demands is the main factor in early morning and late afternoon (green bar), while during the middle of the day is the charging of the storage media (orange bar). Regarding seasonality, it is interesting to note that all systems show an increased reliance on the electric grid to meet demand during winter, and especially in autumn. In contrast, during spring and summer, all systems contribute a larger share of electricity to the grid, with the grid's participation being more evenly distributed throughout the hours of the day.

Figure 72 compares the seasonal electricity efficiency of all systems.

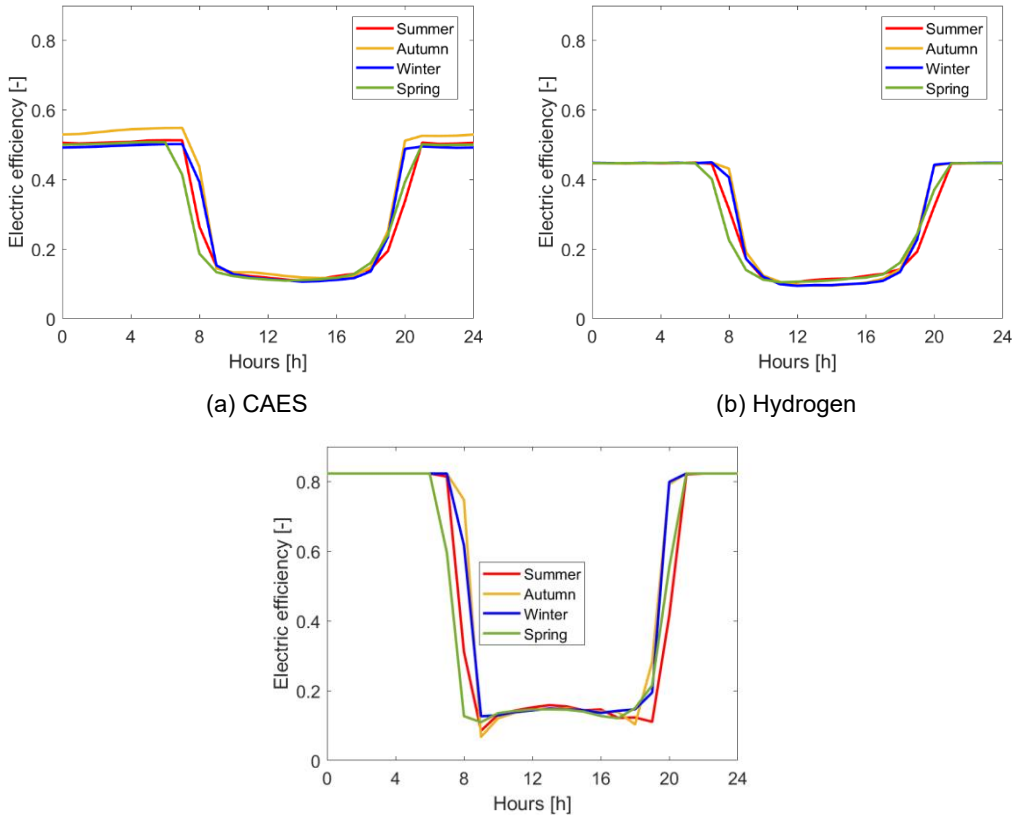

(a) CAES

(b) Hydrogen

(c) Lithium-ion battery

Figure 72: Seasonal hourly average electric efficiency disregarding the grid - Rio de Janeiro.

All systems exhibit stable operation during discharge, with minimal fluctuations over time. This stability is due to the design, which ensures that the withdrawal of air or hydrogen from the storage tank or electricity drawn for the lithium-ion batteries, aligns with the electric demand. In the CAES system, Figure 72(a), the average electric efficiency is slightly higher, during discharge, in autumn compared to other seasons. As shown in Figure 43, the system achieves greater round-trip efficiency at lower pressure levels, since compressing air at higher pressures requires more power. So, efficiency is influenced by seasonal variations, due to the different fluctuations of pressure inside the tank, being autumn the season with lower pressure level. In contrast, hydrogen storage does not experience the same pressure-related efficiency variations. The discharge efficiency is primarily governed by the SOFC, which operates under fixed pressure and temperature conditions, hence efficiency remain unaffected by seasonality. This is reflected in Figure 72(b), where the system's efficiency remains relatively constant during discharge periods in all seasons. The same behaviour is observed in the lithium-ion battery system, shown in Figure 72(c), as it operates stably with high and constant efficiency. During the charging phase, the main influencing

factor is the PV panels, which have an average efficiency of 16.4%, causing a noticeable efficiency drop in all systems. While the performance of compressors and the electrolyzer also plays a role, their impact is less significant than that of the PV panels. This effect is expressed by observing the results for the batteries, which does not experience such drop due to its constant efficiency. Comparing the systems, the CAES system demonstrates a higher annual average electric efficiency of 34.2%, than the hydrogen system of 29.4%. Both are lower when compared with the lithium-ion battery system which a result of 48.5%.

Figure 73 presents the seasonal electric efficiency considering the effect of the electric grid.

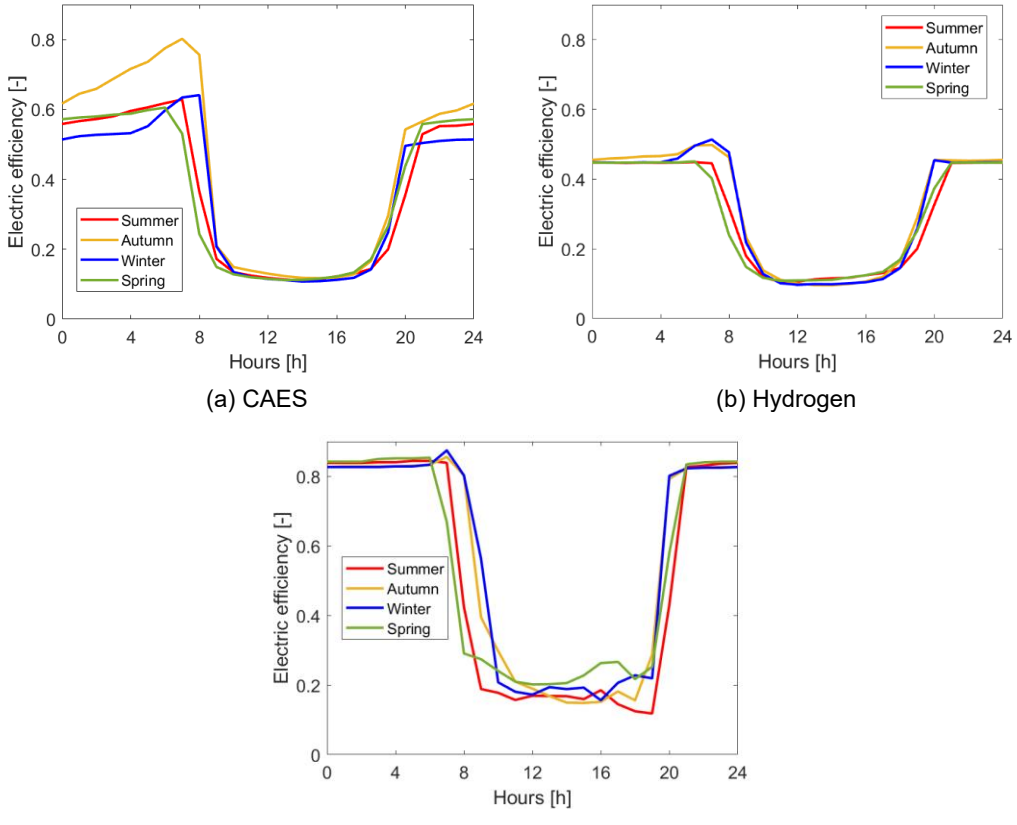

(a) CAES

(b) Hydrogen

(c) Lithium-ion battery

Figure 73: Seasonal hourly average electric efficiency considering the grid – Rio de Janeiro.

The result in Figure 73 presents the influence of the grid on the electric efficiency. The effect of the grid is stronger on the CAES system rather than the hydrogen or lithium-ion battery systems, as it was verified by Figure 67. Focusing on the CAES system, autumn season has the highest increases, as it is the season with more influence of the grid on the system. The hydrogen system has a slightly increase being more prominent on the winter, while the lithium-ion battery efficiencies experiences minimal increases. Considering the grid, the electric

efficiency increases for the CAES system to 37.6%, hydrogen system to 30.2%, and to 52.8% for the lithium-ion battery system.

Figure 74 compares all monthly average efficiencies for the CAES and hydrogen systems, not considering the grid contribution. The lithium-ion battery system is evaluated with the results considering and disregarding the grid influence as it cannot supply the heating and cooling demand without the auxiliary systems.

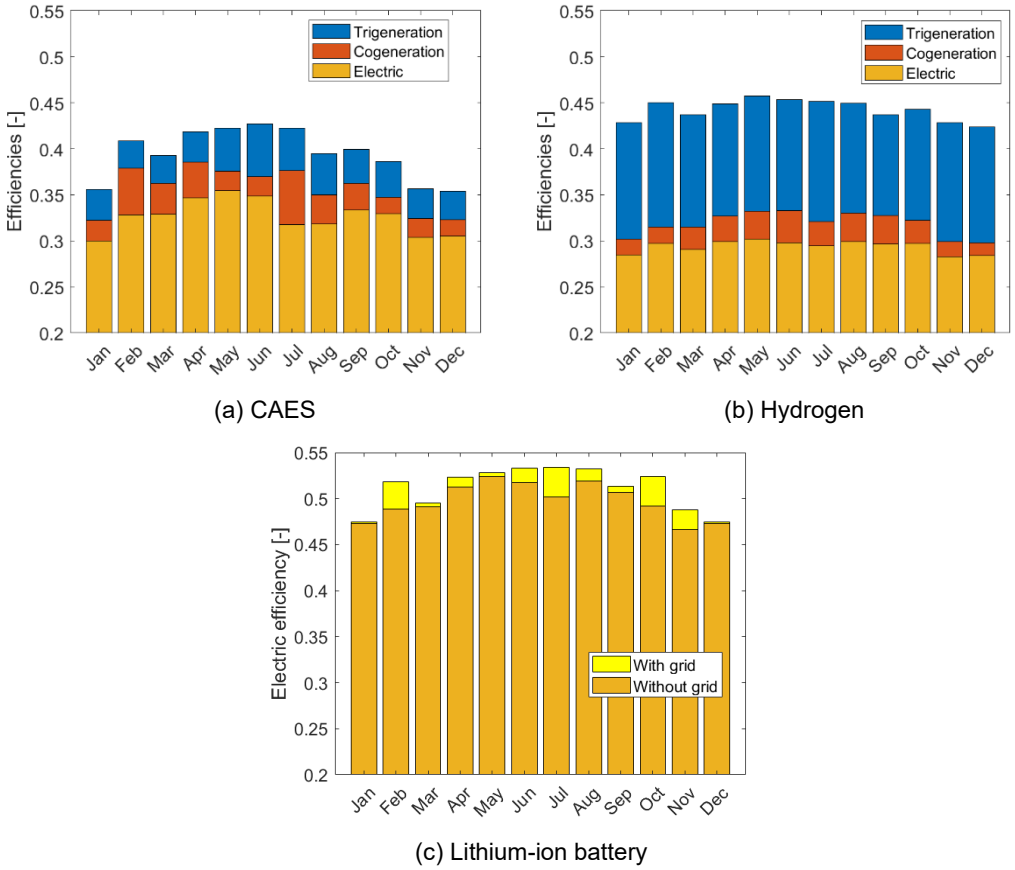

(a) CAES

(b) Hydrogen

(c) Lithium-ion battery

Figure 74: Monthly average efficiencies disregarding the grid – Rio de Janeiro.

It can be observed that both CAES and hydrogen systems benefit from the addition of heat and cooling supply. Referring to Figure 74(b), the hydrogen system maintains relatively stable efficiencies throughout the year, with minimal monthly variations. The range of variation are withing 1.9%, 3.5% and 3.4% for the electric, cogeneration and trigeneration efficiencies respectively. In contrast, Figure 74(a), the CAES system exhibits greater fluctuations in efficiency across different months, with values of 5.5%, 6.3% and 7.3% for the electric, cogeneration and trigeneration efficiencies respectively. Observing the efficiencies from the lithium-ion battery system, Figure 74(c), it can be seen that it has low variation from each month, and that the grid influence brings slight increases.

Table 28 presents the average electric, cogeneration, and trigeneration efficiencies for each for each seasonal period and the entire year.

Table 28: Average electric, cogeneration and trigeneration efficiencies – Rio de Janeiro.

System	Period	Electric	Cogeneration	Trigeneration
CAES	Summer	31.75	35.16	38.32
	Autumn	34.93	37.68	42.40
	Winter	32.38	36.00	40.36
	Spring	31.18	33.03	36.42
	Year	32.37	35.33	39.25
	Seasonal max. var. (%)	3.67	6.51	7.21
Hydrogen	Summer	29.05	31.03	43.82
	Autumn	29.97	33.04	45.31
	Winter	29.67	32.61	44.60
	Spring	28.8	30.66	43.19
	Year	29.37	31.83	44.22
	Seasonal max. var. (%)	1.94	3.67	2.33
Battery	Summer	46.84	-	-
	Autumn	50.69	-	-
	Winter	50.28	-	-
	Spring	46.20	-	-
	Year	48.50	-	-

By observing the results in Table 28, it can be seen that over the course of the year, higher overall efficiencies are observed during the colder months (autumn and winter), whereas efficiency tends to be lower in the hotter months (spring and summer). The results also confirm the higher seasonal relative variations for the CAES system, compared to the other systems, among all considered efficiencies. From the results, it is possible to observe that the hydrogen system experienced substantial increase efficiency when considered the supply of cold, when compared to the CAES system.

Figure 75 presents the efficiency relative increase from the electric to cogeneration, and from cogeneration to trigeneration.

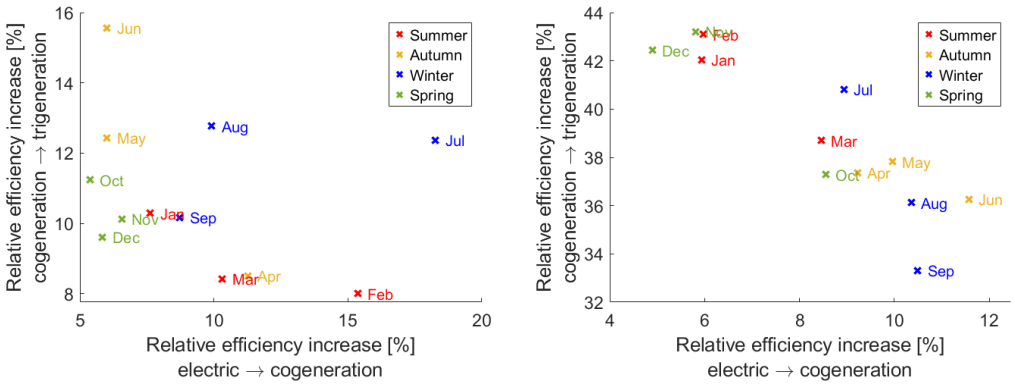

(a) CAES (b) Hydrogen

Figure 75: Monthly average efficiencies relative increase disregarding the grid – Rio de Janeiro.

Figure 75 illustrates distinct efficiency improvement trends for the CAES and hydrogen systems. In the hydrogen system, Figure 75(b), efficiency gains follow

seasonal variations. The most significant increases from electric to cogeneration efficiency occur during colder months with June showing the highest rise (11.57%). Conversely, the transition from cogeneration to trigeneration sees the greatest improvements during warmer months especially in November and December (43.2%). The CAES system, depicted in Figure 75(a), does not exhibit the same pattern, as most results cluster in the bottom-left corner, indicating minimal efficiency gains. However, certain months, such as June and July, show relatively higher improvements.

5.2.1.3. Exergy

Exergy destruction associated with the PV panels are substantially higher than the rest of the system. With an average exergy efficiency of 15.6%, it was verified that exergy destruction among CAES, hydrogen and lithium-ion battery systems were 17.8, 6.3 and 60.5 times higher, respectively, compared to all of the components in their respective systems.

Figure 76 presents the exergy destruction shares among all components of the CAES system.

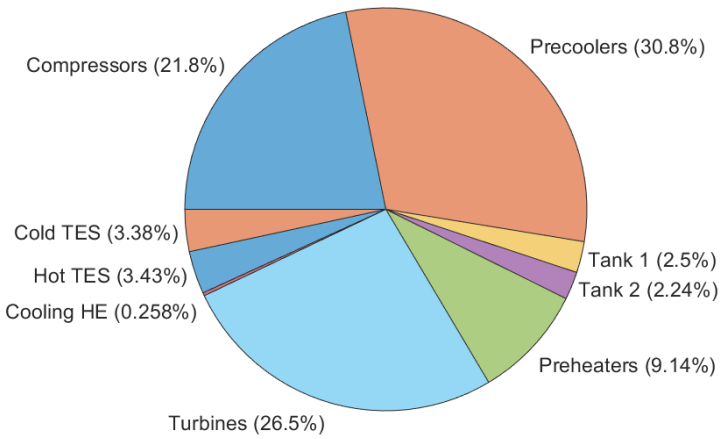

Figure 76: CAES system components exergy destruction shares (PV panels are disregarded) – Rio de Janeiro.

Regarding the CAES system, the charging path is responsible for most of exergy destruction, by considering the main components (compressors and precoolers), with 52.6% of all exergy destruction. Discharging contributes for 35.6% considering only turbines and preheaters. The high solar radiation during the year, results in a high amount of energy being stored into the storage tanks. In this procedure, it is expected a high amount of exergy destruction in the chain. The

precoolers has a higher share when compared to the compressors due to the high heat exchanges between air and water. Considering the discharge path, the turbines concentrate most of the exergy destruction due to air expansion, followed by the preheaters, which does not deal with high temperature differential as the precoolers. All storage media have a lower destruction compared to the rest of the system, however, they should not be disregarded as they account together to almost 11% of all exergy destruction rate together.

Figure 77 presents the exergy destruction shares of the components present in the hydrogen system.

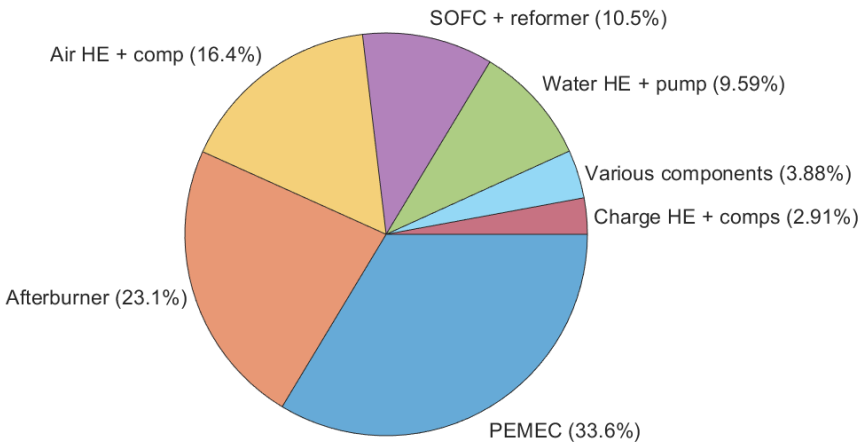

Figure 77: Hydrogen system components exergy destruction shares (PV panels are disregarded) - Rio de Janeiro.

Hydrogen system has a different behaviour considering exergy destruction. In this case, discharge concentrates most of the exergy destruction. It is seen that charging procedure concentrates 36.5% of exergy destruction, while the other 63.5% is spread among the components involved in the discharging. The main reasons that justify these results is the high temperature operation (800 °C), which can be verified with the high exergy losses in both air and water heat exchangers, and also the procedure of combustion in the afterburner and chemical reaction in SOFC and reformer. Regarding the charging procedure, the majority of exergy destruction in seen in the PEMEC, responsible for the chemical reaction of generating the hydrogen. The heat exchangers and compressors does present non-negligible exergy destruction, but as verified in Figure 35, the power to compress the hydrogen is greatly lower than the one needed for generating it. The various components described in the picture are all the ones which by themselves

presented low rates of exergy destruction – mixer, hydrogen heat exchanger, expansion valve, and both thermal energy storages.

Figure 78 displays the seasonal daily average exergy destruction rate of the components in each system, and Table 29 presents the sum of the corresponding values.

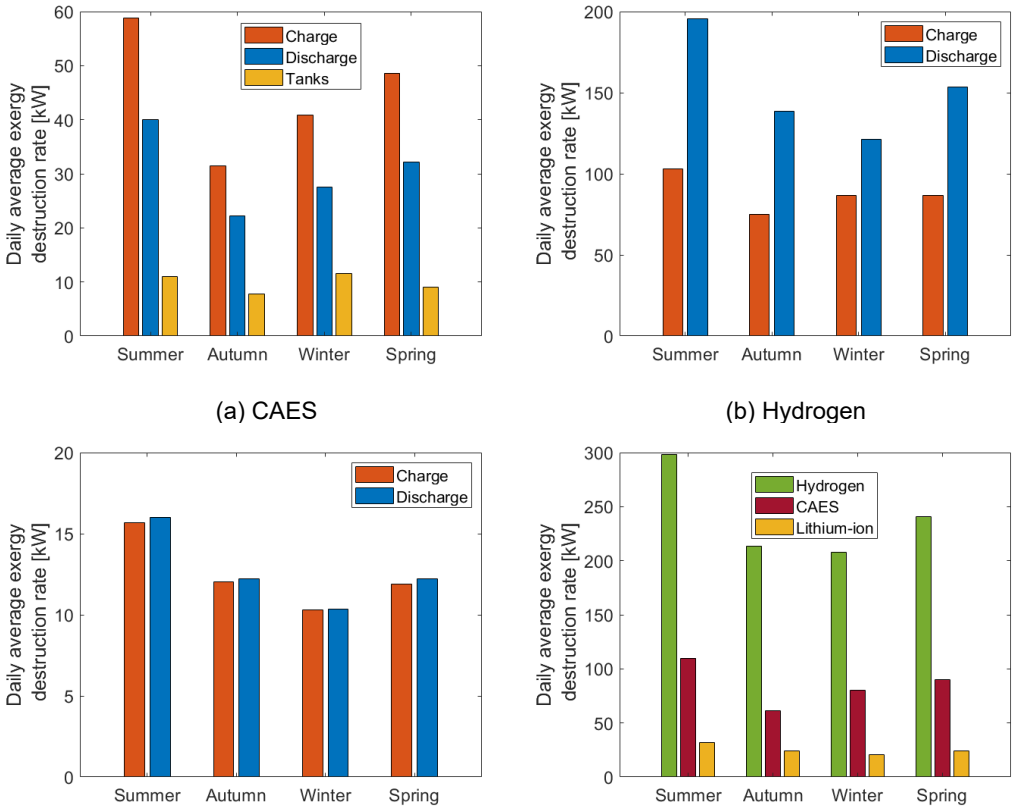

(a) CAES

(b) Hydrogen

(c) Lithium-ion battery

(d) All systems

Figure 78: Seasonal daily average exergy destruction rate – Rio de Janeiro.

Table 29: Daily average exergy destruction rate - Rio de Janeiro.

System	Summer	Autumn	Winter	Spring	Year
CAES	109.83	61.58	79.94	89.82	85.22
Hydrogen	298.47	213.70	208.12	240.47	239.94
Battery	31.66	24.25	20.67	24.12	25.14

By verifying Table 29 and Figure 78, it is possible to assess the different scales of exergy destruction in both systems. CAES system has a daily average exergy destruction rate of 85.2 kW throughout the year, while the hydrogen system averages 240.0 kW, and the lithium-ion battery system 25.1 kW. Table 29 and Figure 78(d) also highlights that exergy destruction is highest during summer, whereas autumn and winter exhibit the lowest rates. Hydrogen system, Figure 78(b), has high rates of daily average exergy destruction, especially during discharge procedure. This comes from the fact of dealing with chemical reaction with hydrogen and natural gas – which is an extra input into the system - as main

fuels in the operation, which have higher standard specific chemical exergy in comparison to air. Comparing the three of them, methane has the highest standard chemical exergy of 831.20 kJ/mol, followed by hydrogen with 236.09 kJ/mol and oxygen with 3.97 kJ/mol. The CAES system, Figure 78(a), differently from the hydrogen, has higher destruction rates during charging rather than discharge. Lithium-ion batteries, Figure 78(c), presents similar rates of destruction in both procedures as it is assumed a constant efficiency operation.

Figure 79 presents the seasonal exergy efficiency of all systems.

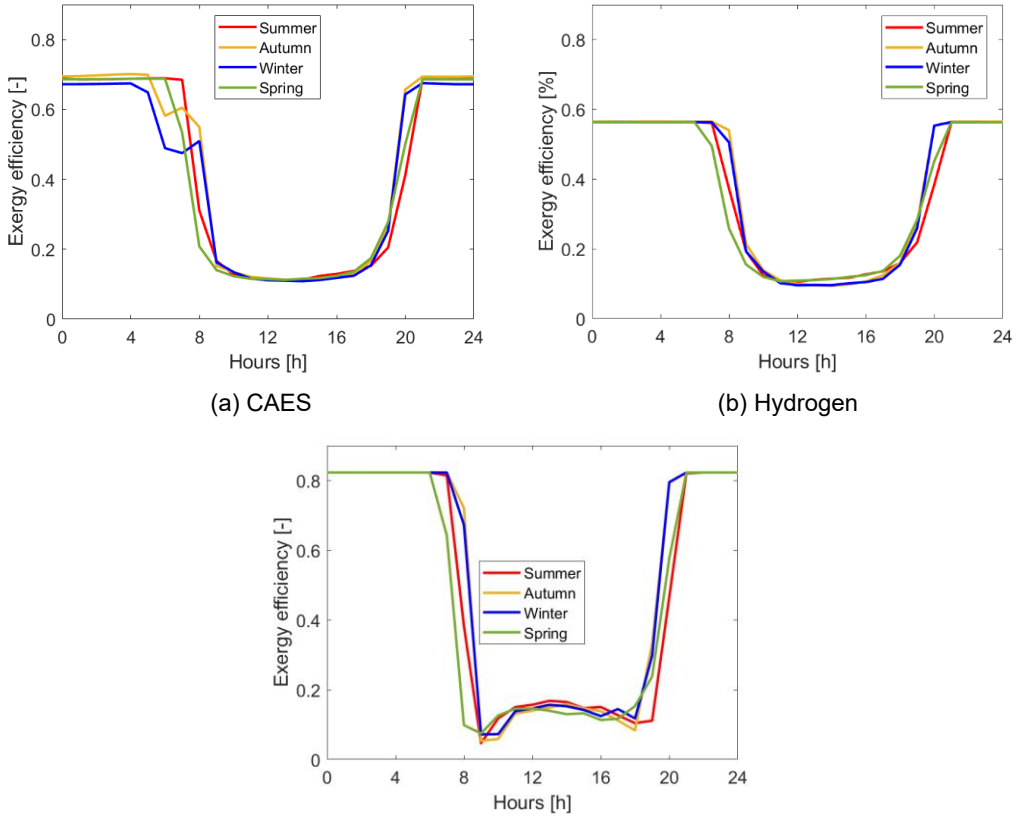

(a) CAES

(b) Hydrogen

(c) Lithium-ion battery

Figure 79: Seasonal hourly average exergy efficiency disregarding the grid – Rio de Janeiro.

Exergy efficiency has a pretty similar trend when compared to the electric efficiency in Figure 72. Similarly, discharging process has a stable result, with the CAES system presenting seasonal variations (due to the change of the physical exergy of the stored air) and hydrogen and lithium-ion battery systems having almost no variation at all. Charging procedure is again dominated by the photovoltaic panel operation. Table 30 presents the seasonal and entire year average exergy efficiency of all systems.

Table 30: Average exergy efficiency - Rio de Janeiro.

System	Summer	Autumn	Winter	Spring	Year	Seasonal max. var. [%]
CAES	40.8	42.5	40.2	40.3	40.7	4.4
Hydrogen	35.2	36.7	36.2	34.9	35.8	2.5
Battery	47.3	50.3	50.4	46.1	48.5	4.9

From the results shown in Table 30 it is possible to observe that the values for the seasonal relative variation are minimal, and that the higher efficiencies are once again observe during the colder months – autumn and winter.

5.2.1.4. Exergoeconomy

Figure 80 presents the exergoeconomy of the main parameters involved in the charging process.

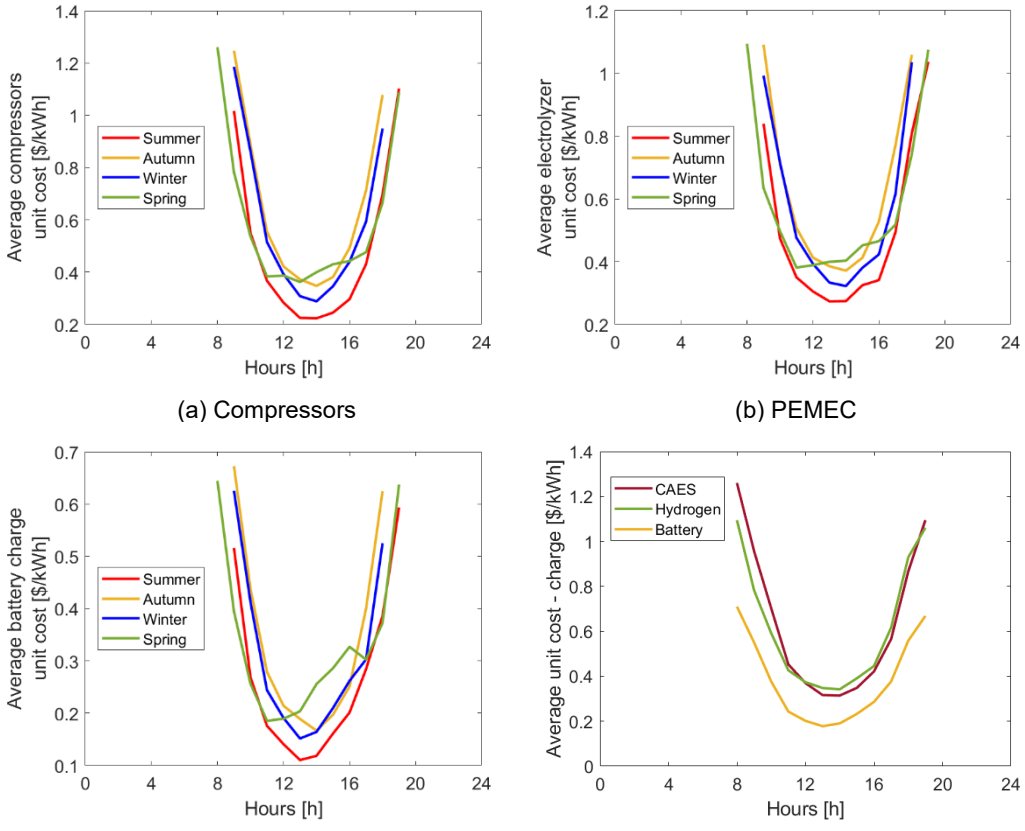

(a) Compressors

(b) PEMEC

(c) Lithium-ion battery

(d) All three – annual average

Figure 80: Seasonal hourly average charging unit cost – Rio de Janeiro.

By observing Figure 80, the unit cost during charge has a similar behaviour for all three systems. Unit cost has a lower value at the time which the solar radiation is stronger, hence storing air/hydrogen/electricity at such conditions

would be cheaper and favourable. This reflects the effects of the seasons, which unit cost has its lower point during summer for all three systems, even though this difference is not significant compared to other seasons, suggesting that unit cost is mainly driven by the capital cost. By observing Figure 80(d), the main difference among all three systems comes from the capital cost of the charging chain. Despite the hydrogen system has been downsized in this study, it results is almost the same compared to the CAES system.

Table 31 displays the average charging unit cost of all systems.

Table 31: Average charging unit cost - Rio de Janeiro.

System	Summer	Autumn	Winter	Spring	Year	Seasonal max. var. [%]
CAES	0.49	0.65	0.59	0.60	0.58	15.52
Hydrogen	0.50	0.62	0.57	0.59	0.57	12.28
Battery	0.30	0.38	0.34	0.37	0.35	14.28

Table 31 presents the seasonal average values for each system. The results confirm that summer benefits from higher solar radiation, leading to the lowest unit cost among all systems. Additionally, all ESSs show similar seasonal variations from the annual average, reflecting the similar effect of seasonality upon them.

Figure 81 displays the unit cost of the stored energy vector.

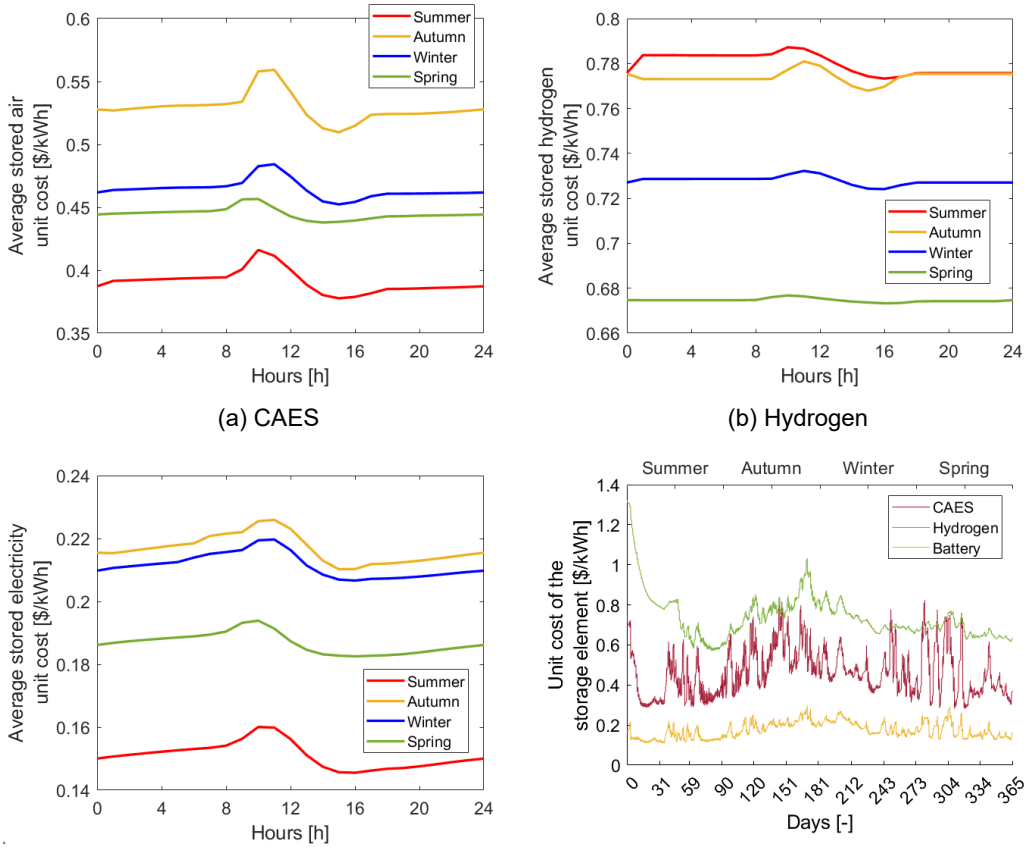

(a) CAES

(b) Hydrogen

(c) Electricity withing the battery

(d) All three – daily

Figure 81: Seasonal average hourly unit cost of the stored energy vector – Rio de Janeiro.

A similar trend in the unit cost of stored air, hydrogen, and electricity is observed in Figure 81. Initially, all systems start with a fully charged storage tank and are charged at a consistent power rate of 15 kW, resulting in different starting points for each system. As seen in Figures 81(a), (b), and (c), the unit cost slightly increases in the early morning, then decreases as solar radiation intensifies throughout the day. At night, the unit cost slightly rises again due to the discharging process. Seasonality significantly impacts the unit cost of stored energy, with lower values during warmer seasons and higher values in colder seasons. This variation occurs because the storage tank is periodically recharged with new energy, which has a lower unit cost in hotter seasons—reducing the overall stored unit cost—or a higher unit cost in colder seasons, leading to an increase. The hydrogen system exhibits a different behaviour in summer, as shown in Figure 81(d). While the unit cost of stored energy decreases across all systems at the beginning of the year, the decline is less pronounced for hydrogen, resulting in a higher average unit cost in summer compared to other seasons. However, the overall downward trend highlights the operational advantages of the system in warmer conditions. When comparing the variation amplitude, the lithium-ion battery system demonstrates more stable results. After the decline in hydrogen unit cost during summer, its fluctuations remain more controlled compared to the CAES system. The high exergetic potential of hydrogen helps mitigate sharp variations, unlike air.

Table 32 presents the average unit cost of the stored energy vector.

Table 32: Average unit cost of stored energy vector - Rio de Janeiro.

System	Summer	Autumn	Winter	Spring	Year	Seasonal max. var. [%]
CAES	0.39	0.53	0.46	0.45	0.46	15.21
Hydrogen	0.78	0.77	0.73	0.67	0.74	9.46
Battery	0.14	0.20	0.19	0.17	0.17	17.64

When comparing average values, the hotter seasons exhibit lower unit costs than the colder ones across all systems. As expected, the hydrogen system has the highest annual average unit cost, followed by CAES, with the battery system having the lowest. The seasonal relative variations suggested a higher value for the lithium-ion battery system, even though it presents lower absolute variations, followed by the CAES and hydrogen systems.

Figure 82 display the unit cost of the main components during discharge.

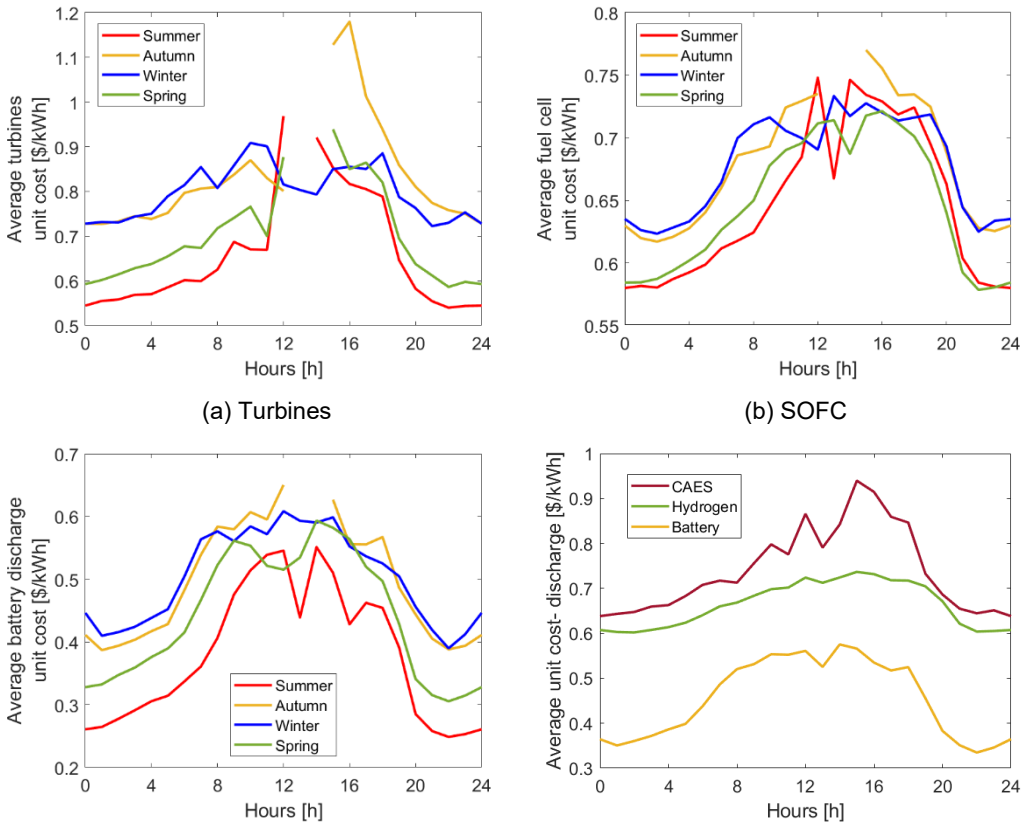

(a) Turbines

(b) SOFC

(c) Lithium-ion battery

(d) All three – annual average

Figure 82: Seasonal hourly average discharging unit cost – Rio de Janeiro.

For all three systems, Figures 82(a), (b) and (c), it has been observed that during the night, the value of the unit cost is lower, and increases as it approaches to the middle of the day. During this period of the day, electric demand is higher, so the value of the unit cost is lower. Regarding the seasonality effect, among the systems, the lower values are associated with the seasons in which the stored means of energy have the lower value, and also higher electricity demand. In other words, the values are lower for summer and spring. Figure 82(d) provides a comprehensive comparison of all systems, highlighting the relationship between the unit cost of the discharging process and the value of the stored energy. In this context, stored electricity, maintains the lowest unit cost throughout the year. Combined with the lower capital cost of the lithium-ion battery system, this results in a lower discharge unit cost compared to the other two systems. While one might expect the hydrogen system to have a higher discharge unit cost, the SOFC electrochemical reaction primarily utilizes hydrogen derived from the reforming process, which relies on natural gas. As a result, the SOFC discharge unit cost remains relatively stable throughout the year, with no significant fluctuations, as observed in Figure 82(b), and relatively low as seen in Figure 82(d).

Table 33 presents the average discharging unit cost.

Table 33: Average discharging unit cost - Rio de Janeiro.

System	Summer	Autumn	Winter	Spring	Year	Seasonal max. var. [%]
CAES	0.65	0.82	0.78	0.69	0.74	12.16
Hydrogen	0.65	0.68	0.68	0.65	0.66	3.03
Battery	0.33	0.43	0.43	0.38	0.39	15.38

The average values presented in Table 33 confirm the trends in discharging unit cost. Both summer and spring show the lowest unit costs, which are linked to higher electricity demand.

Appendix D presents a comparison of the base case of CAES and hydrogen system in Rio de Janeiro at different conditions. For both, it is evaluated a case with no lower operational limits set, and hydrogen system has a case not considering the downsizing of the charging components. This comparison aims to presents the effects of setting the operational conditions of the systems, shown in Section 4.4.

Exergoeconomic factor relates the two distinct cost sources: non-exergy-related and exergy related. Low values of this variable indicates that cost saving could be achieved by enhancing the system's efficiency, and high value suggest reducing investment cost at the expense of exergy efficiency. The annual hourly average exergoeconomic factor for each season is evaluated in Figure 83.

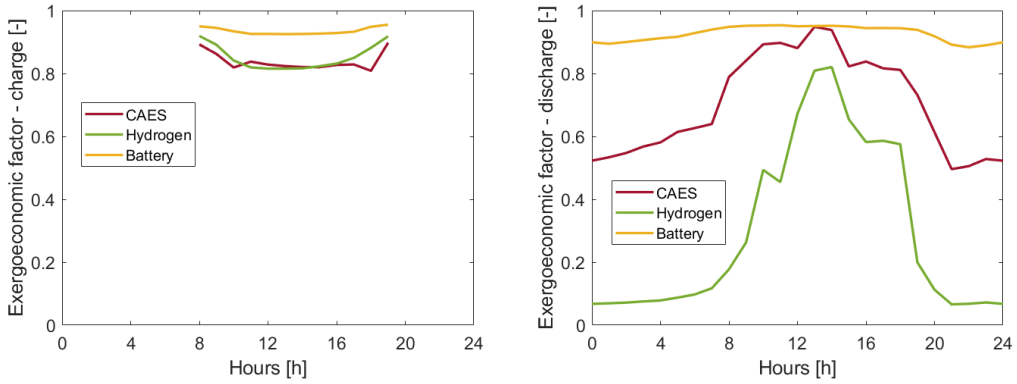

(a) Charge (b) Discharge

Figure 83: Annual hourly average exergoeconomic factor – Rio de Janeiro

During charge, Figure 83(a), the exergoeconomic factor for all three system is considered to be high (higher than 0.8), elucidating the high capital cost for the system, or even the overestimation on the system sizing, especially the PV panels. The increases in the exergoeconomic factor during discharge, shown in Figure 83(b), can be attributed to the greater contribution of the PV panels, which results in a lower reliance on the discharging infrastructure to meet the electricity demand.

The exergoeconomic factor decreases as the power output of the system increases at night. For both CAES and lithium-ion battery systems, the value is considered high, but for the hydrogen system the value is low, which explicit the higher exergy destruction.

The average results for exergoeconomic factor are displayed in Table 34.

Table 34: Average exergoeconomic factor - Rio de Janeiro.

System	Summer		Autumn		Winter		Spring		Year	
	Cha	Dis	Cha	Dis	Cha	Dis	Cha	Dis	Cha	Dis
CAES	0.84	0.69	0.85	0.70	0.83	0.70	0.83	0.72	0.84	0.70
Hydrogen	0.85	0.22	0.85	0.30	0.84	0.32	0.85	0.30	0.85	0.29
Battery	0.94	0.93	0.94	0.92	0.93	0.93	0.94	0.93	0.94	0.93

Cha – charging; Dis - discharging

When comparing the annual average results of the systems, it appears that both the CAES and lithium-ion battery systems could benefit from reduced capital investment. This could be achieved by either downsizing the system, which would increase reliance on the grid, or by investing in ways to reduce component costs. On the other hand, the hydrogen system would benefit from better exergy efficiency during discharge operations. From a seasonal perspective, all systems exhibit low variations throughout the year during both charging and discharging processes.

Figure 84 demonstrates the relative cost of both paths.

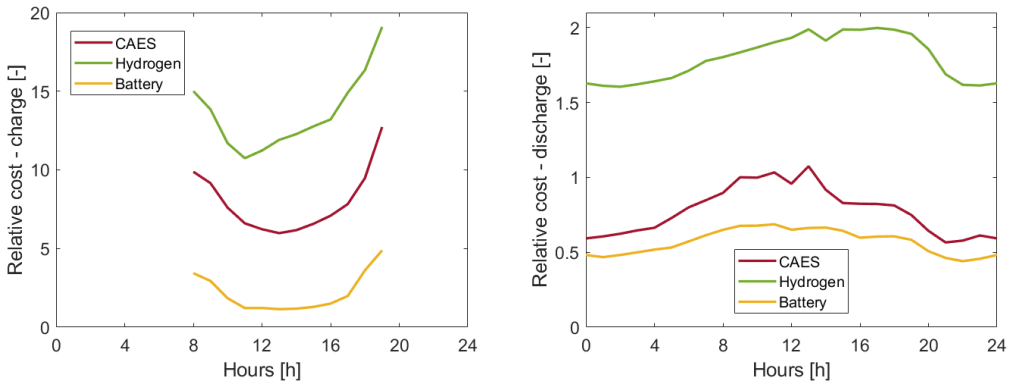

(a) Charge (b) Discharge

Figure 84: Annual hourly average relative cost – Rio de Janeiro.

The relative cost represents the increase from the average unit cost of a system's fuel and product. As shown in Figure 84, all three systems exhibit a similar pattern during both charging and discharging. During charging, the relative cost is at its lowest when solar radiation is at its peak, a trend that aligns with the unit cost (Figure 80) for all systems and is expected to be reflected here as well. A similar pattern is observed during discharging—when electricity demand is highest, the unit cost of key components in the process decreases, leading to a reduction in the

unit cost of the electricity produced. In the charging phase, the hydrogen system shows the highest values due to the high capital cost of the electrolyzer, despite its downsizing. A similar trend occurs during discharge, where the higher capital cost of not only the SOFC, but the whole chain considered, compared to turbines and batteries, leads to a greater increase in the product unit cost relative to its fuel.

Table 35 show the average values for the relative cost for both charging and discharging procedures.

Table 35: Average relative cost - Rio de Janeiro.

System	Summer		Autumn		Winter		Spring		Year	
	Cha	Dis	Cha	Dis	Cha	Dis	Cha	Dis	Cha	Dis
CAES	8.04	0.75	7.49	0.70	7.00	0.84	7.76	0.79	7.57	0.77
Hydrogen	14.13	1.75	13.34	1.77	12.22	1.83	13.52	1.83	13.28	1.79
Battery	2.38	0.54	2.30	0.52	1.95	0.57	2.38	0.56	2.25	0.55

Cha – charging; Dis - discharging

The values in Table 35 present the results for all three systems. It is evident that seasonality has minimal impact on the results compared to the average annual values. Among the three systems, the CAES system presented the highest relative variations in both charging and discharging (both in winter), with 7.53% and 9.10%, respectively.

Finally, the cost of operation is assessed in Figure 85.

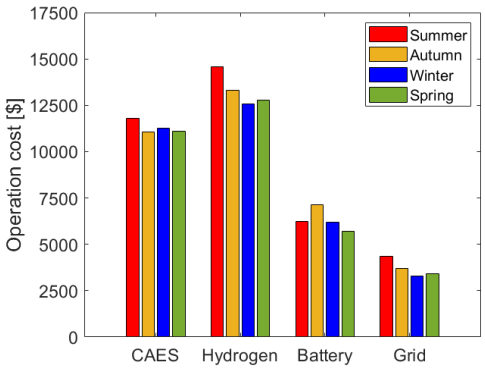

Figure 85: Seasonal operational cost – Rio de Janeiro.

The hydrogen system would be the most expensive comparing with all options. Summer is usually the season where the operation of the system is more costly, due to the higher electric demand, but there is not a substantial difference among the seasons. For both CAES and lithium-ion battery systems, the solution of decreasing the operational cost would be downsize the system and have a higher reliance on the grid, at the expense of possibly more emissions. For the hydrogen system, decreasing the capital cost of both electrolyzer and fuel cell are

the best solution for a less expensive system. The PV panels, which is common to all three systems, is also responsible for a good share on the operation cost, due to its capital cost. Not only that, but the unit cost associated with the stored energy is primarily driven by its operation. The downsizing of the PV panels could result in a less expensive system overall; however, it would result in a higher reliance of the grid. Solely relying on the grid, both electric and natural gas, the operational cost for the whole year is 14,762.22$. The hydrogen system had the highest cost of 53,285.00$ (+260.9%), followed by the CAES system with 45,230.13$ (+206.4%), and the lithium-ion battery system with 25,250.91$ (+71.0%). Both hydrogen and CAES systems presents high operational cost, which implies the need for incentives to more cost-effective system to make them a competitive option. The lithium-ion battery system, as it is, seems a good option for ESS from an economic point of view.

5.2.1.5. Environmental

In an attempt to perform the environmental analysis, two different cases are analysed: one utilizing natural gas in the auxiliary system and operation of the fuel cell, and the other using biogas for the same applications.

Figure 86 observes the CO_2 equivalent emission avoided by the system by utilizing natural gas. Negative values correspond to effective emission, and positives are the ones avoided by utilizing the system.

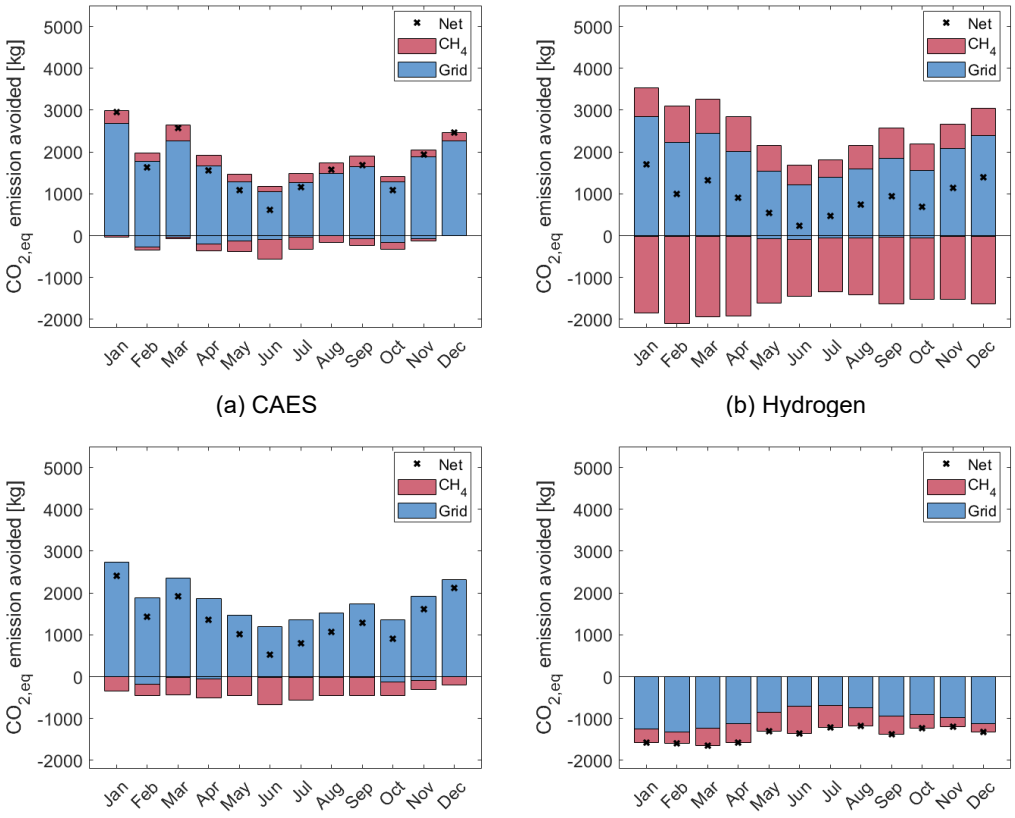

(a) CAES (b) Hydrogen

(c) Lithium-ion battery (d) Business as usual

Figure 86: Monthly CO_2 equivalent emission avoided – Rio de Janeiro.

It is considered two different ways of emitting CO_2, by the use of the electric grid (blue bars), and the use of natural gas (orange bars). Among the three systems, the CAES system is the one able to avoid more emission, as shown in Figure 86(a). Its operation does not involve the utilization of any fuel, and the recovery of heat during compression allows the hot TES to increase its temperature and provide partially the heat demand. The operation of the hydrogen system, Figure 86(b), involves the withdraw of natural gas from the grid to be reformed into hydrogen, resulting in significant emissions of CO_2. The system configuration allows to also partially provide the heat demand, diminishing the reliance on the natural gas. An attempt to lower the consumption of natural gas would be increasing the amount of hydrogen being withdrawn from storage tank. The lithium-ion battery system, Figure 86(c), is not able to supply the heat, so it relies on the auxiliary system, using the natural gas burner. Comparing the net emission avoided of all systems, in order, CAES had the highest amount with 20.34 ton, followed by batteries with 16.46 ton, and hydrogen with 11.09 ton. It is possible to observe in all previous cases the seasonality effect, which the net emission avoidance is higher in the warmer months compared to the cold ones. It is also

interesting to compare the application of the ESSs to the business as usual case, solely relying on the grid, Figure 86(d). In this case, only effective emissions are seen, with summer and spring have the highest emissions, and total emission of 16.6 tons.

Figure 87 presents the values for specific emissions for the two different scenarios – with natural gas and biogas.

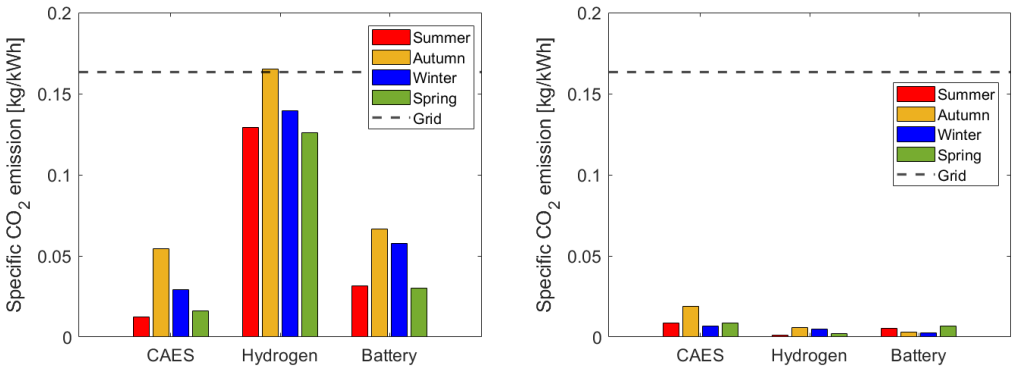

(a) Using natural gas (b) Using biogas

Figure 87: Seasonal average specific CO_2 emission- Rio de Janeiro.

Figure 87(a) presents the specific CO_2 emissions for each system when using natural gas as fuel or as a heat source with the support of the auxiliary system, and Figure 87(b) utilizes biogas instead. In both, the specific emission when solely relying on the grid (electric and natural gas) is represented as the reference for comparison. In Figure 87(a), both CAES and lithium-ion battery systems achieve emission levels below the reference due to their ability to significantly reduce grid dependency, thereby avoiding substantial CO_2 emissions. Conversely, the hydrogen system exhibits higher CO_2 emissions compared to the other systems, primarily due to the natural gas reforming process, which promotes effective emissions. It is important to state that the use of this system is lower than the emissions by the ones represented by the actual scenario of utilizing the grid, displaying that even though there are relative emission in operation, they are lower than the actual case. Figure 87(b) depicts an alternative scenario where biogas replaces natural gas, resulting in zero CO_2 emissions. As shown, the specific emissions for all systems decrease significantly in this case. However, the combination of the utilization of PV panels, energy storage and a biogas, even though not competitive from an economic standpoint, allow to greatly decrease the emissions during operation being more than three times lower than the specific emissions from the reference. In this scenario, the CAES would be the system with

more emissions, due to its higher reliance on the electric grid (as shown in Figure 67).

Figure 88 presents the CO_2 equivalent emission comparison between the system utilizing both natural gas and biogas.

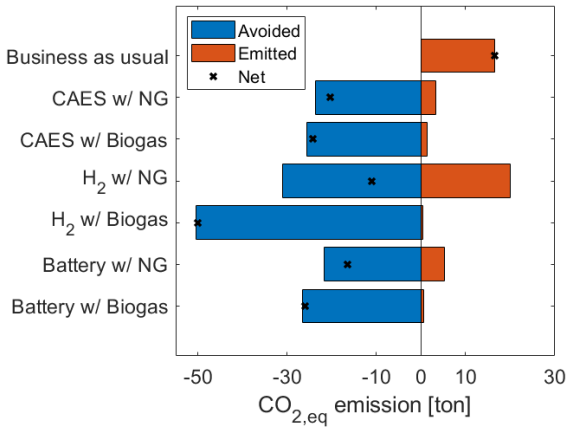

Figure 88: Systems annual total CO_2 equivalent emission considering one year of operation – Rio de Janeiro.

Figure 88 presents the CO_2 equivalent emission for all systems and by using the actual scenario of electric and natural gas grid. It can be seen by incorporating any of the considered ESS, the net emissions are always negative compared to the actual case, which corresponds to an effective emission of 16.6 ton of CO_2 equivalent. By the incorporation of the biogas instead of natural gas, the advantage is even higher. In the CAES and lithium-ion battery systems, nearly all CO_2 emissions originate from the auxiliary system. By incorporating biogas, both systems approach zero emissions during operation. The hydrogen system is the most impacted with biogas utilization, as using it as fuel for the reforming process eliminates CO_2 emissions. As a result, its operation becomes environmentally friendly, with any remaining emissions stemming only from grid dependence. In comparison, the net avoided emissions increase by 351.2% for the hydrogen system, 19.5% for the CAES system, and 57.8% for the lithium-ion battery system. By the end of the year, the hydrogen system is able to avoid 50.05 ton of CO_2 equivalent emissions, the CAES system 24.3 ton, and the lithium-ion battery system 26.05 ton.

There is not a defined commercial value for utilizing biogas in residential buildings, so two cases were considered to evaluate economic aspects, which considers the cost of using biogas to be half and double the original cost of the natural gas. It is interesting to evaluate the cost per emission avoided of the

system, relating both economic and environmental perspectives. Figure 89 compares the base case with both scenarios of biogas.

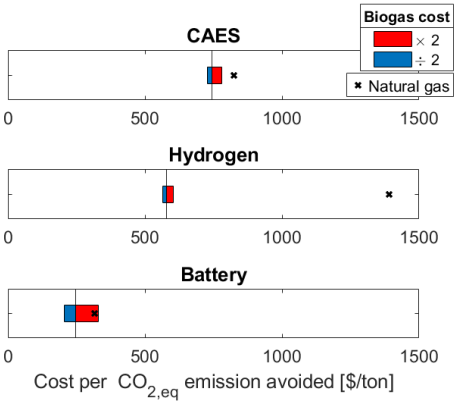

Figure 89: Sensitivity analysis of the cost per CO_2 equivalent emission avoided using biogas – Rio de Janeiro.

As shown in Figure 89, hydrogen system undergoes a significant change when biogas gas replaces natural gas, concerning the cost per CO_2 emissions avoided. For natural gas use, its value reaches 824.8 $/ton for the CAES system, 1,391.1 $/ton for the hydrogen system, and 317.4 $/ton for the lithium-ion battery system. When switching to biogas (no variation to its cost), these values decrease to 744.9 $/ton, 578.0 $/ton, and 246.5 $/ton, respectively. The results also highlight cost variations, with increases represented in red and decreases in blue. These variations have minimal impact on the final outcome, as the reduction in emissions is significantly greater than the cost fluctuation, except for the lithium-ion battery system. It is observed in this case, that the cost increases are greater than the benefits of further increasing the avoidance of CO_2 emission. Table 36 presents the values of the cost, net emission and cost per CO_2 emissions avoided for each system, by considering natural gas and biogas (assuming double the cost of natural gas).

Table 36: Main economic and environmental aspects of all systems utilizing natural gas and biogas (double the cost) - Rio de Janeiro.

	Parameter	CAES	Hydrogen	Battery
Natural gas	Cost [$]	45,230	53,285	25,251
	Net emission [ton]	- 20.34	- 11.09	- 16.45
	Cost per emission avoided [$/ton]	824.8	1,391.1	317.4
Biogas	Cost [$]	46,692	55,062	28,756
	Net emission [ton]	-24.30	-50.05	-25.95
	Cost per emission avoided [$/ton]	744.9	578.0	246.5
Relative variation [%]	Cost [$]	3.23	3.34	13.88
	Net emission [ton]	19.50	351.34	57.76
	Cost per emission avoided [$/ton]	-9.69	-58.45	-22.34

The results reinforce the benefits of using biogas, especially for the hydrogen system. Being able to lower the cost per emission avoided leverage the feasibility of its use, as it could be use as carbon credit lowering even further the total operational cost. However, this value is still significantly higher than the values established in the market (137) – about 2 $ per tonne of CO_2 equivalent.

5.2.2. France

5.2.2.1. General

Figure 90 display the evolution of the storage media for all three systems.

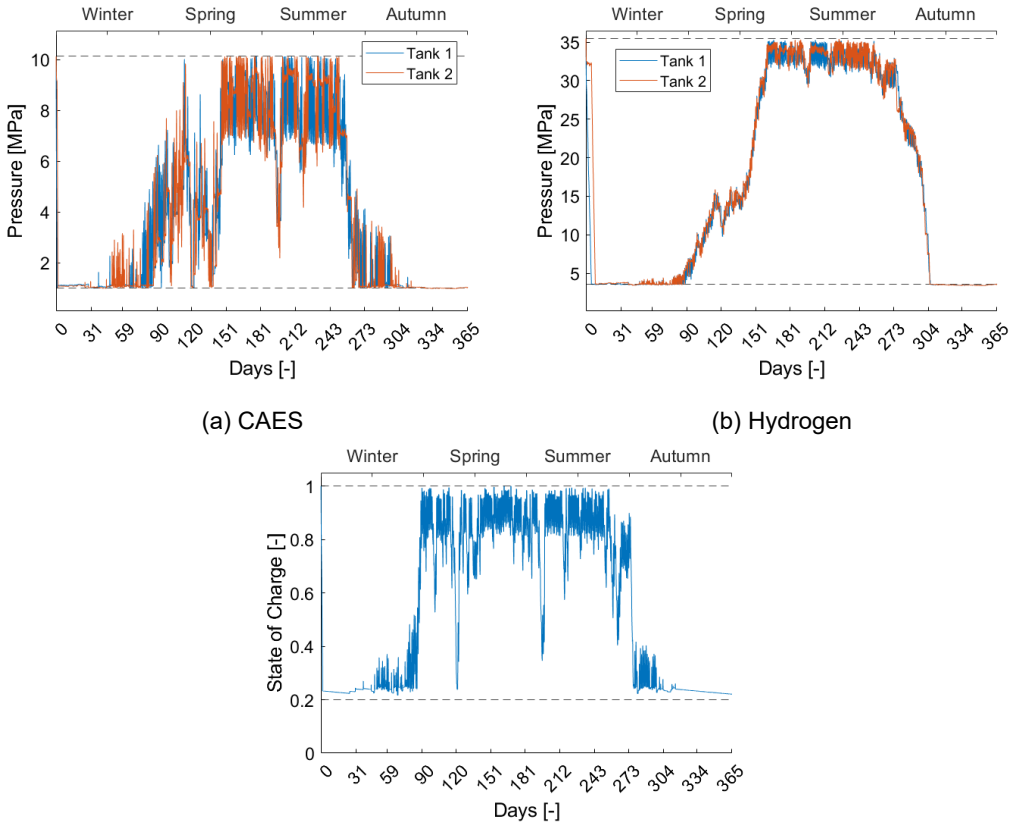

(a) CAES

(b) Hydrogen

(c) Lithium-ion battery

Figure 90: Storage media behaviour as a function of time – Lyon.

Figure 90 highlights the key differences in system operation between Rio de Janeiro and Lyon. Across all three systems, maintaining independence from the grid proves challenging during colder seasons due to limited solar radiation. This constraint not only reduces electricity generation from PV panels but also restricts energy storage capacity. Additionally, electricity demand peaks during these

seasons, as it can be seen in Figure B2 in the Appendix B. In contrast, as warmer months approach, both heat and electricity demand decrease while solar radiation increases, enabling the systems to better meet energy needs and keep storage media nearly full. However, by the end of the year, energy storage is depleted across all systems, resulting in empty storage tanks at the start of the following year. These findings highlight the hybrid system's limitations in this region, making it a viable solution primarily during warmer months. When comparing the average pressure and SOC levels of the ESSs, it is seen that the CAES system has it at 37.6% from the maximum pressure, the hydrogen system at 47.5%, and the lithium-ion battery system at 55.2 %.

Figure 91 presents the current density operation for both PEMEC and SOFC.

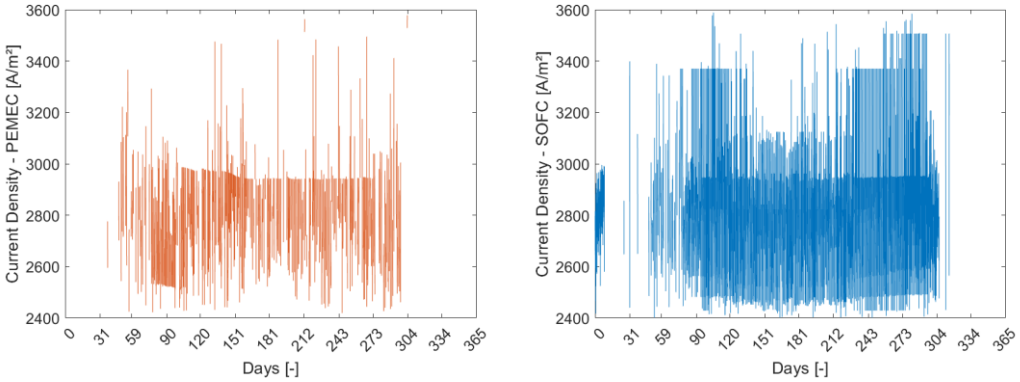

(a) PEMEC (b) SOFC

Figure 91: Operational current density as function of time – Lyon.

Figure 91 illustrates the current density operation. Under the specified conditions, the PEMEC mostly operated at a current density of 2940 A/m², while the SOFC operated at 2770 A/m², with deviations of less than 20% from their respective design conditions.

5.2.2.2. Energy

Figure 92 presents the energy management of all system.

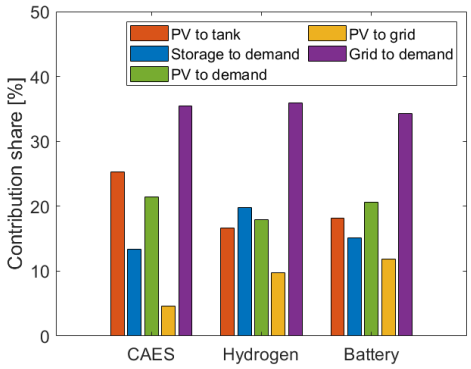

Figure 92: Energy management for all three systems - Lyon.

Figure 92 highlights a similar pattern across all systems, particularly in their reliance on the grid, shown in purple, to meet electricity demand (34.3% to 35.9%). The PV area is selected based on building constraints, such as rooftop and parking lot space; however, expanding this area would likely reduce the grid's contribution. The lithium-ion battery system operates near full capacity most of the time, enabling it to send more energy back to the grid, represented in yellow (4.6% to 11.9%). The hydrogen system can independently sustain electricity demand for longer, depicted in blue(13.3% to 19.8%). Lastly, the CAES system, due to its larger storage capacity, can retain more energy, as shown by the orange bars (16.6% to 25.3%).

Figures 93 to 96 presents the energy management of all system across the seasons.

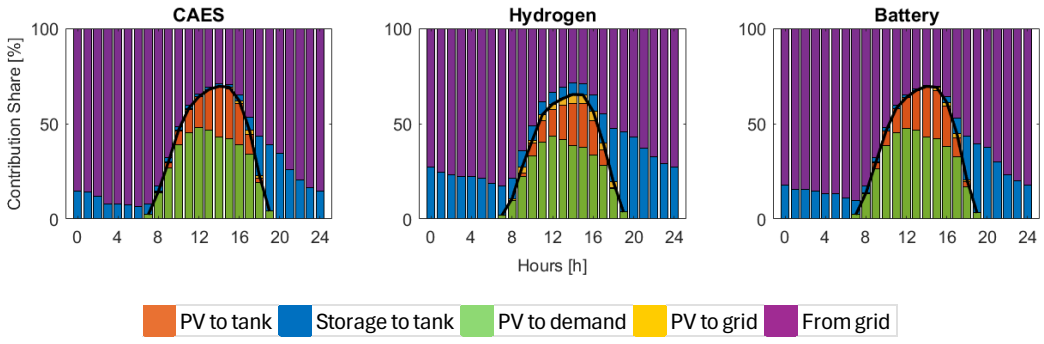

Figure 93: Winter hourly average energy assessment - Lyon.

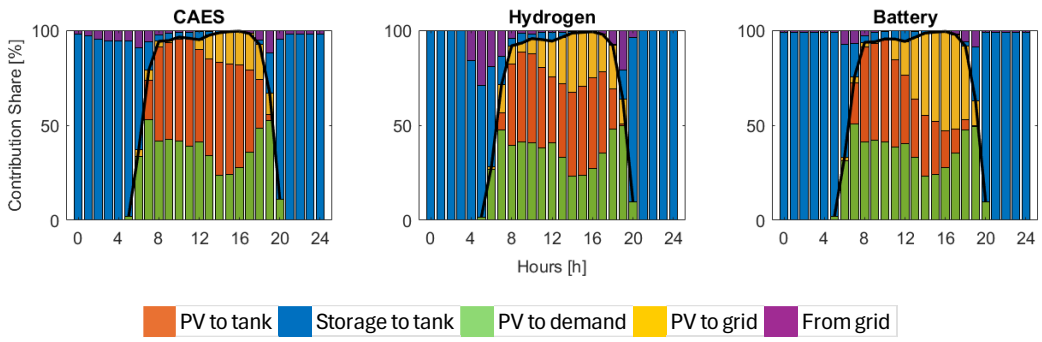

Figure 94: Spring hourly average energy assessment - Lyon.

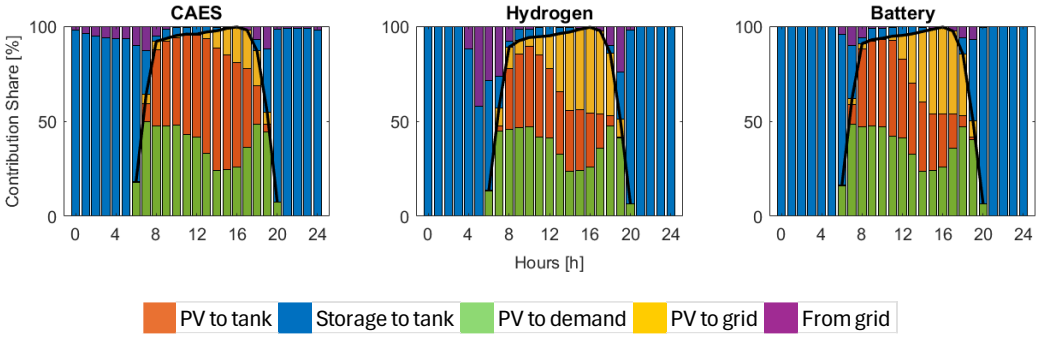

Figure 95: Summer hourly average energy assessment - Lyon.

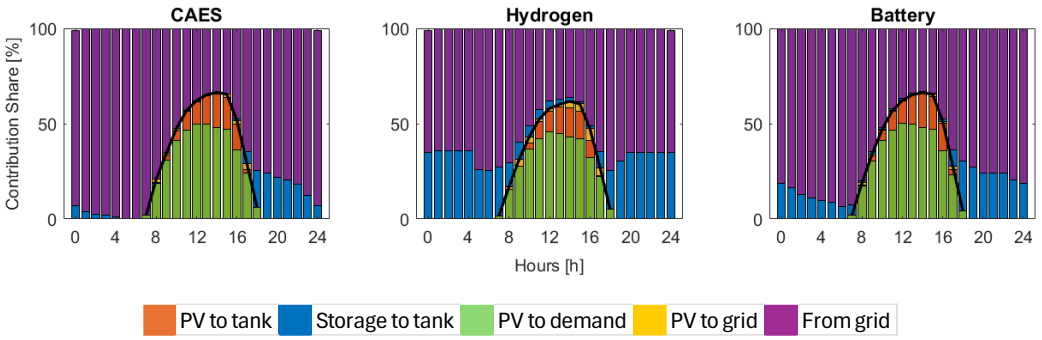

Figure 96: Autumn hourly average energy assessment - Lyon.

From Figures 93 to 96, a trend can be observed across the systems. During winter and autumn, all systems face challenges in meeting electricity demand using PV panels and storing energy in storage media. However, the hydrogen system performs better in supplying electricity during these seasons. In contrast, during spring and summer, due to increased solar radiation, all systems can meet most of the demand while storing energy, without depending on the electric grid. Similar to the case in Brazil, grid participation increases at night, with energy storage being more prominent in the late afternoon. The effect of seasonality is significant, as the low solar radiation in winter and autumn makes it difficult to store energy in the tanks, while during summer and spring, the tanks are mostly full.

Figure 97 presents the seasonal electric efficiency of all systems disregarding the grid.

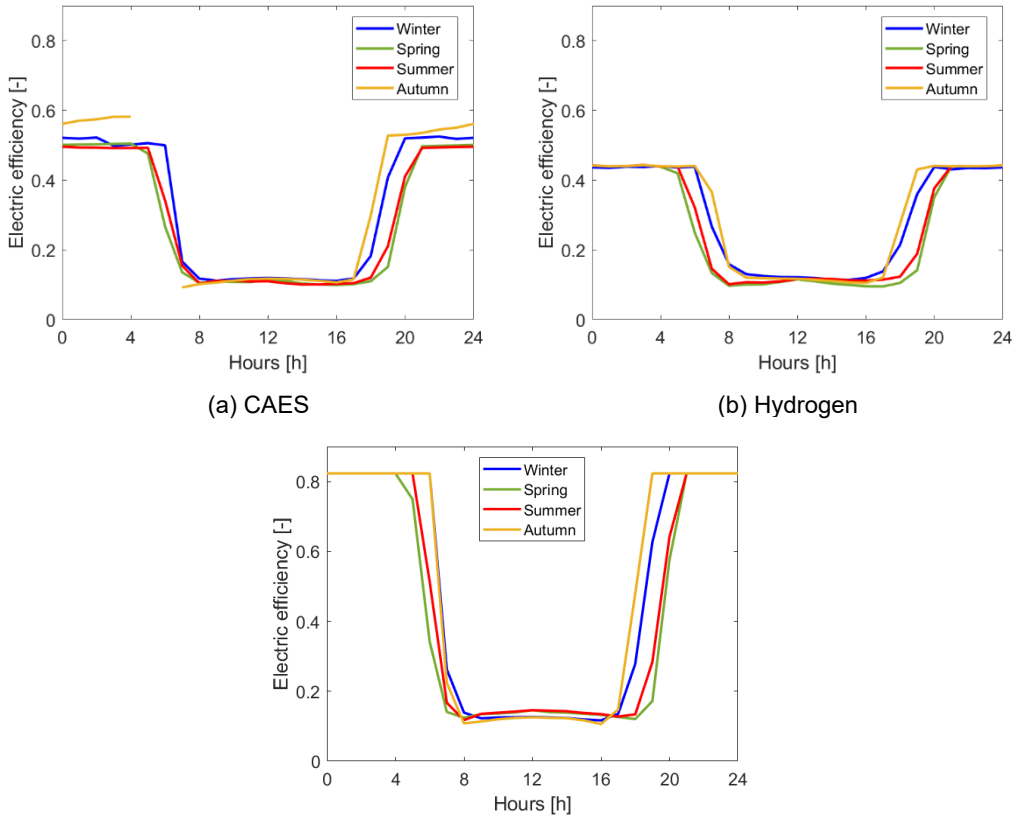

(a) CAES

(b) Hydrogen

(c) Lithium-ion battery

Figure 97: Seasonal hourly average electric efficiency disregarding the grid - Lyon.

Similar to the findings in Rio de Janeiro, all systems operate under stable conditions with minimal seasonal variations. The CAES system demonstrates higher efficiency during autumn due to the use of low-pressure storage tanks, while the hydrogen system remains unaffected by this factor. The PV panels contribute to a reduction in efficiency during the charging process, with an annual average efficiency of 12.6%. The CAES system achieved an annual efficiency of 28.2%, while the hydrogen system recorded 26.5% and the lithium-ion battery of 42.9%.

Figure 98 illustrates the seasonal electric efficiency considering the grid.

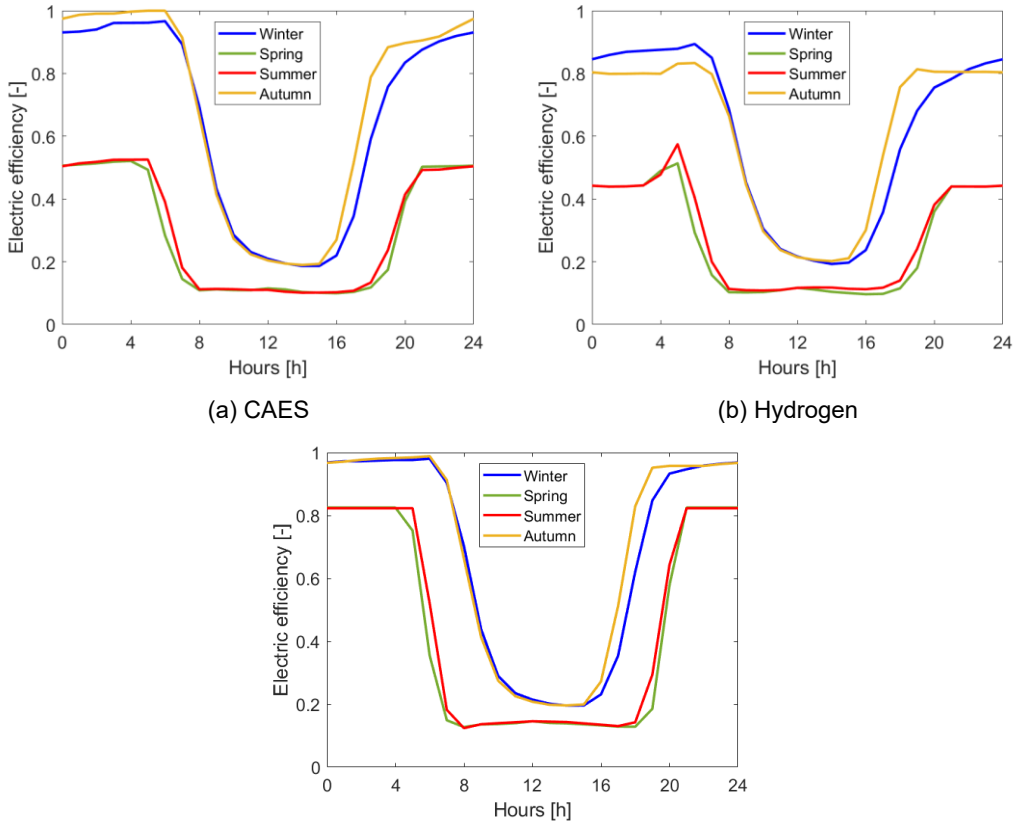

(a) CAES

(b) Hydrogen

(c) Lithium-ion battery

Figure 98: Seasonal hourly average electric efficiency considering the grid - Lyon.

In both systems, the significant impact of the electric grid on the results is evident when compared with Figure 97. As noted earlier, during winter and autumn, both systems primarily depend on the electric grid to meet energy demands, causing their efficiency to align closely with the grid's efficiency (close to unity). When comparing the all systems, the CAES system achieves a higher efficiency of 47.3%, while the hydrogen system reaches 43.6% and the lithium-ion battery of 66.6%.

Table 37 shows the seasonal average values for the efficiencies considering and disregarding the electric grid.

Table 37: Electric efficiencies considering and disregarding the electric grid - Lyon.

System	Winter		Spring		Summer		Autumn		Year	
	w/o G	w/ G	w/o G	w/ G	w/o G	w/ G	w/o G	w/ G	w/o G	w/ G
CAES	31.5	64.2	27.4	28.2	28.0	29.3	32.1	68.1	29.8	47.4
Hydrogen	28.7	60.2	24.7	26.0	25.9	27.6	29.5	60.7	27.2	43.2
Battery	48.9	82.8	40.1	42.4	42.4	44.2	49.1	87.2	42.9	66.6

wo G – without grid; w G – with grid

The values shown in Table 37 confirm the behaviour depicted in Figures 97 and 98. When the grid is considered, the system's efficiency significantly improves during the colder seasons. Without the grid, these months still see higher efficiency due to operation at lower pressure ratios, and more time spent in the discharge phase rather than charging. Considering the results disregarding the grid, the lithium-ion battery system has the highest seasonal relative variation with 14.0%, followed by hydrogen system with 9.2%, and CAES with 8.0%.

Figure 99 display the monthly average efficiencies for both systems.

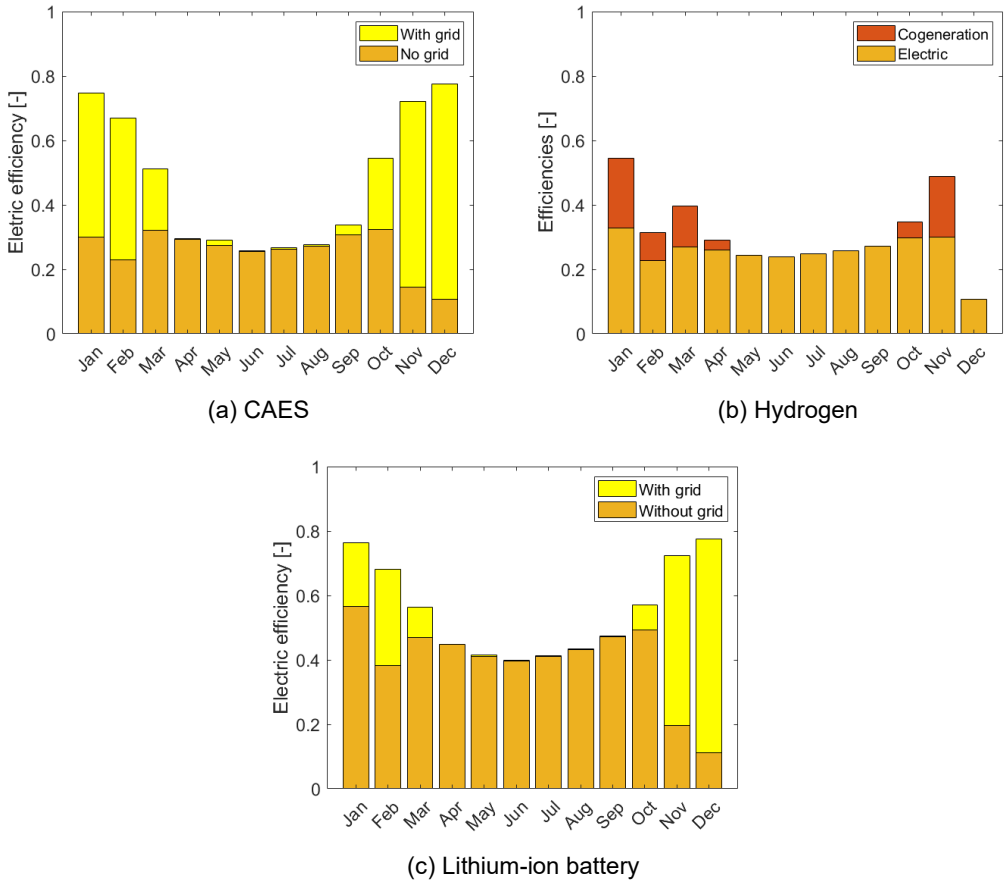

(a) CAES

(b) Hydrogen

(c) Lithium-ion battery

Figure 99: Monthly average efficiencies - Lyon.

Figure 99(a) illustrates the results for the CAES system, focusing solely on electric efficiency (both with and without grid involvement). These findings align with those previously shown in Figures 97 and 98. The results also implies that the months which the electric efficiency is closer to unit, are the months with a higher grid reliance. Meanwhile, Figure 99(b) depicts the results for the hydrogen system, which can meet heat demand when the SOFCs are operational, particularly during the colder months. However, it is important to note that, under the defined conditions, only 8.83% of the heat demand is supplied by the system. Similarly to the CAES system results, Figure 99(c) shows the electric efficiency of the lithium-

ion battery system when the grid is considered and not. As previously, the months with more activity of the grid, during winter and autumn, are the ones which presents a higher increase in efficiency, while during summer and spring, grow is less expressive.

Figure 100 presents the potential of both systems to supply a possible cooling demand by maintaining the proposed architecture.

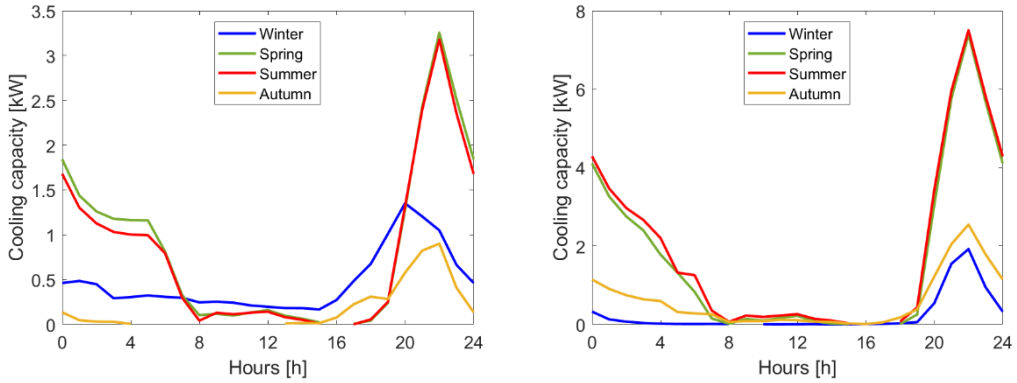

(a) CAES (b) Hydrogen

Figure 100: Seasonal hourly average cooling potential - Lyon.

Both systems demonstrate the ability to supply cooling, particularly during the warmer months. The hydrogen system has greater potential, leveraging the hot exhaust gases from the SOFC and the absorption chiller. Similarly, the CAES system can provide cooling by utilizing the cold air released at the outlet of the air turbines. Meeting cooling demands enhances the overall efficiency and attractiveness of both systems for operation. It is difficult to determine whether the curve would be suitable for providing cooling in the Lyon case, as there are no reference curves for such behaviour. However, it is observed that the lowest potential occurs between 8:00 AM and 6:00 PM, a period when people are typically away from home. Consequently, the cooling potential would be concentrated during the hours when residents are returning home from work, school, or other activities, as well as during nighttime while they sleep.

5.2.2.3. Exergy

Once again, the PV exergy destruction was left out of the following analysis, as it has higher rates compared to the other components. It is 25.7 times higher than the CAES system, 8.47 times the hydrogen, and 95.7 times for the lithium-ion batteries.

Figure 101 display the annual exergy destruction share of the components in the CAES system.

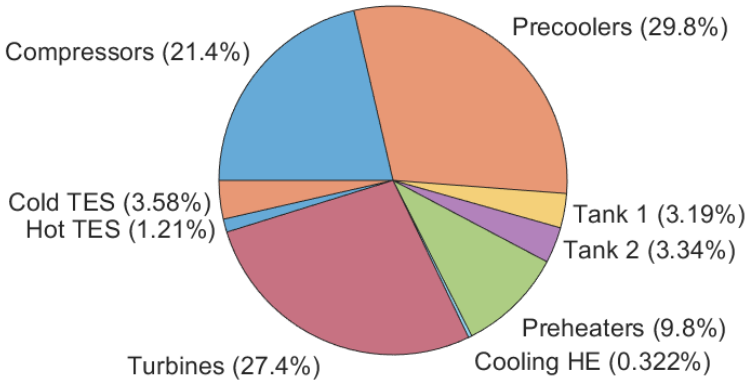

Figure 101: CAES system components exergy destruction shares (PV panels are disregarded) – Lyon.

Similar to the Brazilian case, the charging phase exhibits the highest exergy destruction, primarily attributed to the precoolers and compressors. It is worth remembering that during the sizing of the systems, the charging components are bigger than the discharging ones, so it could be expected to have higher rates of exergy destruction. During the discharge phase, the turbines account for the majority of exergy destruction. It is interesting to note that, despite evaluating the CAES system in different cities, the components exhibit nearly the same share of exergy destruction, regardless of the location.

Figure 102 displays the exergy destruction shares for the components considered in the hydrogen system.

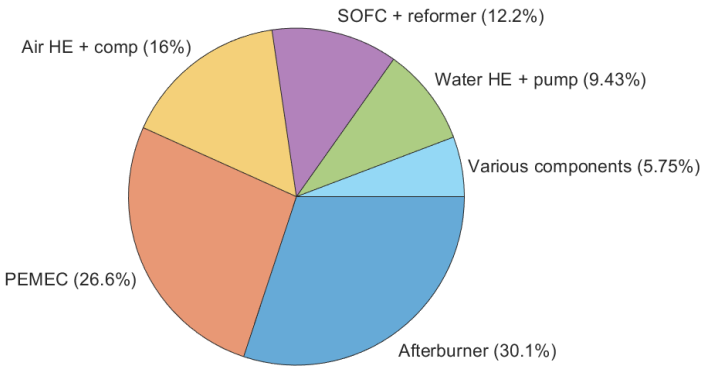

Figure 102: Hydrogen system components exergy destruction shares (PV panels are disregarded) - Lyon.

Similarly to the Rio de Janeiro case, the discharging phase concentrates most of the exergy destruction and have the afterburner as the component with the

higher rates. For Lyon, the afterburner also has the highest share among all components, differently from Rio de Janeiro (Figure 77), where the PEMEC takes the spot. The difference relies on the impact of the downsizing of the system.

Figure 103 presents the daily average exergy destruction of the main components in each system.

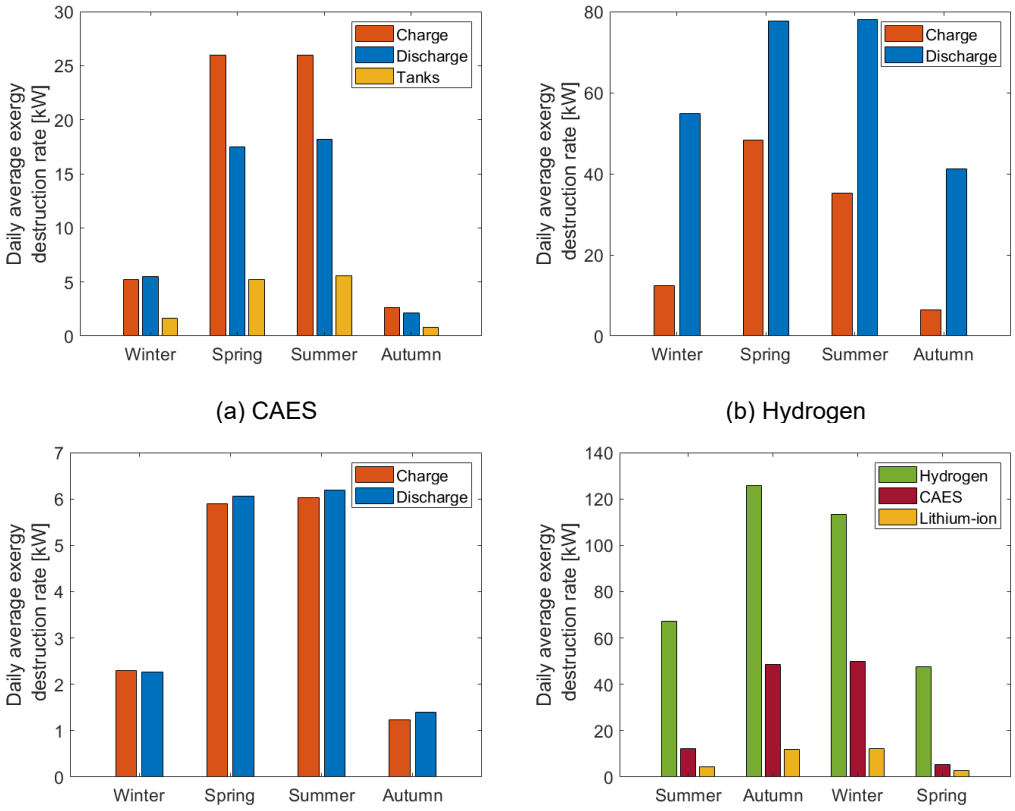

(a) CAES

(b) Hydrogen

(a) Lithium-ion battery

(d) All systems

Figure 103: Seasonal daily average exergy destruction rate - Lyon.

Table 38: Daily average exergy destruction rate - Lyon.

System	Winter	Spring	Summer	Autumn	Year
CAES	12.39	48.71	49.75	5.52	29.09
Hydrogen	67.26	125.83	113.29	47.72	88.52
Battery	4.56	11.96	12.21	7.85	9.14

It is insightful to compare the results from Figure 103 and Table 38 to the ones observed in Rio de Janeiro. Firstly, it can be seen that the systems presented the same behaviour with regarding the exergy destruction rates during charging and discharging procedures. Comparatively, among the ESSs, the hydrogen system is the one presenting higher destruction, followed by the CAES and then lithium-ion battery system. Also, seasonality plays a major role, as warmer seasons presented the higher destruction rates. Comparing the results between cities, the CAES system from Rio de Janeiro presents daily average exergy destruction rate

2.9 times the ones seen in Lyon, and both hydrogen and lithium-ion battery systems 2.7 times.

Figure 104 presents the seasonal exergy efficiency of all systems.

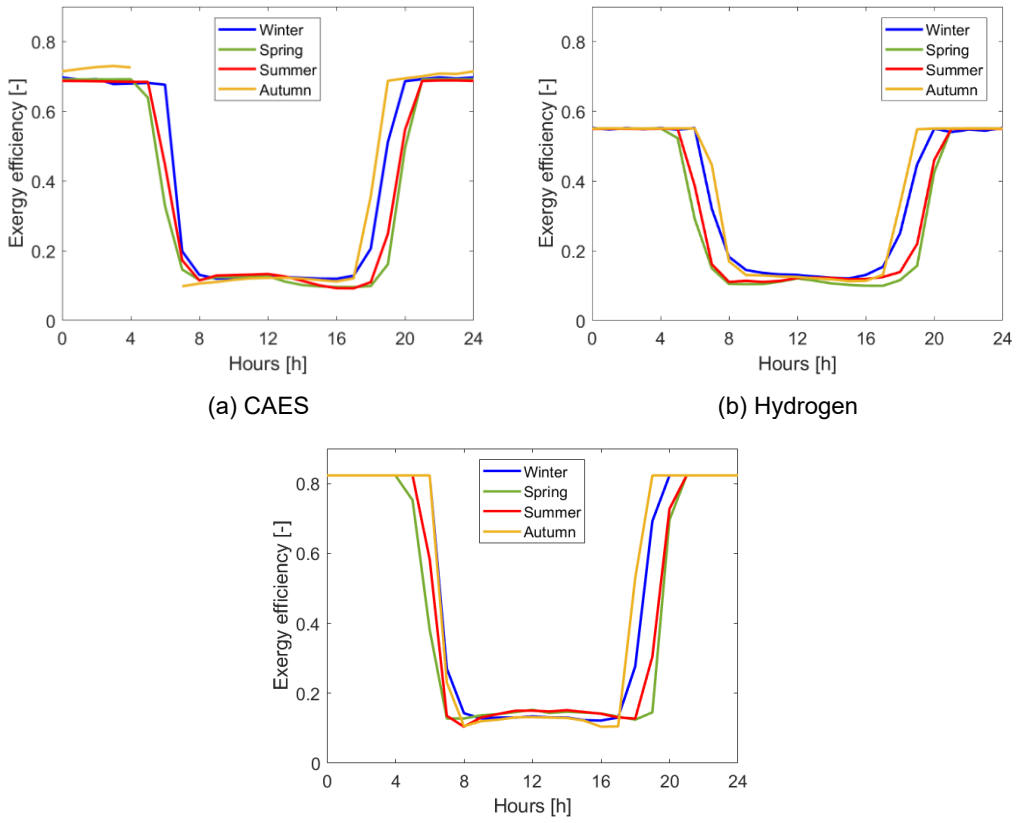

(a) CAES

(b) Hydrogen

(c) Lithium-ion battery

Figure 104: Seasonal hourly average exergy efficiency disregarding the grid - Lyon.

As shown in Figure 104, the exergy efficiency for all systems follows the same trend as their respective electrical efficiency, shown in Figure 97. During charging, the efficiency is strongly influenced by the photovoltaic panels, while during discharging, it remains stable due to the strategy of precisely matching the demand.

Table 39 presents the average exergy efficiency of each system.

Table 39: Average exergy efficiency - Lyon.

System	Winter	Spring	Summer	Autumn	Year	Seasonal max. var. [%]
CAES	40.5	35.5	36.9	39.7	38.2	7.1
Hydrogen	35.1	29.7	31.2	36.1	33.0	10.0
Battery	49.0	40.9	43.2	48.9	45.5	10.0

Mirroring the trend observed in electric efficiency, the colder months exhibit higher average exergy efficiency compared to the hotter months. The operation at lower pressures in the storage tank, for the CAES system, and extended

discharging periods contribute to the overall efficiency increase during these months for all EESs.

5.2.2.4. Exergoeconomy

Figure 105 presents the average unit cost of the main components during the charging procedure.

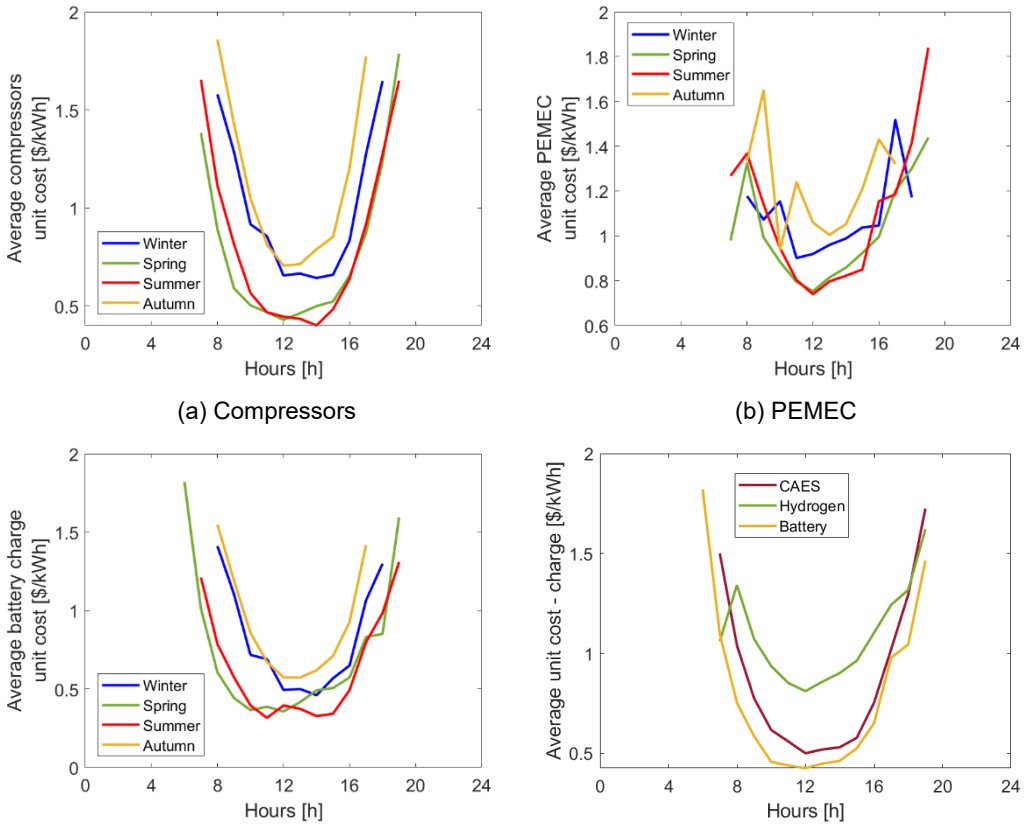

(a) Compressors

(b) PEMEC

(c) Lithium-ion battery

(d) All three – annual average

Figure 105: Seasonal hourly average charging unit cost – Lyon.

The average unit cost follows a similar trend to the Brazilian case, reaching its lowest point when solar radiation is at its peak, as more energy can be stored during this period. Consequently, the cost is lower in summer and spring compared to autumn and winter, though the difference is not significant. This pattern is consistent across all three systems. As shown in Figure 105(d), the unit costs of all systems are comparable, with the hydrogen system exhibiting overall higher values. As previously discussed, this is due to the higher capital investment required for the PEMEC compared to batteries and compressors.

Table 40 presents the average charging unit costs.

Table 40: Average charging unit cost – Lyon.

System	Winter	Spring	Summer	Autumn	Year	Seasonal max. var. [%]
CAES	1.00	0.79	0.83	1.11	0.94	18.08
Hydrogen	1.09	1.02	1.10	1.22	1.11	9.90
Battery	0.90	0.81	0.70	1.00	0.85	17.64

When comparing their annual average values, the hydrogen system has the highest charging unit cost, followed by the CAES system, and the lithium-ion battery system. Seasonally, summer and spring have the lowest unit costs across all systems, as the higher solar radiation enables energy to be stored at lower costs. Similarly to the previous case of Rio de Janeiro, CAES and lithium-ion battery systems have presented the highest values of seasonal relative variation.

Figure 106 presents the average unit cost of the stored energy vector.

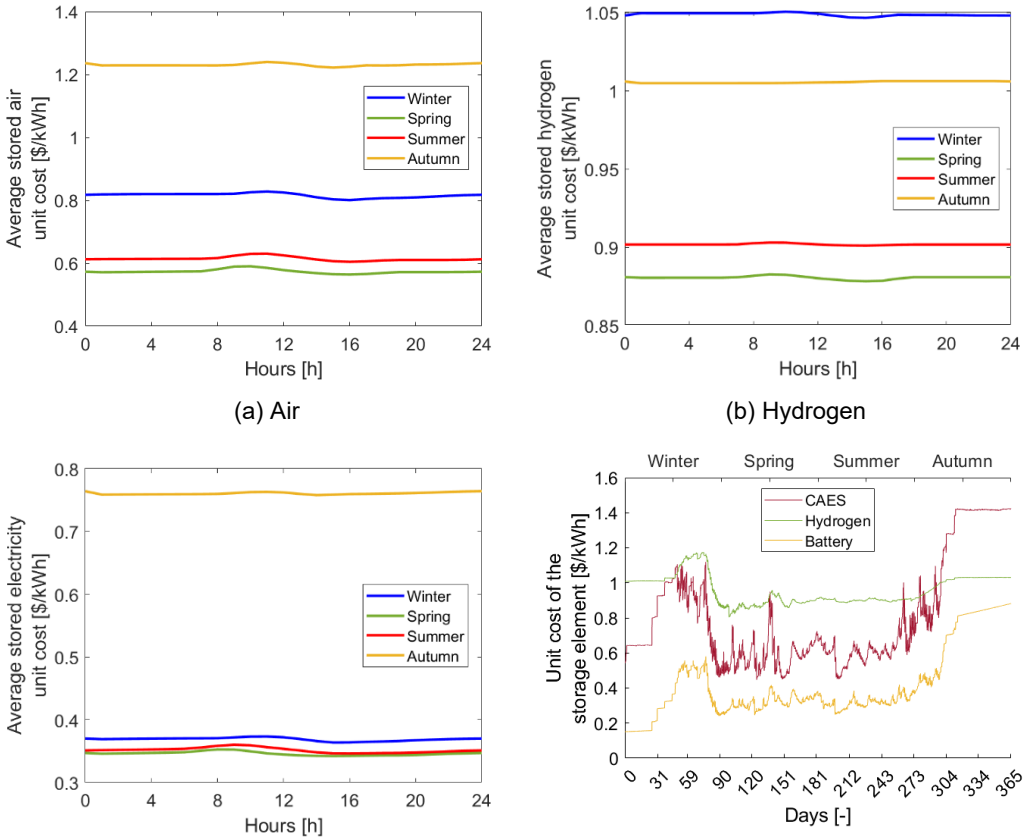

(a) Air

(b) Hydrogen

(c) Electricity withing the battery

(d) All three – daily.

Figure 106: Seasonal hourly average unit cost of the stored energy vector – Lyon.

Across all three systems, summer and spring exhibit the lowest average values for stored energy (air, hydrogen, or electricity). In contrast, the behaviour differs during winter and autumn: for the CAES and lithium-ion battery systems, the average value is higher in autumn, while for the hydrogen system, it is higher

in winter. This can be explained by examining Figure 106(d), which shows the evolution of unit costs. During winter, there is an increase in unit costs across all systems, attributed to higher operational costs due to lower solar radiation. As spring begins, all systems are able to store energy at a lower cost, reducing the average value and keeping it stable until autumn, when it begins to rise again. The increase observed by the hydrogen system is not as high as the other two systems, justifying the results observed in Figure 106(b).

Table 41 shows the seasonal average unit cost of the stored energy vector.

Table 41: Average unit cost of stored energy vector - Lyon.

System	Winter	Spring	Summer	Autumn	Year	Seasonal max. var. [%]
CAES	0.82	0.57	0.61	1.23	0.81	51.85
Hydrogen	1.05	0.88	0.90	1.00	0.96	9.37
Battery	0.33	0.32	0.32	0.71	0.42	69.05

When evaluating the average values for the three systems, electricity from the lithium-ion battery system has the lowest unit cost, followed by the air in the CAES system, and for hydrogen. These average values reflect the trends shown in Figure 106(d), with summer and spring having lower unit costs, and winter and autumn the higher ones. The maximum seasonal relative variation seen for both CAES and lithium-ion battery systems is a reflect of the behaviour seen either winter or autumn, with the sharp increase in the unit cost, furthering emphasizing the unfavourable condition to store energy.

Figure 107 presents the seasonal average unit cost of the main components during the discharging procedure, and Table 42 the corresponding average results.

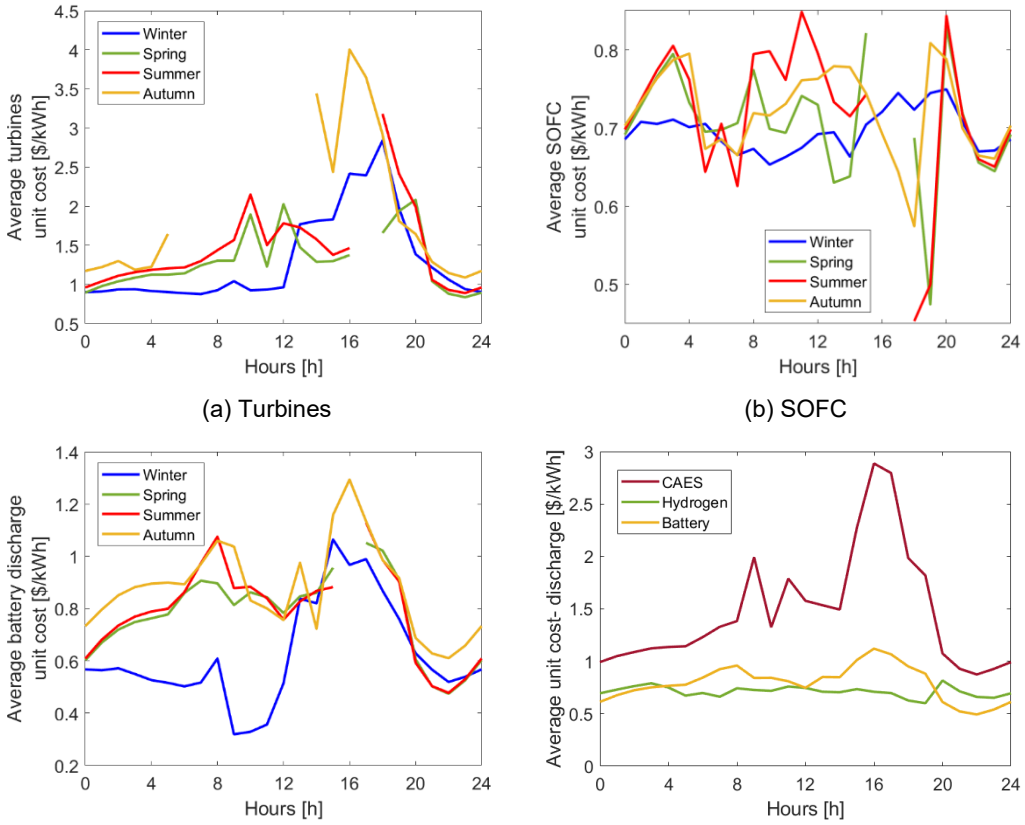

(a) Turbines

(b) SOFC

(c) Lithium-ion battery

(d) All three – annual average

Figure 107: Seasonal hourly average discharging unit cost – Lyon.

Table 42: Average discharging unit cost - Lyon.

System	Winter	Spring	Summer	Autumn	Yearly	Seasonal max. var. [%]
CAES	1.29	1.28	1.45	1.99	1.50	14.67
Hydrogen	0.70	0.71	0.72	0.72	0.71	1.45
Battery	0.54	0.67	0.69	0.76	0.67	19.40

The average unit cost during the discharge phase is mainly influenced by the unit cost of the stored energy vector (used as fuel) and the electricity demand. By observing Table 42 can be seen that autumn has the highest average values among all seasons, reflecting what was seen in Figure 106. When comparing all three systems, the CAES system has the highest average unit cost at, followed by hydrogen system, and lithium-ion battery system. Both CAES and lithium-ion battery systems exhibit high seasonal relative variations, being a consequence of the high variations seen for the stored energy vector. In contrast, as the hydrogen system mainly relies on the use of natural gas during reforming for operation, it presents more stable results throughout the year and lower unit cost. Comparing to the results from Rio de Janeiro, the price of the natural gas in France is not as expensive as the one seen in Brazil, which has one of the most expensive worldwide.

Figure 108 presents the exergoeconomic factor for all three systems.

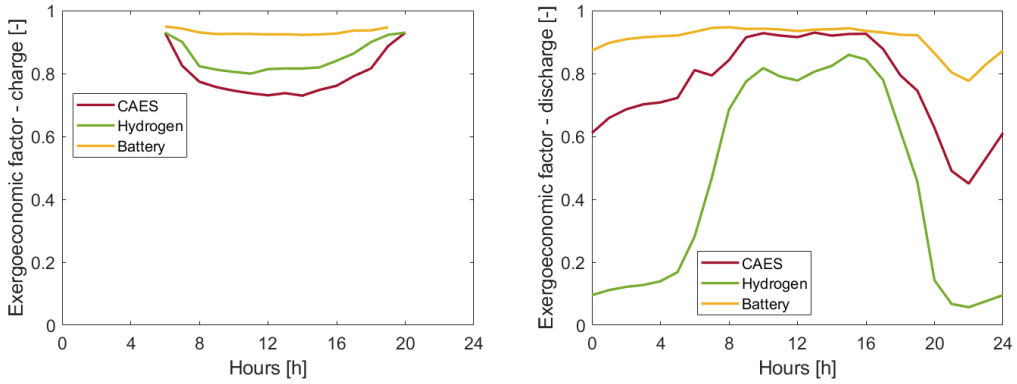

(a) Charge (b) Discharge

Figure 108: Annual hourly average exergoeconomic factor – Lyon.

The behaviour of the exergoeconomic factor is similar to that observed in Figure 83, for Rio de Janeiro. During the charging phase, as shown in Figure 108(a) all values are notably high, reflecting the significant capital cost of the system, likely due to an overestimation of the PV panel size. A similar trend is evident during the discharge phase, shown in Figure 108(b), where the value increases around midday, as less discharge is seen between 7h and 20h so the value tends to increase towards the charging values. The hydrogen system shows a decrease in the exergoeconomic factor when operating independently of the PV panels, attributed to high exergy losses.

For comparison, the average results are summarized in Table 43.

Table 43: Average exergoeconomic factor - Lyon.

System	Winter		Spring		Summer		Autumn		Year	
	Cha	Dis	Cha	Dis	Cha	Dis	Cha	Dis	Cha	Dis
CAES	0.82	0.74	0.78	0.75	0.76	0.72	0.84	0.78	0.80	0.75
Hydrogen	0.86	0.42	0.83	0.43	0.85	0.42	0.87	0.42	0.85	0.42
Battery	0.94	0.88	0.93	0.92	0.93	0.91	0.93	0.89	0.93	0.90

Cha – charging; Dis - discharging

The results in Table 43 indicate low seasonal variation in the exergoeconomic factor during both charging and discharging processes. All three systems would benefit from a reduction in capital cost investment, particularly during the charging phase, which could be achieved by downsizing the PV panels. During discharge, the hydrogen system would benefit from more efficient procedures from an exergetic perspective, while the other two systems could also focus on reducing capital costs, similar to the results in Rio de Janeiro.

Figure 109 presents the relative cost for all three systems, and Table 44 the average relative cost.

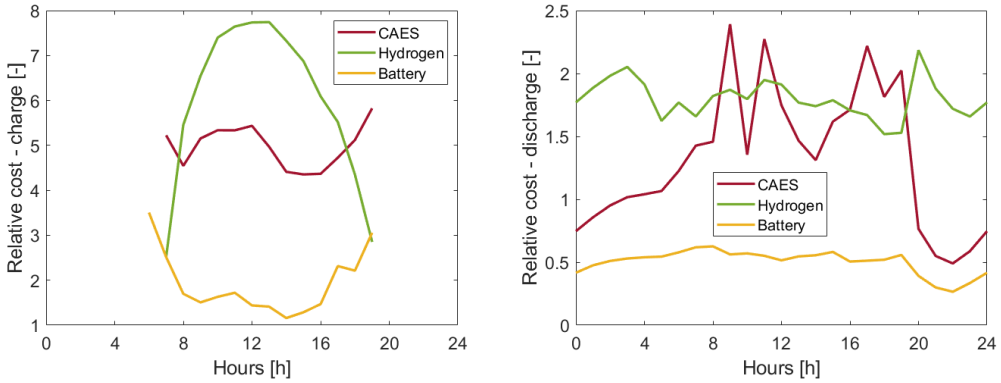

(a) All three - discharging (b) All three - charging

Figure 109: Annual hourly average relative cost – Lyon.

Table 44: Average relative cost - Lyon.

System	Winter		Spring		Summer		Autumn		Year	
	Cha	Dis	Cha	Dis	Cha	Dis	Cha	Dis	Cha	Dis
CAES	6.25	1.00	4.61	1.38	4.87	1.44	5.70	1.10	5.36	1.23
Hydrogen	5.55	1.66	6.26	1.87	6.05	1.85	5.52	1.78	5.84	1.79
Battery	3.25	0.41	1.91	0.51	1.77	0.50	2.63	0.41	2.39	0.46

Cha – charging; Dis - discharging

Each of the three systems exhibits distinct characteristics in terms of relative cost during the charging phase, Figure 109(a). The CAES system initially experiences an increase in unit cost, followed by a decline until reaching its lowest point, which coincides with peak solar radiation. This suggests that the compressors are oversized for early morning operation, leading to air storage at a higher unit cost. A similar trend is observed in the hydrogen system; however, its unit cost peaks during periods of intense solar radiation. This behaviour is attributed to the downsizing of the PEMEC—investing in a larger system would allow for greater hydrogen storage, thereby reducing the unit cost of stored energy, particularly in summer and spring, and allowing to a higher substitution of natural gas in the process. However, this approach would naturally increase overall system investment costs. In contrast, the lithium-ion battery system follows the expected pattern, with the relative cost reaching a minimum around midday. Observing Table 44, it is possible to observe the seasonal relative variations, especially for the CAES and lithium-ion battery systems, which have considerable higher values during winter and autumn, compared to summer and spring. The maximum values seen are for each system respectively of 16.6% and 36.0%. Hydrogen system experiences lower seasonal variations, maximum of 7.2%.

The discharge relative cost, Figure 109(b), for both the CAES and lithium-ion battery systems follows a similar trend, decreasing overnight and rising as the day begins due to increased electricity demand. In contrast, the hydrogen system

exhibits a different pattern, maintaining an almost constant value throughout the day, with minor peaks during the night and morning. This system presents higher values, primarily due to the expenses associated with its entire discharge chain. Additionally, the curves for the battery and hydrogen systems appear more stable throughout the year, whereas the CAES system experiences more noticeable fluctuations. Evaluating the maximum relative variation during discharge, the CAES system has the highest value of 18.7%, followed by the lithium-ion with 10.9%, and hydrogen system of 7.3%.

The results indicated by the relative cost and storage media behaviour (Figure 90) would suggest that for the case of Lyon, the system should be sized to accommodate the operation solely considering summer and spring, hence calculating its sizing and hydrogen share according to the interaction between electricity demand and PV power (Figure 29) output during these two seasons.

Figure 110 displays the operation cost of all system and the grid.

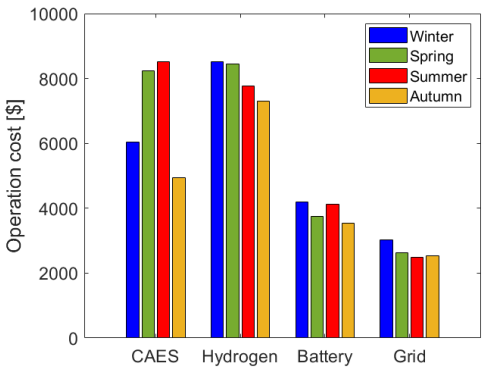

Figure 110: Seasonal operational cost - Lyon.

Figure 110 provides an estimate of the operational costs for all systems. Despite being downsized, the hydrogen system has the highest operational cost, primarily due to the expenses associated with producing, storing, and utilizing hydrogen during operation. The CAES system exhibits similar operational costs during summer and spring, even with twice the capacity of the hydrogen system. Meanwhile, the lithium-ion battery system has an operational cost comparable to the electrical grid, attributed to its simpler architecture. In terms of annual operational costs, solely operating with the grid, the result is 9,307.73$. Evaluating the same results for all systems, the hydrogen one has the highest total at 32,031.70$ (+244.1%), followed by the CAES system at 27,721.20$ (+197.8%), the lithium-ion battery system at 15,603.69$ (+67.6%). Similarly to Rio de Janeiro, both CAES and hydrogen systems presented elevated operational cost, which

would indicate the need for incentives for more cost-effective systems in order to make them competitive.

5.2.2.5. Environmental

The adaptation of the system from the Brazilian case to the French context primarily depends on the strategy for meeting heat demand. In Rio de Janeiro, heat is typically supplied by natural gas from the grid, which is not the case in Lyon. Therefore, heat pumps are considered as the auxiliary system for all three configurations. As in the previous analysis, the use of biogas instead of natural gas was also evaluated. However, this substitution is only relevant for the hydrogen system, as it relies on gas for reforming.

Figure 111 presents the CO_2 emissions avoided from the systems.

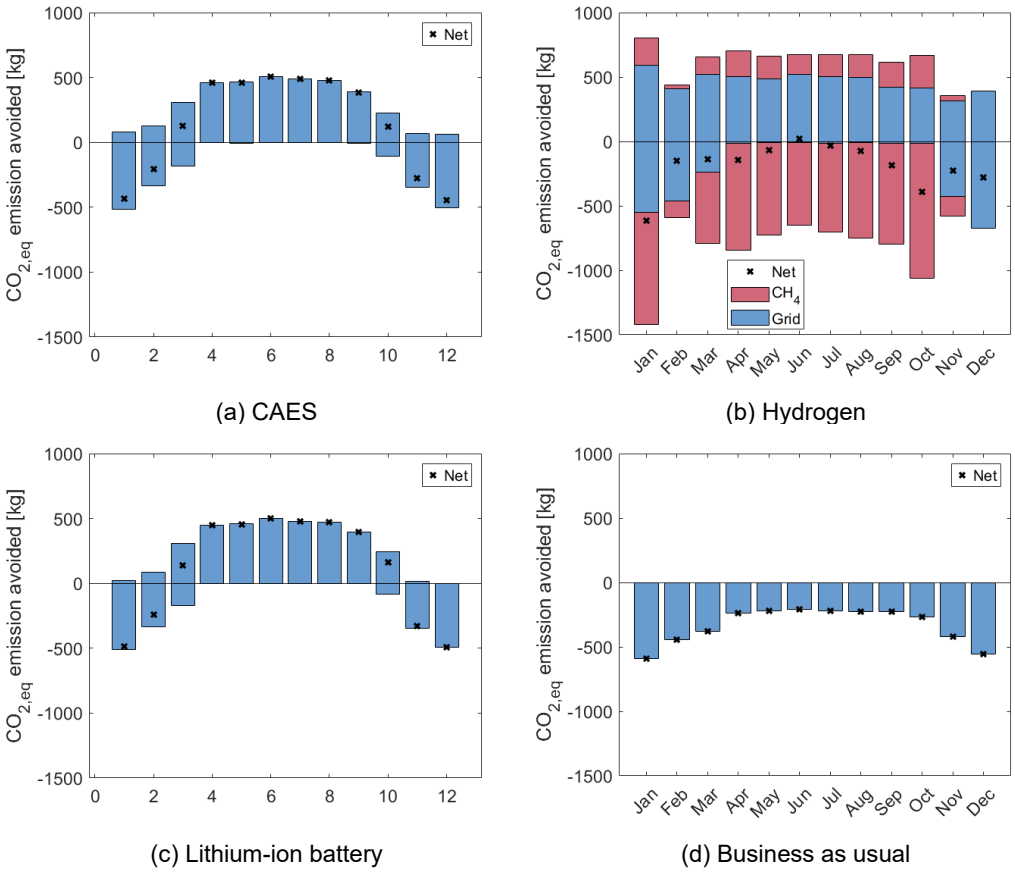

(a) CAES (b) Hydrogen

(c) Lithium-ion battery (d) Business as usual

Figure 111: Monthly CO_2 equivalent emission avoided – Lyon.

The CAES and lithium-ion battery systems exhibit a similar profile regarding CO_2 equivalent emissions avoided, Figures 111(a) and (c). Since they focus solely on electrical energy, the emissions avoided are attributed to reducing grid usage.

Both systems effectively avoid emissions during the warmer months due to their ability to meet energy demands and store surplus energy. However, during colder months, they struggle to sustain the demand and rely heavily on the grid. In contrast, the hydrogen system, Figure 111(b), performs poorly in avoiding emissions because its operation depends on natural gas. To address this issue, the share of hydrogen used during operation could be increased, or biogas could be utilized, as it has no environmental impact due to its zero emissions. Figure 111(d) presents the results from relying solely on the grid, resulting in effective emissions, especially in the colder months. It is interesting to observe across all system, the better performance in avoiding CO_2 emissions during both summer and spring, as all ESSs are capable of supplying the electricity and storing energy.

Figure 112 presents the specific CO_2 emission for all systems.

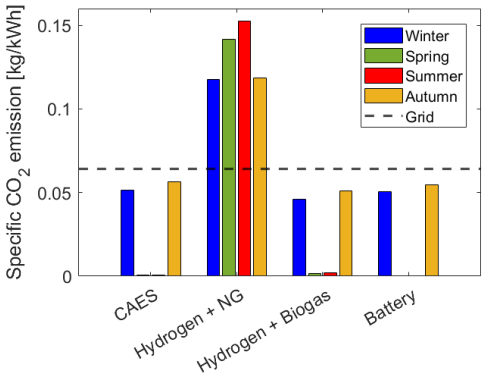

Figure 112: Seasonal average specific CO_2 emission - Lyon.

Figure 112 illustrates the specific CO_2 emissions for all systems. As expected, the CAES and lithium-ion battery systems exhibit similar results throughout the year. During winter and autumn, their specific emissions align closely with electric grid values, while in summer and spring, emissions are nearly negligible. In contrast, the hydrogen system shows significantly higher emissions compared to the other systems and the grid across all seasons due to its reliance on natural gas. It is seen that winter and autumn have lower specific emissions as the system takes advantage for suppling heat during operation. However, when natural gas is replaced with biogas, the specific emissions drop dramatically, yielding results comparable to the other two systems.

Finally, the total emissions are compared for all systems in Figure 113.

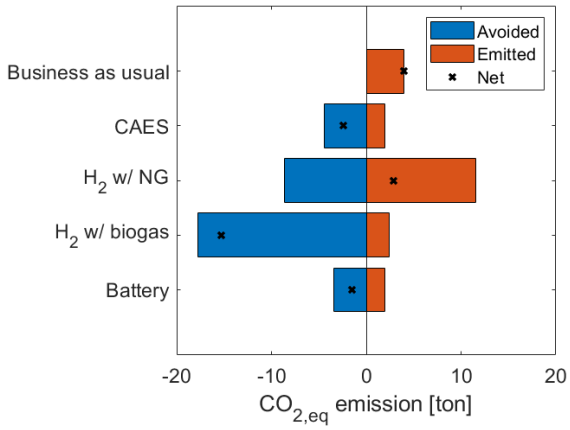

Figure 113: All three systems CO_2 equivalent emission considering one year of operation - Lyon.

Figure 113 shows the total CO_2 equivalent emissions for all systems. The CAES and lithium-ion battery systems achieved similar net emissions avoided, at 2.45 tons and 1.49 tons, respectively. In contrast, the hydrogen system, when using natural gas, resulted in a net effective emission of 2.46 tons. It is important to compare with the actual case (business as usual) of running solely on the electric grid, which has a net emission of 3.99 ton. Even though the hydrogen system is responsible for emitting CO_2, the net result is slightly lower than the current case. As previously mentioned, switching to biogas could address this issue by shifting the effective emissions to avoided emissions, resulting in a net avoided emission of 15.33 tons.

By analysing total emissions and operational costs, the cost of CO_2 avoided can be estimated for each system. Over a full year of operation, the CAES, hydrogen and lithium-ion battery systems incurred costs per CO_2 avoided of 2,859.7 $/ton, 14,793.7 $/ton and 1,148.4 $/ton, respectively. When biogas is utilized for hydrogen system, with double the cost of natural gas, the total operational cost increases to 32,732.40 $, and cost per CO_2 emission avoided severely decreases to 1,176.0 $/ton, representing a relative increase of 2.18% and decrease of 92.1% compared to the case considering natural gas, respectively. Putting the cost per CO_2 emission avoided, for all systems, the results are particularly high when considering market benchmarks (137) which show a value of 2$ per ton of CO_2 equivalent. This is primarily because the system struggles to avoid emissions throughout the year, not only due to operational challenges but also because France already has a well-established clean energy mix.

5.3. Optimization through Design of Experiments

Design of Experiments is utilized to perform a multi-variable evaluation on different parameters of the system. As discussed in Section 4.6, the Pareto Chart is utilized to rank the variables in question, and their interactions.

5.3.1. Pareto chart

All 17 cases described in Section 4.7 are simulated for both the CAES and hydrogen systems. Key parameters relevant to the analysis were selected, and the Student's t-test was applied to evaluate the interactions between variables. For the CAES system, the analysed variables include storage tank volume, PV panel area, and the number of household residents. In the hydrogen system, the considered parameters are hydrogen share, current densities of both PEMEC and SOFC, and storage tank pressure.

Tables 45 and 46 present the results of the Student's t-test for all selected parameters, accounting for linear, quadratic, and interaction coefficients as defined in Eq. (207). A threshold value determines whether an interaction is statistically significant. Values highlighted in red exceed this threshold and have a strong influence on the parameter, either enhancing or inhibiting its effect. For each parameter, the three most influential interactions are identified and ranked.

Table 45: Pareto Chart results for the CAES system.

4E	y	Variable	Mean	1L Tank Volume	1Q Tank Volume	2L PV Area	2Q PV Area	3L Householders	3Q Householders	1L by 2L	1L by 3L	2L by 3L
Energy	1	Electric efficiency (wo/ grid)	296.94	3.63	0.16	-7.06	0.18	11.68	-2.91	-4.13	4.29	3.18
	2	Electric efficiency (w/ grid)	150.00	-3.22	1.14	-20.11	2.36	24.76	0.84	-1.32	0.91	-6.34
	3	Cogeneration efficiency (wo/ grid)	335.89	-4.81	2.37	-12.37	0.64	17.63	-0.29	-0.72	-0.75	-1.90
	4	Cogeneration efficiency (w/ grid)	196.99	-3.43	1.23	-21.66	2.54	27.14	0.57	-1.54	1.07	-6.50
	5	Trigeneration efficiency (wo/ grid)	427.27	-4.21	2.15	-14.91	1.07	18.85	-1.80	-1.84	0.54	-1.03
	6	Trigeneration efficiency (w/ grid)	233.62	-3.37	1.20	-22.41	2.58	27.86	0.46	-1.77	1.39	-6.51
	7	Grid participation	39.78	-7.88	1.46	-39.26	6.25	45.09	4.91	0.67	-1.50	-19.81
Exergy	8	Exergy efficiency (wo / grid)	609.17	2.17	0.06	-2.08	-1.05	22.12	-5.31	-3.81	3.92	6.63
	9	Exergy destruction turbine	141.39	6.98	-1.79	27.21	-3.22	4.61	-4.57	2.48	-0.82	13.03
	10	Exergy destruction compressor	157.41	5.65	-1.25	26.44	-3.77	11.61	-6.11	0.48	1.35	15.90
Exergoeconomy	11	Unit cost compressor	144.08	0.04	-0.73	12.94	-0.47	-8.01	0.11	-0.42	-0.08	0.77
	12	Unit cost turbine	464.99	-11.82	7.02	13.74	3.14	-17.72	6.73	2.28	-9.12	-16.57
	13	Unit cost compressed air	69.77	-3.89	1.59	-0.16	-0.27	-0.04	0.70	1.15	-2.35	-2.05
	14	Exergoeconomic factor discharge	364.26	-5.37	0.25	-13.35	0.59	17.23	-2.38	-3.91	5.94	1.56
	15	Exergoeconomic factor charge	639.41	1.47	1.30	-2.44	2.52	-1.00	1.31	-3.15	2.94	-6.84
	16	Relative cost discharge	214.10	9.95	-2.59	3.75	-3.52	2.73	-2.55	-0.61	2.77	6.84
	17	Relative cost charge	450.71	6.66	-1.93	-37.64	3.99	24.23	3.95	3.55	-4.51	-10.47
	18	Operational cost	254.96	9.67	-1.23	28.58	-3.97	23.71	-5.98	2.23	-1.40	15.38
Environment	19	CO_2 emission avoided	250.35	4.88	-0.94	84.41	-5.25	-25.83	-7.64	0.83	0.54	20.97
	20	Cost of CO_2 avoided	825.66	28.28	-5.86	-11.04	-13.81	121.24	-16.30	4.07	-6.52	14.46

1st - Gold	2nd - Silver	3rd - Bronze	Significant

Table 46: Pareto Chart results for the hydrogen system.

4 E	y	Variable	Mean	1L Hydrogen Share	1Q Hydrogen Share	2L Current Density	2Q Current Density	3L Tank Pressure	3Q Tank Pressure	1L by 2L	1L by 3L	2L by 3L
Energy	1	Electric efficiency (wo/ grid)	5963.97	-13.16	-7.16	-68.20	1.09	1.79	-0.13	10.73	2.51	-0.51
	2	Electric efficiency (w/ grid)	747.58	58.01	23.65	-22.72	3.30	-2.89	-1.31	-11.45	-1.75	-0.50
	3	Cogeneration efficiency (wo/ grid)	3704.71	-18.56	-4.25	-21.15	0.85	0.60	0.59	8.34	1.09	-0.20
	4	Cogeneration efficiency (w/ grid)	970.15	60.26	24.92	-24.34	3.38	-3.10	-1.19	-12.12	-1.92	-0.47
	5	Trigeneration efficiency (wo/ grid)	4696.31	-35.78	-9.74	-45.25	0.62	1.86	0.50	11.00	1.81	-0.26
	6	Trigeneration efficiency (w/ grid)	2325.62	52.26	23.22	-40.32	3.21	-2.71	-1.11	-9.11	-1.57	-0.54
	7	Grid participation	38.71	62.27	25.95	-14.66	3.31	-4.19	-0.61	-13.19	-3.01	-0.36
Exergy	8	Exergy efficiency (wo/ grid)	4994.47	-76.55	-4.85	43.55	-2.86	-1.39	0.46	4.61	2.13	-0.26
	9	Exergy destruction SOFC	409.90	-18.56	-12.54	-105.61	-3.12	1.95	0.25	12.84	1.43	-0.17
	10	Exergy destruction PEMEC	307.50	47.15	-13.95	-29.77	2.60	0.00	-0.19	4.23	-0.01	0.22
Exergoeconomy	11	Unit cost PEMEC	731.22	-23.62	3.83	-68.97	6.81	-1.43	0.90	3.54	1.44	0.66
	12	Unit cost SOFC	1652.77	51.85	0.07	-168.54	13.02	5.43	-0.06	-8.55	0.65	-0.39
	13	Unit cost stored H_2	637.10	-12.01	3.06	-44.77	5.66	3.65	0.69	3.01	0.20	-1.38
	14	Exergoeconomic factor discharge	543.81	39.18	21.74	-15.16	1.45	-3.55	-0.36	-7.79	-1.52	0.21
	15	Exergoeconomic factor charge	2920.93	-24.87	13.24	18.77	-1.28	-5.44	-0.38	-6.91	0.73	0.53
	16	Relative cost discharge	1403.28	-136.84	8.72	-38.51	-0.03	-6.01	0.62	1.01	-0.95	0.41
	17	Relative cost charge	331.96	0.34	2.08	-49.34	-5.42	-1.91	0.33	6.12	1.28	-0.19
	18	Operational cost w/ natural gas	588.01	27.64	-20.45	-33.69	1.29	3.24	0.26	9.43	0.81	-0.01
	19	Operational cost w/ biogas (x2)	597.59	30.99	-19.98	-35.18	1.30	3.09	0.25	9.33	0.73	-0.03
	20	Operational cost w/ biogas (/2)	586.01	26.06	-20.78	-33.09	1.29	3.34	0.28	9.52	0.86	-0.01
Environmental	21	CO_2 emission avoided w/ natural gas	791.62	143.09	-19.56	7.66	-1.13	3.33	-0.51	9.68	2.62	0.38
	22	Cost of CO_2 avoided w/ natural gas	1390.40	-3.80	-76.87	-87.39	7.53	6.21	1.88	25.12	0.54	-0.19
	23	Cost of CO_2 avoided w/ biogas (x2)	605.40	52.42	-22.25	-44.80	5.59	1.89	0.11	4.40	-0.22	-0.14
	24	Cost of CO_2 avoided w/ biogas (/2)	565.30	44.99	-23.97	-40.98	5.28	2.14	0.15	4.84	0.00	-0.11
	25	CO_2 emission avoided w/ biogas	1033.84	-60.18	-25.77	23.66	-3.73	3.87	0.69	12.13	2.86	0.39

1st - Gold	2nd - Silver	3rd - Bronze	Significant

It is hard to have a grasp on which variable is more significant on the overall system. The ranking system gives a qualitative idea on which parameter have a higher impact on the evaluated parameters. By observing Table 45, the number of habitants and the PV area are the most significant variables, including their interaction. Both variables are directly related to the interaction between electric demand and the power output from the PV panels that rules the system, Figure 25. Table 46, for the hydrogen system, describes that the hydrogen share, current density, and their interaction are the most significant parameters. Both variables

are directly related to the operation of both SOFC and PEMEC, in other words, the amount of hydrogen being produced, consumed and withdrawn from the storage tank. It is interesting to observe that in both systems, the variable related to the storage tank is not as significant as the other two.

To evaluate the robustness of the models, the coefficient of determination R^2 and adjusted R^2 are evaluated in Figures 114 and 115.

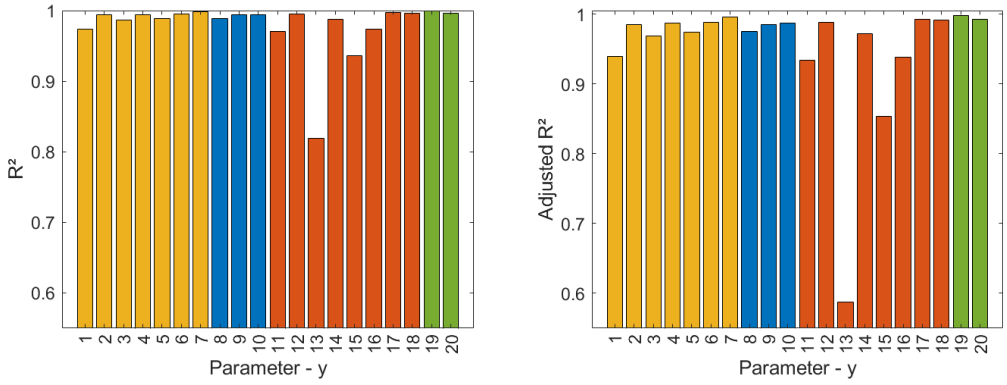

(a) R^2 (b) Adjusted R^2

Figure 114: CAES system model robustness.

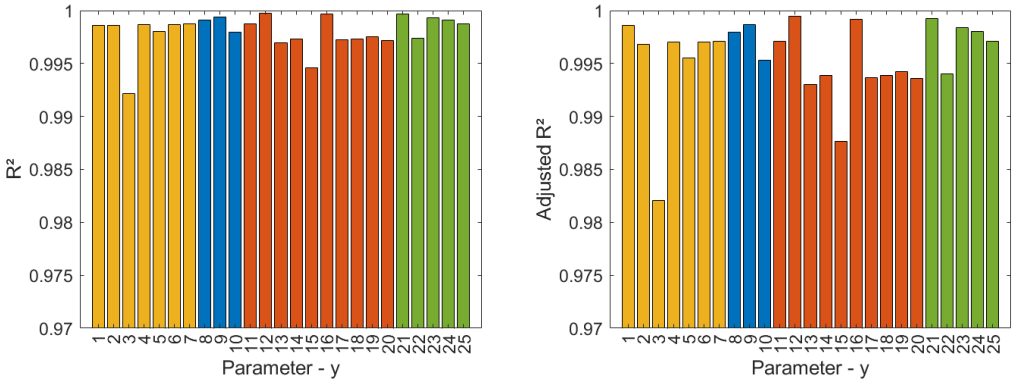

(a) R^2 (b) Adjusted R^2

Figure 115: Hydrogen system model robustness.

R^2 is a statistical metric that quantifies the proportion of variance in the dependent variable explained by the independent variables in a regression model. Adjusted R^2 is a refined version that accounts for the number of predictors, making it a more reliable measure of the model's goodness of fit. By observing Figure 114, it is clear that the model is robust enough to represent the physics of the system, with almost all R^2 close to unity, having only the unit cost of the stored air (parameter 13) to have a decrease value of 0.81. This result is significantly reduced when evaluating the adjusted R^2, as well as of the result for the charging exergoeconomic factor. Figure 115 display the results for the hydrogen system, and the results that the model have an even better performance, having the worst

result for cogeneration efficiency disregarding the grid (parameter 3) with a R^2 adjusted of 0.98.

5.3.2. Response surfaces

This section displays the response surfaces of some parameters presented in Tables 45 and 46. To do so, two of the three variables are chosen for the evaluation and third one remains at the middle level, as shown in Section 4.6.

5.3.2.1. CAES system

As a reminder, this section examines three key variables: storage tank volume, PV area, and the number of inhabitants in the building. By selecting the PV area and the number of inhabitants, it is possible to assess the interaction between PV power output and the system's electricity demand, as well as the overall sizing of charging and discharging chain. Additionally, the storage volume plays a crucial role in evaluating system sizing, and its impact on the final cost, and the emissions avoided by reducing reliance on the grid. As a reminder for the middle levels, the PV area corresponds to 429 m^2, storage tank volume of 39 m^3, and the number of householders of 48.

Figure 116 presents the results for the trigeneration efficiency.

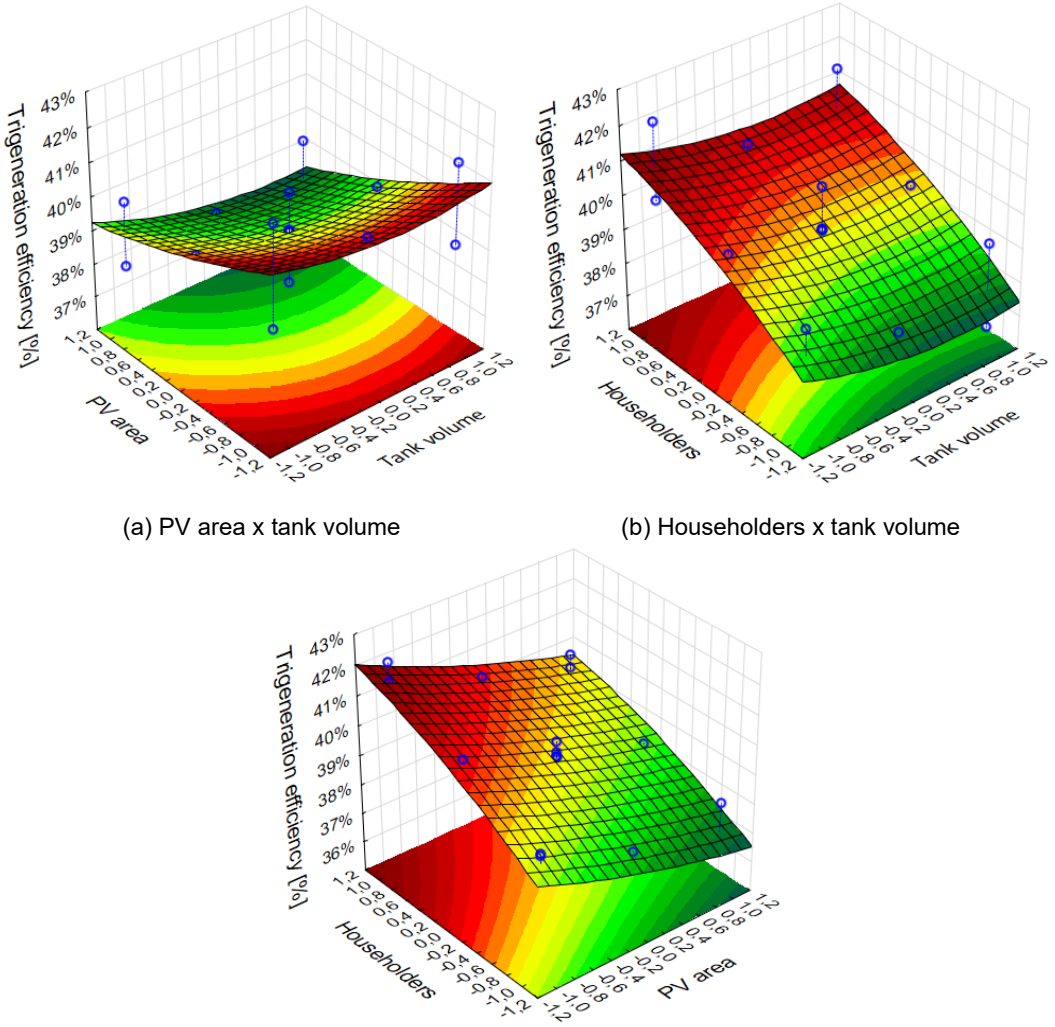

(a) PV area x tank volume

(b) Householders x tank volume

(c) Householders x PV area

Figure 116: Trigeneration efficiency – Rio de Janeiro.

All three variables under consideration influence the trigeneration efficiency, with the tank volume having the least impact, as shown in Figures 116(a) and (b). This observation aligns with the Pareto chart findings (Table 45). Additionally, the number of householders has a slightly greater effect than the PV area on the results. An increase in electric demand enables the system to operate with tanks at lower pressures, while an increase in PV area enhances its contribution to the system's energy management. However, this also reduces the overall efficiency by aligning it with the PV system's efficiency and promoting operation at higher pressures.

Figure 117 demonstrate the effect of both PV area and number of householder on the grid share of the system.

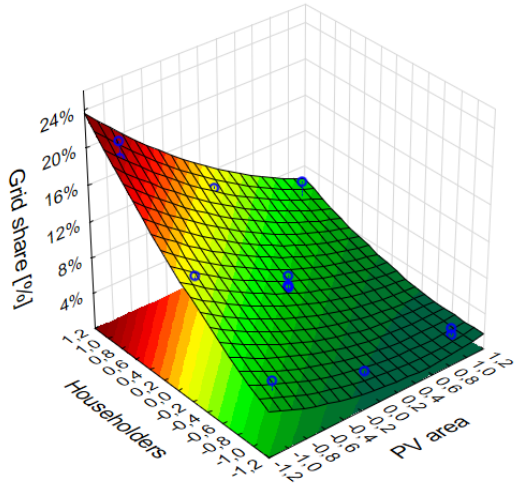

Figure 117: Electricity from grid share as a function of PV area and number of householders – Rio de Janeiro.

As electric demand increases, the system struggles in supplying it for prolonged times, finding itself mostly depleted and relying more on the electric grid to supply any demand. The PV panels heavily contribute to the grid participation, as they are responsible for the storage tanks status. A higher amount of PV panels is able to maintain the pressure levels of storage tanks higher, and so decreasing the reliance on the electric grid, while a smaller PV area would result in a higher dependency of the grid.

As shown in Figure 114, the average unit cost of stored air displayed the lowest R^2 and adjusted R^2 values, indicating that the interpretation of the results requires complementary investigation to be considered reliable. However, since the unit cost of the turbines depends on this value, it was decided to discuss the observed trend.

Figure 118 presents the unit cost of the stored air.

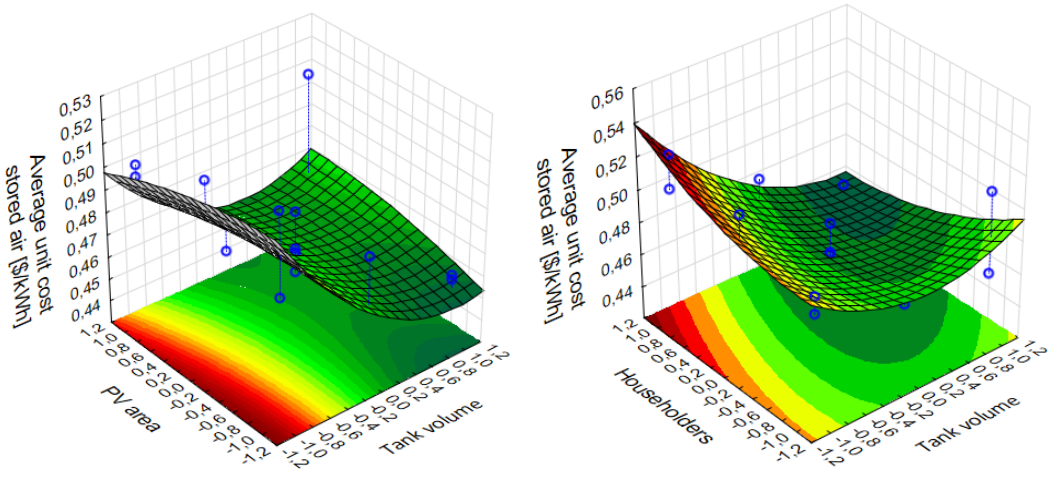

(a) PV area x tank volume

(b) Number of householders x tank volume

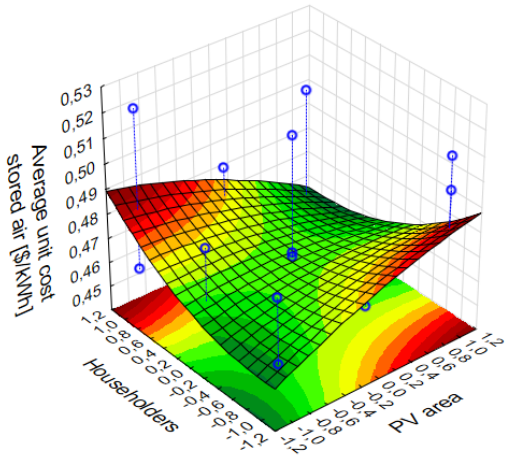

(c) Number of householders x PV area

Figure 118: Stored air unit cost – Rio de Janeiro.

Increasing the storage tank volume, while raising operational costs, also enhances air storage capacity, potentially lowering the unit cost of stored air. This behaviour suggests the existence of an optimal storage volume under the given conditions, as illustrated in Figures 118(a) and (b), where a minimum value may emerge under certain conditions. Figure 118(c) highlights an intriguing trend featuring a saddle point: operating at either the minimum or maximum levels of both PV area and household occupancy leads to a reduction in the unit cost of stored air. A higher demand, supported by a larger PV area, results in lower unit storage costs despite the increased sizing of all components. Conversely, when one factor (household occupancy or PV area) is at its maximum while the other is at its minimum, the unit cost of stored air peaks. Operating at either extreme lead to system upscaling, which is not effectively balanced by the minimal counterpart in the charge/discharge chain. This highlights that system sizing adjustments should be made holistically rather than through isolated changes.

Figure 119 illustrates the average unit cost for both compressors and turbines.

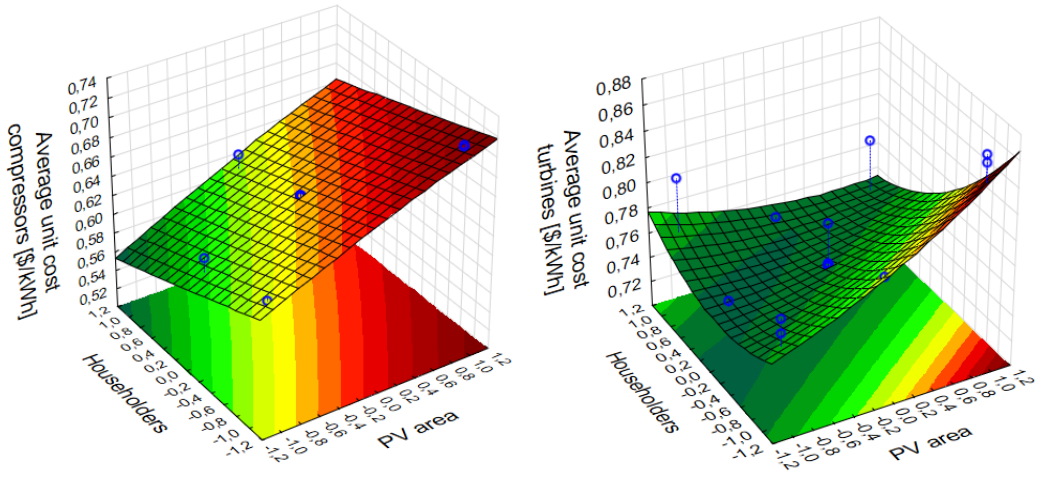

(a) Compressors (b) Turbines

Figure 119: Average unit cost as a function of PV area and number of householders – Rio de Janeiro.

The unit cost of the compressors, shown in Figure 119(a), follows the decrease of PV area, as its values is a direct consequence of the unit cost associated with their power output. Decreasing its size also decreases the capital cost associated with it and possibly have a lower cost operation. The variables related to the number of householders and tank volume have minimal impact on these results. The turbines, Figure 119(b), exhibit more complex behaviour, influenced by the unit cost of the stored air. The PV area significantly impacts the unit cost of the stored air, as expected from the compressor results, and consequently the one for the turbines. The increase of electric demand would decrease the unit cost of turbines operation, meeting its favourable condition, as seen in Figure 82. However, it can at some conditions experience an increase due to the cost of the stored air, Figure 118(c).

Figure 120 presents the operational cost of the system.

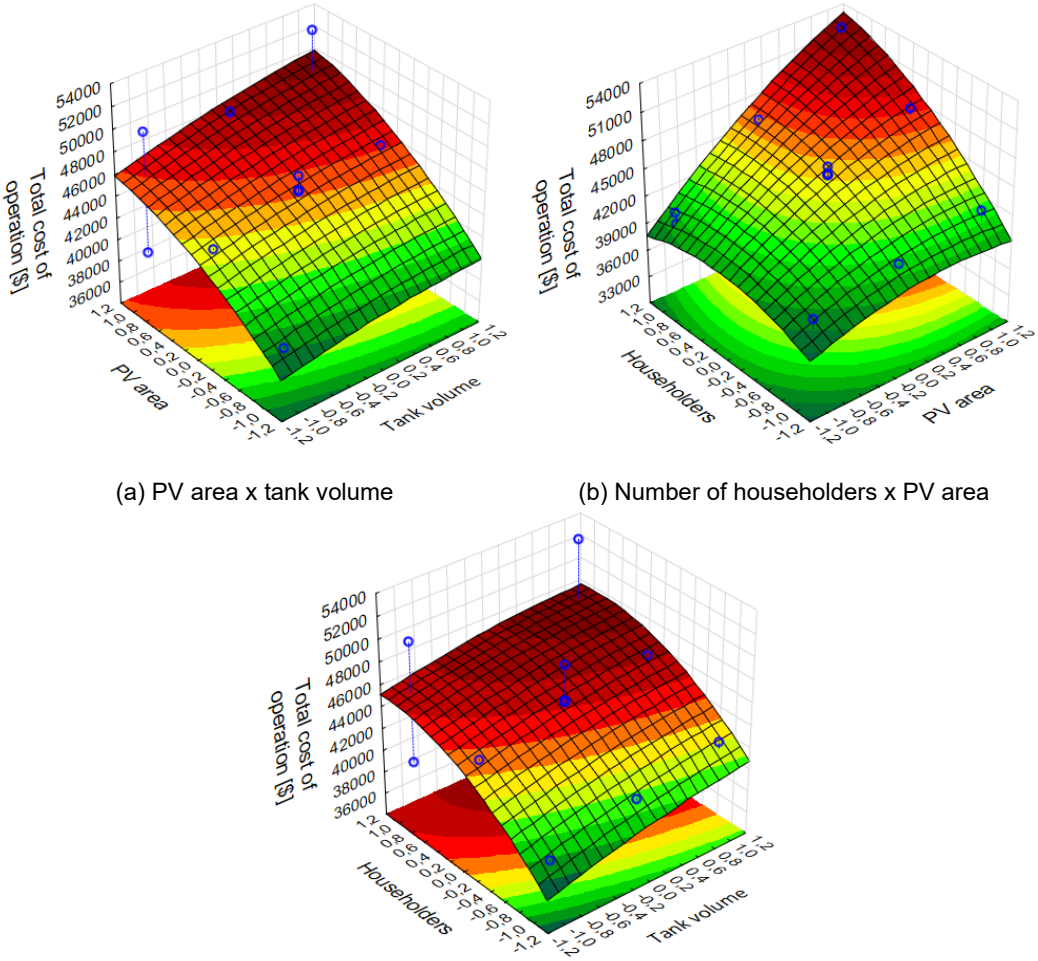

(a) PV area x tank volume

(b) Number of householders x PV area

(c) Number of householders x tank volume

Figure 120: Operational cost – Rio de Janeiro.

The PV area has a significantly greater impact on the system's operational cost compared to the tank volume or the number of householders. This suggests the potential for downsizing the system; however, doing so would increase reliance on the grid. As anticipated, an increase in the number of householders (and thus electrical demand) leads to higher operational costs. Interestingly, even a minimal PV area can accommodate the rise in electricity demand. While storage sizing also influences operational costs, its impact is less pronounced. It is also worth noting that a decrease in the demand (number of householders) the system is able to sell more energy back to the grid, decreasing the cost of operation.

Figure 121 presents both the CO_2 equivalent emissions avoided, and the cost of avoided CO_2 emission.

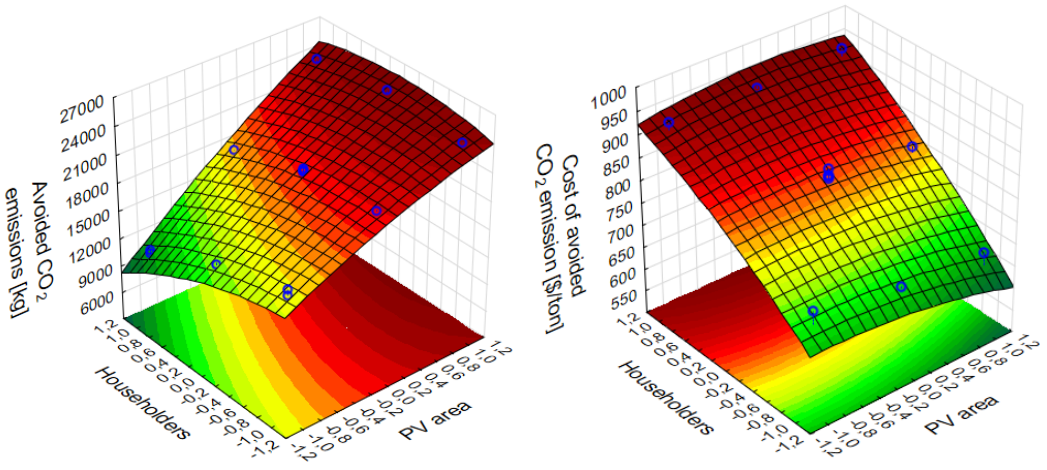

(a) Avoided CO_2 emissions (b) Cost of avoided CO_2 emission

Figure 121: CAES system environmental parameters as a function of PV area and number of householders – Rio de Janeiro.

The PV area plays the most significant role in reducing CO_2 emissions, as PV panels help minimize the grid's impact on the system. There is a clear interaction between PV panels and electric demand. Under all conditions, PV panels contribute to increased CO_2 avoidance. However, when at its minimum, it cannot support higher electric demand, leading to fewer emissions avoided. Conversely, when the PV area is at its maximum, it can sustain higher electric demand, resulting in greater emissions avoidance. The results in Figure 121(b) indicate that the PV area has a minimal impact on the cost of avoided CO_2 emissions. As observed earlier, an increase in PV area leads to both higher emissions avoidance and increased operational costs. A similar trend is evident for smaller PV areas, suggesting a balance between these effects. However, a reduction in electricity demand allows more energy to be exported to the grid, lowering operational costs. Conversely, greater reliance on the grid leads to higher emissions.

5.3.2.2. Hydrogen system

For the hydrogen system evaluation, three different variables were selected: hydrogen share, current density and storage tank's pressure. By selecting all these variables, it is possible to focus on the analysis of hydrogen generation and consumption to supply the system.

Figure 122 presents the trigeneration efficiency for the hydrogen system.

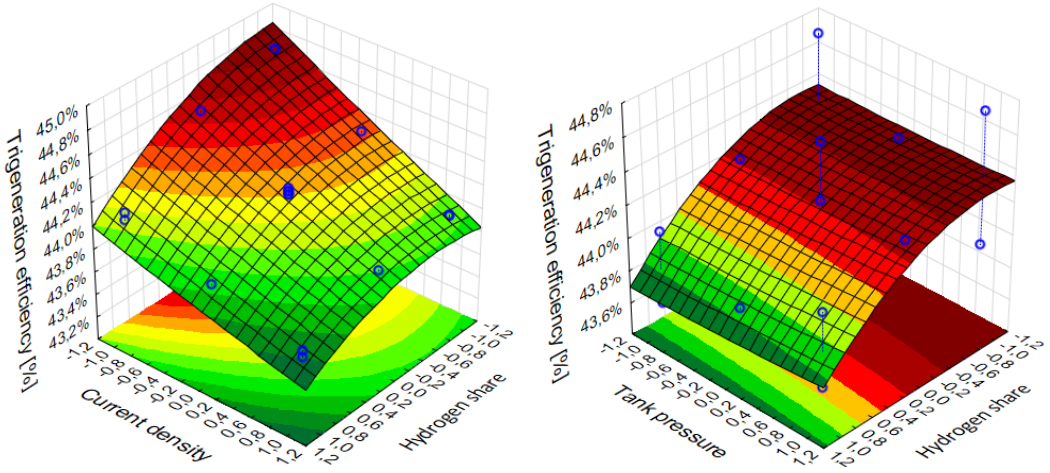

(a) Current density x hydrogen share (b) Tank pressure x hydrogen share

Figure 122: Trigeneration efficiency – Rio de Janeiro.

The hydrogen share and current density are the key factors influencing trigeneration efficiency, as illustrated in Figure 122, and expected in Table 46. However, when analyzing the different levels of the hydrogen system, it becomes evident that variations in either current density or hydrogen share have minimal effects on trigeneration performance (less than 2%). The impact of the storage tank is even less significant. This indicates that the inflow and outflow of hydrogen within the system have little influence on the overall efficiency in meeting demand.

Figure 123 display the electric grid participation in supplying its demand.

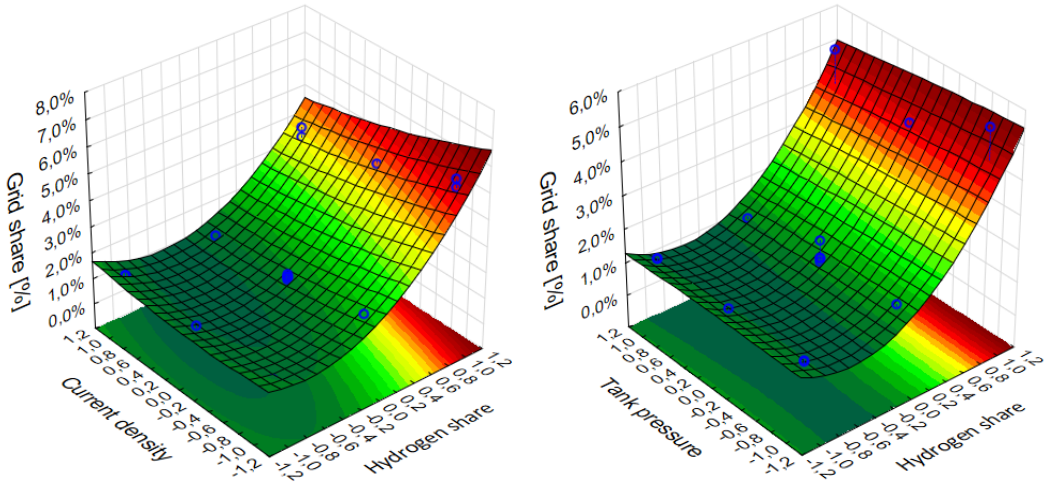

(a) Current density x hydrogen share (b) Tank pressure x hydrogen share

Figure 123: Electricity from grid share – Rio de Janeiro.

The grid's participation exhibits a complex behaviour, appearing to reach a minimum value at certain points. Increasing the amount of hydrogen withdrawn from the storage tank leads to its rapid depletion, thereby increasing reliance on

the grid. Meanwhile, current density affects the system by either increasing hydrogen generation or consumption. At low hydrogen shares, grid reliance slightly increases with higher current density, whereas the opposite trend is observed at high hydrogen shares.

Figure 124 presents the average unit cost of the PEMEC, stored hydrogen and SOFC.

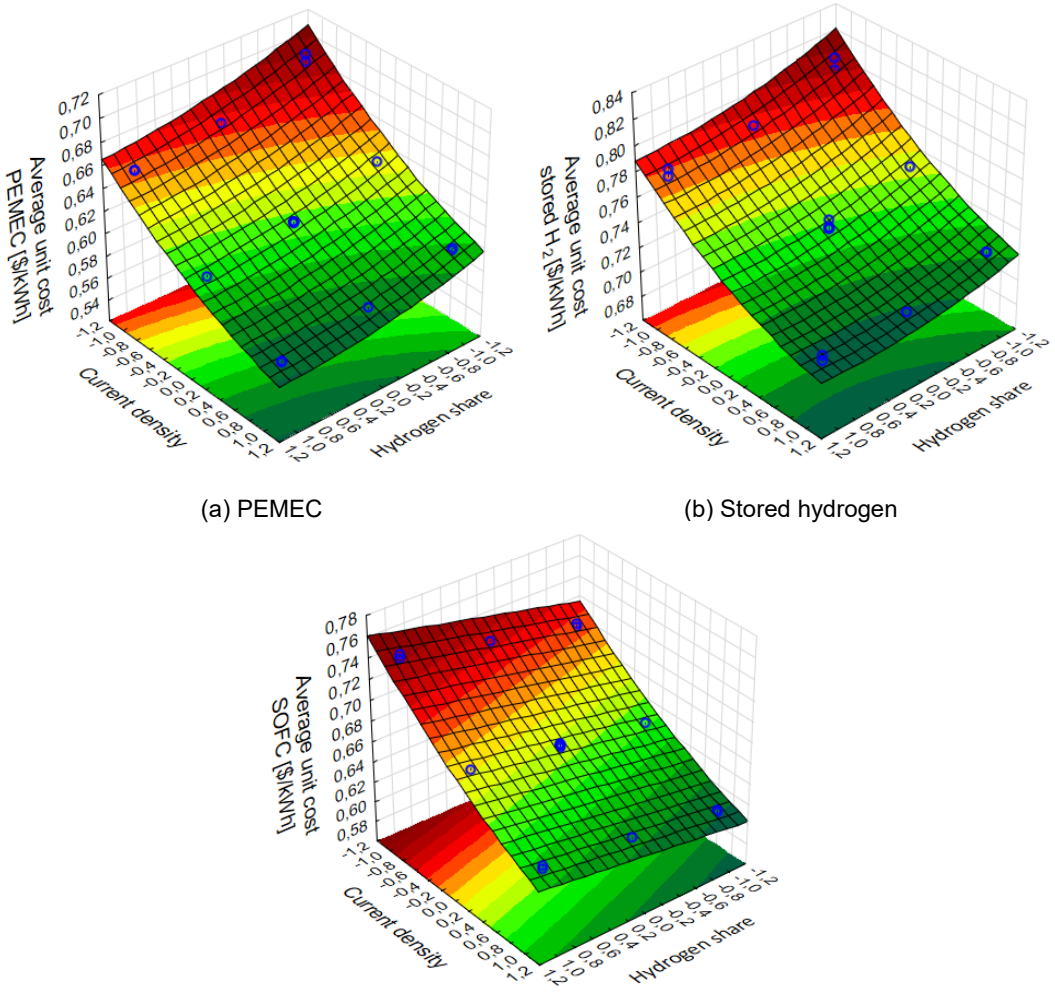

(a) PEMEC

(b) Stored hydrogen

(c) SOFC

Figure 124: Average unit cost as a function of current density and hydrogen share – Rio de Janeiro.

As verified in Table 46, tank pressure has a minor impact on the results, while current density and hydrogen share play the most significant roles. Regarding the PEMEC, Figure 124(a), operating at higher current densities enables greater hydrogen production, thereby reducing its average unit cost by storing more energy in the process. Combined with the increased utilization of hydrogen from the storage tank, this allows for storing lower-cost hydrogen during operation. This directly affects the results for stored hydrogen, which exhibit a similar trend, as

shown in Figure 124(b). The SOFC follows a different trend than the PEMEC in terms of hydrogen share, Figure 124(c). The unit cost decreases slightly with this variable, as it indicates a higher use of natural gas, which is less expensive than hydrogen. Increasing the current density enables the SOFC to operate at higher power levels, thereby reducing its unit operating cost. In both Figures 124(a) and (c), the increase of current density allows to have a smaller number of stacks for electrolyzer and fuel cell, decreasing the unit cost during the process.

The parameters related to environmental analysis and operational cost considering the use of natural gas are show in Figure 125.

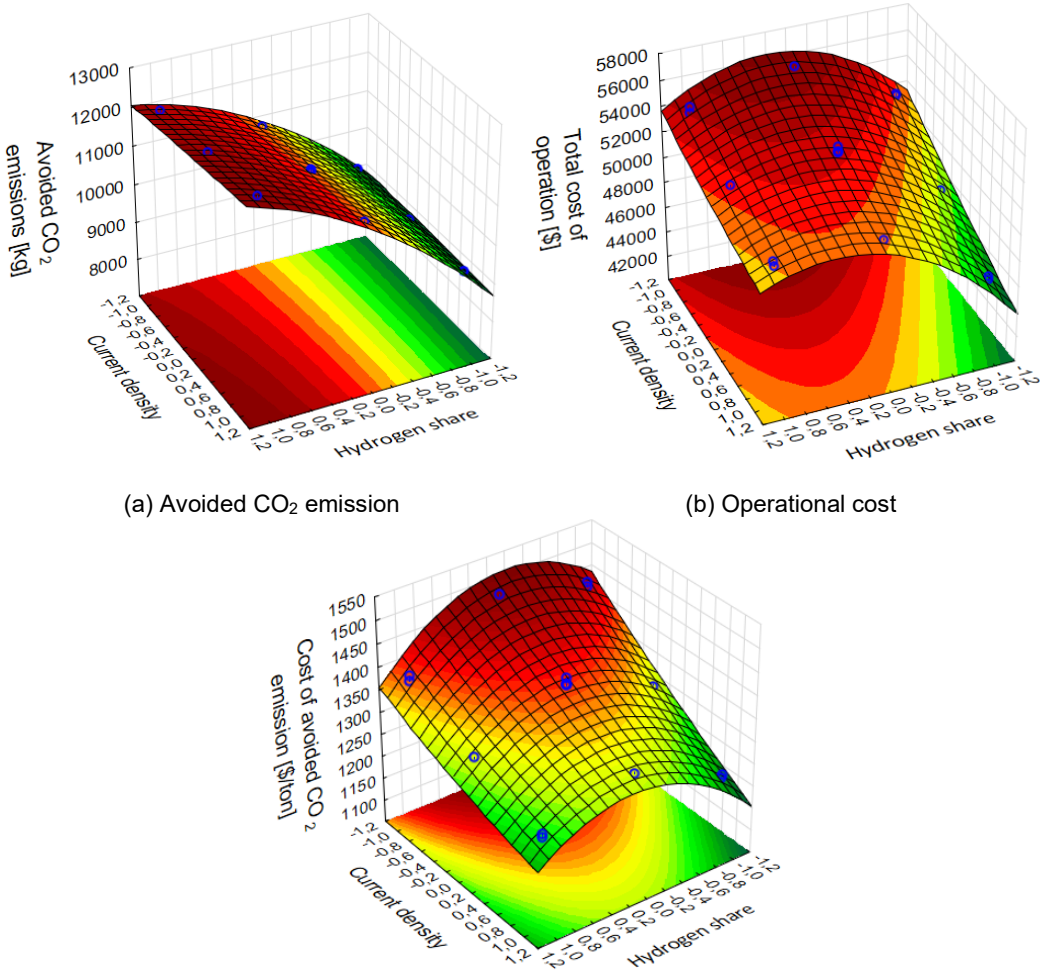

(a) Avoided CO_2 emission

(b) Operational cost

(c) Cost of avoided CO_2 emission

Figure 125: Hydrogen system economic and environmental parameters as a function of current density and hydrogen share using natural gas – Rio de Janeiro.

The avoided CO_2 equivalent emissions are significantly influenced by the hydrogen share. The greater the hydrogen usage, the more CO_2 equivalent emissions are avoided due to the substitution of natural gas. In comparison, current density and tank pressure have a less significant impact on this parameter. The

cost of operation is primarily influenced by the hydrogen share, which interestingly follows a parabolic trend, having its lowest value at lower hydrogen shares. This is due to the increased reliance on natural gas from the grid, which has lower cost than the hydrogen generated through the charging process. The costs reductions associated with the increase of this parameter, is a reflect on a higher reliance on the electric grid, which offers lowers costs associated. Additionally, higher current density reduces the cost associated with stored hydrogen, thereby lowering the overall operational cost, as well as potentializing the use of the system to store and utilized energy. When combining both findings in Figure 125(c), it is possible to visualize a parabolic behaviour suggesting a worst scenario. Having the condition set of maximizing the use of the system (higher levels), an increased avoidance of emission is accompanied by a moderate operational cost resulting in a lower cost of avoided CO_2 emission, while the opposite condition offers increase values for such a parameter.

Figure 126 displays the total cost, the amount of CO_2 emissions avoided, and the cost per avoided CO_2 emissions when biogas is considered.

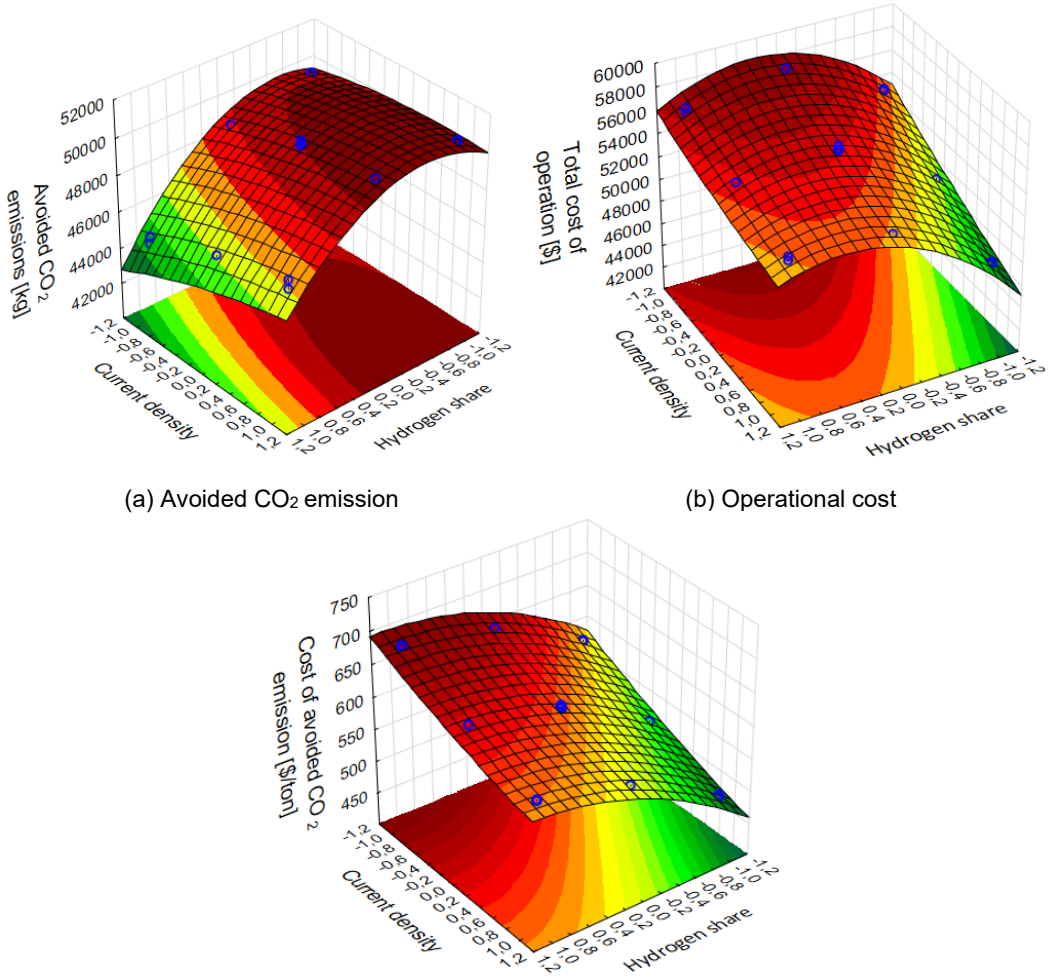

(a) Avoided CO_2 emission

(b) Operational cost

(c) Cost of avoided CO_2 emission

Figure 126: Hydrogen system economic and environmental parameters as a function of current density and hydrogen share using biogas double the price of natural gas – Rio de Janeiro.

It is interesting to note the differences in results between Figure 125 and 126 when transitioning from natural gas to biogas. Relying less on stored hydrogen while using more biogas leads to greater CO_2 avoidance, as shown in Figure 126(a). Additionally, since biogas is a more cost-effective option compared to hydrogen, this operating condition results in lower operational costs, as depicted in Figure 126(b). Conversely, when stored hydrogen has a larger share in the system, CO_2 avoidance decreases because the storage tanks deplete more quickly, leading to greater reliance on the electric grid and reduced biogas consumption, as seen in Figure 126(a). This, in turn, slightly lowers operational costs, as shown in Figure 126(b). Both Figures 126(a) and (b) suggest the presence of an optimal point when varying the hydrogen share, which is attributed to the interaction between the ESS and the electric grid. While current density has a lesser impact on the evaluated parameters, a higher current density is clearly

beneficial in terms of operational costs. Lastly, the cost-effectiveness of CO_2 avoidance improves when more biogas is utilized (less stored hydrogen), as illustrated in Figure 126(c). Despite biogas' higher decarbonization potential, these results highlight the limitations of relying solely on generated hydrogen. A complete transition from natural gas to biogas is not considered feasible due to high demand, making green hydrogen a flexible and complementary energy source.

5.4. Chapter conclusion

This chapter presents the results for all three systems in the cities of Rio de Janeiro and Lyon. All systems presented similar behaviour concerning both charging and discharging procedures. When applied to Rio de Janeiro, they operated continuously throughout the year, as the city located in the southern hemisphere experiences moderate solar radiation in autumn and winter and strong solar radiation in spring and summer. In this context, PV panels emerged as the key component of the systems, supplying electricity during the day and storing excess energy in tanks or batteries. Their integration with storage systems significantly reduced dependence on the electric grid, leading to a substantial reduction in CO_2 equivalent emissions. Emissions avoidance were further improved by considering the utilization of biogas. Both CAES and hydrogen systems demonstrated the capability to meet all three energy demands—electricity, heating, and cooling. The CAES system showed higher electric and cogeneration efficiencies than the hydrogen system, which, however, demonstrated superior trigeneration efficiency due to its more effective use of hot exhaust gases.

The exergoeconomic analysis enabled a comparison of all three systems from a financial perspective. Despite system downsizing, the hydrogen system had the highest operational costs, highlighting the economic challenges associated with its components. In contrast, the lithium-ion battery system exhibited the lowest costs. Additionally, the exergoeconomic factor, particularly during the charging phase, was relatively high across all systems, indicating that capital costs—especially for PV panels—should be reduced to improve overall cost efficiency.

When applied in Lyon, the system encountered significant challenges. The low solar radiation during autumn and winter severely limited energy storage capacity, making the system heavily dependent on the electric grid. As a result, meeting heat demand during these months was unfeasible, particularly for the

CAES and lithium-ion battery systems. During warmer seasons, both the CAES and hydrogen systems showed potential for supplying cooling demands. The application of the ESSs presented the potential to diminish CO_2 emissions by avoiding the reliance on the electric grid.

When comparing both cities, both systems operate more efficiently in Rio de Janeiro than in Lyon. In both locations, the CAES system demonstrates higher efficiency in both electric and cogeneration performance. However, the hydrogen system achieves better trigeneration efficiency by utilizing hot exhaust gases for providing cooling with the absorption chiller. Additionally, in both cities, the hydrogen system experiences greater exergy destruction during operation due to the high chemical exergy inherent to the hydrogen.

The Design of Experiment analysis confirmed that the models are reliable (with one exceptions) with R^2 ranging from 0.982 to 1. They provided insights into how certain parameters respond to variations in system variables. For the CAES system, the interaction between PV power output and electricity demand is the primary factor influencing system performance, while tank volume has minimal impact. This suggests that small-scale CAES system applications would have a limited effect on residential buildings, and its deployment should be focused on larger capacities. For the hydrogen system, the analysis revealed that hydrogen generation and consumption have little to no impact on overall system efficiency but significantly affect environmental and economic aspects. Additionally, tank pressure had negligible influence on the evaluated parameters, indicating that operating at lower pressures, if necessary, would not negatively affect system performance.

Currently, the lithium-ion battery system presents as the most suitable option for both cities, particularly from an economic perspective. However, as ESS technologies continue to develop and capital costs decline, in particular for hydrogen system, which is the less mature technology, this scenario could change. In the case of Rio de Janeiro, the hydrogen system has the advantage of meeting all three energy demands, with high operational costs being its primary drawback. A reduction in these costs, especially with the integration of biogas, could make the system more viable. Additionally, improvements in efficiency would allow a greater share of stored hydrogen to be utilized, further enhancing the system's benefits. For Lyon, the effectiveness of any system is significantly impacted by the low solar radiation in autumn and winter. This suggests that energy storage solutions would be more suitable for warmer seasons or in combination with alternative renewable energy sources.

6
Conclusion/future works

This study examines the integration of three distinct ESSs — CAES, hydrogen, and lithium-ion batteries— coupled to photovoltaic panels in a residential building, in both Lyon (France) and Rio de Janeiro (Brazil). The system operates based on the interaction between the PV panels power output and the building's electricity demand. When excess energy is available, it is stored, while during energy deficits, the stored hydrogen or compressed air is used to generate the required electricity. Additionally, the system harnesses its architecture to meet heating and cooling demands. If any demand remains unmet, auxiliary systems are activated – natural gas burner in Brazilian case, heat pumps in French case, and electric grid on both cases.

Tools for assessing the performance of an ESS over a full year of operation are introduced. These tools encompass the logic for charging and discharging storage medias, the operational adjustments of compressors/electrolyzers and turbines/fuel cells, a method for determining the share of hydrogen extracted from storage tanks, component sizing (including compressors, turbines, electrolyzers, fuel cells, and storage media), operational constraints (minimum and maximum limits), and a strategy to ensure all energy demands are met.

Comparing both cities, Rio de Janeiro showed more potential of applying any of the systems as throughout the year it experiences high solar radiation, being able to store more energy, thus less use of the grid to supply energy. Additionally, the CAES and hydrogen systems were able to consistently supply all demands. Ultimately, in Lyon only the electric demand is supplied in warmer months, when heat demand is not present. However, both systems presented potential in supplying cooling, if necessary. It was also possible to verify that the application of all EESs systems in Lyon are more affected by the seasonality effect, as the system experiences more drastic changes in weather conditions compared with Rio de Janeiro.

Electric, cogeneration, trigeneration efficiencies: When comparing efficiencies between the two cities, Rio de Janeiro has a slight advantage over Lyon, as it can meet a higher share of the energy demand under the given conditions. Between the CAES and hydrogen systems, CAES demonstrates higher

electrical and cogeneration efficiency due to lower losses. However, in terms of cooling supply, the hydrogen system benefits from the integration of an absorption chiller. In Rio de Janeiro, the CAES system achieves average annual electrical, cogeneration, and trigeneration efficiencies of 32.37%, 35.33%, and 39.25%, respectively, while the hydrogen system reaches 29.37%, 31.83%, and 44.22%, and the lithium-ion batteries have a sole average annual electrical efficiency of 48.5%. In Lyon, the CAES and lithium-ion battery systems has an annual average electrical efficiency of 28.59% and 42.9%, respectively, while the hydrogen system achieves 26.49%, with a cogeneration efficiency of 29.46%.

Exergy analysis: The PV panels exhibit the highest rates among all components, due to factors such as solar radiation and their size. Therefore, higher losses are expected in the Brazilian city compared to the other location. When comparing the systems, hydrogen one experiences a higher rate of exergy destruction, attributed to the inherently high standard chemical exergy of hydrogen and methane. In CAES systems, the majority of exergy destruction occurs during the charging process, particularly in the precoolers and compressors, while during discharge, it is mainly concentrated in the turbines. In contrast, the hydrogen system sees most exergy destruction during discharge, primarily in the afterburner and heat exchangers (air and water). During the charging process, the majority of losses occur in the PEMEC, with only a small contribution from the compressors and heat exchangers. Differently from previous systems, the lithium-ion battery system presents almost a similar exergy destruction rate during both charging and discharging.

Exergoeconomic analysis: In all systems, the exergoeconomic factor is notably high during charge mode. During discharge mode, it remains high for the lithium-ion battery system, moderate for CAES system, and low for the hydrogen system. These results suggest that capital costs are elevated and could be reduced at the expense of exergy efficiency. One potential solution is downsizing the photovoltaic panels, which would, in turn, reduce the size of the charging-related components—key cost drivers of the entire system. As a result, the costs associated with storing air, hydrogen, and electricity would decrease, leading to more cost-effective operation during both charging and discharging. Additionally, downsizing would lower the relative cost (the difference between the unit cost of fuel and the product) during storage, further improving economic feasibility. If operating solely on the grid, the annual cost for Rio de Janeiro would be 14,762.22$. When integrating energy storage, the relative increase cost to the grid would be 260.91% for the hydrogen system, 206.4% for the CAES, and 71.0% for

the lithium-ion batteries. In Lyon, the standalone grid operation results in an annual cost of 9,307.73$. Considering the hydrogen system, the relative cost increase would be 244.1%, for CAES 197.8%, and lithium-ion batteries 67.6%.

Environmental analysis: The CAES system significantly reduces CO_2 equivalent emissions in Rio de Janeiro. This reduction is primarily due to its ability to generate electricity and decrease dependence on the natural gas grid. Lithium-ion battery systems have a slightly lower impact in mitigating CO_2 emissions, as they still rely on the natural gas grid for heating in Brazil. In Lyon, both systems contribute to reducing CO_2 emissions, but their effectiveness is not as pronounced. The hydrogen system, however, exhibits different performance in each city. Since its operation depends on natural gas reforming, it generates associated emissions. In Rio de Janeiro, the emissions avoided by reducing reliance on the electric and natural gas grids outweigh those produced by reforming, making hydrogen a beneficial option. In contrast, this advantage is less evident in Lyon, where the French energy matrix is cleaner due to lower dependence on natural gas. The CAES system applied to Rio de Janeiro was able to avoid the net emissions of 20.34 tons of CO_2 equivalent, while in Lyon this number is lower, 2.45 tons. The lithium-ion battery system has a slightly worse performance, by avoiding 16.46 tons and 1.49 tons in Rio de Janeiro and Lyon, respectively. Finally, the hydrogen system in Rio de Janeiro has a net avoidance of 11.09 tons, while in Lyon it is responsible for a net emission of 2.46 ton.

Substitution of natural gas by biogas: In this scenario, the only emissions during operation would stem from reliance on the electric grid for power. With this adjustment, the CO_2 mitigation potential of CAES and lithium-ion battery systems increases, as they further reduce dependence on fossil fuels. The hydrogen system also becomes a more viable option in Lyon and gains even greater potential in Rio de Janeiro. In Brazil, the CAES system can prevent net 24.3 tons of CO_2 equivalent emissions, the hydrogen system 50.05 tons, and the lithium-ion battery system 26.05 tons. In France, only hydrogen system can rely on biogas, having a net CO_2 avoidance of 15.33 tons. These results highlight that ESSs are more advantageous in Rio de Janeiro, primarily due to their greater ability to store energy and reduce reliance on both the electric and natural gas grids. Additionally, compared to Lyon, Rio de Janeiro's energy matrix has higher CO_2 equivalent emissions. This suggests that deploying ESSs is most beneficial in regions with abundant renewable energy sources (such as solar or wind) and an energy matrix with high CO_2 emission rates.

Cost of CO_2 equivalent emission as metric: This metric reflects the relationship between system operating costs and emissions reduction potential. When biogas is used, emissions avoidance increases significantly across all applicable systems, leading to a notable decrease in the cost per unit of CO_2 avoided. However, the cost of biogas for residential applications remains uncertain, so two scenarios were analysed: one where biogas costs twice and another where it costs half of the natural gas market value. The results indicate that this price variation has minimal impact on the cost-effectiveness of emissions reduction compared to the environmental benefits gained. In Rio de Janeiro, the cost per ton of CO_2 equivalent avoided considering biogas for each system is 745 $/ton for CAES, 578 $/ton for the hydrogen, and 247 $/ton for the lithium-ion battery. This is a significant decrease from the case utilizing natural gas, which had the parameter value of 824 $/ton, 1,391 $/ton and 317 $/ton for the CAES, hydrogen and lithium-ion battery system, respectively. In Lyon, the respective values (considering biogas) are 2,856 $/ton, 1,176 $/ton and 1,148 $/ton. As previously discussed, integrating biogas offers clear advantages, particularly for the hydrogen system. However, large-scale implementation—such as replacing natural gas in the grid—remains challenging due to high demand and infrastructure constraints. A more feasible approach to integrating biogas into the hydrogen system would involve increasing the share of hydrogen drawn from storage tanks. In Rio de Janeiro, another effective strategy to reduce reliance on the natural gas grid would be increasing electrification, such as using heat pumps, rather than depending solely on biogas.

Design of Experiments multi-parametric analysis: . For the CAES system, different sizes of PV panels, buildings, and storage tanks were analysed. The results showed that PV panel size and building energy demand were the most influential factors, while storage tank volume had a minimal impact on overall performance. This suggests that for small-scale applications, the introduction of CAES system may have a lesser effect compared to the influence of PV panels. For the hydrogen system, key variables examined included hydrogen share, current density, and storage pressure. The study revealed that electrolyzers and fuel cells operating conditions were the primary factors affecting system performance, directly influencing the pressure inside the storage tank. Since storage pressure determines the amount of hydrogen that can be stored, the findings suggest that maintaining a lower pressure level could be feasible, offering potential safety benefits and enabling the use of smaller storage tanks, thereby

slightly reducing system costs. Overall, PV panel size and electricity demand are the primary drivers shaping the performance of ESSs.

In conclusion, the implementation of ESSs still faces significant challenges, with economic viability being the primary hurdle, as all evaluated systems exhibited high operational costs. However, a key advantage of these systems is their potential to reduce CO_2 emissions by decreasing reliance on the grid. To make them more feasible, substantial reductions in capital costs and improvements in efficiency are necessary. At present, for both cities the lithium-ion battery system appears to be the most viable option, particularly when biogas is incorporated. Looking ahead, the hydrogen system holds great promise as an energy storage solution for both cities, especially if cost reductions and efficiency enhancements are achieved. Comparing with the other two systems, CAES and lithium-ion battery, the electrolyzers and the fuel cells have more space for achieving both features, as they have not yet achieved its development maturity. Once this future scenario comes into reality, it is possible to have a better utilization of energy, namely using more of the generated hydrogen, further increasing the avoidance of CO_2 emissions during operation, and make the system more competitive.

In the future, several directions for further research are suggested:

- Apply the systems to other consumers with varying demand profiles and climate conditions. It would also be valuable to explore areas with energy mixes that have high CO_2 equivalent emissions and different renewable energy sources. Additionally, other types of buildings with different demands and higher consumption, such as hospitals, offices, and shopping centres, could be studied.
- Use real-world components—such as compressors, turbines, electrolyzers, fuel cells, and heat exchangers—with their actual operation limitation and efficiencies. This would provide a more accurate understanding of system operation and operational costs.
- Evaluate both compressors and turbines with isentropic efficiencies varying with the operational pressure ratio.
- Verify, particularly for Brazil, the operation of different fuels other than the methane for reforming the hydrogen system. Ethanol is a candidate due to its abundancy in the country as well as having lower impact to environment.
- Include a traditional economic assessment and include a risk analysis considering CAPEX and OPEX scenarios. By doing such, a more

accurate analysis on the feasibility of all systems, from an economic point of view, can be provided.

- Perform a more in-depth analysis concerning the environmental impacts of the system by considering a Life Cycle Assessment, by evaluating other categories of impacts, such as the utilization of the materials in production, and including the decommissioning effect. An exergetic evaluation could also be performed by evaluating the material treatment during the components manufacturing process (138).
- Explore different system configurations and the potential integration of lithium-ion batteries with other storage technologies. Lithium-ion batteries would be more suitable for operations with lower to moderate power demands, while turbines and fuel cells would be more effective for higher power requirements. In case of Rio de Janeiro, further electrification could be considering by substituting the use of natural gas burner to heat pumps, as the case for Lyon. Use of lithium-ion batteries also would solve the issue of ramp up time (not considered in this work) of both CAES and hydrogen systems.
- For the hydrogen system, a better strategy could be found to define the hydrogen energy share. Instead of using a fixing value, it is interesting to find a method that identifies the actual conditions of the system and either increase or decrease the share.
- After conducting the complex annual evaluation, simplify the process into an efficiency model that could be applied to hybrid artificial neural networks (ANNs). This approach could optimize the system and identify the best configuration for each setup.

Appendices

A.
Thermodynamic properties of mixture

As stated, the Peng-Robinson equation of state is utilized to calculate the thermodynamic properties of the fluids in the hydrogen system. Indeed, the utilization of Peng-Robinson equation overcomes the limitations of the REFPROP regarding operational temperatures. The mixing rule is applied to for calculating the thermodynamic properties of the exhaust gases leaving the afterburner. The following section describes the procedure to evaluate the enthalpy and entropy of methane, carbon monoxide, carbon dioxide, hydrogen, water, oxygen, nitrogen, and their mixture.

A.1.
Equation of State

The equation of state (EoS) represents the P-V-T behaviour of both liquid and vapour states of a substance. The first equation was developed by Van der Waals, Eq. (A1):

$$P = \frac{\bar{R} \cdot T}{V - b} - \frac{a}{V^2} \tag{A1}$$

Where P is the pressure in MPa, $\bar{R}$ is the universal gas constant in kJ/(kmol.K), T is temperature in K, and V is the molar volume in m³/mol, *a* and *b* are positive constant and specific for a given species. When their value is null, the ideal gas equation is retrieved.

Other EoS are developed, and can be generically expressed by Eq. (A2):

$$P = \frac{R \cdot T}{V - b} - \frac{a(T)}{(V + \varepsilon b) \cdot (V + \sigma b)} \tag{A2}$$

ε e σ are EoS constants.

The correct attribution to the aforementioned parameters will results in the following equation of state: van der Waals (vdW), Redlich/Kwong (RK), Soave/Redlich/Kwong (SRK), and Peng-Robinson (PR) (139). The values are described in Table A1.

Table A1: Equation of State parameters **(139)**.

Equation of State	$\boldsymbol{a(T_r)}$	$\boldsymbol{\sigma}$	$\boldsymbol{\varepsilon}$	$\boldsymbol{\Omega}$	$\boldsymbol{\psi}$
vdW	1	0	0	1/8	27/64
RK	$T_R^{-1/2}$	1	0	0,08664	0,42748
SRK	$\alpha_{SRK}(T_r,\omega)$	1	0	0,08664	0,42748
PR	$\alpha_{PR}(T_r,\omega)$	$1+\sqrt{2}$	$1-\sqrt{2}$	0,07780	0,45724
$\alpha_{SRK}(T_r,\omega)=\left[(1+0.480+1.574\omega-0.176\omega^2)\cdot\left(1-T_r^{1/2}\right)\right]^2$					(A3)
$\alpha_{PR}(T_r,\omega)=\left[(1+0.37464+1.54226\omega-0.26992\omega^2)\cdot\left(1-T_r^{1/2}\right)\right]^2$					(A4)
vdW – van der Waals; RK – Redlich/Kwong; SVR – Soave/Redlich/Kwong; PR – Peng-Robinson					

$$T_r = \frac{T}{T_c} \tag{A5}$$

$$P_r = \frac{P}{P_c} \tag{A6}$$

Where Ω and ψ are EoS constants, ω is the acentric factor (dimensionless), and the subscript *r* corresponds to the reduced condition, and *c* to the critical point.

The determination of the parameters *b* and *a(T)* in Eq. (A2) is extracted from the critical constants for temperature and pressure. Due to the horizontal inflection of the isothermal at critical point, the following mathematical conditions is imposed, Eqs. (A7-A8):

$$\left(\frac{\partial P}{\partial V}\right)_{T_c} = 0 \tag{A7}$$

$$\left(\frac{\partial^2 P}{\partial V^2}\right)_{T_c} = 0 \tag{A8}$$

The differential of Eq. (A2) results into expression that equal to null, returns $P = P_c, T = T_c$ e $V = V_c$. The parameters *a* and *b* can be related to the critical temperature and pressure as follow, Eqs. (A9-A10) (139):

$$b = \Omega \cdot \frac{R \cdot T_c}{P_c} \tag{A9}$$

$$a(T) = \psi \frac{\alpha(T_r, \omega) \cdot R^2 \cdot T_c^2}{P_c} \tag{A10}$$

The solution of the cubic equation results in three different roots. The smallest corresponds to the liquid state, the highest to the vapour state, and the intermediary is thermodynamically unstable.

Usually, the equation of state is described by the compressibility factor. As such, two non-dimensional variables (*q* and *β*) are defined, Eqs. (A11-A13) (139):

$$V = \frac{Z \cdot R \cdot T}{P} \tag{A11}$$

$$\beta = \frac{b \cdot P}{R \cdot T} = \Omega \cdot \frac{P_r}{T_r} \tag{A12}$$

$$q = \frac{Z - \beta}{b \cdot R \cdot T} = \frac{\psi \cdot a(T_r, \omega)}{\Omega \cdot T_r} \tag{A13}$$

Finally, Eq. (A2) can be adapted into two different ways: for vapour root, Eq. (A14), and liquid root, Eq. (A15):

$$Z = 1 + \beta - q \cdot \beta \frac{Z - \beta}{(Z + \varepsilon\beta) \cdot (Z + \sigma\beta)} \tag{A14}$$

$$Z = \beta + (Z + \varepsilon\beta) \cdot (Z + \sigma\beta) \cdot \left(\frac{1 + \beta - Z}{q \cdot \beta}\right) \tag{A15}$$

A.2.
Residual properties

By definition, a residual property is the difference between the actual state and the ideal gas at the same temperature and pressure conditions, Eq. (A16) (140):

$$M_r = M - M^{ig} \tag{A16}$$

From a practical perspective, the equation divides the calculus of the properties into two parts: the calculation of the properties assuming an ideal gas (*ig*), and the calculus of residual property (*r*), which nature is to correct the values from the ideal gas.

It is necessary, to calculate the thermodynamic properties, only to know the initial (*i*) and final (*f*) states, Figure A1. So, the variation is given by the following equation, Eq. (A17):

$$M_f - M_i = \left(M_f - M_f^{ig}\right) + \left(M_f^{ig} - M_i^{ig}\right) - \left(M_i - M_i^{ig}\right) \tag{A17}$$

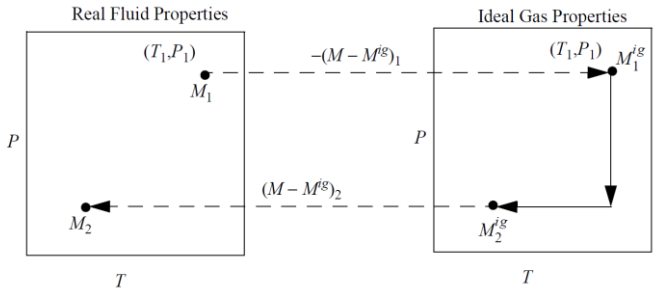

Figure A1: Calculation of a generic property M using departure function **(140)**.

The Peng-Robinson Equation of State can be utilized to calculate specific residual enthalpy and entropy, Eqs. (A18-A19):

$$h_r = (h - h_{id}) = \bar{R} \cdot T \cdot (1 - Z) + \left(\frac{a - T \cdot \frac{da}{dT}}{2\sqrt{2b}}\right) \cdot \ln\left(\frac{Z + 2.414b}{Z - 0.414b}\right) \tag{A18}$$

$$s_r = (s - s_{id}) = -\bar{R} \cdot \ln(Z - b) - \frac{1}{2\sqrt{2}b} \cdot \frac{da}{dT} \cdot \ln\left(\frac{Z + 2.414b}{Z - 0.414b}\right) \tag{A19}$$

Once the residual thermodynamic property is known, a reference state is also chosen, and the finally the property of interest can be calculated for the given temperature and pressure, Eqs. (A20-A21):

$$h = (h - h_{id})_{T,P} + \int_{T_r}^{T} c_p \cdot dT - (h - h_{id})_r + h_r \qquad \text{(A20)}$$

$$s = (s - s_{id})_{T,P} + \int_{T_r}^{T} \frac{c_p}{T} \cdot dT - (s - s_{id})_r + s_r - R \cdot \ln \frac{P}{P_r} \qquad \text{(A21)}$$

The first and third terms of Eqs. (A20-A21) are calculated using the equation of state for a given temperature and pressure, and the reference state, respectively. The fourth term is substituted by the values predetermined by the reference state. Finally, the second term is an integral of the specific heat at constant pressure, which limits are determined by the reference state and temperature of interest (140).

Table A2 display the parameters of Eq. (A22) utilized in the calculation of the heat capacity of each considered fluid.

$$c_{p,0} = A + B \cdot \frac{T}{1000} + C \cdot \left(\frac{T}{1000}\right)^2 + D \cdot \left(\frac{T}{1000}\right)^3 + \frac{E}{\left(\frac{T}{1000}\right)^2} \qquad \text{(A22)}$$

Table A2: Heat capacity parameters **(141)**.

Fluid	Temperature [K]	A	B	C	D	E
Methane	298 - 1300	-0.70	108.48	-42.52	5.86	0.68
	1300 - 6000	85.81	11.26	-2.11	0.14	-26.42
Carbon Monoxide	298 - 1300	25.57	6.10	4.05	-2.67	0.13
	1300 - 6000	35.15	1.30	-0.21	0.01	-3.28
Carbon Dioxide	298 - 1200	25.00	55.19	-33.69	7.95	-0.14
	1200 – 6000	58.17	2.72	-0.49	0.04	-6.45
Water	298 -500	-203.61	1523.29	-3196.41	2474.46	3.86
	500 - 1700	30.09	6.83	6.79	-2.53	0.08
	1700 - 6000	41.96	8.62	-1.50	0.10	-11.16
Hydrogen	298 - 1000	33.07	-11.36	11.43	-2.77	-0.16
	1000 - 2500	18.56	12.26	-2.86	0.27	1.98
	2500 - 6000	43.41	-4.29	1.27	-0.10	-20.53
Oxygen	100 - 700	31.32	-20.24	57.87	-36.51	-0.01
	700 - 2000	30.03	8.77	-3.99	0.79	-0.74
	2000 - 6000	20.91	10.72	-2.02	0.15	9.25
Nitrogen	100 - 500	28.99	1.85	-9.65	16.64	0.00
	500 -2000	19.51	19.89	-8.60	1.37	0.53
	2000 - 6000	35.52	1.13	-0.20	0.01	-4.55

A.3.
Mixing rule

To estimate the P-v-T relation of gas mixture, the mixing rule is developed by the RKS and PR equations of state, both dependent on the parameters *a* and *b*. Soave proposed the following rule to determine both coefficients, Eqs. (A23-A24) (140):

$$a = \sum_{i=1}^{C}\sum_{j=1}^{C} y_i \cdot y_j \cdot a_{ij} \tag{A23}$$

$$b = \sum_{i=1}^{C} y_i \cdot b_i \tag{A24}$$

Peng and Robinson adapted the parameter *a* by introducing the new parameter known as the binary interaction parameter $k_{i,j}$, Eqs. (A25-A26) (142):

$$a_{ij} = \left(1 - k_{ij}\right) \cdot \sqrt{a_i} \cdot \sqrt{a_j} \tag{A25}$$

$$k_{ij} = 1 - \left[\frac{2\left(v_{c,i} \cdot v_{c,j}\right)^{\frac{1}{6}}}{\left(v_{c,i}^{\frac{1}{3}} + v_{c,j}^{\frac{1}{3}}\right)}\right]^3 \tag{A26}$$

A.4.
Validation

The results for each considered fluid is shown in Figure A2, which the full line corresponds to the property calculated by utilizing the equation of state, and the scatter data is taken from the NIST database (143).

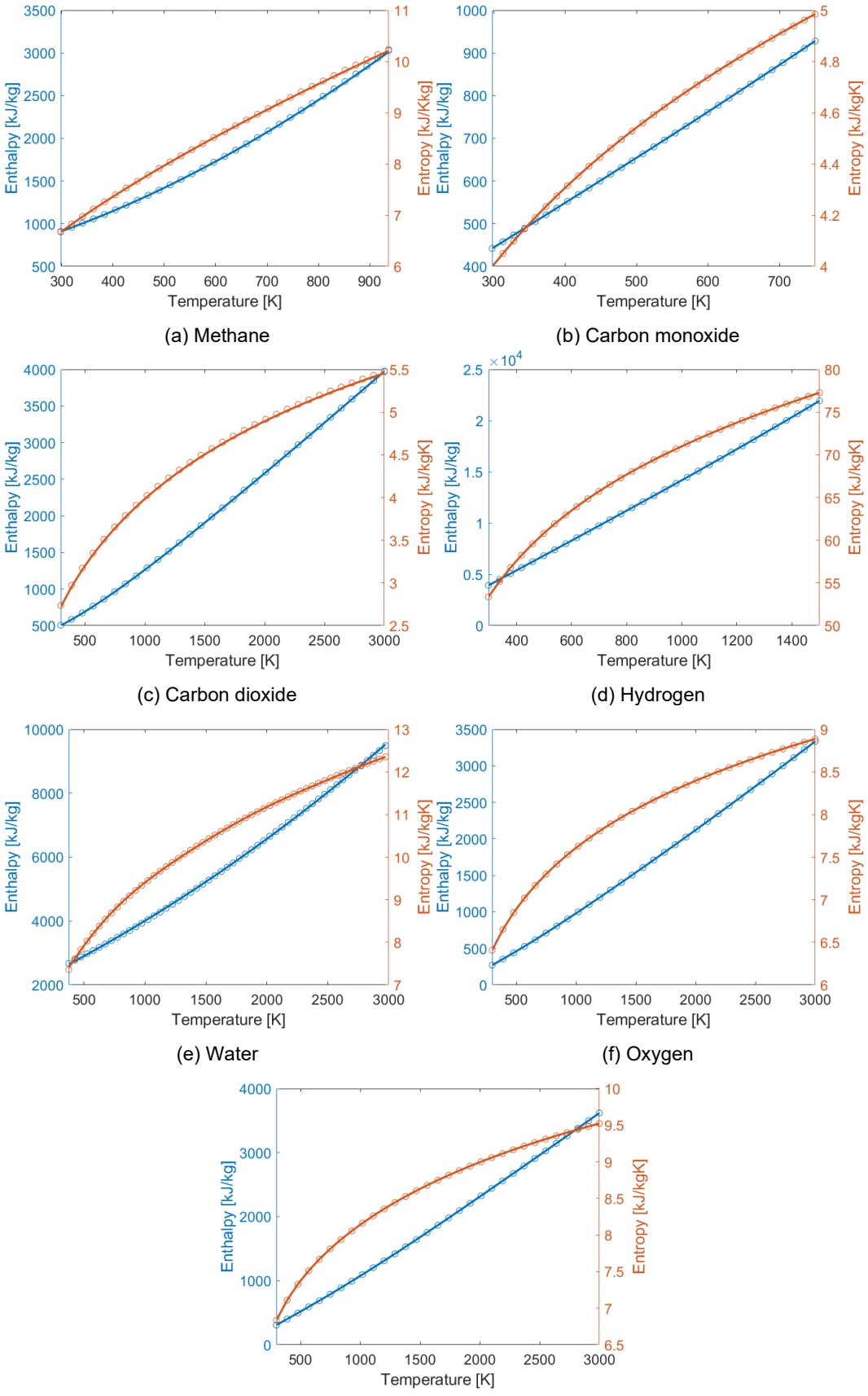

Figure A2: Enthalpy and entropy validation in function of temperature at ambient pressure.

Observing Figure A2, it can be seen a good agreement between the numerical procedure and the data from NIST, indicating the robustness of the model. The same model was validated for the use of mixture in previous works (144).

B.
Seasonal Data

This section has the intention to bring a better understanding of the seasonality on the building's demands and solar radiation, by splitting the results in Figures B1 and B2.

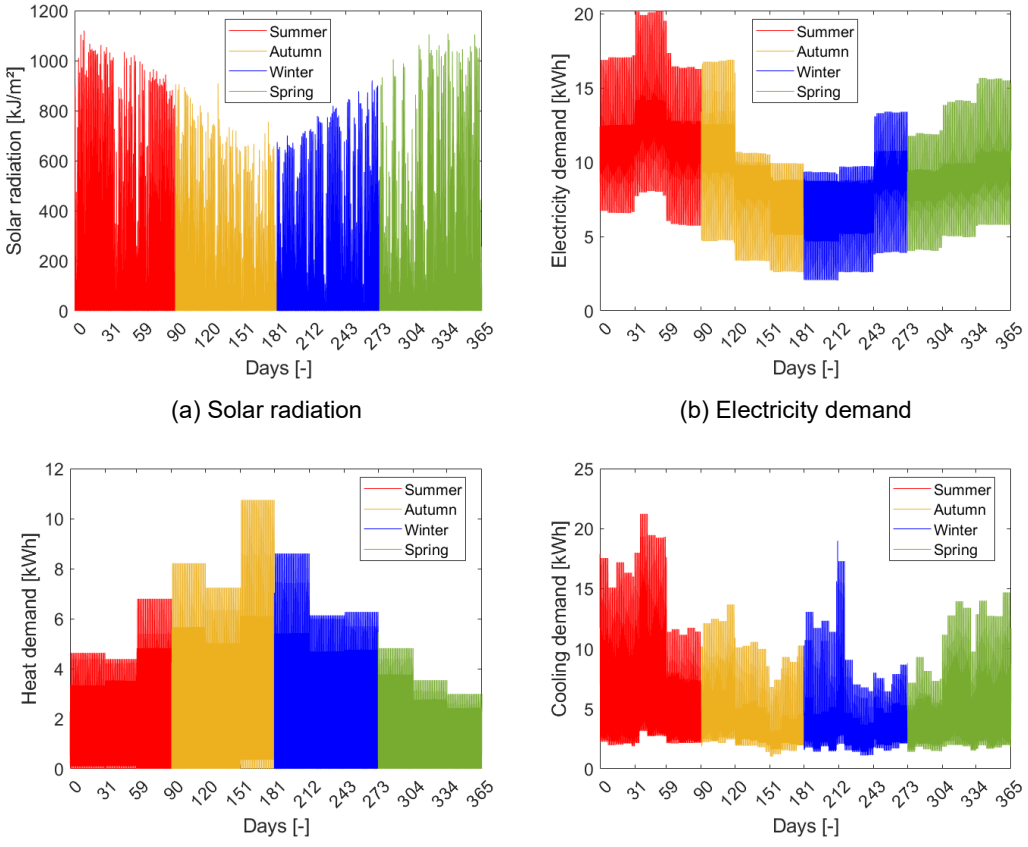

(a) Solar radiation

(b) Electricity demand

(c) Heat demand

(d) Cooling demand

Figure B1: Brazilian seasonal data.

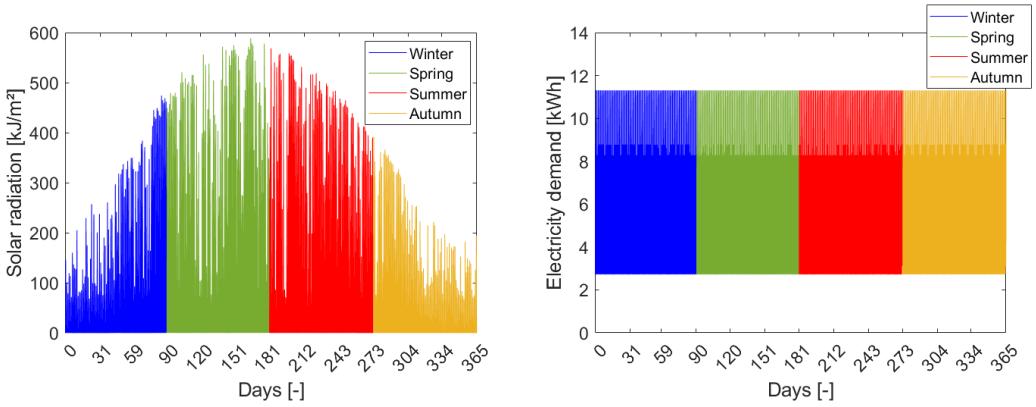

(a) Solar radiation

(b) Electricity demand

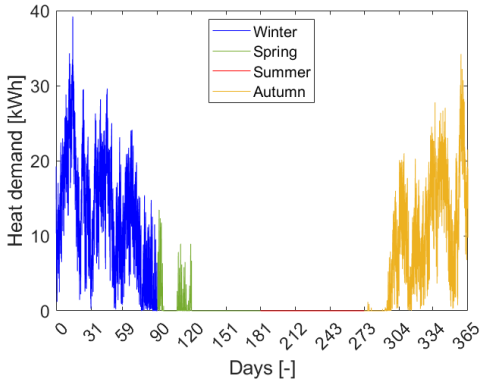

(c) Heat demand

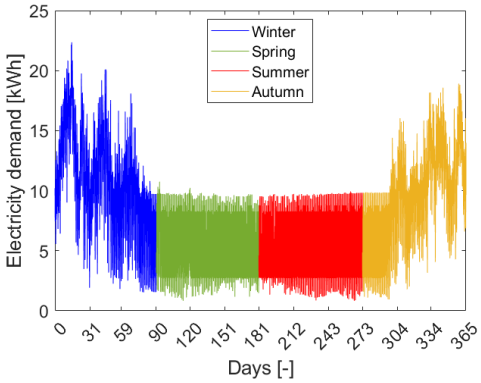

(d) Final electricity demand

Figure B2: French seasonal data.

C. Boxplots

A boxplot is a method utilized to demonstrate graphically the locality, spread and skewness groups of numerical data by their quartiles. They also have lines, known as whisker, extending from the box indicating the variability outside the upper and lower quartiles. Any data beyond the mark of the whiskers are known as outliers.

They are standardized by displaying the dataset based on different numbers:

- Minimum: (0th percentile): Smallest data point that is not an outlier.
- First quartile: (25th percentile), Q1: median of the lower half of the set.
- Median: (50th percentile): middle data point in the set.
- Third quartile: (75th percentile), Q3: median of the upper half of the set.
- Maximum: (100th percentile): Maximum data point that is not an outlier.

- Interquartile range (IQR): distance between first and third quartiles.

Figure C1 displays a representation of a boxplot together with a normal distribution.

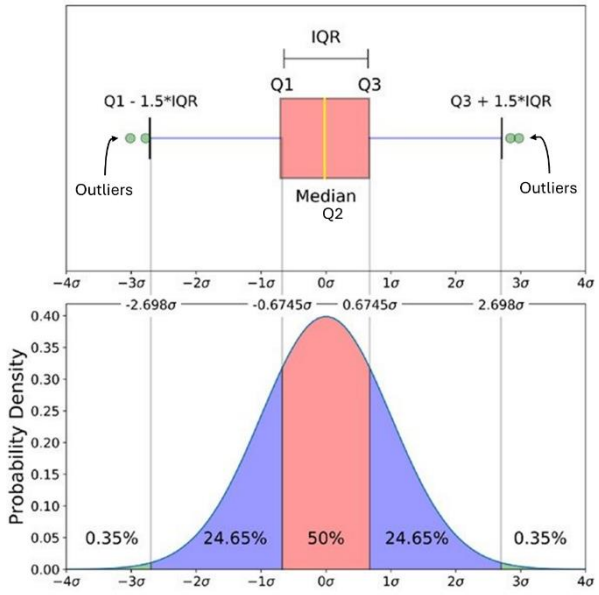

Figure C1: Boxplot and uniform distribution representation.

Figure C2 presents the boxplot of the procedure described in Section 4.5 for all three systems in both cities.

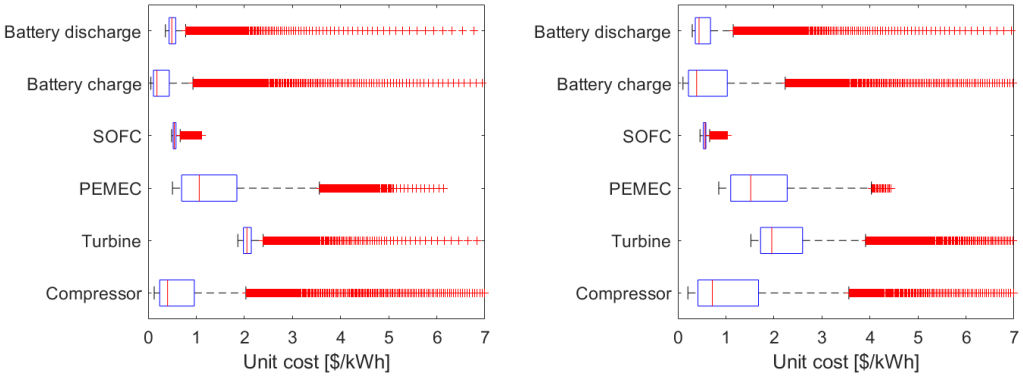

(a) Rio de Janeiro (b) Lyon

Figure C2: Boxplot of equipment in all three systems.

It is interesting to observe the distribution among all systems. Both SOFC and PEMEC have a less spread distribution as both components cannot operate at very low power rates due to its own limitations (low current densities). In the case of both CAES and lithium-ion battery systems, the data is more spread, as it can be seen by the outliers. Among all cases, it is possible to observe that median

is closer to Q1, and the upper (right) whisker is longer, indicating that the distribution is not symmetric, rather right-skewed (positive skew).

D.
The effect of setting operational limits

The intention of this section is to presents the effects of setting the operational limits of both systems. The results presented considers the case of Rio de Janeiro, comparing the base cases presented in Chapter 5, with the cases with no limits for minimum operational power, and in the case of hydrogen system the case without the downsizing of the PEMECs representing a bigger system.

Figure D1 presents the unit cost of charging, stored compressed air, and discharging of the CAES system.

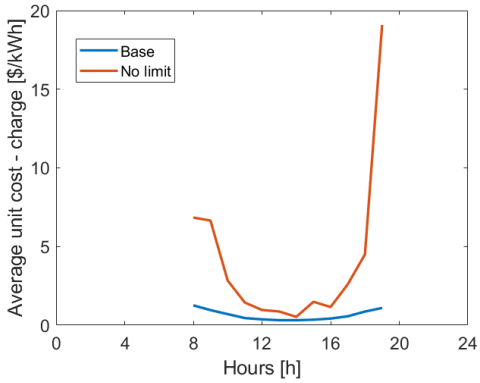

(a) Charge

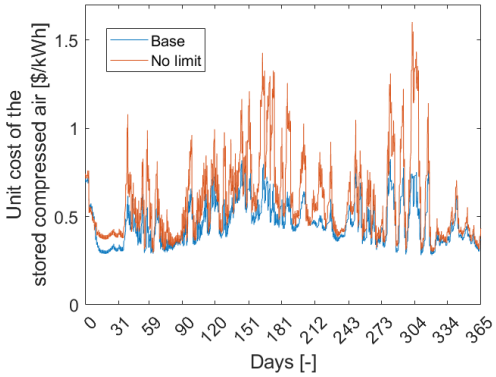

(b) Stored compressed air

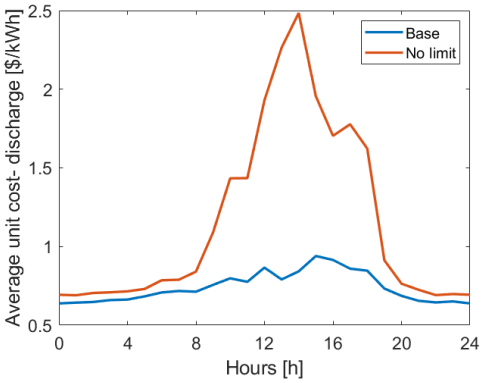

(c) Discharge

Figure D1: Effects of setting operational limits – CAES system.

By observing Figure D1 the effect of setting operational limits is clear. In Figure D1(a) and (c), there is a sharp increase in the values whenever there is a low value of charging or discharging power. In the case of charging, it is seen in the beginning of morning and late night and discharging around midday when the turbines and PV panels works together. Figure D1(b) presents the value of the unit

cost of the stored compressed air, and it observed the increased values for the case without limiting, allowing to stored air at unfavourable conditions. When comparing the annual average value for each illustrated case, the base case had 0.58 $/kWh, 0.46 $/kWh, and 0.74 $/kWh for the charging, stored and discharge unit cost, respectively. For the no-limit case, the values are higher – 4.44 $/kWh, 0.58 $/kWh, and 1.15 $/kWh. The considerable difference during charge is given for specific conditions, which resulted in considerable high unit costs.

Figure D2 shows the results for the hydrogen system.

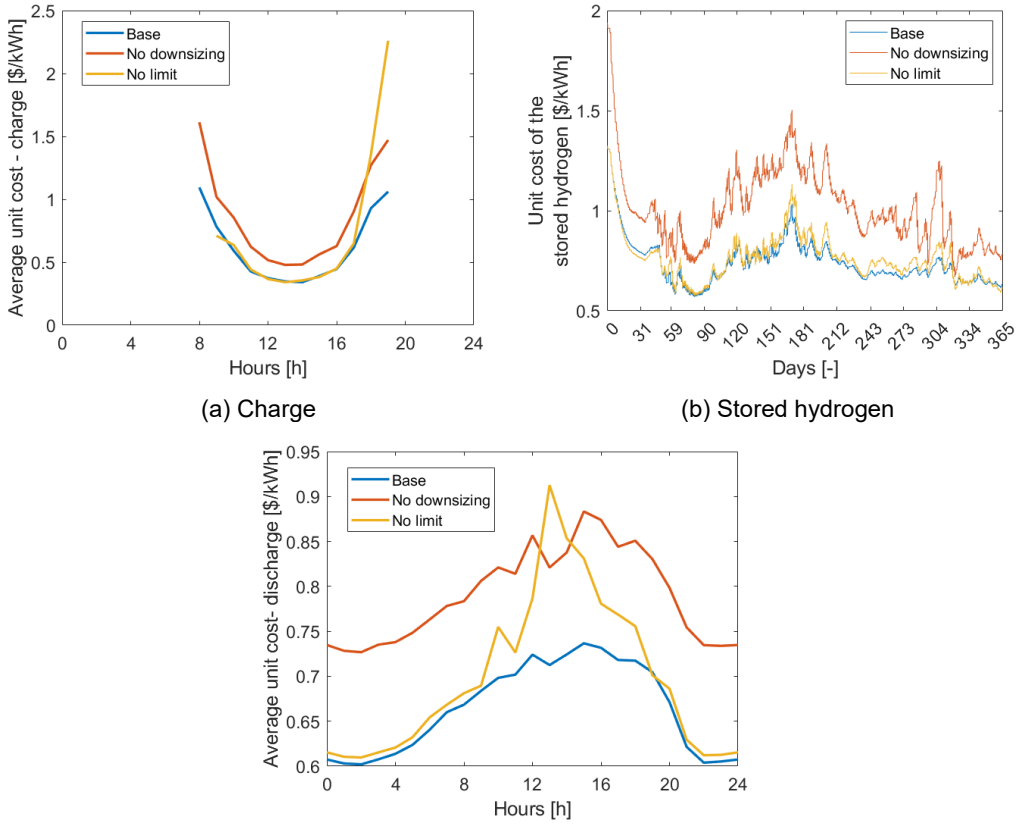

(a) Charge

(b) Stored hydrogen

(c) Discharge

Figure D2: Effects of setting operational limits - hydrogen system.

Figure D2 reflects the same effects seen in Figure D1 whether lower charging and discharge powers, the unit cost increases. This effect is seen in Figures D2(a) and (c), and also in opposite cases (higher charge and discharge power) the unit cost is almost similar. Figure D2(b) shows the minimal differences between the base case and the one without limitations. The effect of having a bigger size is also clear. In Figure D2(a) having a higher PEMEC stack directly results in a higher unit cost, implying a considerable higher value for the unit cost of stored hydrogen, Figure D2(b). Consequently, it results in an operation during discharge with a higher unit cost. To better illustrate the results, the annual average values for the

unit cost of aforementioned cases are calculated. For the base case, the values for charge, stored, and discharge are 0.57 $/kWh, 0.74 $/kWh, and 0.66 $/kWh, respectively. For the no-downsizing case the values are 0.81 $/kWh, 1.01 $/kWh and 0.79 $/kWh. Finally, for the lower no-limit case the values are 0.67 $/kWh, 0.76 $/kWh and 0.79 $/kWh.

The results presented illustrates the effects on optimizing the numerical model via exergoeconomy, having an operation at better conditions. All presented cases, results in different operational costs and net emissions. It is interesting setting the operational limits for having a better condition of operation, which also matches the integration of the EESs with the electric grid.

References

[1] UNFCCC. **The Paris Agreement**. Available at: <https://unfccc.int/process-and-meetings/the-paris-agreement>. Accessed at: 28 jan. 2025.

[2] IPCC. **Global Warming of 1.5°C: IPCC Special Report on Impacts of Global Warming of 1.5°C above Pre-industrial Levels in Context of Strengthening Response to Climate Change, Sustainable Development, and Efforts to Eradicate Poverty**. United Kingdom: Cambridge University Press, 9 jun. 2022. Available at: <https://www.cambridge.org/core/product/identifier/9781009157940/type/book>. Accessed at: 28 jan. 2025.

[3] IEA. **Net Zero Roadmap: A Global Pathway to Keep the 1.5 °C Goal in Reach - 2023 Update**. France, 2024. Available at: <https://www.iea.org/reports/net-zero-roadmap-a-global-pathway-to-keep-the-15-0c-goal-in-reach>.

[4] IEA. **Renewables 2024 - Analysis and forecast to 2030**. France, 2024. Available at: <https://www.iea.org/reports/renewables-2024>.

[5] EMPRESA DE PESQUISA ENERGÉTICA. **Balanço Energético Nacional (BEN) 2024: Ano base 2023**. Brazil, 2024. Available at: < https://www.epe.gov.br/pt/publicacoes-dados-abertos/publicacoes/balanco-energetico-nacional-2024>

[6] MINISTÈRE DE LA TRANSITION ÉCOLOGIQUE ET DE LA COHÉSION DES TERRITOIRES. **Chiffres clés de l'énergie**. France, 2024. Available at: <https://www.statistiques.developpement-durable.gouv.fr/edition-numerique/chiffres-cles-energie-2024/>.

[7] BAZDAR, E. et al. Compressed air energy storage in integrated energy systems: A review. **Renewable and Sustainable Energy Reviews**, v. 167, p. 112701, out. 2022.

[8] OLABI, A. G. et al. Critical review of energy storage systems. **Energy**, v. 214, p. 118987, jan. 2021.

[9] DINÇER, I.; ROSEN, M. A. **Thermal Energy Storage Systems and Applications**. 5th ed. United States of America: John Wiley & Sons Ltd, 2021.

[10] RAZMI, A. R. et al. A green hydrogen energy storage concept based on parabolic trough collector and proton exchange membrane electrolyzer/fuel cell: Thermodynamic and exergoeconomic analyses with multi-objective optimization. **International Journal of Hydrogen Energy**, v. 47, n. 62, p. 26468–26489, jul. 2022.

[11] ZHANG, Z. et al. A review of technologies and applications on versatile energy storage systems. **Renewable and Sustainable Energy Reviews**, v. 148, p. 111263, set. 2021.

[12] KOOHI-FAYEGH, S.; ROSEN, M. A. A review of energy storage types, applications and recent developments. **Journal of Energy Storage**, v. 27, p. 101047, fev. 2020.

[13] ABDIN, Z. et al. Hydrogen as an energy vector. **Renewable and Sustainable Energy Reviews**, v. 120, p. 109620, mar. 2020.

[14] U.S. DEPARTMENT OF ENERGY. **Hydrogen Storage**. Available at: <https://www.energy.gov/eere/fuelcells/hydrogen-storage>. Accessed at: 22 fev. 2025.

[15] IEA. **Global Hydrogen Review 2024**. France, 2024. Available at: <https://www.iea.org/reports/global-hydrogen-review-2024>.

[16] IRENA. **Hydrogen: a renewable energy perspective**. Abu Dhabi, 2019. Available at: <https://www.irena.org/publications/2019/Sep/Hydrogen-A-renewable-energy-perspective>.

[17] IRENA. **Green hydrogen cost reduction: scaling up electrolysers to meet the 1.5^0 C climate goal**. Abu Dhabi, 2020. Available at: <https://www.irena.org/publications/2020/Dec/Green-hydrogen-cost-reduction>.

[18] EMPRESA DE PESQUISA ENERGÉTICA; MINISTÉRIO DE MINAS E ENERGIA. **Bases para a Consolidação da Estratégia Brasileira do Hidrogênio**. Brazil, 2021. Available at: <https://www.epe.gov.br/pt/publicacoes-dados-abertos/publicacoes/nota-tecnica-bases-para-a-consolidacao-da-estrategia-brasileira-do-hidrogenio>.

[19] EMPRESA DE PESQUISA ENERGÉTICA; MINISTÉRIO DE MINAS E ENERGIA. **Plano Nacional de Energia 2050**. Brazil, 2020. Available at: <https://www.epe.gov.br/pt/publicacoes-dados-abertos/publicacoes/Plano-Nacional-de-Energia-2050>.

[20] MINISTÉRIO DE MINAS E ENERGIA. **Programa Nacional do Hidrogênio, Plano de trabalho trienal 2023-2025**. Brazil, 2023. Available at: <https://www.gov.br/mme/pt-br/programa-nacional-do-hidrogenio-1>.

[21] GOVERNO BRASILEIRO. **Lei n° 14.948, de 2 de agosto de 2024**. Available at: <https://www.in.gov.br/web/dou/-/lei-n-14.948-de-2-de-agosto-de-2024-576003914>. Accessed at: 28 jan. 2024.

[22] MINISTÈRE DE L'ECONOMIE DES FINANCES ET DE LA SOUVERAINETÉ INDUSTRIELLE ET NUMÉRIQUE. **Stratégie nationale pour le développment de l'hydrogène décarboné en France**. France, 2020. Available at: <https://www.ecologie.gouv.fr/sites/default/files/documents/DP%20-%20Strat%C3%A9gie%20nationale%20pour%20le%20d%C3%A9veloppement%20de%20l%27hydrog%C3%A8ne%20d%C3%A9carbon%C3%A9%20en%20France.pdf>.

[23] MINISTÈRE DE L'ECONOMIE DES FINANCES ET DE LA SOUVERAINETÉ INDUSTRIELLE ET NUMÉRIQUE. **Accélérer le déploiement de l'hydrogène, clé de voûte de la décarbonation de l'índustrie**. France, 2023. Available at: <https://presse.economie.gouv.fr/02022023-dossier-de-presse-accelerer-le-deploiement-de-lhydrogene-cle-de-voute-de-la-decarbonation-de-lindustrie/>.

[24] EUROPEAN COMISSION. **Fuel Cell Technology in the European Union - Status report on technology development, trends, value chains & markets**. Luxembourg, 2024. Available at: <https://publications.jrc.ec.europa.eu/repository/handle/JRC139352>.

[25] TOKYO GAS CO., LTD. **Residential Fuel Cell ENE-FARM**. Available at: <https://www.challenge-zero.jp/en/casestudy/469>. Accessed at: 24 fev. 2025.

[26] ZAINAL, B. S. et al. Recent advancement and assessment of green hydrogen production technologies. **Renewable and Sustainable Energy Reviews**, v. 189, p. 113941, jan. 2024.

[27] IRENA. **Green hydrogen: A guide to policy making**. Abu Dhabi, 2020. Available at: <https://www.irena.org/publications/2020/Nov/Green-hydrogen>.

[28] HERNÁNDEZ-GÓMEZ, Á.; RAMIREZ, V.; GUILBERT, D. Investigation of PEM electrolyzer modeling: Electrical domain, efficiency, and specific energy consumption. **International Journal of Hydrogen Energy**, v. 45, n. 29, p. 14625–14639, maio 2020.

[29] STEMPIEN, J. P.; SUN, Q.; CHAN, S. H. Solid Oxide Electrolyzer Cell Modeling: A Review. **Journal of Power Technologies**, p. 32, 2013.

[30] OZTURK, M.; DINCER, I. A comprehensive review on power-to-gas with hydrogen options for cleaner applications. **International Journal of Hydrogen Energy**, v. 46, n. 62, p. 31511–31522, set. 2021.

[31] TOGHYANI, S. et al. Optimization of operating parameters of a polymer exchange membrane electrolyzer. **International Journal of Hydrogen Energy**, v. 44, n. 13, p. 6403–6414, mar. 2019.

[32] ZHANG, K. et al. Status and perspectives of key materials for PEM electrolyzer. **Nano Research Energy**, v. 1, p. e9120032, dez. 2022.

[33] ZHANG, L. et al. **Electrochemical Water Electrolysis; Fundamentals and Technologies**. 1st ed. United States of America: CRC Press, 2020.

[34] SINGH, M.; ZAPPA, D.; COMINI, E. Solid oxide fuel cell: Decade of progress, future perspectives and challenges. **International Journal of Hydrogen Energy**, v. 46, n. 54, p. 27643–27674, ago. 2021.

[35] WU, Z. et al. Combined biomass gasification, SOFC, IC engine, and waste heat recovery system for power and heat generation: Energy, exergy, exergoeconomic, environmental (4E) evaluations. **Applied Energy**, v. 279, p. 115794, dez. 2020.

[36] CHITSAZ, A.; HOSSEINPOUR, J.; ASSADI, M. Effect of recycling on the thermodynamic and thermoeconomic performances of SOFC based on trigeneration systems; A comparative study. **Energy**, v. 124, p. 613–624, abr. 2017.

[37] SADAT, S. M. S.; MIRABDOLAH LAVASANI, A.; GHAEBI, H. Economic and thermodynamic evaluation of a new solid oxide fuel cell based polygeneration system. **Energy**, v. 175, p. 515–533, maio 2019.

[38] SINGHAL, S. C.; KENDALL, K. **High Temperature Solid Oxide Fuel Cells: Fundamentals, Design and Applications**. 1st ed. United Kingdom: Elsevier, 2003.

[39] SINGHAL, S. C. Solid oxide fuel cells for power generation: Solid oxide fuel cells for power generation. **Wiley Interdisciplinary Reviews: Energy and Environment**, v. 3, n. 2, p. 179–194, mar. 2014.

[40] ADAMS, T. A. et al. Energy Conversion with Solid Oxide Fuel Cell Systems: A Review of Concepts and Outlooks for the Short- and Long-Term. **Industrial & Engineering Chemistry Research**, v. 52, n. 9, p. 3089–3111, 6 mar. 2013.

[41] MAHATO, N. et al. Progress in material selection for solid oxide fuel cell technology: A review. **Progress in Materials Science**, v. 72, p. 141–337, jul. 2015.

[42] STAMBOULI, A. B.; TRAVERSA, E. Solid oxide fuel cells (SOFCs): a review of an environmentally clean and efficient source of energy. **Renewable and Sustainable Energy Reviews**, v. 6, n. 5, p. 433–455, out. 2002.

[43] SHRI PRAKASH, B.; SENTHIL KUMAR, S.; ARUNA, S. T. Properties and development of Ni/YSZ as an anode material in solid oxide fuel cell: A review. **Renewable and Sustainable Energy Reviews**, v. 36, p. 149–179, ago. 2014.

[44] ZAKARIA, Z. et al. A review of solid oxide fuel cell component fabrication methods toward lowering temperature. **International Journal of Energy Research**, v. 44, n. 2, p. 594–611, fev. 2020.

[45] CHELMEHSARA, M. E.; MAHMOUDIMEHR, J. Techno-economic comparison of anode-supported, cathode-supported, and electrolyte-supported SOFCs. **International Journal of Hydrogen Energy**, v. 43, n. 32, p. 15521–15530, ago. 2018.

[46] ZHENG, N. et al. Thermodynamic performance analysis of a novel PEMEC-SOFC-based poly-generation system integrated mechanical compression and thermal energy storage. **Energy Conversion and Management**, v. 265, p. 115770, ago. 2022.

[47] MEHDIKHANI, V. et al. Thermodynamic and exergoeconomic assessment of a new combined power, natural gas, and hydrogen system based on two geothermal wells. **Applied Thermal Engineering**, v. 206, p. 118116, abr. 2022.

[48] ZHAO, H. et al. Thermodynamic performance analysis of a novel energy storage system consist of asymmetric PEMEC and SOFC combined cycle. **Energy Conversion and Management**, v. 286, p. 117077, jun. 2023.

[49] WANG, H. et al. Energy, exergetic and economic analysis and multi-objective optimization of atmospheric and pressurized SOFC based trigeneration systems. **Energy Conversion and Management**, v. 239, p. 114183, jul. 2021.

[50] LIU, Y.; HAN, J.; YOU, H. Exergoeconomic analysis and multi-objective optimization of a CCHP system based on SOFC/GT and transcritical CO2 power/refrigeration cycles. **Applied Thermal Engineering**, v. 230, p. 120686, jul. 2023.

[51] WANG, X.; DUAN, L.; ZHENG, N. Thermodynamic analysis of a novel tri-generation system integrated with a solar energy storage and solid oxide fuel cell – Gas turbine. **Applied Thermal Engineering**, v. 219, p. 119648, jan. 2023.

[52] GAO, B.; ZHOU, Y. Multi-objective optimization and posteriori multi-criteria decision making on an integrative solid oxide fuel cell cooling, heating and power system with semi-empirical model-driven co-simulation. **Energy Conversion and Management**, v. 325, p. 119371, fev. 2025.

[53] WANG, J.; AL-ATTAB, K. A.; YEW HENG, T. Techno-economic and thermodynamic analysis of solid oxide fuel cell combined heat and power integrated with biomass gasification and solar assisted carbon capture and energy utilization system. **Energy Conversion and Management**, v. 280, p. 116762, mar. 2023.

[54] YOU, H. et al. Thermodynamic, exergoeconomic and exergoenvironmental analyses and optimization of a solid oxide fuel cell-based trigeneration system. **International Journal of Hydrogen Energy**, v. 48, n. 66, p. 25918–25938, ago. 2023.

[55] LU, Z. et al. Exergoeconomic evaluation of novel solid oxide fuel cell-integrated solar combined cycle with different solar integration modes. **International Journal of Hydrogen Energy**, v. 48, n. 47, p. 18064–18082, jun. 2023.

[56] GHORBANI, SH. et al. Exergoeconomic and exergoenvironmental analyses of an integrated SOFC-GT-ORC hybrid system. **Energy**, v. 206, p. 118151, set. 2020.

[57] CHITGAR, N.; MOGHIMI, M. Design and evaluation of a novel multi-generation system based on SOFC-GT for electricity, fresh water and hydrogen production. **Energy**, v. 197, p. 117162, abr. 2020.

[58] GRIFFITHS, I. et al. Solid oxide fuel cells with integrated direct air carbon capture: A techno-economic study. **Energy Conversion and Management**, v. 315, p. 118739, set. 2024.

[59] YANG, S. et al. Energy, exergy and exergo-economic analysis of a novel SOFC based CHP system integrated with organic Rankine cycle and

biomass co-gasification. **International Journal of Hydrogen Energy**, v. 53, p. 1155–1169, jan. 2024.

[60] BUDT, M. et al. A review on compressed air energy storage: Basic principles, past milestones and recent developments. **Applied Energy**, v. 170, p. 250–268, maio 2016.

[61] ZHOU, Q. et al. A review of thermal energy storage in compressed air energy storage system. **Energy**, v. 188, p. 115993, dez. 2019.

[62] YAO, E. et al. Multi-objective optimization and exergoeconomic analysis of a combined cooling, heating and power based compressed air energy storage system. **Energy Conversion and Management**, v. 138, p. 199–209, abr. 2017.

[63] HE, X.; LI, C.; WANG, H. Thermodynamics analysis of a combined cooling, heating and power system integrating compressed air energy storage and gas-steam combined cycle. **Energy**, v. 260, p. 125105, dez. 2022.

[64] XU, Z. et al. Thermodynamic and economic analysis of the combined cooling, heating, and power system coupled with the constant-pressure compressed air energy storage. **Journal of Energy Storage**, v. 96, p. 112753, ago. 2024.

[65] RAHIMIMOTLAGH, Z.; AHMADI, A. Energy, exergy, exergoeconomic and exergoenvironmental analysis and optimization of combined solar, SRC cycles with compressed air energy storage (CAES) and methane production system. **Energy Conversion and Management**, v. 317, p. 118855, out. 2024.

[66] RAHBARI, H. R. et al. Quantification of realistic performance expectations from trigeneration CAES-ORC energy storage system in real operating conditions. **Energy Conversion and Management**, v. 249, p. 114828, dez. 2021.

[67] SHI, K.; ASGARI, A. Energy, exergy, and exergoeconomic analyses and optimization of a novel thermal and compressed air energy storage integrated with a dual-pressure organic Rankine cycle and ejector refrigeration cycle. **Journal of Energy Storage**, v. 47, p. 103610, mar. 2022.

[68] XUE, X. et al. Performance analysis of a compressed air energy storage incorporated with a biomass power generation system. **Applied Thermal Engineering**, v. 248, p. 123281, jul. 2024.

[69] DIB, G. et al. Thermodynamic simulation of a micro advanced adiabatic compressed air energy storage for building application. **Applied Energy**, v. 260, p. 114248, fev. 2020.

[70] DIB, G. et al. Modelling small-scale trigenerative advanced adiabatic compressed air energy storage for building application. **Energy**, v. 237, p. 121569, dez. 2021.

[71] ALIRAHMI, S. M.; RAZMI, A. R.; ARABKOOHSAR, A. Comprehensive assessment and multi-objective optimization of a green concept based on a

combination of hydrogen and compressed air energy storage (CAES) systems. **Renewable and Sustainable Energy Reviews**, v. 142, p. 110850, maio 2021.

[72] BAZDAR, E.; NASIRI, F.; HAGHIGHAT, F. An improved energy management operation strategy for integrating adiabatic compressed air energy storage with renewables in decentralized applications. **Energy Conversion and Management**, v. 286, p. 117027, jun. 2023.

[73] MIGLIARI, L.; MICHELETTO, D.; COCCO, D. A hydrogen-fuelled compressed air energy storage system for flexibility reinforcement and variable renewable energy integration in grids with high generation curtailment. **Energy Conversion and Management**, v. 306, p. 118308, abr. 2024.

[74] YANG, Y. et al. Battery energy storage system size determination in renewable energy systems: A review. **Renewable and Sustainable Energy Reviews**, v. 91, p. 109–125, ago. 2018.

[75] HANNAN, M. A. et al. Battery energy-storage system: A review of technologies, optimization objectives, constraints, approaches, and outstanding issues. **Journal of Energy Storage**, v. 42, p. 103023, out. 2021.

[76] MAMA, M. et al. Comprehensive review of multi-scale Lithium-ion batteries modeling: From electro-chemical dynamics up to heat transfer in battery thermal management system. **Energy Conversion and Management**, v. 325, p. 119223, fev. 2025.

[77] ROSATI, A.; FACCI, A. L.; UBERTINI, S. Techno-economic analysis of battery electricity storage towards self-sufficient buildings. **Energy Conversion and Management**, v. 256, p. 115313, mar. 2022.

[78] SARAVANAMUTTOO, H. I. H.; ROGERS, G. F. C.; COHEN, H. **Gas turbine theory**. 7th ed. Harlow, England ; New York: Pearson, 2017.

[79] DIB, G. et al. **Thermodynamic simulation of compressed air energy storage systems**. Lyon: INSA Lyon, 2020.

[80] SIMPSON, A.; LUTZ, A. Exergy analysis of hydrogen production via steam methane reforming. **International Journal of Hydrogen Energy**, v. 32, n. 18, p. 4811–4820, dez. 2007.

[81] DUFFIE, J. A.; BECKMAN, W. A. **Solar Engineering of Thermal Processes**. United States of America: Wiley, 2013. v. Fourth

[82] HOSSEINI, M.; DINCER, I.; ROSEN, M. A. Hybrid solar–fuel cell combined heat and power systems for residential applications: Energy and exergy analyses. **Journal of Power Sources**, v. 221, p. 372–380, jan. 2013.

[83] PETELA, R. Exergy of Heat Radiation. **Journal of Heat Transfer**, 1964.

[84] ZHANG, Y. et al. Thermodynamic analysis of energy conversion and transfer in hybrid system consisting of wind turbine and advanced adiabatic compressed air energy storage. **Energy**, v. 77, p. 460–477, dez. 2014.

[85] ZHANG, Y. et al. The thermodynamic effect of thermal energy storage on compressed air energy storage system. **Renewable Energy**, v. 50, p. 227–235, fev. 2013.

[86] FACCI, A. L. et al. Trigenerative micro compressed air energy storage: Concept and thermodynamic assessment. **Applied Energy**, v. 158, p. 243–254, nov. 2015.

[87] INCROPERA, FRANK. P. et al. (EDS.). **Introduction to heat transfer**. 6th ed. Hoboken, NJ: Wiley, 2011.

[88] SHAPIRO, H. N.; MORAN, M. J. **Fundamentals of Engineering Thermodynamics**. 5th ed. United Kingdom: John Wiley & Sons Ltd, 2006.

[89] ZHAO, X. et al. Biogas Reforming to Syngas: A Review. **iScience**, v. 23, n. 5, p. 101082, maio 2020.

[90] CHOUHAN, K. et al. Simulation of steam reforming of biogas in an industrial reformer for hydrogen production. **International Journal of Hydrogen Energy**, v. 46, n. 53, p. 26809–26824, ago. 2021.

[91] JARUNGTHAMMACHOTE, S.; DUTTA, A. Thermodynamic equilibrium model and second law analysis of a downdraft waste gasifier. **Energy**, v. 32, n. 9, p. 1660–1669, set. 2007.

[92] KAUR, G. **Solid Oxide Fuel Cell Components**. Switzerland, Springer International Publishing, 2016.

[93] COLPAN, C.; DINCER, I.; HAMDULLAHPUR, F. Thermodynamic modeling of direct internal reforming solid oxide fuel cells operating with syngas. **International Journal of Hydrogen Energy**, v. 32, n. 7, p. 787–795, maio 2007.

[94] NI, M.; LEUNG, M. K. H.; LEUNG, D. Y. C. Parametric study of solid oxide fuel cell performance. **Energy Conversion and Management**, v. 48, n. 5, p. 1525–1535, maio 2007.

[95] CHOI, P. A simple model for solid polymer electrolyte (SPE) water electrolysis. **Solid State Ionics**, v. 175, n. 1–4, p. 535–539, nov. 2004.

[96] GHOLAMIAN, E. et al. Evolutionary based multi-criteria optimization of an integrated energy system with SOFC, gas turbine, and hydrogen production via electrolysis. **International Journal of Hydrogen Energy**, v. 43, n. 33, p. 16201–16214, ago. 2018.

[97] KIANFARD, H.; KHALILARYA, S.; JAFARMADAR, S. Exergy and exergoeconomic evaluation of hydrogen and distilled water production via combination of PEM electrolyzer, RO desalination unit and geothermal driven dual fluid ORC. **Energy Conversion and Management**, v. 177, p. 339–349, dez. 2018.

[98] ZHANG, X. et al. Conventional and energy level based exergoeconomic analysis of biomass and natural gas fired polygeneration system integrated with ground source heat pump and PEM electrolyzer. **Energy Conversion and Management**, v. 195, p. 313–327, set. 2019.

[99] NI, M.; LEUNG, M. K. H.; LEUNG, D. Y. C. Energy and exergy analysis of hydrogen production by a proton exchange membrane (PEM) electrolyzer plant. **Energy Conversion and Management**, v. 49, n. 10, p. 2748–2756, out. 2008.

[100] COSTAMAGNA, P. et al. Electrochemical model of the integrated planar solid oxide fuel cell (IP-SOFC). **Chemical Engineering Journal**, v. 102, n. 1, p. 61–69, ago. 2004.

[101] CHOUDHARY, T.; SANJAY. Thermodynamic assessment of SOFC-ICGT hybrid cycle: Energy analysis and entropy generation minimization. **Energy**, v. 134, p. 1013–1028, set. 2017.

[102] TIAN, M. et al. Thermodynamic analysis of an integrated solid oxide fuel cell, Organic Rankine Cycle and absorption chiller trigeneration system with CO2 capture. **Energy Conversion and Management**, v. 171, p. 350–360, set. 2018.

[103] AKRAMI, E. et al. Exergy and exergoeconomic assessment of hydrogen and cooling production from concentrated PVT equipped with PEM electrolyzer and LiBr-H2O absorption chiller. **International Journal of Hydrogen Energy**, v. 43, n. 2, p. 622–633, jan. 2018.

[104] NAFCHI, F. M. et al. Performance assessment of a solar hydrogen and electricity production plant using high temperature PEM electrolyzer and energy storage. **International Journal of Hydrogen Energy**, v. 43, n. 11, p. 5820–5831, mar. 2018.

[105] URSÚA, A.; GANDIA, L. M.; SANCHIS, P. Hydrogen Production From Water Electrolysis: Current Status and Future Trends. **Proceedings of the IEEE**, v. 100, n. 2, p. 410–426, fev. 2012.

[106] URSÚA, A. et al. Influence of the power supply on the energy efficiency of an alkaline water electrolyser. **International Journal of Hydrogen Energy**, v. 34, n. 8, p. 3221–3233, maio 2009.

[107] SÁNCHEZ, M. et al. Semi-empirical model and experimental validation for the performance evaluation of a 15 kW alkaline water electrolyzer. **International Journal of Hydrogen Energy**, v. 43, n. 45, p. 20332–20345, nov. 2018.

[108] HEYWOOD, J. B. **Internal combustion engine fundamentals**. 2nd ed. New York: McGraw-Hill, 1988.

[109] HEROLD, K. E.; RADERMARCHER, R.; KLEIN, S. A. **Absorption Chillers and Heat Pumps**. 2nd ed. United States of America: CRC Press, 2016.

[110] MAROCCO, P. et al. Optimal design of stand-alone solutions based on RES + hydrogen storage feeding off-grid communities. **Energy Conversion and Management**, v. 238, p. 114147, jun. 2021.

[111] LI, D. et al. Combined capacity and operation optimisation of lithium-ion battery energy storage working with a combined heat and power system. **Renewable and Sustainable Energy Reviews**, v. 140, p. 110731, abr. 2021.

[112] KLEIN, S.; NELLIS, G. **Thermodynamics**. 1st ed. United States of America: Cambridge University Press, 2012.

[113] BEJAN, A.; TSATSARONIS, G.; MORAN, M. **Thermal Design & Optimization**. 1st ed. United States of America: John Wiley & Sons Ltd, 1996.

[114] TSATSARONIS, G.; CZIESLA, F. Thermoeconomics. Em: **Encyclopedia of Physical Science and Technology**. 3rd ed. United States of America: Elsevier, 2001.

[115] BANIAMERIAN, Z. et al. How pressure affects costs of power conversion machinery in compressed air energy storage; Part I: Compressors and expanders. **Journal of Energy Storage**, v. 89, p. 111791, jun. 2024.

[116] SU, D. Comprehensive thermodynamic and exergoeconomic analyses and multi-objective optimization of a compressed air energy storage hybridized with a parabolic trough solar collectors. **Energy**, v. 244, p. 122568, abr. 2022.

[117] RAZMI, A. et al. Thermodynamic and economic investigation of a novel integration of the absorption-recompression refrigeration system with compressed air energy storage (CAES). **Energy Conversion and Management**, v. 187, p. 262–273, maio 2019.

[118] GREENER. **Estudo Estratégico: Geração Distribuída 2024**. Available at: <https://www.greener.com.br/estudo/estudo-estrategico-geracao-distribuida-2024/>.

[119] BANIAMERIAN, Z. et al. How pressure affects costs of power conversion machinery in compressed air energy storage; Part I: Compressors and expanders. **Journal of Energy Storage**, v. 89, p. 111791, jun. 2024.

[120] OUR WORLD IN DATA. **Carbon intensity of electricity generation**. Available at: <https://ourworldindata.org/grapher/carbon-intensity-electricity?tab=chart&country=BRA~FRA>. Accessed at: 30 jul. 2024.

[121] EMPRESA DE PESQUISA ENERGÉTICA. **Metodologia: projeção de curva de carga horária**. , 2020. Available at: <https://www.epe.gov.br/sites-pt/publicacoes-dados-abertos/publicacoes/PublicacoesArquivos/publicacao-476/NT%20Metodologia%20Proje%C3%A7%C3%A3o%20Carga%20Hor%C3%A1ria_EPE-NT-EPE-DEA-005-2020.pdf>

[122] PROCEL. **Relatório com cenário tendencias sobre posse de equipamentos elétricos e os impactos na demand por energia elétria - Análise dos resultados da PPH 2019**. Brazil, 2023. Available at: <https://www.gov.br/mme/pt-br/assuntos/ee/publicacoes-e-estudos/RelatorioP2_Final.pdf>

[123] ASSOCIATION INTERPROFESSIONNELLE POUR LE DÉVELOPPMENT DE L'EFFICACITÉ ÉNERGÉTIQUE. **Carte des zones climatiques**. Available at: <https://www.aidee.fr/upload/actu/document/Carte_des_zones_climatiques.pdf>.

[124] NATURGY. **Tarifas - Rio de Janeiro**. Available at: <https://www.naturgy.com.br/atendimento/tarifas/tarifa_rio_de_janeiro/>. Accessed at: 16 fev. 2025.

[125] LIGHT. **Tarifas Baixa Tensão**. Available at: <https://www.light.com.br/Documentos%20Compartilhados/Entenda-Conta-Casa-Arquivos-Relacionados/Tarifas%20Baixa%20Tens%C3%A3o.pdf>. Accessed at: 16 fev. 2025.

[126] AGENCE FRANCE ELECTRICITÉ. **Quel est le prix de l'électricité à Lyon ?** Available at: <https://www.agence-france-electricite.fr/prix-electricite/ville/lyon/>. Accessed at: 16 fev. 2025.

[127] GLOBAL PETROL PRICE. **France natural gas price**. Available at: <https://www.globalpetrolprices.com/France/natural_gas_prices/>. Accessed at: 16 fev. 2025.

[128] ANTONY, J. **Design of Experiments for Engineers and Scientists**. 2nd ed. United Kingdom, Elsevier, 2014.

[129] SUNPOWER. **210 Solar Panel**. 2007.

[130] IOROI, T. et al. Thin film electrocatalyst layer for unitized regenerative polymer electrolyte fuel cells. **Journal of Power Sources**, v. 112, n. 2, p. 583–587, nov. 2002.

[131] CROTOGINO, F.; MOHMEYER, K. U.; SCHARF, D. R. **Huntorf CAES: More than 20 Years of Successful Operation**. At: SOLUTION MINING RESEARCH INSTITUTE (SMRI) SPRING MEETING. 2001.

[132] XIA, C. et al. A simplified and unified analytical solution for temperature and pressure variations in compressed air energy storage caverns. **Renewable Energy**, v. 74, p. 718–726, fev. 2015.

[133] KUSHNIR, R.; DAYAN, A.; ULLMANN, A. Temperature and pressure variations within compressed air energy storage caverns. **International Journal of Heat and Mass Transfer**, v. 55, n. 21–22, p. 5616–5630, out. 2012.

[134] RAJU, M.; KUMAR KHAITAN, S. Modeling and simulation of compressed air storage in caverns: A case study of the Huntorf plant. **Applied Energy**, v. 89, n. 1, p. 474–481, jan. 2012.

[135] TAO, G.; VIRKAR, A. Intermediate temperature solid oxide fuel cell (IT-SOFC) research and development activities at MSRI. **Nineteenth annual ACERC&ICES conference, Utah**, fev. 2005.

[136] MAHMOUDI, S. M. S.; KHANI, L. Thermodynamic and exergoeconomic assessments of a new solid oxide fuel cell-gas turbine cogeneration system. **Energy Conversion and Management**, v. 123, p. 324–337, set. 2016.

[137] WORLD BANK. **State and Trends of Carbon Pricing 2024**. Washington, DC, 2024.

[138] VALERO, A.; VALERO, A. Thermodynamic Rarity and the Loss of Mineral Wealth. **Energies**, v. 8, n. 2, p. 821–836, 26 jan. 2015.

[139] SMITH, J. M. et al. **Introduction to chemical engineering thermodynamics**. 8th ed. United States of America: McGraw-Hill Education, 2018.

[140] ELLIOT, J. R.; LIRA, C., T. **Introductory Chemical Engineering Thermodynamics**. 2nd ed. United States of America: Pearson, 2012.

[141] NIST. **NIST Chemistry WebBook**. Available at: <https://webbook.nist.gov/chemistry/>. Accessed at: 18 dez. 2024.

[142] POLING, B. E.; PRAUSNITZ, J. M.; O'CONNEL, J. P. **The Properties of Gases and Liquids**. 5th ed. United States of America: McGraw Hill, 2001.

[143] LEMMON, E. W.; HUBER, M. L.; MCLINDEN, M. O. **NIST Standard Reference Database 23: Reference Fluid Thermodynamic and Transport Properties-REFPROP, Version 9.1**. , 2013.

[144] SANSON PORTELLA CARVALHO, J. E. et al. Numerical assessment of critical properties of nanofluids: Applications to nanorefrigerants and nanolubricants. **Journal of Molecular Liquids**, v. 318, p. 113938, nov. 2020.